Application of a Discrete Element Model to the Analysis of Granular Soil Recovery in an Offshore Tubular Vibrocore

Prepared by

Sam Bryant Wegener

A dissertation submitted in partial fulfilment of the requirements for a Master of Science in Civil Engineering

Prepared for

Dr Denis Kalumba (supervisor)

Johnny Lai Sang (co-supervisor)

Gert Raubenheimer (co-supervisor)

University of Cape Town

Department of Civil Engineering

September 2015

Preface

This dissertation was prepared for Dr Denis Kalumba in partial fulfilment of the requirements for the degree of Master of Science in Engineering, in Civil Engineering.

The research described in this dissertation was conducted as part of the Research and Development Department of De Beers Marine Pty(Ltd) – henceforth referred to as DBM. The research objectives were developed to align with the interests of DBM, and the investigation was facilitated by DBM software and equipment. However, this dissertation is the product of the Civil Engineering Department of the University of Cape Town.

I, Sam Bryant Wegener, declare that I know the meaning of plagiarism and that all of the work in this dissertation, save for that which is properly acknowledged, is my own. I have used the Harvard method for citation and referencing.

Mr Sam Bryant Wegener
MSc Candidate

Signed by candidate

30/09/2015
Date

Dr Denis Kalumba
Senior Lecturer - University of Cape Town

Signed by candidate

30/09/2015
Date

Mr Johnny Lai Sang
Engineer - De Beers Marine Pty(Ltd)
Co-Supervisor

Signed

Signed

23/09/2015
Date

Mr Gert Raubenheimer
Engineer - De Beers Marine Pty(Ltd)
Co-Supervisor

Signed

Signed

23/09/2015
Date

"Essentially, all models are wrong, but some are useful..."

George E.P. Box - 1987

Application of a Discrete Element Model to the Analysis of Granular Soil Recovery in an Offshore Tubular Vibrocore

A dissertation submitted in partial fulfilment of the requirements for a Master of Science in Civil Engineering, at the University of Cape Town

Prepared by

Sam Bryant Wegener

Supervised by Dr Denis Kalumba

Co-supervised by Johnny Lai Sang and Gert Raubenheimer

For my parents

Acknowledgements

Firstly, my sincere thanks to my supervisor, Dr Denis Kalumba, whose enthusiasm, knowledge, and consideration throughout the review of my work was and is greatly appreciated. His passion for geotechnical engineering was contagious and his attention to detail highly motivational.

I am extremely grateful to De Beers Marine Pty(Ltd) for funding my second year of postgraduate study, for allowing me to use their equipment, resources, and modelling software, and for accommodating me in their fine offices during completion of this research. The hospitality, approachability, and professionalism of the DBM staff made working in the offices and test facility an enjoyable experience. Special thanks must go to my co-supervisors, Mr Johnny Lai Sang and Mr Gert Raubenheimer, whose expertise, interest and feedback were invaluable contributions. Without their help, this dissertation would not have been possible.

I also wish to express my appreciation to the following people:

- Oscar Peterson and his team: Siza Mashicolo, Siphiwo Mgedle, Zandiba Seti, and Emecca Tsala. Their swift, precise and expert help with the physical testing is very much appreciated.
- Imraan Parker, for his assistance with the operation and licensing of Rocky DEM software
- Urban Burger and Gerhard de Vries, for taking the time to provide detailed information that supported this research.
- The staff of the UCT Civil Engineering Laboratory, for their guidance and help with obtaining and using laboratory equipment
- My undergraduate bursars, Stefanutti Stocks Marine (Pty) Ltd, for allowing me the opportunity to pursue postgraduate research, and for playing a significant role in fuelling my passion for engineering
- The UCT Postgraduate Funding Office, for their funding assistance over the course of my masters
- And lastly, thanks to my friends for their support during my completion of this work. With your help, many a woblem can be solved.

Synopsis

Background and objectives

As the human need for ocean resources accelerates, offshore geotechnics continues to grow and become ever more relevant. Seabed soil sampling is crucial in deep-water engineering projects or geological studies where a detailed knowledge of the seabed geology is required. Deep-sea vibrocoring is a relatively new offshore sampling technique. The system consists of a vertical, tubular core barrel with a sharp cutting edge at its lower end vibrated into the seabed by a high-frequency, low-amplitude vibratory motor.

In the past, success of a coring operation has been judged primarily by the length of the recovered core. More recently, studies have given focus to the problems associated with achieving soil specimens in which the in-situ sedimentary structure is preserved. In practice, the core recovery ratio - defined as the ratio between the sampled length of core sediment and the length of core barrel penetrated into the soil - is frequently less than unity. Literature suggests that the physical processes governing the dynamic interaction between core barrel and soil are poorly understood. Through review of relevant literature, and the execution of both physical testing and numerical modelling, this study aimed to a) Develop a calibrated 3D discrete element model of a given vibrocore-soil system, and b) Investigate the soil mechanics phenomena influencing the disturbance and recovery of vibrocore soil samples.

Review of literature

Background research was conducted to aid the completion and interpretation of physical testing and numerical modelling, as well as provide insight into the engineering concepts essential to this dissertation. It began with a broad overview of marine sediments and offshore subsoil exploration. This was followed by a more detailed study of pertinent seabed coring techniques. The concept of core sample quality was then developed, with focus given to various factors that influence sample quality. This led to a critical review of the physical processes that govern recovery in core samples. Lastly, the theory and limitations of the discrete element method (DEM) were summarised and relevant applications of the method studied.

According to literature, a decrease in core recovery within a descending sample tube often results due to a 'soil plug' forming within the core barrel. Plugging occurs when friction between the inner wall of the barrel and the accumulating sediment column imposes a vertical stress on the soil immediately below the core aperture that exceeds the bearing capacity of the soil. This leads to the soil immediately below the cutting head flowing around, rather than entering, the barrel. The extent of soil plugging in a sample is a highly non-linear phenomenon dependent on a number of vibrocore system variables.

In developing an understanding of how the soil plug mechanism is influenced by the cyclic action of vibrocores, a clear lack of geotechnical literature on the subject was noted. To date, no studies have been found that investigate the recovery of gravels in offshore vibrocores.

Physical sonic vibrocore testing

All physical testing was conducted using a large-scale Sonic VibroCore (SVC) test rig at the DBM Research and Development Test Facility in Paarden Eiland, Cape Town. The soil samples used were poorly-graded gravels consisting mostly of hard, quartzitic sandstone particles. Grain sizes ranged

between 16mm and 64mm in diameter. Seven separate core sampling 'tests' were conducted. For each test, the boundary conditions, gravel grading, sample preparation and core barrel penetration properties were, as close as practically possible, held constant.

For the seven samples tested the average initial void ratio was 0.51 and the average specific gravity of particles 2.474. Core barrel inner and outer diameter were 150.4mm and 177.8mm, respectively. Penetration rate and motor rotation frequency were manually operated to be 24mm/s and 157Hz, respectively. Final penetration depth was ~1.975m. During testing, the following variables were measured: core barrel penetration rate, motor rotation frequency, vertical force on core barrel, core barrel vibratory amplitude and cumulative recovery ratio.

Results showed that the core recoveries were poor, averaging 53%. For all tests, the change in vertical force acting on the core barrel with penetration depth showed similar increasing trends, with the maximum compressive force on the barrel approximately 65kN. This peak force occurred within the final ~0.25m of penetration. A decrease in recovery with increasing void ratio was observed. During the descent of the core barrel, its harmonic displacement amplitude increased from ~0.34mm to ~0.50mm, indicating a marked increase in the soil stiffness with penetration depth.

Numerical discrete element modelling

The physical testing provided input data for the assembly and calibration of the DEM model. All numerical modelling was completed using Rocky Discrete Element Method (DEM) Software. It was deemed impractical to investigate the modelling of soil particle sizes smaller than that of the gravels tested. This was due to a) The unique problems associated with coring into gravel observed in the past by DBM engineers, and b) The exponential increase in DEM computational requirements with decreasing particle size.

To reduce the computational expense of the modelled gravel micro-scale behaviour, the percentage of spherical particles in the simulated soil was far higher than that of the observed true soil. Simpler particle geometries yielded lower computational demands. Nonetheless, the gravel was modelled to include a fraction of angular and sub-angular particles: 11%. The specification of particle friction and stiffness properties was based on recommendations made in relevant literature. The specific gravity and void ratio of the simulated soil, as well as the core barrel geometry, frequency, amplitude, and penetration rate, were based on that measured during physical testing.

Through use of statistical methods, the difference between the numerical and physical results was shown to be negligible. Force-penetration plots and cumulative recovery ratios were the basis for comparison. Therefore, the DEM model was considered an accurate simplified representation of the more complex physical system. Further assessment of the numerical output showed that the vibrocore penetrated in a primarily partially plugged mode, with significant compaction occurring below the cutting head. The 'bulb' of influence extending below the base of the descending barrel in which soil was disturbed was approximately 0.65m in height. This was estimated through analysis of the change in void ratio of various soil elements below the penetrating cutting head. The density of soil within the sample tube decreased from a maximum at the cutting head base to a minimum at the top of sampled core.

Table of Contents

List of figures

List of tables

Notation

The selection of notation in this dissertation was based on the standard nomenclature adopted by the International Society of Soil Mechanics and Geotechnical Engineering (ISSMGE). However, some symbols have been selected to conform to other engineering or mathematical disciplines incorporated into this dissertation. The distinctions are made clear in the text.

Symbols are defined where they first appear in the text. Those which appear several times are listed below. When a symbol represents a quantity having dimensions, the dimensions are listed along with the symbol. The SI unit convention was utilised. If no dimension is indicated, the symbol represents a number.

Acronyms

2D	Two-dimensional
3D	Three-dimensional
API	American Petroleum Institute
ARH	Angular; High sphericity
ARL	Angular; Low sphericity
ARM	Angular; Medium sphericity
BS	British Standard
CPT	Cone penetration test
DBM	De Beers Marine Pty(Ltd)
DEM	Discrete Element Method
ESSS	Engineering Simulation and Scientific Software
FEM	Finite Element Method
HAR	Horizontal Aspect Ratio
ICR	Inside Clearance Ratio
IFR	Incremental Filling Ratio
ISSMGE	International Society for Soil Mechanics and Geotechnical Engineering
KS	Kolmogorov-Smirnov
KSR	Kolmogorov-Smirnov Ratio
NGI	Norwegian Geotechnical Institute
OCR	Outside Clearance Ratio
PC	Portable Computer
PSD	Particle Size Distribution
PSM	Particle Shape Matrix
RDH	Rounded: High sphericity
RDL	Rounded; Low sphericity
RDM	Rounded; Medium sphericity
RR	Recovery Ratio
SAH	Sub-angular; High sphericity
SAL	Sub-angular: Low sphericity
SAM	Sub-angular; Medium sphericity
SG	Strain Gauge
SI	*Systéme International*
SQD	Superquadric Degree
SRH	Sub-rounded: High sphericity
SRL	Sub-rounded; Low sphericity
SRM	Sub-rounded; Medium sphericity
STACOR	Stationary Piston Corer
SVC	Sonic Vibrocore
SWGOSIF	Subsea Working Group of the Offshore Soil Investigation Forum

UCT	University of Cape Town
VAR	Vertical Aspect Ratio

Symbols

a (m/s^2)	Acceleration
A (m/s^2)	Acceleration amplitude
A_B (m^2)	Cross-sectional area of core barrel
A_{Bi} (m^2)	Cross-sectional area inside core barrel
A_R	Area ratio of sampler cutting head
C	Coefficient of variability
c_{eq}	Equivalent damping coefficient
C_U	Coefficient of uniformity
C_Z	Coefficient of curvature
d (m)	Penetration depth
D_{be} (m)	External diameter of the core barrel
D_{bi} (m)	Inside diameter of the core barrel
d_{crit} (m)	Critical penetration depth
D_e (m)	External diameter of sampler cutting head
dF (N)	Incremental friction force
D_i (m)	Inside diameter of sampler cutting head
D_r	Relative density
D_{sb} (m)	Inside diameter of sample bin
dz (m)	Incremental soil element thickness
E (N/m^2)	Young's modulus of elasticity
e	void ratio
e	Base of natural logarithms (Euler's number)
e_0	Initial void ratio
E_B (N/m^2)	Stiffness of core barrel material
F (N)	Force
F'_v (N)	Effective vertical force
F_B (N)	Vertical force on core barrel
f_n (Hz)	Undamped natural frequency
f_r (Hz)	Frequency of rotation
G_s	Specific gravity
h (m)	Height of soil element
H_{sb} (m)	Height of soil within sample bin
I_d	Disturbance index
k (N/m)	Linear/Normal stiffness
K	Lateral earth pressure coefficient
K_0	At-rest lateral earth pressure coefficient
K_a	Active lateral earth pressure coefficient
K_{max}	Maximum K
K_p	Passive lateral earth pressure coefficient
K_{avg}	Average between K_a and K_p
k_{eq} (N/m)	Equivalent stiffness
k_m (N/m)	Stiffness due to motor
k_s (N/m)	Stiffness due to soil
l (m)	Depth from top of soil plug to soil disc element
L (m)	Height of soil sampled within core barrel; Length of soil plug
m (kg)	Mass
m_0 (kg)	Mass of empty sample bin
m_1 (kg)	Mass of sample bin and dry gravel

m_2 (kg)	Mass of sample bin and saturated gravel
m_{ru} (kg)	Mass of rotating unbalance
m_s (kg)	Mass of soil particles
P (MPa)	Hydraulic pressure of SVC system
P_B (m)	Core barrel perimeter
q_{ub} (N/m^2)	Ultimate bearing capacity pressure
r (m)	Radius of rotation
r	Correlation coefficient
t (s)	Time
t_s (s)	Time of Rocky simulation
v (m/s)	Velocity
V (m^3)	Volume
V_s (m^3)	Volume of solids
V_{TOT} (m^3)	Total volume of soil sample
V_v (m^3)	Volume of voids
V_W (m^3)	Volume of water
w_d (N)	Weight of dynamic SVC components
x (m)	Displacement
$\dot{x}$ (m/s)	Velocity of particle
$\ddot{x}$ (m/s^2)	Acceleration of particle
X (m)	Harmonic response magnitude
β	Frequency ratio
γ' (N/m^3)	Effective unit weight
δ (degrees)	Interface friction angle
ε	Strain
ε_B	Core barrel axial strain
ε_{B1}	Core barrel axial strain calculated using Eq. A3.2
ε_{B2}	Core barrel axial strain calculated using Eq. A3.3
ε_{Bm}	Measured core barrel axial strain
ε_C	Strain of SVC cradle
ζ	Damping ratio
θ (rad)	Angular displacement
μ	Statistical mean
ρ (kg/m^3)	Density
ρ_s (kg/m^3)	Density of physical soil particles
ρ_{sm} (kg/m^3)	Density of modelled soil particles
ρ_w (kg/m^3)	Density of water
σ	Standard deviation
σ_v (N/m^2)	Vertical stress
τ (N/m^2)	Shear stress
ϕ (degrees)	Angle of internal friction
ω_n (rad/s)	Undamped natural frequency
ω_r (rad/s)	Angular frequency of rotation

Units

Hz	Hertz (cycles per second)
kg	Kilogram
m	Metre
mm	Millimetre
kN	Kilonewton
N	Newton
rad	Radians
s	Seconds
t	Tonne
Ω	Ohm

1. Introduction

1.1. Background and context

1.1.1. Vibrocoring: History and basic description

Vibrocoring is a technique used to sample soil in both onshore and offshore geotechnical practice. It is a form of drive sampling where a hollow, cylindrical core barrel, with a sharp cutting edge at its lower end, is driven into the ground by vibratory means (Fig. 1.1). This distinguishes vibrocoring from percussion coring where the coring tube is hammered, not vibrated, into the soil. Vibrocoring, also sometimes referred to as vibracoring, was developed in the 1960s. According to Woodward and Sloss (2013), early devices relied on a vertical 'pile-driving' effect from a modified jack hammer. Only in the late 1970s was a true mechanical vibration effect engineered by mounting a concrete vibrator onto the sampling tube.

Weaver and Schultheiss (1990) claimed that the success of a coring operation has too often been judged primarily by the length of the recovered core. More recently, geotechnical studies have given focus to the problems associated with achieving a soil specimen of higher quality. When assessing the quality of a soil sample obtained through coring, Lunne and Long (2006) claim that there are two aspects that need to be considered: a) The influence of the sampling process on the laboratory measured mechanical properties of the soil specimen – i.e. the disturbance of the core sample, and b) Whether or not the sample is representative of the depth from which it is thought to have been recovered - i.e. the recovery ratio (RR) of the core sample. The RR is defined as the ratio between the recovered length of core sediment and the length of core barrel penetrated into the soil. Therefore, an ideal specimen, in which the stratigraphy of the sampled ground is preserved, would have a recovery ratio of unity. However, due to the physical processes governing barrel-soil interaction during vibrocore penetration, ideal recovery is very rarely achieved in practice.

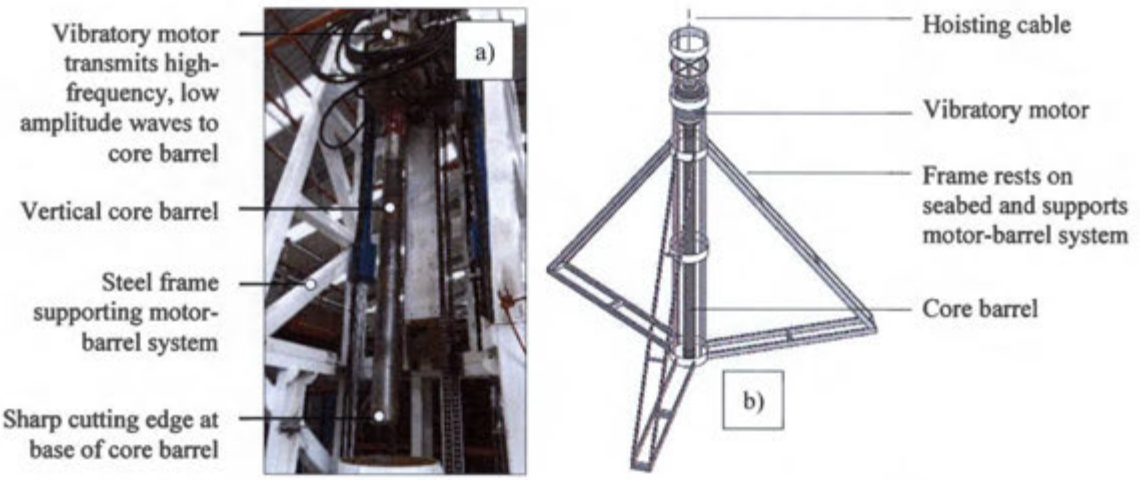

Figure 1-1: a) Land-based vibrocore test rig; b) Typical seabed vibrocore rig

1.1.2. The need for offshore subsoil exploration

The importance of a geotechnical site investigation in successful onshore engineering practice is emphasised commonly in geotechnical engineering texts (e.g. Clayton *et al.*, 1995; Craig, 2004; Das, 2010; Shukla & Sivakugan, 2011). Offshore practice is no different. The motives for offshore subsoil exploration or seabed sampling depend on the nature of the project in question. Very rarely are explorations conducted without an end objective in mind (Fugro, 2001). A list of potential reasons for performing subsoil exploration was given by Das (2010). Of these reasons, the two most relevant to deep-water vibrocoring would be: a) Determining the nature of soil at the site and its stratification, and b) Obtaining disturbed and undisturbed soil samples for visual identification and appropriate laboratory tests. Both the above-described tasks are common to offshore projects where a detailed knowledge of the seabed geology is crucial. Such projects include:

- Marine geological studies, where records of the palaeoenvironment are developed (Skinner & McCave, 2003),
- Deep-water mining, where seabed mineral and aggregate prospecting is required (Fugro, 2001), or
- Subsea structure design, where acquiring subsoil data is essential towards facilitating successful foundation design, installation and operational integrity (Power & Colliat, 2000).

1.1.3. Offshore geotechnics: A growing and unique discipline

Over the past 30 years, the fields of offshore and onshore geotechnical engineering have tended to diverge. Offshore geotechnics grew out of onshore practice. However, the two fields are distinguished by fundamental differences in geology, site investigation techniques and construction methods. For example, offshore site investigations are far more expensive than those of onshore practice, typically costing several million US dollars. Seabed soils often differ radically from onshore soils due to factors such as marine organism remains, gas seeps, and seabed landslides (Randolph & Gourvenec, 2011).

Thus, according to Dean (2010), offshore geotechnical engineering is now considered a mature, specialised discipline of civil engineering, with its own unique challenges. It requires knowledge from a number of physical science and engineering fields, including structural engineering, marine geology, geophysics, fluid mechanics, and oceanography. Jeng and Brandes (2011) state that offshore geotechnics will continue to grow and become ever more relevant as human need for ocean resources accelerates.

At this stage, it worth defining the term 'offshore'. It is easier to do so by first considering the term 'coastal', as the two words are often confused. 'Coastal' refers to the zone where the land meets the sea – a region of indefinite width that extends inland from wave-influenced shores

to the first major change of topography (United States Army Corps of Engineers, 2006). Conversely, 'offshore' refers to environments at greater distances from shore. Offshore wave climates are dissimilar to that of coastal regions and water depths are greater, reaching up to thousands of metres. Typically, turbulence from offshore or 'deep-water' wave action does not lift seabed sediments into suspension.

1.1.4. Overview of numerical methods in geomechanics

Due to its inherently particulate nature, natural soil is anisotropic, heterogeneous, and exhibits a complex stress-strain relationship. The complexity of real soil response to imposed loading or changing boundary conditions is recognised and discussed widely in geotechnical engineering literature (e.g. Lambe and Whitman, 1969; Das, 2010; Lees, 2012). To simulate or approximate soil behaviour, various numerical methods have been developed and used in the field of geomechanics. These methods are split into two categories: continuum methods or particle-based methods. The latter includes the discrete element method (DEM).

Successful use of numerical continuum methods in geomechanics is well-documented (e.g. Potts and Zdravković, 1999). Such methods include the finite-difference and finite-element methods (FEM). In these analyses, the soil is idealised as a continuum, the behaviour of which is defined mathematically by some constitutive (stress-strain) relation. Clark and Hird (2012) emphasise that the accuracy of such analyses depends strongly on the quality of the underlying constitutive models.

The selection of a constitutive law is, according to Cundall (2001), a major drawback in using continuum methods in geomechanics. Naylor (1978) and Cundall and Strack (1979) wrote that, to date, no satisfactory constitutive relationships had been established. More recent texts suggest the same: Potts and Zdravković (1999) and Lees (2012) both claim that there exists no single stress-strain law capable of capturing all aspects of soil behaviour with a reasonable number of input parameters. While many hundreds of constitutive soil models have been developed and used, each model has its own strengths and weaknesses, and are often "excessively complicated with many obscure parameters" (Cundall, 2001:41). In addition, O'Sullivan *et al.* (2006) state that the continuum approach does not explicitly consider the particle-scale interactions underlying the macro-scale soil response.

The discrete, or distinct, element method (DEM) was developed by Cundall and Strack (1979). It is a particle-based numerical method that captures the complicated behaviour of the soil material with simple assumptions and contact laws at interparticle contacts. However, particle-based numerical methods, developed almost 40 years ago, are currently not used widely in geomechanics in place of continuum methods. Cundall (2001) provides an explanation: Application of the DEM to large-scale problems is currently difficult or impossible due to its high computational demands; only within 20 years will it be feasible for particle-based analyses to replace continuum analyses.

1.2. Numerical modelling: Its value in geotechnical practice

Modelling is defined by Barbour and Krahn (2004) as the process by which a simplified mathematical system is constructed from a more complex physical reality to serve as a basis for design. Numerical methods (or models), such as the FEM or DEM, are often used to assist in developing the appropriate mathematical abstraction or approximation. This is different to analytical methods, where an exact or 'closed form' solution is obtained. Burland (1987) presented a view on the role of modelling in geotechnical engineering: He forwarded that geotechnical practice requires an understanding of a) The ground profile established from a site investigation, b) The definition of soil behaviour provided from field and laboratory measurements, and c) The application of this understanding through the use of modelling. These three parts were linked to form what is now referred to as the 'Burland Triangle'. Barbour and Krahn (2004) state the Burland Triangle (Fig. 1.2) has been discussed widely and expanded considerably since it was first introduced. It is worth noting that all three parts of the triangle are interlinked and supported by experience.

The ideas of Barbour and Krahn (2004) and Burland (1987) can be applied to the context of this dissertation. A model calibrated to the physical testing of a vibrocore-soil system provides a means to further understand the observed soil behaviour of this seabed-sampling system. In the case of a DEM model, insight into the particle-scale interactions between vibrocore and soil is provided. In addition, a calibrated model allows multiple vibrocoring 'tests' to be computed without additional costs due to labour, equipment, materials, or fuel. Such simulations may be conducted to investigate the influence of various system parameters on soil recovery – e.g. vibrational frequency and amplitude, rate of core barrel penetration, or core barrel geometry.

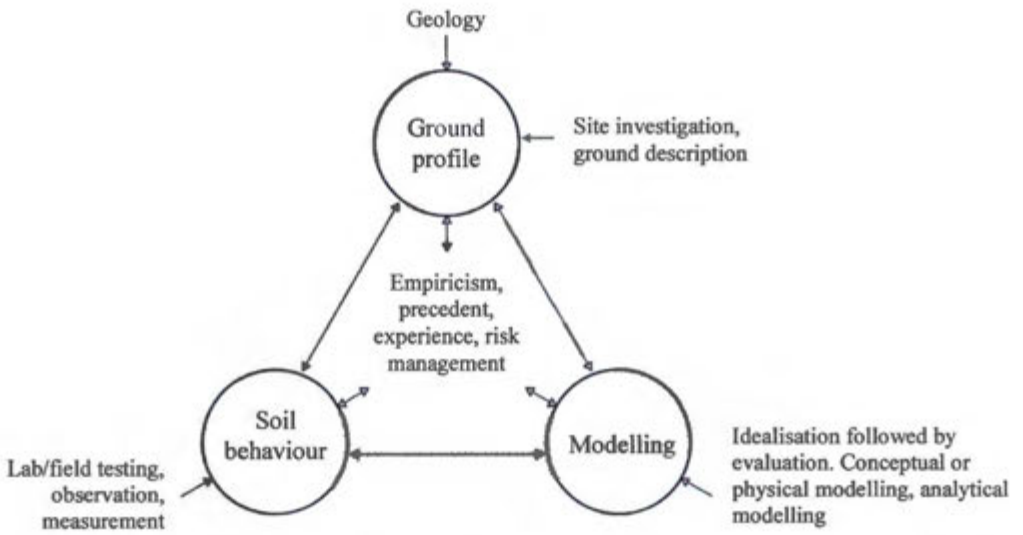

Figure 1-2: The expanded Burland Triangle
Adapted from Barbour and Krahn (2004)

1.3. Themes and objectives of study

1.3.1. Objectives

The main objective of this study was to – through reviewing relevant literature and conducting physical testing and numerical modelling - identify and investigate the soil mechanics phenomena controlling the recovery of granular seabed soils in vibrocores. In doing so, the following sub-objectives were developed:

- Calibrate a three-dimensional (3D) DEM model to the physical results of vibrocoring tests conducted in saturated soil,
- Assess the physical results, offering insight into the observed macro-scale response of the vibrocoring system, including soil recovery and forces required for barrel penetration, and
- Assess the numerical results, offering insight into the modelled micro-scale response of the vibrocoring system, including barrel-soil interaction and soil deformation below the penetrating barrel head

1.3.2. Scope and delimitation

Soil and structural mechanics formed the basis of this study, which focussed on the physical processes governing the dynamic penetration of an open-ended, rigid, tube into a granular medium.

All physical testing was conducted at the DBM Research and Development Test Facility in Paarden Eiland, Cape Town. The facility consists of various model-scale and large-scale equipment for the analysis of offshore mining operations. A large-scale Sonic VibroCore (SVC) test rig was used for this study. The soil samples used were poorly-graded gravels. The selection of gravel as the tested soil type was based on the experience of DBM engineers in their use of the SVC. Previous testing showed that a very coarse, granular geology had a more problematic and less predictable effect on the mechanical SVC system than that of finer-grained sands and clays (Raubenheimer, 2015). Research focussed on the coring response of gravel was therefore considered to be of practical value.

All numerical modelling was completed using Rocky DEM Software – henceforth referred to as Rocky. Rocky is a powerful, 3D DEM program that simulates particle behaviour. It was deemed impractical to investigate the modelling of soil particle sizes smaller than that of the gravels tested. This was due to a) The unique problems associated with coring into gravel observed in the past by DBM engineers, and b) The exponential increase in DEM computational requirements with decreasing particle size.

In both the physical and numerical work, focus was not given to the retrieval or extraction of the core barrel from the soil. Rather, the research was concerned only with the act of core barrel penetration.

1.4. Structure of dissertation

The body of this dissertation was written to consist of five parts, with references and appendices detailed in a sixth and final part (Fig. 1.3). Each part is split into a number of chapters. The chapters, in turn, consist of sections and sub-sections.

Part I aimed to present a review of literature of the coring of seabed soils. It consists of five chapters: Chapter 2 – Offshore subsoil exploration techniques; Chapter 3 – Core sample quality: Recovery and disturbance; Chapter 4 – Soil plugging in core samplers; Chapter 5 – The DEM: Theory and application; and Chapter 6 – Summary and discussion: Part I.

Part II contains only one chapter, Chapter 7, in which an overview of the methods used in conducting this research was provided.

In **Part III**, the physical testing work was detailed. The SVC system was described in Chapter 8 and the specific SVC test methodology stated in Chapter 9. The SVC test results were presented and discussed in Chapter 10. Part III is summarised and concluded in Chapter 11.

Part IV detailed the numerical modelling work and its calibration to the physical results. It was divided into three chapters: Chapter 12 – Assembly of Rocky discrete element model, Chapter 13 – Numerical results: Variance and calibration, and Chapter 14 – Summary and conclusions: Part IV.

In **Part V**, more detailed results of the calibrated DEM model were provided and discussed in Chapter 15, which were then summarised and concluded in Chapter 16. Overall conclusions for the dissertation are provided in Chapter 17. The body of the dissertation ends in Chapter 18 with recommendations for future research.

Part VI consists of references specified in Chapter 19, followed by appendices.

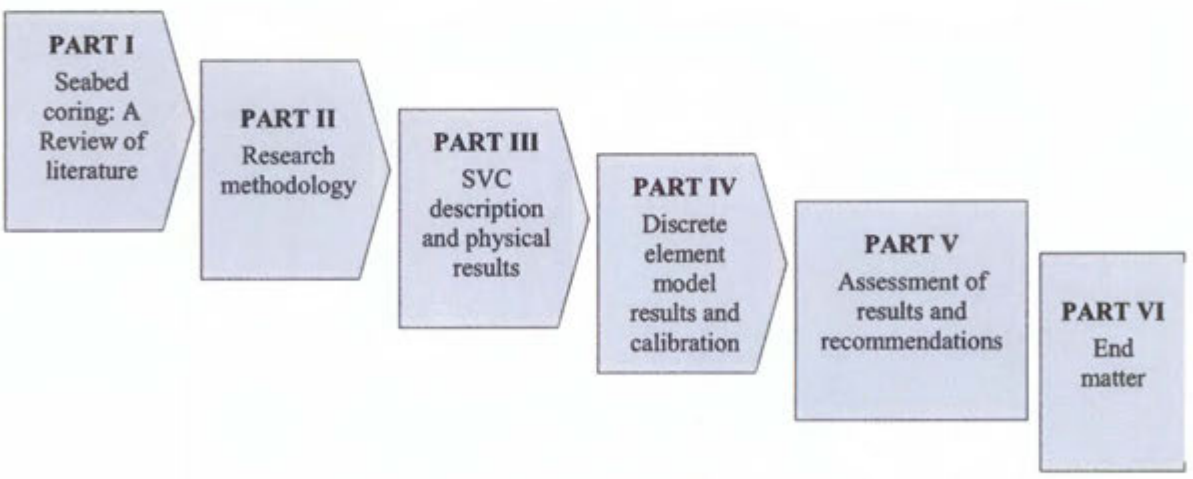

Figure 1-3: Structure of dissertation

PART I

Seabed coring: A review of literature

Part I Contents

Chapter 2 - Offshore subsoil exploration techniques:

A broad overview of marine sediments and offshore subsoil exploration is provided, followed by a more detailed study of pertinent seabed coring techniques.

Chapter 3 - Core sample quality: Disturbance and recovery

The concept of core sample quality is developed. Various factors that influence the quality of a soil sample are reviewed.

Chapter 4 - Soil plugging in core samplers

A critical review of the physical processes that govern recovery in core samples is presented. Focus is given to the soil mechanics principles influencing barrel-soil interaction.

Chapter 5 - The DEM: Theory and application

The theory and limitations of the DEM are summarised; Relevant applications of the method are studied.

Chapter 6 – Summary and discussion: Part I

The findings of the literature reviewed in Part I are summarised and discussed.

2. Offshore subsoil exploration techniques

2.1. Marine sediments and seabed variability

Marine sediments are principally classified as either terrigenous or pelagic. Terrigenous sediments are transported from land; pelagic sediments settle through the water column. Terrigenous sediments are usually grains of minerals formed from the erosion or rocks. They are supplied by rivers, coast erosion, or glacial activities, and are classified based on the size of their particles. Pelagic sediments form either from insoluble remains of marine organisms (bigenous), e.g. shells, skeletons, teeth; or are formed when particles are transported by wind into the ocean before settling through the water column (lithogenous). They are generally more fine-grained and are classified according to their composition (Randolph & Gourvenec, 2001).

The seabed is rarely uniform, flat, or featureless. The National Oceanic and Atmospheric Administration (2003) specifies the primary factors influencing the distribution of sediments in the ocean to be: a) The age of the underlying crust, b) Tectonic history of the ocean crust, c) Nature and location of sediment source, and d) Nature of the processes delivering sediments to deposition location. Sediment is usually thickest near continents and thinnest on newly formed mid-oceanic ridges. Rivers, as the largest source of sediment in the ocean, contribute approximately 20 billion tonnes of sediment to the world's oceans every year (Randolph & Gourvenec, 2011). Figure 2.1, a digital model of sediment distribution in the oceans surrounding Africa, shows that sediments of the greatest thickness are found near mouths of the largest rivers.

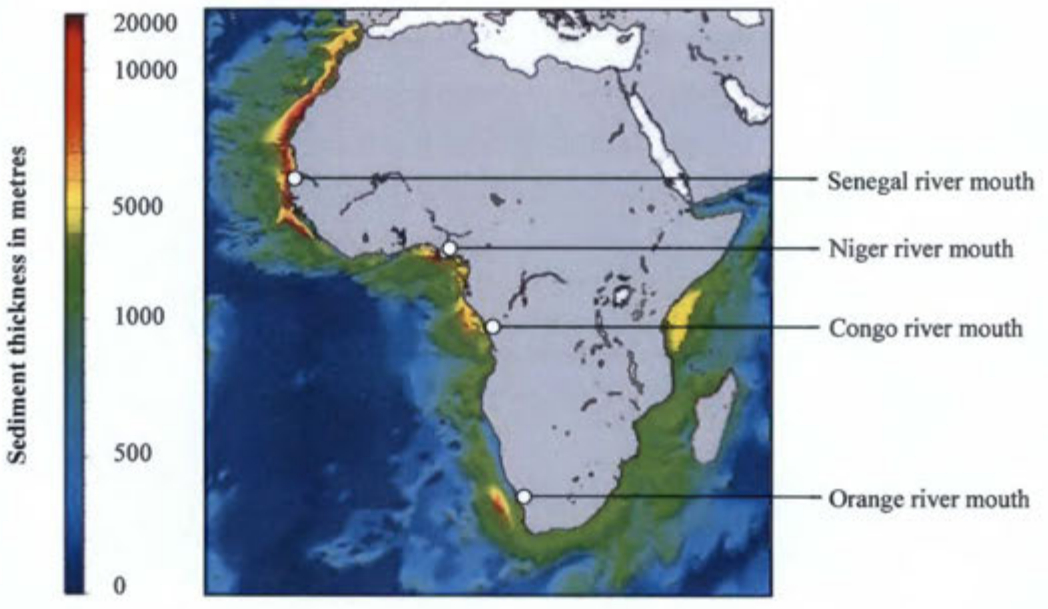

Figure 2-1: Sediment thickness of the oceans surrounding Africa
Adapted from NOAA (2003)

2.2. Common subsoil exploration techniques

In both onshore and offshore practice, the types of subsoil exploration techniques available are both numerous and well-documented (Power & Colliat, 2000; Fugro, 2001; Danson, 2005; Das, 2010; Dean, 2010; Randolph & Gourvenec, 2011). The equipment and methods used in deep-water soil investigations differ significantly to those used in coastal or onshore environments. For a given offshore project, the chosen technique for soil data collection is dependent on a number of factors, including water depth, project type, nature of soil data required, and equipment cost. A detailed review of all offshore soil investigation methods was beyond the scope of this investigation. Nonetheless, research into the classification of common offshore subsoil exploration techniques proved useful in providing background information to this study.

Figure 2.2 shows that offshore subsoil exploration techniques fall into one of two broad categories: geotechnical or geophysical. Geophysical surveys provide information on the seabed topography, features, and obstructions. However, such surveys do not provide sufficient geotechnical data for engineering purposes. Thus, geophysical methods are typically followed by geotechnical investigations (Power & Colliat, 2000). These investigations are usually conducted from specialist vessels specifically fitted for deploying and handling sampling or testing equipment on the seabed (Fugro, 2001; Danson, 2005, Randolph & Gourvenec, 2011).

In this study, focus was given to primary seabed drive sampling techniques - that is, common geotechnical coring systems that are lowered to the seabed from a vessel and controlled via an umbilical cable. Such devices include gravity corers, piston corers and vibrocorers.

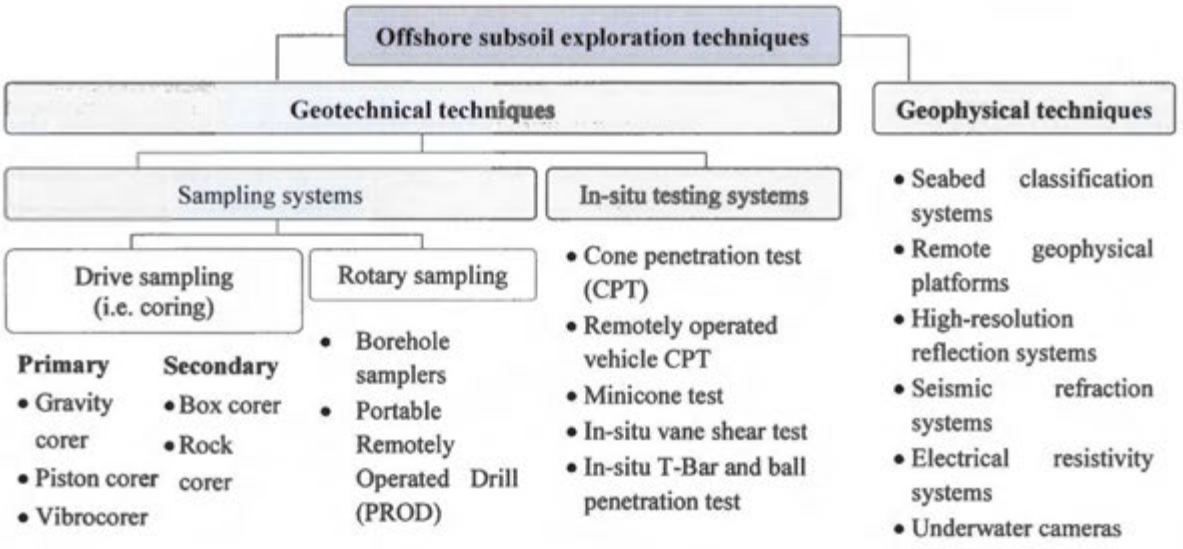

Figure 2-2: Classification of common offshore subsoil exploration techniques

After BS 5930 (1999), Power & Colliat (2000), Fugro (2001), and Danson (2005)

2.3. Overview of primary seabed coring techniques

Ideally, a retrieved core sample is representative of the depositional environment or landscape being investigated, and preserves the in-situ sedimentary structure. More simply, the core sample should be as long as possible, with minimal stretching, compression, or mixing of the collected sedimentary layers (Woodward & Sloss, 2013). While many coring techniques are available, no single corer is suitable for all settings and applications. Each coring technique has its own particular set of advantages and disadvantages.

Much literature has been published on the mechanics and shortcomings of corers penetrating the seabed under the act of gravity. This literature provided the basis for developing an understanding of soil-corer interaction under vibratory action. Thus, vibrocoring was reviewed in conjunction with gravity corers and two common piston corers. Presented below are the basic properties of these coring devices (summarized in Table 2.1).

2.3.1. Gravity corer

A gravity corer (Fig. 2.3) consists of an open-ended, tubular steel core barrel, in which is inserted a plastic liner to hold the soil sample. External barrel diameters are typically 60-100mm, but can reach 120mm (Lunne & Long, 2006). Barrel lengths range between 1-6m (Fugro, 2001). On top of the barrel is a set of weights, totalling between 0.5-1.0 tonnes. When lowered to within 5-10m of the seabed, the corer is allowed to fall freely and gravity acting on the device drives the barrel into the soil. The penetrating end of the tube is fitted with a cutting head and a concave spring-steel core-catcher to retain the sediment during retraction of the corer (Danson, 2005). Penetration depths are as much as 5m (Woodward & Sloss, 2013).

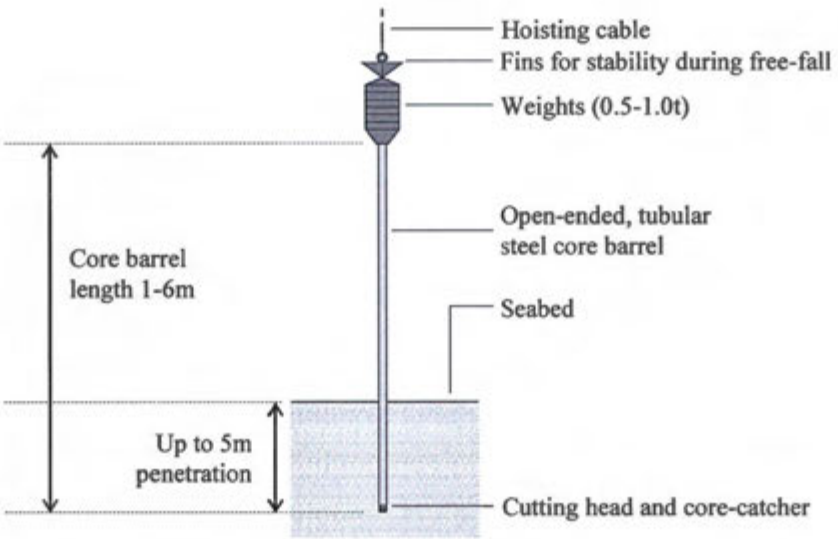

Figure 2-3: Schematic diagram of typical gravity corer

Adapted from Danson (2005)

Gravity corers are, according to Woodward and Sloss (2013), the simplest device for sampling seabed sediments and are particularly useful where relatively short cores are required for palaeoenvironmental studies. It can be deployed from a wide range of vessels, is inexpensive, easy to operate, and a rapid means of obtaining a core sample in water depths of up to several thousand metres (Weaver & Schultheiss, 1990; Fugro, 2001). However, a free-fall winch is required for deployment, and gravity-driven penetration in stiff clays or granular soils is poor (Power & Colliat, 2000; Fugro, 2001; Danson, 2005).

2.3.2. Kullenberg piston corer

For most of the 20th century, gravity corers with no piston were the most common equipment used to recover seabed soil samples (Lunne & long, 2006). However, there was a need to recover longer and higher quality soil samples. This led to the introduction of piston corers by Kullenberg (1947, quoted by Buckley *et al.*, 1994). While many other piston coring devices were developed over the late 20th century, Skinner & McCave (2003) claim that the Kullenberg-type piston corer (Fig. 2.4) remains the most practical and widely used coring device for obtaining deep-sea sediment cores

Piston corers, like gravity corers, penetrate the seabed under the act of gravity, dropping in free-fall from a limited height. However, the core barrel contains a piston, which encloses the lower end of the cutting shoe until penetration into the seabed starts (Lunne & Long, 2006). Ideally, the piston remains stationary at the sediment-water interface, reducing internal barrel-soil-friction and allowing deeper penetration than gravity corers (Weaver & Schultheiss, 1990). The piston is usually connected directly to the hoisting cable, or there is an independent piston cable.

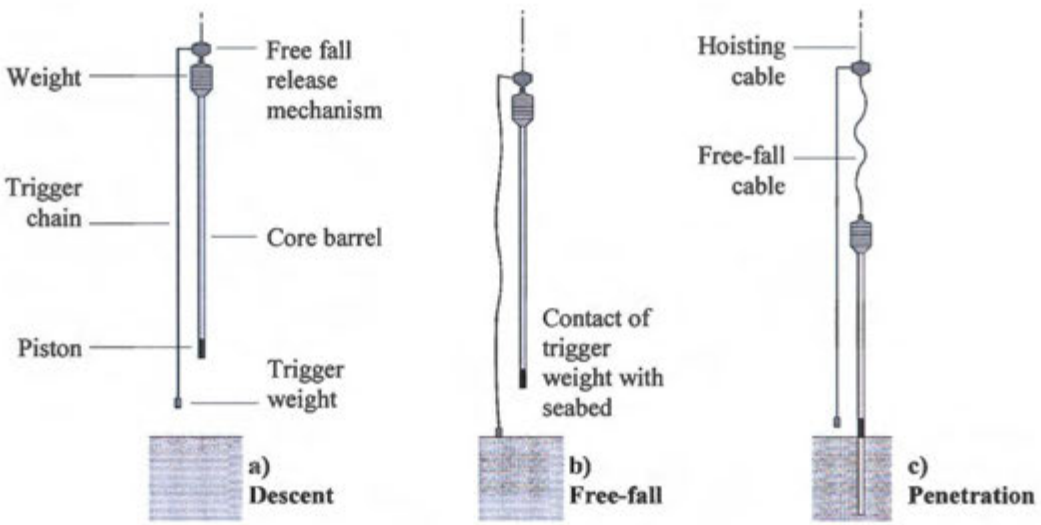

Figure 2-4: Schematic diagram of Kullenberg piston corer
Adapted from Lunne and Long (2006)

In the case of a Kullenberg piston corer, the free-fall height is controlled by a release mechanism. As the device is deployed, a latch retains the weighted core barrel. Extending from the latch is a boom, suspended from which is a weight at the end of a trigger chain. The length of the trigger chain is equal to the barrel length plus the desired free-fall distance. When the weight touches the seabed, the latch is released and the corer is set into free fall (Fugro, 2001). Danson (2005) states that, when correctly operated, Kullenberg corers can produce 30m cores in soft soils. However, the device requires skilled operatives and problems are frequently encountered with the behaviour and movement of the piston (Skinner & McCave, 2003).

2.3.3. Stationary piston corer (STACOR)

The STACOR (Fig. 2.5) is described by Lunne and Long (2006) as the most advanced coring system that penetrates the seabed under the act of gravity. It was developed with the aim to a) Increase sample diameters and recover a larger volume of sediment, b) Reduce disturbance to the sediment during sampling, c) Increase the weight of the corer to allow deeper penetrations, and d) Achieve an effectively stationary piston. The STACOR includes a mechanical pulley system that maintains the piston immobile and level with a fixed base-plate. The base-plate is a tubular steel frame, 1.5m in diameter, which rests on the sediment-water interface outside the core barrel. Core barrel lengths can reach 35m, with external diameters as much as 170mm. The device weighs 5-10t, has been used successfully in water depths of up to 5800m, and has produced cores of 34m. However, while the STACOR yields sediment corers of high quality, it is disadvantaged by major practical draw-backs: Skilled operatives are required and it is time-consuming to deploy (Skinner & McCave, 2003; Lunne & Long, 2006).

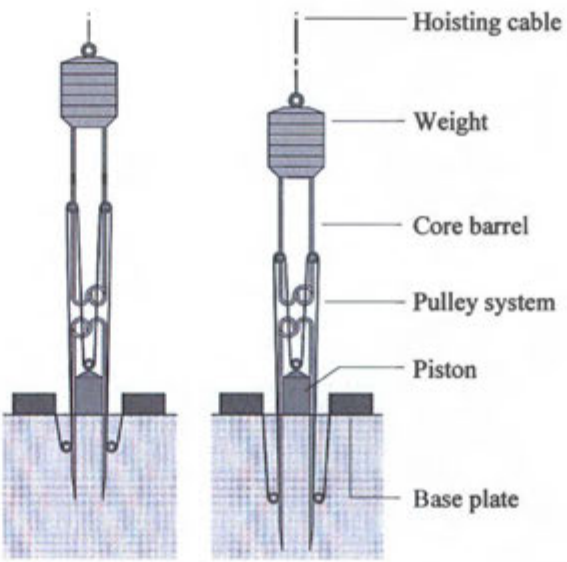

Figure 2-5: Schematic diagram of STACOR mechanism

Adapted from Lunne & Long (2006)

2.3.4. Vibrocorer

According to Kennett (1982), gravity and piston corers are unsatisfactory for use in granular soils due to poor penetration. Thus, vibrocorers, are used where greater penetration of dense sand and gravels, or stiff clays, is needed. The core barrel and sample retention systems of a vibrocorer are similar to that of gravity and piston corers (Danson, 2005). Smith (1998), Power and Colliat (2000), and Woodward and Sloss (2013) describe the principle of vibrocorer penetration into saturated soil: A vibratory motor, containing a rotating asymmetrical weight, is connected to the top of the core barrel (Fig. 2.6). The motor transmits high-frequency (100-200Hz), low-amplitude (0.1-1.0mm) waves along the core barrel, leading to its vibration in the vertical direction. These vibrations result in liquefaction of a 1-2mm thick layer of sediment both inside and outside the sample tube, reducing sediment-barrel friction, and allowing deeper penetration. Kennett (1982) and Smith (1998) claim cores of 15m length can be obtained. Vibrocorers are used widely in the site investigation industry and can be deployed in water depths up to 1000m (Danson, 2005). Weaver and Schultheiss (1990) claim the main limiting factor is the power supply cable. Vibrocoring is described by Power and Colliat (2000) as a cost effective technique for recovering material in most types of soil. However, it is disadvantaged by the size and weights of its components (Woodward & Sloss, 2013). A 6m vibrocorer can weigh up to two tonnes.

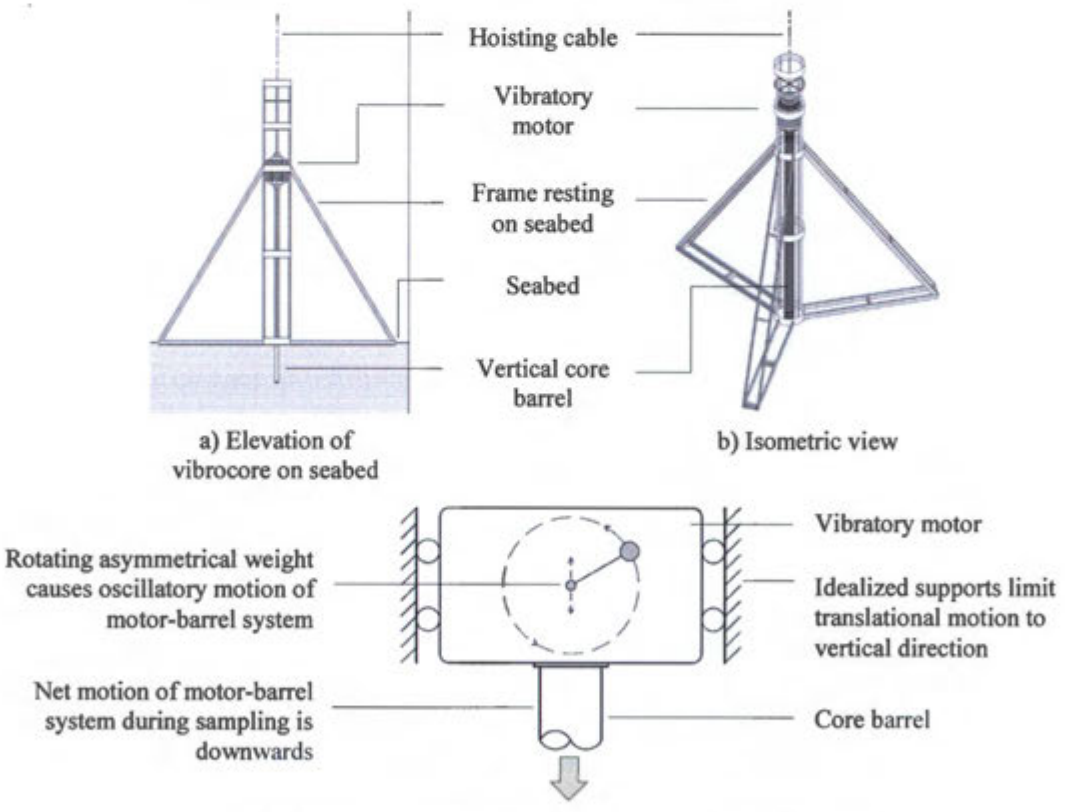

Figure 2-6: Depictions of a typical vibrocore

Table 2-1: Summary of basic properties of primary seabed coring techniques

After Kennett, 1982; Weaver and Schultheiss, 1990; Smith, 1999; Power and Colliat, 2000; Fugro, 2001; Skinner and McCave, 2003; Danson, 2005; Lunne and Long, 2006; Woodward and Sloss, 2013.

Coring technique		Description	Advantages	Disadvantages
Gravity coring (Fig. 2.3)		Gravity acts on weighted core barrel (±1t), driving device into seabed Penetration end fitted with a cutting head and a core-catcher to retain the sample Released ±10m above seabed Barrels 60-100mm diameter; <5m penetration depth	Inexpensive and simple Appropriate for water depths up several thousand metres Can be operated from a wide range of vessels	Only appropriate for use in very soft to firm clays Poor penetration in stiff clays or granular soils A winch with free-fall capability is required
Piston coring	Kullenberg-type (Fig. 2.4)	Similar to gravity corer, but with added piston mechanism Weighted corer drops in free fall, triggered by weight at end of chain touching the seabed and releasing a latch Lower end enclosed by piston until soil penetration Ideally, piston remains stationary during penetration, maintaining low relative pressure above soil column	Up to 30m samples in soft soils Eliminates need for free-fall winch Can control free-fall distance The most practical and widely used coring device	Requires skilled operatives Inconsistent piston movement during sampling Limited penetration in stiff clays or granular soils
	STACOR (Fig. 2.5)	Similar to gravity corer, but includes a mechanical pulley system to maintain the piston immobile and level with a fixed base-plate Plate rests on seabed outside the core barrel Base-plate is made of 1.5m diameter tubular steel frame Has been successfully deployed in water depths of 5800m	Larger sample diameter Larger recovered sample Deeper penetration than simple gravity corers; Up to 35m in soft soils	Requires skilled operatives Time-consuming to deploy Limited penetration in stiff clays or granular soils
Vibrocoring (Fig. 2.6)		The barrel and sample retention systems are similar to gravity/piston corers, but barrel driven into seabed by vibratory means Barrel supported by steel frame, and driven by high-frequency (100-200Hz), low-amplitude (0.1-1.0mm) vibratory motor Friction between core barrel and soil is reduced by liquefaction of 1-2mm thick sediment layer surrounding sample tube Used where soil conditions aren't suitable to gravity/piston corers, or where greater penetration is necessary	Vibratory action facilitates greater penetration; Up to 15m recorded in sands, silts, clays and peats Is a cost effective method of recovering material in most types of soil	Size and weight of equipment is large Large deployment vessels are required A typical 6m vibrocorer weighs 2 tonnes Use in deep water is limited by length of power supply cable

3. Core sample quality: Disturbance and recovery

3.1. Preamble to assessment of soil sample quality

The two aspects pertaining to soil quality are soil 'disturbance' and soil 'recovery'. In many ways, soil disturbance may be considered a separate field of study to soil recovery, and therefore not relevant to this research. However, soil disturbance is a multifaceted phenomenon. It was deemed impractical to investigate soil recovery without considering some aspects of soil disturbance to which it is closely related. These features are clarified below.

3.1.1. Soil disturbance: Its meaning in this text

Sampling disturbance influences the effective stress state of a soil sample. Clayton (1995) explains that it may be caused by a number of factors before, during, and/or after the sampling process, and is in most cases unavoidable. Lunne and Long (2006) provide a list of potential causes of sample disturbance: a) Mechanical disturbance, due to core barrel penetration and retrieval, b) Stress relief, when the sample is removed from the ground, c) Techniques used to retrieve the sample onto the ship deck, and d) Various other factors, including extrusion, transportation, sample storage environment, and specimen preparation for laboratory testing.

For a detailed review of the effect of stress relief and sample disturbance on the mechanical properties of a soil, as well as the mitigation of soil disturbance in coring practice, the reader is referred to Clayton *et al.*(1998), Lunne and Long (2006), and Long (2003).

Of the above-mentioned causes of disturbance, only point a) was considered applicable to this research. Any further use of the term 'disturbance' in this dissertation refers specifically to how the stratigraphic integrity of a soil is distorted, or 'disturbed', during core barrel penetration. This disturbing process, where the soil is sheared and displaced by a penetrating tube, directly influences soil recovery.

3.1.2. Soil disturbance during core barrel penetration

The compaction, remoulding, and displacement of soil beneath a penetrating sampler tube can be significant (Fig 3.1a). This disturbance introduces shear distortions in the soil, which according to Clayton *et al.* (1995), can cause a change in effective stress of the soil, and/or effect bonding between soil particles.

Baligh (1985) used the strain path method, an approximate analytic technique, to predict the soil disturbances caused by the penetration of rigid tube samplers in saturated isotropic clays. It was observed that soil elements at the centreline of the sampler experience three distinct phases of shearing (Fig. 3.1b): 1) An initial compression phase beneath the sampler where axial strains increase from zero to a maximum value, 2) An extension phase as the soil enters the tube cutting

edge where the axial strains reverse from compression to extension and attain a maximum value, and 3) A second compression phase inside the sampler tube where the axial strain decreases and attains a constant value.

In continuing the work of Baligh (1985), Baligh *et al.* (1987) stated that in the outer half of the sample tube, strains are large and involve significant gradients, especially near the sampler walls. Conversely, in the inner half of the sample: a) Relatively minor variations in soil strains exist, b) The dominant strain component is the vertical axial strain, and c) The radial and tangential strains are approximately zero. Therefore, reasonable estimates of soil disturbances within the inner half of the core barrel can be obtained from results at the sample centreline.

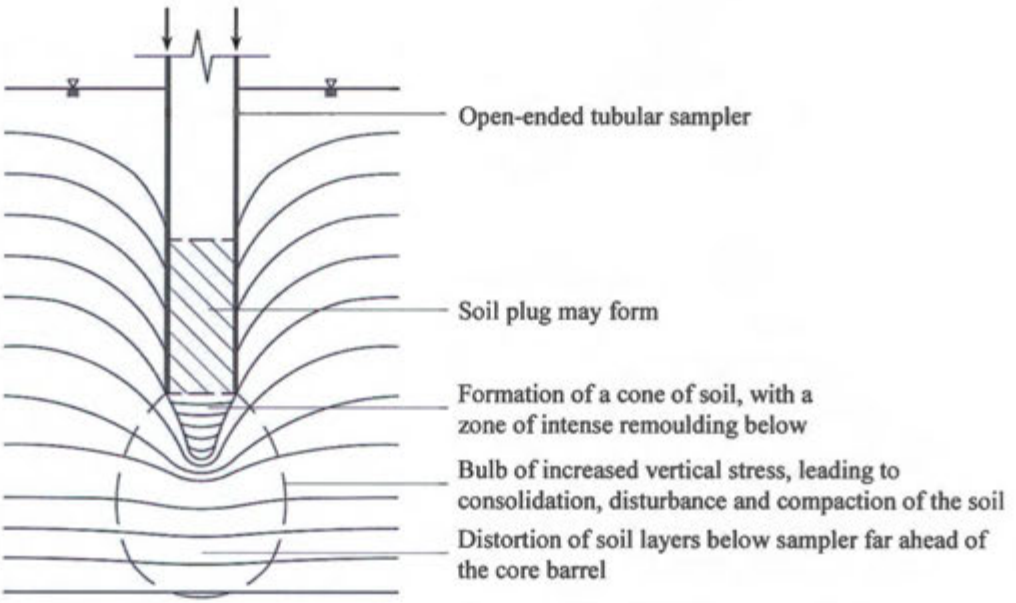

a) Displacement of soil beneath a sampler tube (adapted from Hvorslev, 1949)

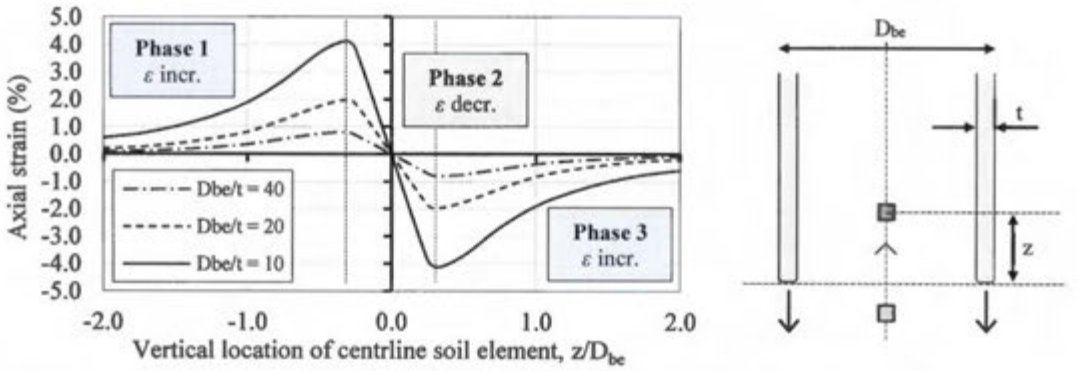

b) Strain paths for an element of soil on the centreline of a tube sampler (adapted from Baligh, 1985)

Figure 3-1: Soil disturbance during core barrel penetration

3.1.3. Criteria for evaluating soil disturbance

The recovery of a sample may be quantified by determining its recovery ratio. It is more difficult to quantify sample disturbance. Many techniques are available for the assessment of sample disturbance. These include X-ray photography, comparison of shear wave velocity measured on a specimen with that obtained in-situ, and the analysis of stress/strain curves and parameters measured in oedometer or triaxial tests (Lunne & Long, 2006).

According to Lunne and Long (2006), the Norwegian Geotechncial Institute (NGI) has, since 1996, used a 'disturbance index' to evaluate sample disturbance on a number of onshore and offshore consulting projects. This index, I_d, is given by $I_d = \Delta e / e_0$, where Δe is the change in void ratio e, and e_0 is the initial void ratio. Use of this index is based on the assumption that the sampling-induced volumetric strain of a high quality core should be close to zero. In other words, its stratigraphic integrity and sedimentary structure should be maintained. Lunne *et al.* (1997, quoted by Lunne and Long, 2006:147) recommended that the volume change be expressed in terms of the change in void ratio relative to the initial void ratio.

3.2. Factors influencing sample quality

Lunne and Long (2006) review the influence of various parameters on the quality of samples produced by piston corers. The parameters are sub-divided into three categories: a) Physical characteristics of the core barrel, b) Techniques for penetrating the sampler into the seabed, and c) Special features of the sampler, e.g. core catcher and piston. This study adopted a similar approach:

3.2.1. Physical characteristics of the core barrel

Clayton *et al.* (1998) state that the detailed design of the sample tube, and particularly its cutting head, is generally considered to be of great importance for good quality sampling. Figure 3.2 shows the various parameters defining the geometry of a core barrel cutting head. The most important sampler characteristics are, according to Lunne and Long (2006), its diameter, wall thickness (or area ratio), cutting shoe angle, inside friction, inside clearance, and outside friction. These features are described below - summarised in Table 3.1.

Core barrel inner diameter

The influence of the core barrel inner diameter was made clear by Hvorslev (1949) who stated: "There can be little doubt that the disturbance of the soil during sampling operation decreases with increasing diameter". Since Hvorslev (1949), the benefits of increasing barrel diameter have been confirmed in numerous studies (e.g. Bouma & Boerma, 1968; Skinner & McCave, 2003). However, barrel diameter is limited by the weight and handling of the core barrel in practice (Lunne and Long, 2006).

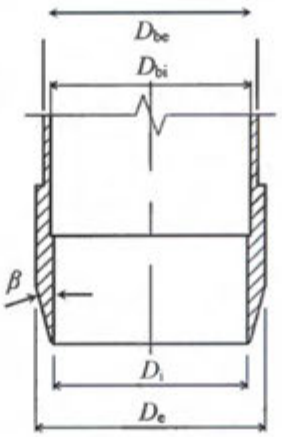

Figure 3-2: Parameters defining cutting head geometry
Adapted from Clayton *et al.* (1995)

Area ratio

The area ratio of a sampling tube is defined as

$$A_R = \frac{D_e^2 - D_i^2}{D_e^2} \qquad (3.1)$$

where D_e and D_i are the external and internal diameters of the core barrel cutting head, respectively. According to Clayton *et al.* (1998), the area ratio of a core barrel cutting head has long been considered to have a most significant impact on tube sampling disturbance. The sampling tube must be thick enough to resist buckling/distortion during penetration, but thin enough to minimize disturbance to the soil.

Clayton *et al.* (1995) state the permissible area ratio to depend on the soil type sampled, its strength and sensitivity, and the purpose of sampling. Lunne and Long (2006) specify an ideal A_R to be less than 17%. However, due to penetration stresses, it is not possible for seabed samplers to have such low wall thicknesses. In practice, A_R is in the range of 40-50% for seabed samplers.

Cutting shoe angle

Clayton *et al.* (1995) explain that the practical need for a large area ratio can be compensated by the use of a small cutting edge taper angle, β. For sampling soft clays, recommended values range between 4-15%. Similar to area ratio, the cutting shoe angle is limited by the strength of the cutting head material. A very small taper angle may lead to bending or buckling of the sampler during soil penetration.

Inside friction and inside clearance

Lunne and Long (2006) state that inside friction is a critical factor influencing the length and quality of the core recovered. The frictional force can be reduced by making the cutting head edge of the core barrel slightly smaller in diameter than the inner diameter of the tube. The inside clearance ratio (ICR), is defined by:

$$ICR = \frac{D_{bi} - D_i}{D_i} \qquad (3.2)$$

where D_{bi} is the internal diameter of the core barrel. Clayton *et al.* (1995) explains how a non-zero ICR allows the sediment to swell once in the sample tube, resulting in a reduction of horizontal stress. While this soil behaviour is not desirable, it is less undesirable than the consequences of adhesion between the soil and the inside of the core barrel. Therefore, Clayton *et al.* (1998) describes the inclusion of inside clearance as a 'necessary evil'. Lunne and Long (2006) recommends an ICR for seabed samplers of less than 0.5%.

Outside friction and outside clearance

The frictional stresses generated between the outside of a core barrel and the soil are transmitted to the soil below the cutting edge. Lunne and Long (2006) describe this to have a disturbing effect on the soil before it enters the sample tube. In addition, outside friction increases the penetration force required. The outside clearance ratio (OCR) is defined by:

$$OCR = \frac{D_e - D_{be}}{D_e} \qquad (3.3)$$

where D_{be} is the external diameter of the core barrel.

Table 3-1: Summary of core barrel features influencing sample quality

After Lunne and Long (2006)

Sampler feature	Ideal situation	Limitations
Core barrel inner diameter	As large as possible	Weight handling on deck
Area ratio	As small as possible	Strength of core barrel material
Cutting shoe angle	As small as possible	Prone to damage during penetration
Inside friction	As small as possible	Available barrel material; permissible ICR
Outside friction	As small as possible	Must be some distance from barrel tip

3.2.2. Sampler penetration techniques and special features

According to Clayton *et al.* (1995), the technique used to drive the sample tube into the seabed can have a severely damaging effect on the soil. For example, the influence of driving a thick-walled sampler into hard soil by repeated blows of a hammer is clearly detrimental. Hvorslev (1949) described and rated driving methods, shown in Table 3.2:

Table 3-2: Methods for core barrel driving
After Hvorslev (1949)

Driving method	Description	Motion	Sample quality
Hammering	Repeated blows of a drop hammer	Intermittent fast motion	Worst
Jacking	Levers or short commercial jacks	Intermittent slow motion	↓
Pushing	Steady force – no interruptions	Continuous uniform motion	
Single blow	Blow of a heavy drop hammer	Continuous fast motion	
Shooting	Force supplied by explosives	Continuous very fast motion	Best

The penetration of gravity and piston corers into the seabed under their own weight can be considered analogous to the single blow driving method. It is worth noting that vibrocoring was not included in Table 3.2 as a driving method. This is because in 1949 vibrocoring was yet to be developed. According Lunne and Long (2006), literature suggests that sampler penetration by pushing is preferable to that by vibration. However, the same paper also stated that there exists no studies comparing the effect of penetration technique on sample quality, and the article in which these claims were made was focussed on soft cohesive deposits.

Special features of the core barrel include its core retainer, piston, and inner liner. Lunne and Long (2006) describe the influence of these features in detail.

3.3. Imperfect soil recovery in coring practice

Skinner and McCave (2003) emphasise that every coring technique influences the sampled sediment column in a particular manner, likely introducing dimensional and structural changes. Therefore, according to Woodward and Sloss (2013), it is very important to record the recovery ratio of a core to assess the extent of vertical disturbance. This section is a review of selected studies in which imperfect recoveries of various core types obtained in practice were evaluated.

3.3.1. Core shortening in gravity cores

Gravity corers are, according to Weaver and Schultheiss (1990), subject to a major source of error: Under-sampling due to sediment 'plugging' in the core barrel. This plugging occurs as a

result of increasing friction between the cored sediment and the inside of the barrel. More specifically, plugging occurs when the force required to move the sampled soil up the barrel exceeds the force required for the barrel and core sample to act as a solid rod for further penetration. Lunne and Long (2006) state that, in soft clays, penetration can be as much as 5m before plugging occurs. In stiff clays, this may be limited to 1m. Intermittent or partial plugging is the cause of core shortening – i.e. a decrease in recovery ratio. Thus, gravity corers can be unreliable in sediments of mixed composition and produce increasingly unreliable results with increasing penetration.

Lunne and Long (2006) claim that the recovery ratio for gravity cores is often less than 70%. Indeed, observed recoveries of cylindrical gravity cores taken in the Irish Sea by Parker and Sills (1990) averaged below 70%.

3.3.2. Vertical disturbances in piston cores

Skinner and McCave (2003) explain that, in a piston core, the frictional drag between core barrel and sampled sediment is counteracted by low relative pressure maintained above the sampled soil and piston. Piston cores are therefore less prone to plugging than gravity cores. However, since their first use in the early 1950s, various problems pertaining to the sampling integrity of piston corers have been observed (Buckley *et al.*, 1994). Such problems are related to behaviour and movement of the piston during and after sampling. Buckley *et al.* (1994) state that, in addition to shortened cores due to plugging, piston cores have yielded highly disturbed samples, or core lengths that exceed the depth of penetration. Various studies suggest that this over-sampling is due to elastic 'piston cable recoil' following the release of the corer (Weaver & Schultheiss, 1990; Buckley *et al.*, 1994; Skinner & McCave, 2003). Cable recoil results upward accelerations of the piston and reductions in internal pressure below the piston.

An additional cause of over-sampling is forwarded by Bouma and Boerma (1968): In many cases the core barrel does not penetrate the seabed to its full length. As a result, the piston may be pulled up as the coring device is pulled out, leading to material below the cutting head flowing into the sample tube. Buckley *et al.* (1994) reported cases where as much as 1.3m of sediment in collected piston core samples resulted from over-sampling. Such samples can lead to miscalculations of sediment deposition rates by a factor of two in geological study, and are of no value for geotechnical analyses.

3.3.3. The need to consider incremental recovery in core samples

Parker and Sills (1990) explain how, in practice, the in-situ soil stratigraphy of a collected core is often 'reconstructed' using an overall correction factor based on the observed cumulative core recovery ratio. Application of such a factor to any given section of the core assumes that the entry of the soil into the core barrel is continuous, or that the final cumulative recovery ratio is constant throughout the sampling process. Results of a series of gravity core tests conducted by Parker

and Sills (1990) suggest the development of entry deficit in gravity cores to be more intermittent than continuous. A cylindrical gravity corer with an internal diameter of 83mm, area ratio of 32.5%, and barrel length of 3.17m, was deployed 34 times to sample silty sand mud in the northeast Irish Sea. The penetration rate of the corer was controlled by the free-fall winch release speed, and varied between 0.15-1.65m/s. Two acoustic transducers were fitted to the core barrel to measure both the corer penetration depth and sediment entry within the core. The results of two of these tests are shown in Figure 3.3. Plotted is the variation of cumulative sediment entry L, cumulative recovery ratio (RR), and incremental filling ratio (IFR) with penetration depth, d. If RR is defined mathematically as L/d, then IFR is given by $\Delta L/\Delta d$, and can be considered the RR over a given depth increment. The effects of plugging can be observed by comparing the cumulative entry lines to the line representing perfect recovery in Figure 3.3a. The significant local variation in IFR compared to the cumulative RR is also shown (Fig. 3.3c and d). The test results reported by Parker and Sills (1990) indicate that all sample measurements showed similar variability in IFR with depth.

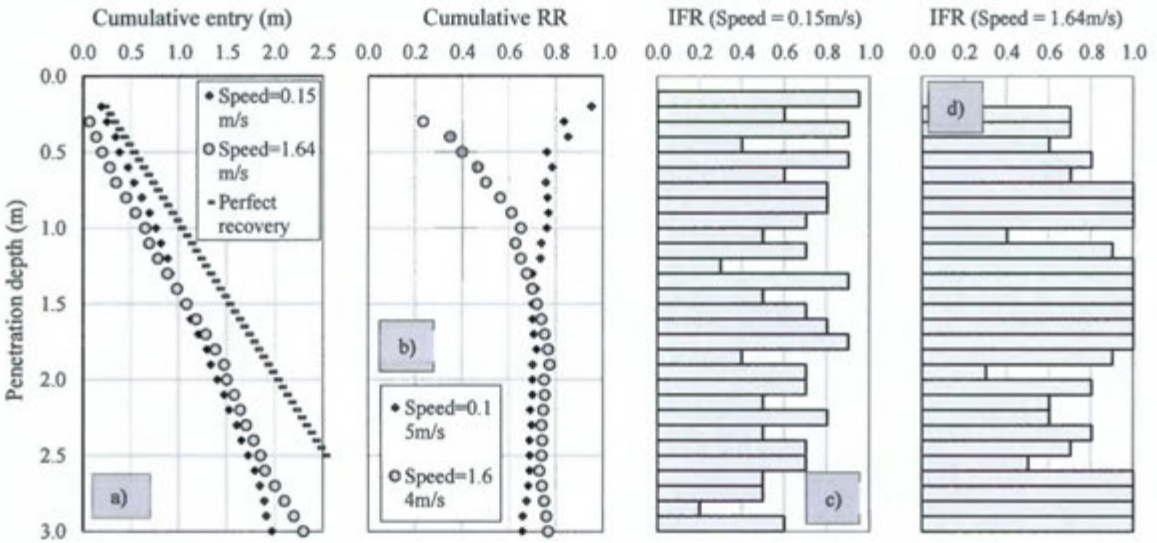

Figure 3-3: Results of gravity core testing in silty sand mud
After Parker and Sills (1990)

3.3.4. Dearth of vibrocoring literature

The reviewed literature shows gravity and piston corers to suffer from a number of practical drawbacks. Vibrocoring is, according to Smith (1998), an improvement over these systems. Many geological texts recognize vibrocoring as a useful seabed sampling technique, but to date very few geotechnical studies have been found that observe or assess soil recovery in vibrocores. Woodward and Sloss (2013) briefly discuss recovery in vibrocores by describing the system to be disadvantaged by soil plugging. It is clear then that plugging is a ubiquitous phenomenon in primary seabed coring devices that directly influences soil recovery. The plugging effect in corers is explored further in the next chapter.

4. Soil plugging in core samplers

4.1. Analogy between samplers and piles

In reviewing soil recovery in vibrocorers, and indeed all primary seabed corers, it was useful to establish an analogy between tubular samplers and cylindrical, open-ended, continuously hollow piles. By doing so, geotechnical studies on the topic of plugging in samplers were supported by the wealth of published literature describing the plugging of soil in offshore piles. The widespread application of open-ended steel tubes for driven piles, particularly for offshore foundations, is highlighted in numerous papers (e.g. Randolph *et al.*, 1991; De Nicola *et al.*, 1997; Henke & Grabe, 2008; Henke & Grabe, 2013). Due to similarities in area ratios between piles and samplers, both Paikowsky *et al.* (1989) and Skinner and McCave (2003) state that a direct geometric analogy exists between these two forms of tubes. In the following review, the terms 'pile', 'sampler tube', and 'core barrel' were considered synonymous.

4.2. The soil plug mechanism

According to De Nicola and Randolph (1997), the physical processes that govern the plugging mechanism during piling installation are poorly understood. This section examines the soil mechanics principles controlling plugging behaviour in tubes penetrating the seabed.

4.2.1. Cumulative friction in a core barrel

Figure 4.1a illustrates a soil element of thickness *dz* inside a core barrel. At this stage, it is assumed that Figure 4.1 represents a gravity corer.

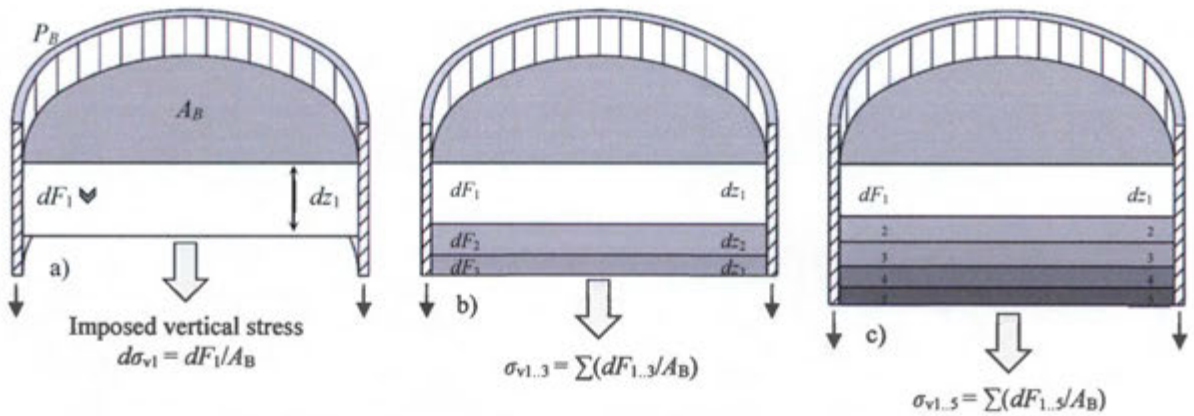

P_B = barrel perimeter; A_B = inside area of barrel; dF = incremental friction; dz = incremental soil element thickness

Figure 4-1: Accumulation of friction inside a core barrel penetrating the seabed

Adapted from Skinner and McCave (2003)

Skinner and McCave (2003) explain that each increment of soil entering the core barrel contributes an increment of friction, dF_i, which depends on the thickness of the soil element, dz_i, its shear strength, and the skin-friction factor between sediment and corer. The development of excess pore pressures in the soil surrounding the sampling tube depend on the speed and nature of the barrel penetration, as well as the soil permeability. In clayey fine-grained marine sediments, it is reasonable to assume undrained conditions. As the barrel descends further (Fig 4.1b and c), the total friction force accumulates due to a rise in contact area between the soil and barrel, and the general increase in shear strength with sediment depth.

Therefore, according to Skinner and McCave (2003), a descending core barrel accumulates an increasing sediment column inside it, subject to an increasing downward frictional drag. This friction is transferred through the soil column and is imposed over the cross-sectional area of the core aperture as a vertical stress, σ_v, on the soil immediately below the corer at that instant in its descent.

4.2.2. Plugging criteria and the three modes of penetration

From static equilibrium it follows that plugging occurs when the vertical stress, σ_v, imposed on the soil about to be sampled exceeds the mobilised bearing capacity, q_{ub}, of this soil. Therefore, formation of a soil plug inside a core barrel a) Is a result of shear failure of the soil immediately below the barrel, causing it to flow around, rather than enter, the core barrel, and b) Results in the sampler penetrating the soil as if it were close-ended. This condition for plugging is accepted widely in the literature (e.g. Randolph *et al.*, 1991; De Nicola & Randolph, 1997; Skinner & McCave, 2003; Henke & Grabe, 2008; Henke & Grabe, 2013). Expressed mathematically, this condition is:

$$\text{If } \sigma_v < q_{ub} \Rightarrow \text{No plugging occurs}$$

$$\text{If } \sigma_v > q_{ub} \Rightarrow \text{Plugging occurs}$$

The simple criteria stated above suggests that a sampler has only two modes of penetration: plugged (IFR = 0) or unplugged (IFR = 1). However, plug formation is a non-linear problem. In addition to the method of sampler penetration, plug formation is dependent on the barrel diameter, penetration depth, and soil properties (Henke and Grabe, 2013). Thus, there is a third mode of penetration: Partially plugged (0<IFR<1) – illustrated in Figure 4.2. Skinner and McCave (2003) state that once σ_v reaches equilibrium with q_{ub}, the two pressures must remain in equilibrium: Any increase in bearing capacity due to increased penetration depth is balanced by sediment continuing to enter the corer to supply sufficient friction. The process of incomplete soil entry, or partially plugged behaviour, represents the squeezing of soil into the sampling tube as σ_v and q_{ub} maintain equilibrium. De Nicola and Randolph (1997) claim that piles penetrate the soil primarily in a partially plugged mode. The IFR results of the gravity cores collected by Parker and Sills (1990), shown in Figure 3.3, support this claim.

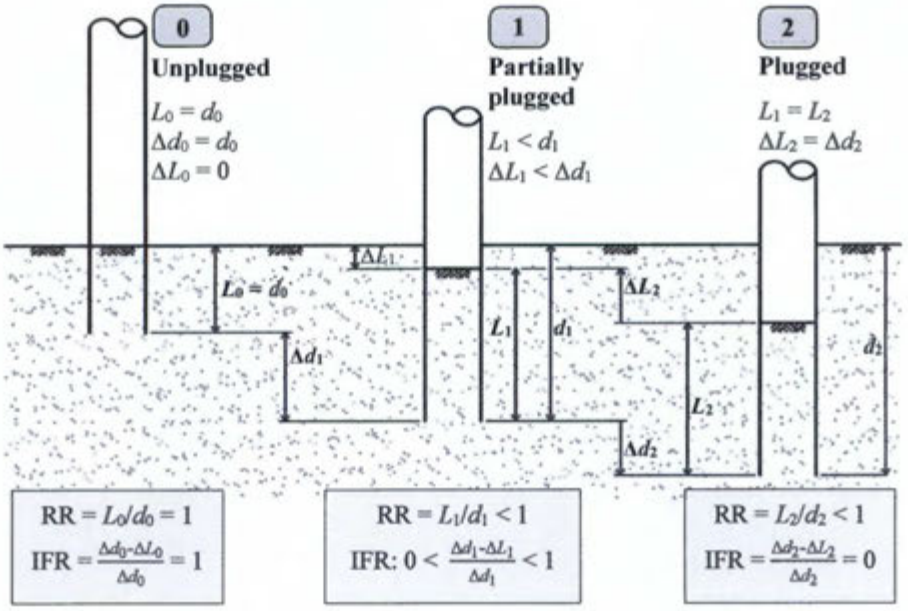

Figure 4-2: The three modes of sampler penetration
Adapted from Paikowsky *et al.* (1989)

4.2.3. Previous research on the variability of incremental recovery

De Nicola and Randolph (1997) conducted a study of the plugging behaviour of driven and jacked open-ended tubular model piles in sand. Figure 4.3 shows selected results from the article. In reviewing this paper, all the dimensions quoted are prototype dimensions. The piles tested were of 1.6m diameter, 0.055m wall thickness, and embedment length between 15-18m. A mechanism was attached to the piles to monitor the IFR during testing. Driven piles were installed using a 50t ram, with a drop height of 1.1m and a driving frequency of 15Hz. Jacked piles were installed at a rate of 50mm/s - assumed to be a drained event.

Model piles were installed into a fine grained silica flour. Flour particle sizes were that of a silt. For scaled testing, Bolton and Lau (1988, quoted by De Nicola & Randolph, 1997) showed that the mechanical properties of the flour and sand to be identical. For the pile tests conducted, sand samples of three different relative densities D_r were prepared: loose (D_r =68%), medium dense (D_r =85%), and dense (D_r =95%). The Cone Penetration Test (CPT) profiles for each of the three samples are shown in Figure 4.3a.

Pile test results showed that, in the vicinity of the pile tip, internal stresses in the soil plug are heavily influenced by the bearing resistance and dilatant characteristics of the soil below the pile toe. Fig 4.3b shows the IFR profiles for piles driven into each of the three soil types. De Nicola and Randolph (1997) state that the IFR is strongly affected by the density of the soil: The loose soil tends to densify within the pile due to vibrations from driving, while the dense soil tends to dilate. The tendency of the dense soil to dilate is particularly evident in the final stages of embedment, where the IFR increases to values greater than 100%.

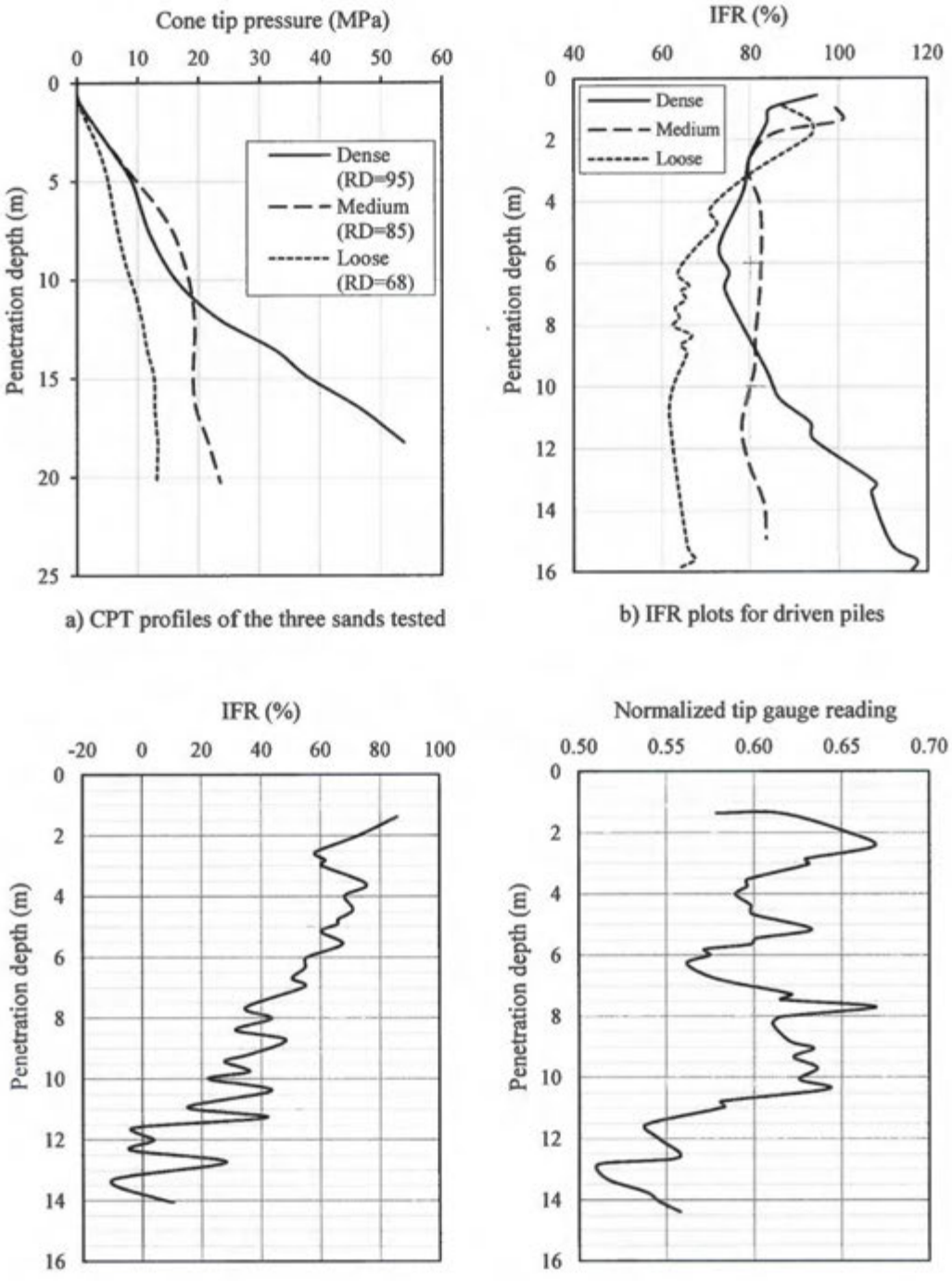

a) CPT profiles of the three sands tested

b) IFR plots for driven piles

Plots for pile jacked into loose sand of c) IFR and d) Normalized tip gauge reading

Figure 4-3: Results of the plugging behaviour in driven and jacked piles in sand

Adapted from De Nicola and Randolph (1997)

It is also interesting to note that in both the CPT and IFR profiles, the profile for the medium dense soil is higher than that of the dense soil in the upper part of the profile. De Nicola and Randolph (1997) explain that, for the soils tested, the maximum volume change within the soil plug was unlikely to exceed 10%. The IFR profiles shown in Figure 5.3b show variation much greater than this. Therefore, the IFR is strongly influenced by another factor: the bearing resistance at the pile tip. This is an expected result. From bearing capacity theory, it is known that an increase in soil density (or reduction in void ratio) results in an increase of bearing capacity (Craig, 2004; Das, 2011).

Figure 4.3c and d must be viewed in conjunction. Fig 4.3c shows the IFR profile for a pile jacked into loose soil. Fig 4.3d is a plot of the bearing stress (measured using strain gauges) acting on the same pile, divided by the local cone resistance. This gives the normalised tip gauge reading, an indication of the vertical force acting on the pile during penetration. In comparing the two plots, a clear trend is evident: Local IFR minimums coincide with local gauge reading maximums, and vice versa. De Nicola and Randolph (1997:849) provide a comprehensive explanation for this, included as a direct quote:

> As the plug stresses build up, inward flow of the soil into the pile is reduced. This has the effect of densifying the soil plug in the region close to the pile tip as this is where the majority of the plug resistance originates. This process continues until the force exerted at the tip exceeds the plug capacity, 'failing' the soil plug. Subsequently, a drop in the local plug stress occurs and fresh soil moves into the pile. The slip-stick nature of this process is evident from the plot of the incremental filling ratio. It is generally recognized that the density of the soil plug varies from a maximum close to the pile tip, to a minimum at the top of the soil plug. However, local variations in density along the length of the soil column have also been shown to exist. These local variations in the plug density most likely arise from the continual process of pile plugging followed by plug failure as described above.

The above passage relates closely to the description of partial plugging given by Skinner and McCave (2003). It also serves as a reasonable explanation for the local variation of IFR results obtained by Parker and Sills (1990) for gravity corers - shown in Figures 3.3c and d. This suggests that, although the modes of penetration differ between the tests conducted by Parker and Sills (1990) and De Nicola and Randolph (1990), the 'slip-stick' process of soil flow into a core barrel occurs in both gravity and driven corers.

4.2.4. The imposed vertical stress: Analytical solution and discussion

In developing an equation for the effective vertical pressure $\sigma_v^{'}$ imposed on the soil beneath the core barrel aperture, the system illustrated in Figure 4.4 was considered – adapted from Randolph *et al.* (1991). Figure 4.4 shows free body diagram of the forces acting on an infinitesimal disc of the soil plug within a hollow, open-ended, cylindrical core barrel. A drained analysis was assumed: Barrel penetration is constant, without vibration, and sufficiently slow - and the soil sufficiently permeable - to prevent the development of excess pore pressures. A shear stress at the barrel wall, τ, acts on the soil disc, as well as effective vertical stresses at top and bottom. The

disc has effective unit weight γ', height dl, circumference πD_{bi} and cross-sectional area $\pi D_{bi}^2/4$, where D_{bi} is the internal diameter of the core barrel. L is the total length of the soil plug, and l represents the depth from the top of the soil plug to the soil disc considered.

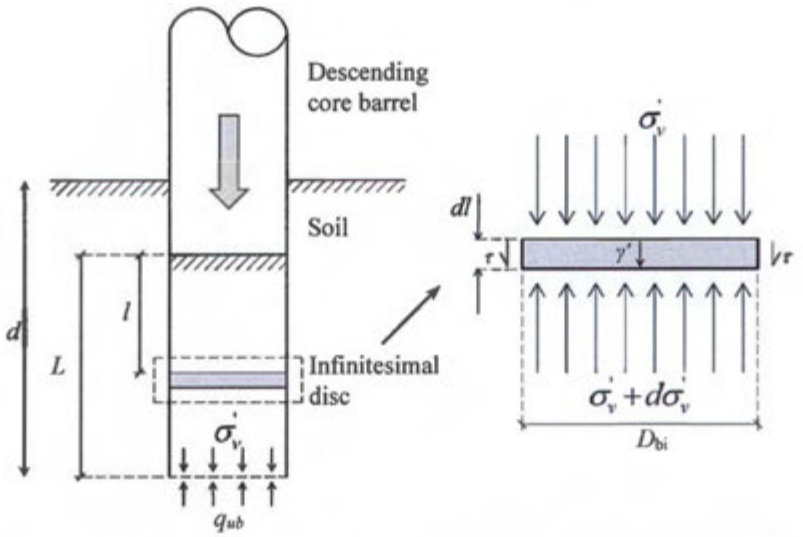

Figure 4-4: Forces acting on an infinitesimal disc of the soil plug
Adapted from Randolph *et al.* (1991)

Vertical equilibrium of forces acting on the soil disc at any depth l shows that the force due to upwards effective vertical stress is equal to the forces due to the downwards shear stress, effective stress, and weight of the soil plug. Expressed mathematically:

$$\Sigma F_v = 0 \Rightarrow \frac{\sigma_v' \pi D_{bi}^2}{4} + \frac{\gamma' \pi D_{bi}^2}{4} dl + \tau \pi D_{bi} dl = \left(\sigma_v' + d\sigma_v'\right)\frac{\pi D_{bi}^2}{4} \qquad (4.1)$$

Equation 4.1 can be simplified to:

$$\frac{d\sigma_v'}{dl} = \frac{4}{D_{bi}}\tau + \gamma' \qquad (4.2)$$

According to de Nicola and Randolph (1997), the internal stresses between the soil and barrel wall may be expressed as $\tau = K\sigma_v' \tan\delta$, where K is the ratio of horizontal to vertical effective stress at the barrel wall (i.e. the lateral earth pressure coefficient), and δ is the interface friction angle. Therefore, Equation 4.2 becomes:

$$\frac{d\sigma_v'}{dl} = \frac{4K\tan\delta}{D_{bi}}\sigma_v' + \gamma' \qquad (4.3)$$

Equation 4.3 is a linear first-order differential equation. By multiplying both sides of the equation by factor $e^{\int \frac{-4K\tan\delta}{Dbi} dl} = e^{\frac{-4K\tan\delta}{Dbi} l}$, and introducing the condition $\sigma_v'\big|_{l=0} = 0$, an expression can be derived for the effective vertical force at $l = L$, given by:

$$\sigma_v' = \frac{\gamma' D_{bi}}{4K\tan\delta}\left(e^{\frac{4K\tan\delta}{Dbi}L} - 1\right) \qquad (4.4)$$

where e is Euler's number for the base of natural logarithms – not to be confused with soil void ratio, e. Multiplying the vertical stress by the disc area, vertical force is expressed as:

$$F_v' = \frac{\gamma' D_{bi}^3}{16K\tan\delta}\left(e^{\frac{4K\tan\delta}{Dbi}L} - 1\right) \qquad (4.5)$$

Figure 4.5 shows plots of Equation 4.5 for various values of K. In plotting this equation, the soil was assumed to be a cohesionless gravel of saturated unit weight 22kN/m^3. The angles of soil internal friction ϕ' and interface friction δ were chosen to be 40° and 35°, respectively (American Petroleum Institute [API], 2003). An arbitrary core barrel diameter of 150.4mm was chosen. The figure shows a clear exponential increase in vertical force with depth. A significant influence of the estimated value of K on F_v' can also be noted. To offer a crude estimate the depth at which initial plugging occurs, the force due to the estimated bearing capacity of the soil, $Q_{ub} = q_{ub}(\pi D_{bi}^2/4)$, was also plotted. The bearing capacity pressure q_{ub} was approximated using the general bearing capacity equation described in Das (2011). The intersection of the F_v' and Q_{ub} curves indicates the theoretical depth at which a soil plug forms. F_v' can therefore also be considered to represent the upwards bearing force required for soil entry into the barrel. It is apparent from the plot that the sampled soil will likely plug within the first 2m of penetration. Considering that chosen soil parameters are those of a dense gravel, it is reasonable to expect plugging within this depth.

In interpreting the force curves, it is important to remember two assumptions inherent to the application of Equation 4.5: Firstly, the depth of barrel penetration d is equal to the soil plug length, L; and secondly, K is constant – both with depth and in its distribution along the length of the soil plug. In reality, once a plug forms, L will not equal d, and the increase of F_v' with d will adjust to be somewhat less radical. Furthermore, it is expected that K will decrease from a maximum greater than unity close to the barrel tip, to minimum at the top of the soil column (De Nicola & Randolph, 1997). The graph should not be viewed as an accurate representation of the development of F_v' with d. The F_v' plots shown would only occur in practice if the soil being sampled had an impossibly high bearing capacity.

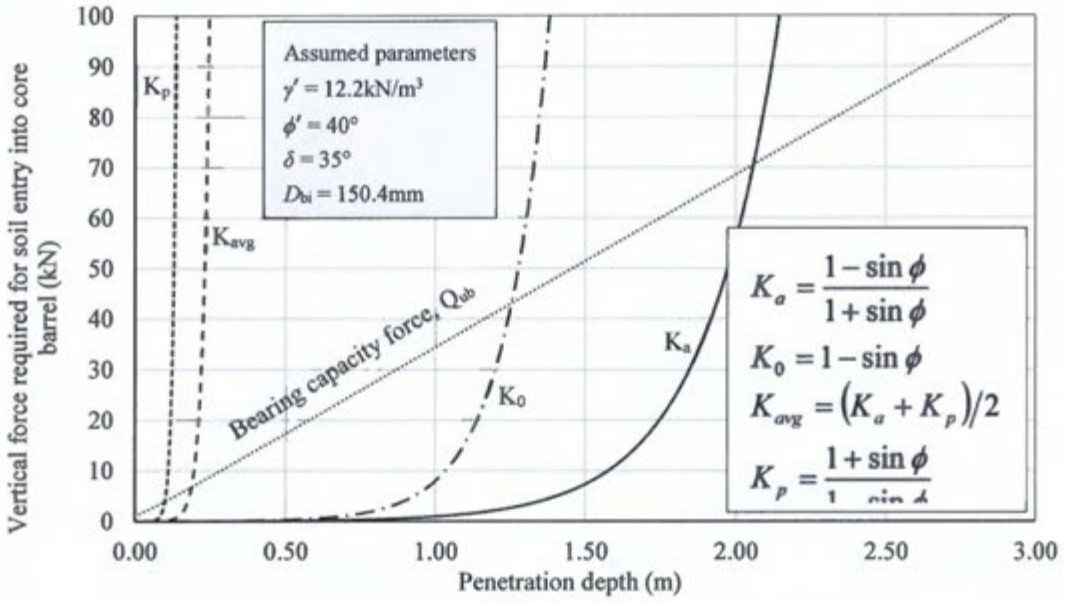

Figure 4-5: Vertical force required for entry of soil into penetrating core barrel

F'_v plotted according to Equation 4.5 for specified parameters and various values of K

The highly non-linear nature of the soil plug mechanism is clear through derivation and critical review of Equation 4.5. Only the barrel diameter D_{bi} can be considered constant with penetration depth. For cohesionless soil, the interface friction angle δ can be estimated from Table 4.1 (API, 2003). However, Skinner and McCave (2003) state that it is expected the friction factor will also evolve with penetration. Perhaps the greatest uncertainty is that surrounding the value of the lateral earth pressure K and its variation with both penetration depth, d, and depth within the soil plug, l. De Nicola and Randolph (1997) propose a variation of K along the length of the soil column for the design of open-ended, tubular piles – illustrated in Figure 4.6. The distribution shows that K is a maximum for the first internal diameter from the pile tip, and then reduces to a minimum value as shown in the figure. The value of K_{max} may be expressed as a function of the soil relative density D_r as: $K_{max} = D_r/100$. It must be emphasised that the K distribution shown in Figure 4.6 was recommended for the calculation of pile design bearing capacity. As such, it serves as a crude estimate of the lateral pressure variation within a penetrating sample tube.

Table 4-1: Soil-pile friction angles for cohesionless soil

After API (2003)

Soil type	Soil-pile friction angle, δ (°)
Very loose sand, Loose sand-silt, Medium silt	15
Loose sand; Medium sand-silt; Dense silt	20
Medium sand; Dense sand-silt	25
Dense sand; Very dense sand-silt	30
Dense gravel; Very dense sand	35

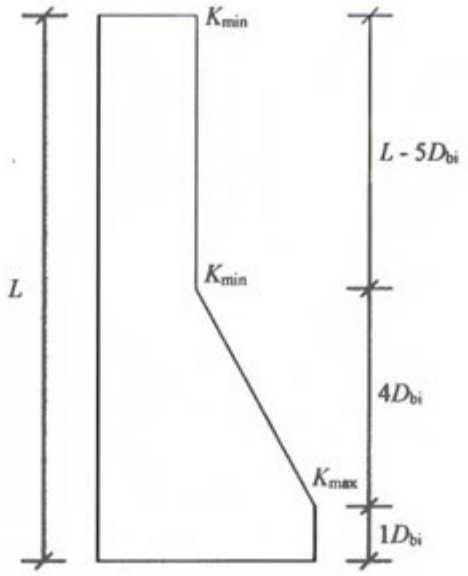

Figure 4-6: Lateral earth pressure coefficient profiles for the design of piles

Adapted from De Nicola and Randolph (1997)

4.3. Vibrocoring considerations

Osinov (2013) and Osinov *et al.* (2013) explain that, in the case of a tube vibrated into soil, the effective stresses surrounding the tube are decreased due to excess pore pressures generated from cyclic deformation. The result is a decrease in friction between the soil and tube, as the shear stress between these two mediums is a function of effective stress. Therefore, the force required for soil entry into the oscillating barrel is less than that of a similar barrel penetrating the seabed under gravity.

Furthermore, vibrocompaction of granular soil in the vicinity of the descending barrel head will likely occur, leading to an increase in the bearing capacity of the soil. Since plugging was defined as the condition where $\sigma_v > q_{ub}$, a plug is thus less likely to occur within a vibrocore. Indeed, in a series of finite element investigations and field measurements of open-ended, tubular piles (Henke and Grabe, 2008; and Henke and Grabe, 2013), it was shown that vibro-driven piles are less likely to plug than impact-driven or jacked piles. However, while the benefits of vibratory action have been highlighted, to date no studies have been found that investigate the development of lateral earth pressure coefficients, soil deformation, or recovery in vibrocores. The development of an analytical solution for plug formation inside an oscillating sample tube, which incorporates the extent of vibrocompaction and liquefaction of the sampled soil, was considered beyond the scope of this dissertation.

5. The DEM: Theory and application

In this chapter, the high computational demands of the DEM become apparent through a review of its theory and recent applications.

5.1. Theory of the DEM

This section aims to provide a brief overview of the key assumptions, physical principles and mathematical procedures underlying the DEM. For a complete review of DEM theory, the reader is referred to Cundall and Strack (1979), Jiang and Yu (2006), and O'Sullivan et al. (2006).

The basis of particle-based numerical methods is, according to O'Sullivan et al. (2006), the modelling of a granular material as an assembly of rigid particles. Cundall and Strack (1979) proposed the DEM to determine the equilibrium contact forces and displacements of such an assembly under stress: The method consists of a series of calculations tracing the movements of the individual particles. The movements are the result of boundary disturbances propagating through the discrete particles, where the speed of propagation is dependent on the physical properties of the granular medium.

Thus, a discrete element analysis is a dynamic analysis. The analysis assumes that, over any given time step, velocities and accelerations are constant. The fundamental idea of the DEM is that the time step chosen is sufficiently small to ensure that, during a single time step, disturbances cannot propagate from any particle further than its immediate neighbours. Therefore, at all times, the resultant forces on any particle are calculated only by its interaction with the particles with which it is in contact. This allows the non-linear interaction of a large number of particles to be modelled without the need for an iterative procedure.

5.1.1. The basic calculation cycle

Cundall and Strack (1979) describes the basic DEM calculation cycle to alternate between the application of two physical laws: a) Newton's second law, used to determine the motion of a particle resulting from the forces acting on it, and b) a force-displacement law, used to find contact forces from displacements. In understanding how these forces and displacements are determined during a calculation cycle, consider the basic one-dimensional system consisting of two particle discs shown in Figure 5.1.

For a typical DEM analysis, the calculation cycle described in Figure 5.1 is repeated thousands, millions, or even billions of times – depending on the stiffness properties of the particles and the simulation time. Forces corresponding to the displacements are found using the force-displacement law and the force sums for the two discs are substituted into Newton's second law to determine displacements.

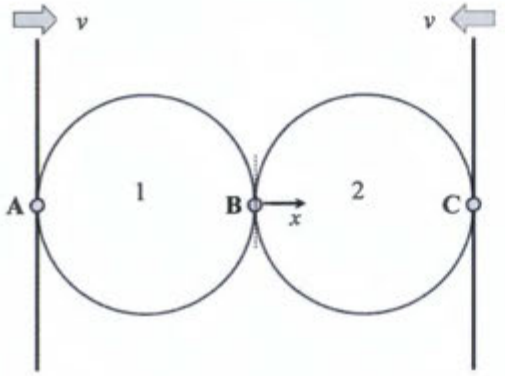

a) $t = t_0$

Two particle discs, labelled 1 and 2, are positioned between a pair of rigid walls

Walls move toward one another at a constant velocity v

At time $t = t_0$, the walls and discs are touching and no contact forces exist

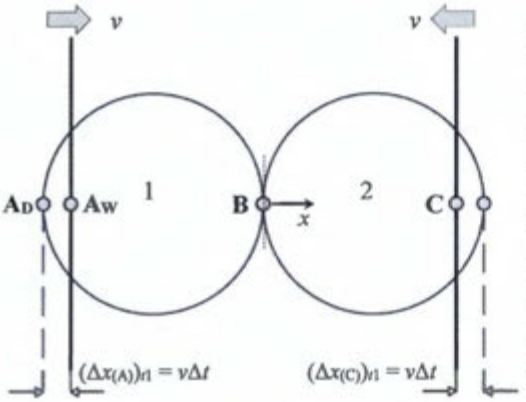

b) $t = t_0 + \Delta t = t_1$

Walls have moved inwards over distances $v\Delta t$

It is assumed that disturbances cannot travel beyond a single disc during one time step

Thus both discs are assumed to maintain their initial positions during time interval from t_0 to t_1

Therefore overlaps exist at time t_1 at contacts A and C and are of magnitude Δx (positive for compression)

Force-displacement law is used to calculate contact forces: $\Delta F_x = k_x(\Delta x)_{t1} = k_x v \Delta t$, where k_x is the normal stiffness and ΔF_x is the increment in normal force

Therefore, at time $t_1 = t_0 + \Delta t$:

$$F_1 = k_x(\Delta x)_{t1} \; ; \; F_2 = -k_x(\Delta x)_{t1}$$

Accelerations $\ddot{x}$ for discs 1 and 2 found using Newton's second law: $\ddot{x}_1 = F_1/m_1 \; ; \; \ddot{x}_2 = F_2/m_2$

Accelerations assumed to be constant over time interval between $t_1 = t_0 + \Delta t$ and $t_2 = t_0 + 2\Delta t$

To determine velocities $\dot{x}$, accelerations are integrated: $[\dot{x}_1]_{t2} = [F_1/m_1]\Delta t \; ; \; [\dot{x}_2]_{t2} = [F_2/m_2]\Delta t$

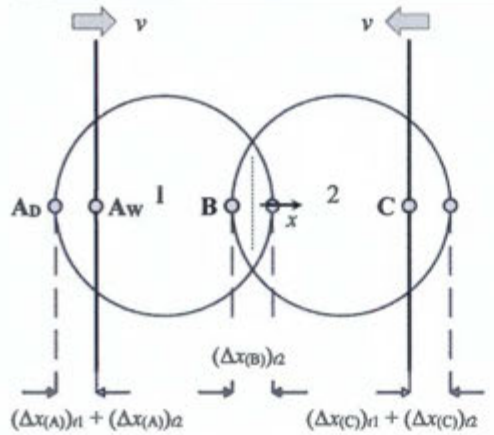

c) $t = t_0 + 2\Delta t = t_2$

The relative displacement increments at contacts A,B and C at time t_2 are calculated from

$$(\Delta x_{(A)})_{t2} = (v - [F_1/m_1]\Delta t)\Delta t$$
$$(\Delta x_{(B)})_{t2} = ([F_1/m_1]\Delta t - [F_2/m_2]\Delta t)\Delta t$$
$$(\Delta x_{(C)})_{t2} = ([F_2/m_2]\Delta t - [-v])\Delta t$$

Figure 5-1: The basic calculation cycle of the discrete element method

Adapted from Cundall and Strack (1979)

5.1.2. More advanced DEM calculations

The basic calculation detailed in Figure 5.1 merely illustrates the cycling between a force-displacement law and law of motion. Cundall and Strack (1979) state that in the more realistic case of an assembly of many particles, the force-displacement law is applied at each contact of any particle. These contact force vectors are then summed to determine the resultant force acting on the particle. Once this has been accomplished for every particle, new accelerations are calculated using Newton's second law.

In standard DEM models, inter-particle contacts can be modelled to include stiffness, damping, friction, and cohesion - as shown in Figure 5.2. O'Sullivan et al. (2006) explain that the divider in the normal direction prevents tensile forces developing between the particles, while the slider in the tangential direction allows particles to move relative to each other. This relative movement occurs only when the contact frictional strength is exceeded – this calculated using a Coulomb-type friction law proposed by Cundall and Strack (1979): $F_{s\max} = F_n \tan\phi + c$, where $F_{s\max}$ is the maximum possible shear force between two particles in contact before relative movement occurs, F_n is the normal force between the two particles, ϕ is the smaller of the interparticle friction angles of the two particles, and c is the smaller of their cohesions.

Since the contact forces between two particles are strongly dependent on their calculated overlap, the geometry of particles within a DEM analysis must be very accurately determined. As a result, particle geometries used in DEM simulations are typically those that can be easily described analytically – usually spheres for three-dimensional analyses. While more complex geometries may be analysed (ellipsoids, polyhedrons), their use increases computational demands as non-linear equations are solved at each contact point (O'Sullivan et al., 2006). The DEM originally proposed by Cundall and Strack (1979) was for dry granular assemblies. Jiang and Yu (2006) detail the DEM theory used to simulate a saturated soil.

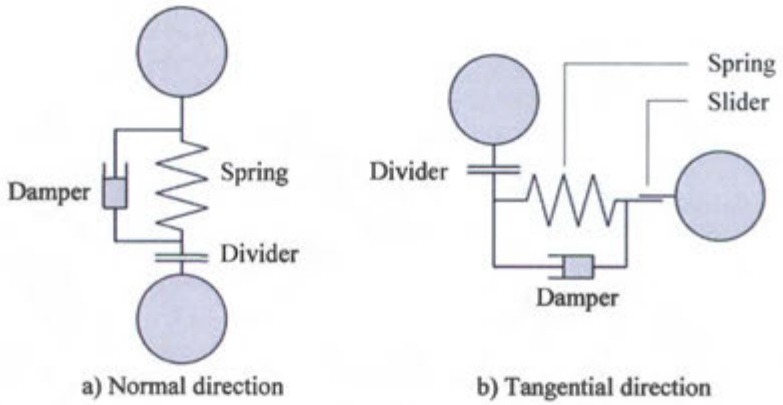

Figure 5-2: Standard contact model of two rigid disks used in DEM

Adapted from Jiang and Yu (2006)

5.2. Application of the DEM and its limitations

The DEM was originally developed for the analysis of rock mechanics problems (Cundall and Strack, 1979). However, the method is capable of analysing granular particle assemblies of any shape. Thus, discrete element modelling is used in a wide variety of disciplines other than geotechnical engineering. Applied physics, chemical engineering, and geology all have an interest in granular materials.

O'Sullivan *et al.* (2006) claims the main drawback of DEM application to be difficulty associated with modelling the large number of particles that exist within soil volumes large enough to be of practical interest to engineers. Similarly, Ng and Meyers (2015) state that full-scale 3D DEM simulations would take a very long time to compute due to the need to model billions of particles. For example, consider a cylindrical specimen 38mm in diameter and 75mm high to be tested in a triaxial apparatus. If this specimen were filled with uniform 0.5mm spherical particles at a void ratio of 0.585 it would contain almost 0.5 million particles. A real soil specimen with a distribution of particle sizes would contain many more than this.

Nonetheless, the DEM is powerful numerical technique of great use in geomechanics. Jiang and Yu (2006) list several aspects of complex soil behaviour that have been examined through use of the method, including creep theory, anisotropy, particle crushing, strain localization, and liquefaction. Ng and Meyers (2015) showed that the DEM accurately simulates the effect of soil dilatancy on the side resistance of a drilled shaft. The importance of the dilatant behaviour of soil in controlling plugging in samplers was emphasised by De Nicola and Randolph (1997). Therefore, the DEM was considered an appropriate numerical method for investigating the micro-scale interactions between a penetrating core barrel and sampled soil.

6. Summary and discussion: Part I

During penetration of a corer into the seabed, a decrease in recovery often results due to a 'soil plug' forming within the barrel. Plugging occurs when friction between the inner wall of the core barrel and the accumulating sediment column imposes a vertical stress on the soil immediately below the core aperture that exceeds the bearing capacity of the soil. This leads to the soil immediately below the core aperture flowing around, rather than entering, the barrel. The soil plug mechanism is a function of a number of factors, such as:

- Geometry of the core barrel cutting head, including its diameter area ratio, inside and outside clearance, and cutting head angle,
- Method and rate of penetration – i.e. gravity driven or vibratory
- Penetration depth,
- Properties of the soil sampled, including its density, shear strength, dilatancy, and coefficient of lateral earth pressure, and
- Friction interface angle between the core barrel and soil.

The last two factors listed above are dependent on the penetration depth. Thus, the extent of soil plugging in a sample, as well as the penetration depth at which it occurs, is a highly non-linear and dynamic phenomenon.

In developing an understanding of how the soil plug mechanism is influenced by the cyclic action of vibrocores, a clear lack of geotechnical literature on the subject was noted. As such, the review was based on studies which gave focus to a) Core samplers penetrating the seabed under the influence of gravity, and b) The installation of driven or jacked open-ended offshore piles. A geometric analogy between samplers and piles was established. Nonetheless, the majority of articles on the subject of piling were concerned with the effect the plug had on pile capacity during static or dynamic service loading, rather than its effect on the soil within the tube during installation. Articles that did provide insight into soil recovery were based on tests conducted in sands or fine-grained cohesive soil.

Therefore, to date, no studies have been found that investigate the recovery of gravels in offshore vibrocores. In compiling Part I, care had to be given in selecting aspects from a wide variety of papers that were deemed relevant to this dissertation. This highlights a clear 'gap' in the literature and provides justification for the research described in Parts II, III and IV

The discrete element method, although computationally expensive, is a powerful numerical technique capable of simulating the motion of every particle within a granular medium. It was therefore considered an appropriate numerical method for investigating the micro-scale interactions between a penetrating core barrel and sampled soil.

PART II

Research methodology

Part II contents

7. Overview of research methodology

The methods used to achieve the objectives of this dissertation were considered to consist of seven phases. The phases were not distinct. Work conducted in a given phase was facilitated by the findings of one or more previous phases. Thus, the development or 'flow' of research was not unidirectional. An overview of the methodology within each of the seven phases is provided in Table 7.1. The broad progression of the research methodology is illustrated in Figure 7.1.

Table 7-1: Overview of research methodology

Phase		Description of methodology
1	Literature review	Background research was conducted to provide insight into the engineering concepts essential to this study. The specific topics of study were selected to aid the completion and interpretation of physical testing and numerical modelling. A broad understanding of the apparatus, advantages, and disadvantages of various primary seabed coring techniques was obtained. The phenomena influencing recovery and disturbance of offshore core samples were reviewed, with focus given to the underlying soil mechanics principles governing soil-barrel interaction. The theory, limitations and applications of the discrete element method were assessed.
2	Physical testing	Seven separate core sampling 'tests' were conducted using SVC apparatus and gravel soil samples. For each test, the boundary conditions, gravel grading, sample preparation, and core barrel penetration properties were, as close as practically possible, held constant. Tests differed in the system variables that were measured before, during, and/or after core barrel penetration. The data measured served two purposes: 1) Provided insight into the macro-scale response of the vibrocore system during sampling, and 2) Provided the basis for calibration of the numerical model to the physical system. Preliminary numerical modelling was conducted simultaneously with the physical testing. This was done to gain an understanding of the input parameters required by the DEM software, ultimately allowing the physical work to be streamlined.
3	Assessment of physical results	With reference to the reviewed literature, the results of the physical testing were evaluated through the processing and analysis of the measured data. Conclusions were drawn regarding the dynamic response and resistance of the soil during sampling, as well as the overall recovery ratio of the achieved cores. The data required for assembly of the numerical model was identified and assessed.
4	Primary numerical modelling	Using the data obtained through SVC testing and various previous studies, the input required for the assembly of the numerical model was selected To decrease the computational requirements of the DEM simulations, the geometric and material properties of the individual gravel particles were simplified Since the DEM simulations were probabilistic and uncertainty surrounded the variance between numerical results, three models of identical input parameters were computed

Phase		Description of methodology
5	Preliminary assessment of numerical results	The variance between the outputs of the three models was evaluated using statistical methods. Conclusions were drawn regarding the differences between the probabilistic results. Through comparing the numerical results to the data measured during SVC testing, it was assessed whether the DEM model simulated the physical system with reasonable accuracy.
6	Detailed assessment of numerical results	Once the accuracy of the calibrated DEM model was confirmed, its output data was processed and assessed in greater detail. Focus was given to the incremental core recoveries, the soil disturbance below the core barrel, and the density of the soil within the sample tube.
7	Development of conclusions and recommendations	Conclusions were drawn based on the assessment of DEM output Based on the findings of the numerical work, suggestions were made for future research using the calibrated DEM model

Ultimately, in calibrating the physical and numerical results, it was evaluated whether the assumptions made in selecting the parameters defining the modelled soil were valid. The following two forms of data were selected as the basis for comparing SVC test and DEM output:

- The relationship between the total vertical force on the core barrel F_B and penetration depth d, termed a F_B-d plot, and
- The cumulative recovery ratio of the core at final penetration depth.

According to the reviewed literature, F_B is a function of all vibrocore system variables – most importantly, the particle properties, and core barrel penetration rate and depth. Thus, the F_B-d plots yielded by numerical calculations were strongly dependent on the assumed simulated particle and core barrel properties. For this reason, such plots were considered an appropriate means to compare the micro-scale behaviour of the real and modelled soil. The similarity in macro-scale real and modelled soil response was indicated by the cumulative recovery ratio results.

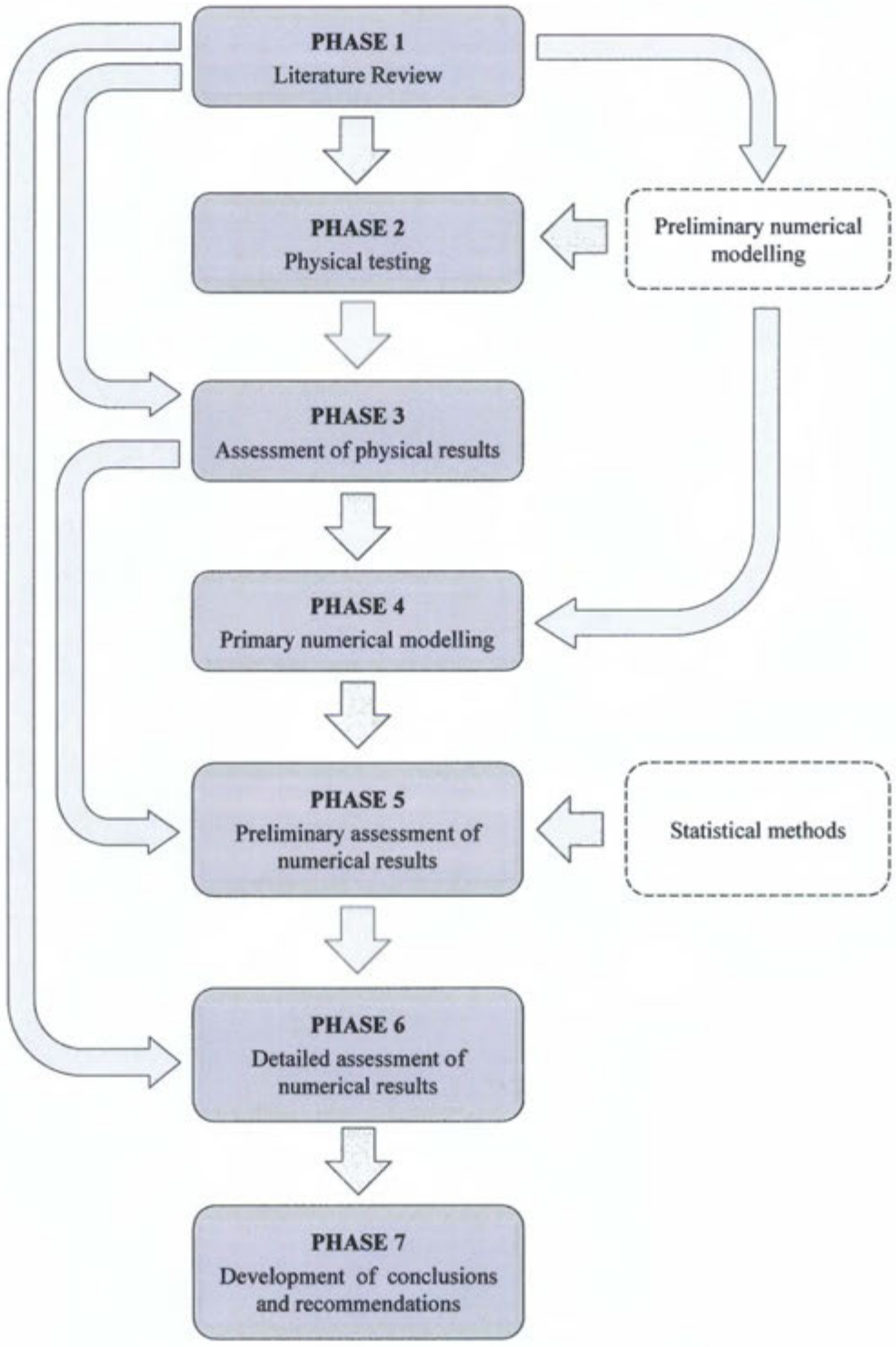

Figure 7-1: Overview of research methodology

PART III

SVC description and physical results

Part III contents

Chapter 8 - Description of sonic vibrocore system

The materials, equipment and monitoring devices of the SVC are detailed.

Chapter 9 - Physical test methodology

The methods used in the SVC testing are reported.

Chapter 10 - Physical testing: Results and discussion

The results of the physical testing are presented and assessed.

Chapter 11 – Summary and conclusions: Part III

The process and findings of the physical testing are summarised

8. Description of sonic vibrocore system

The components of the SVC system were considered to consist of three categories:

i) Soil material: The geologic material to be sampled

ii) Sampling equipment: The apparatus used to sample the soil material or to contain the soil during sampling

iii) Monitoring devices: The various apparatuses used to measure the response of the soil material or sampling equipment during or immediately after coring

8.1. Soil material

The soil material used at the test facility consisted of a wide range of particle sizes, ranging between fine sand (0.2mm) to medium cobbles (100mm). To separate the various particle size fractions within the material, the soil was poured into a rotating sieve chute. The chute consisted of an inclined cylindrical steel mesh, rotating around its longitudinal axis, with sieve openings increasing towards its bottom end. Particles sieved out the chute would fall into bunkers of separate particle size ranges (Fig 8.1). The soil material used in the SVC testing consisted only of gravel particles taken from the 16-32mm and 32-64mm bunkers. These gravels were predominantly well-rounded, very hard quartzitic sandstone, sourced from the Orange River. The material was chosen for use at the facility based on its similarity to the transported, resilient seabed diamond gravels off the coast of Namibia, where DBM is currently mining (Burger, 2015; de Vries, 2015). A 'particle shape matrix' (PSM) was developed to describe the approximate percentage of various particle shape types within the bulk material, based on both their 'sphericity' and roundness – described in Figure 8.2. Through visual inspection, the PSMs of both the 16-32mm and 32-64mm gravels (specified in Table 8.1) were estimated to serve as a reference for when the gravels were modelled in Rocky subsequent to physical testing.

All SVC tests were conducted using gravel of the same grading: A mix consisting of 50% 16-32mm gravel and 50% 32-64mm gravel by mass. This 50/50 gravel mix was referred to as D16-64. Table 8.2 and Figure 8.3 show the particle size distribution (PSD) of the 16-32mm gravel (D16-32), 32-64mm gravel (D32-64), and D16-64. The coefficients of uniformity (C_U) curvature (C_Z) are also indicated. C_U and C_Z are parameters describing the shape of the PSD curve, defined in most soil mechanics texts (e.g. Craig, 2004):

$$C_U = D_{10}/D_{60}$$

$$C_Z = D_{30}^2/D_{10}D_{60}$$

The particle size such that n% of the particles are smaller than that size is denoted by D_n. Results show all three gravels to be poorly-graded. However, relative to the other two samples, the D16-64 gravel was well-graded. The PSD analysis is fully detailed in Appendix 1.

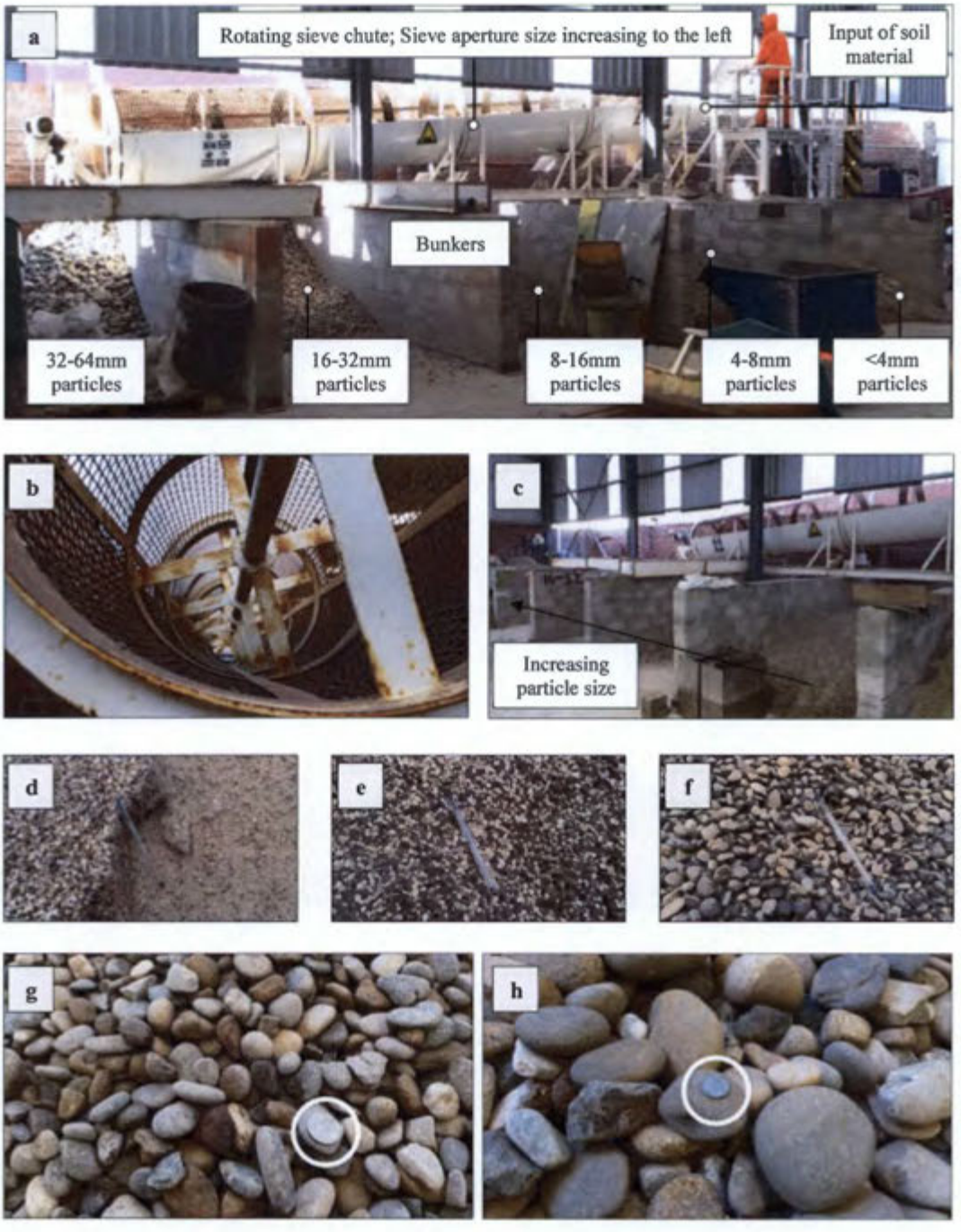

a) The rotating sieve chute and bunkers into which the soil is sieved

b) Inside the rotating sieve chute

c) The bunkers containing the sieved material

d) <4mm diameter particle size sieved material

e) 4-8mm diameter particle size (pen for scale)

f) 8-16mm diameter particle size

g) 16-32 diameter particle size (R2 coin for scale)

h) 32-64 diameter particle size

Figure 8-1: Sieved soil material used at test facility

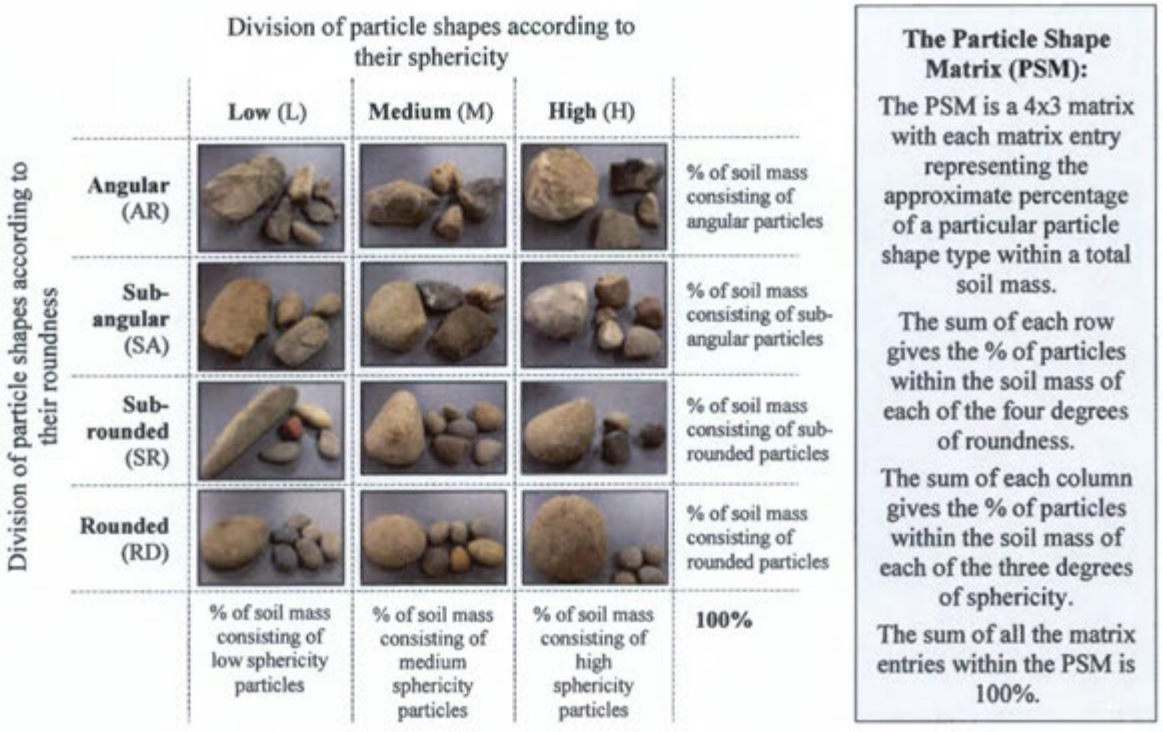

Figure 8-2: Defining and describing the Particle Shape Matrix

Photographed particles are between 16-64mm diameter

Table 8-1: Particle shape matrices of gravels used in SVC testing

a) PSM for 16-32mm gravel

	L	M	H	
AR	2.50	5.50	2.00	10
SA	2.50	5.50	2.00	10
SR	6.25	13.75	5.00	25
RD	13.75	30.25	11.00	55
	25	55	20	100

b) PSM for 32-64mm gravel

	L	M	H	
AR	3.00	5.50	1.50	10
SA	4.50	8.25	2.25	15
SR	9.00	16.50	4.50	30
RD	13.50	24.75	6.75	45
	30	55	15	100

Table 8-2: Particle size distribution of gravel samples used for SVC testing

a) D16-32

$C_U = 1.52$; $C_Z = 0.97$

Sieve Opening (mm)	Percentage passing (%)
32.0	100
26.5	93
19.0	39

b) D16-64

$C_U = 2.81$; $C_Z = 0.66$

Sieve Opening (mm)	Percentage passing (%)
64.0	100
53.0	65
37.5	55
26.5	47
19.0	19

c) D32-64

$C_U = 1.63$; $C_Z = 1.10$

Sieve Opening (mm)	Percentage passing (%)
64.0	100
53.0	71
37.5	14

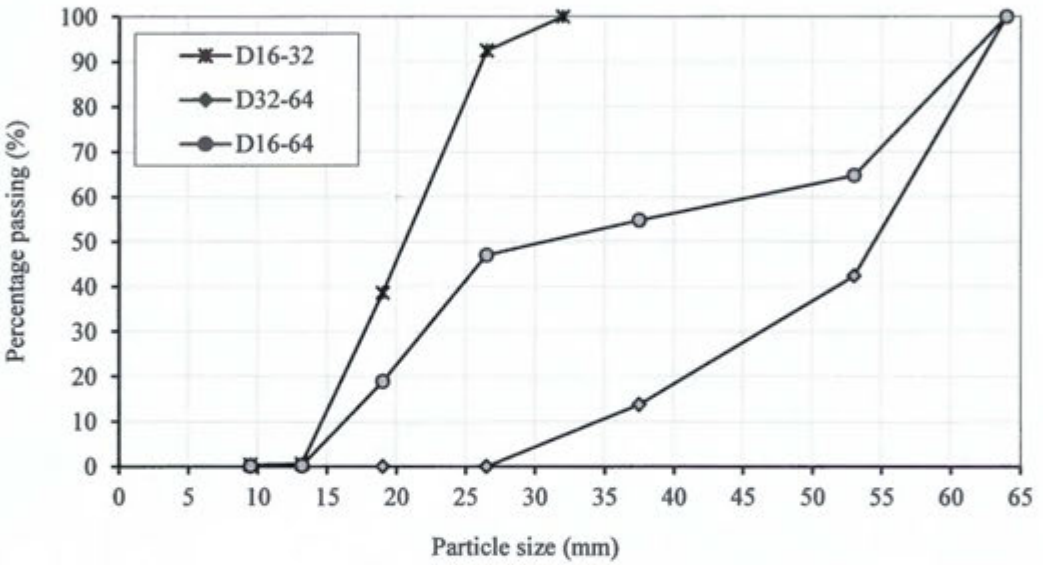

Figure 8-3: Particle size distribution of gravel samples used for SVC testing

Refer to Appendix 1 for detailed account of PSD testing

8.2. Sampling equipment

The sampling equipment of the SVC system consisted of several components, split into two categories:

- Static – parts which are assumed to remain stationary during testing, and
- Dynamic – parts with movement in the vertical direction during testing, the rate of which could be controlled and monitored.

These components are summarised in Table 8.3 and shown in Figures 8.4, 8.5, and 8.6.

Table 8-3: Components of SVC sampling equipment

Component of SVC		Description
Static	Main frame	A 6.4m high, 2m wide truss structure, consisting of 250x250mm hollow square steel cross-sections; Bolted to a specifically designed foundation and supports the vibratory motor and core barrel
	Sample bin	A 2.5m high, hollow, cylindrical steel bin, of 621mm internal diameter; 0.75m^3 volume capacity; Contains the sample soil; Weighs approximately 1t (without sample soil)
Dynamic	Vibratory motor	A motor consisting of a rotating mass unbalance; Rotating mass results in high-frequency, low-amplitude vertical oscillatory motion of the motor; Frequencies are up to 200Hz (hence called 'Sonic'); Amplitudes are a function of the frequency; The motor supports are such that its translational motion is limited to the vertical direction
	Core barrel	Hollow, EN24 high tensile steel tube; 150.4mm inside diameter; 177.8mm outside diameter; 2m long; Has ±100mm threads at the top and bottom for connection to the vibratory motor and cutter head, respectively
	Cutting head	Hollow, cylindrical, steel cutter head; Total height = 344mm; Area ratio = 51%, Cutting shoe angle = 60%; Outside clearance ratio = 4%; Screwed onto core barrel

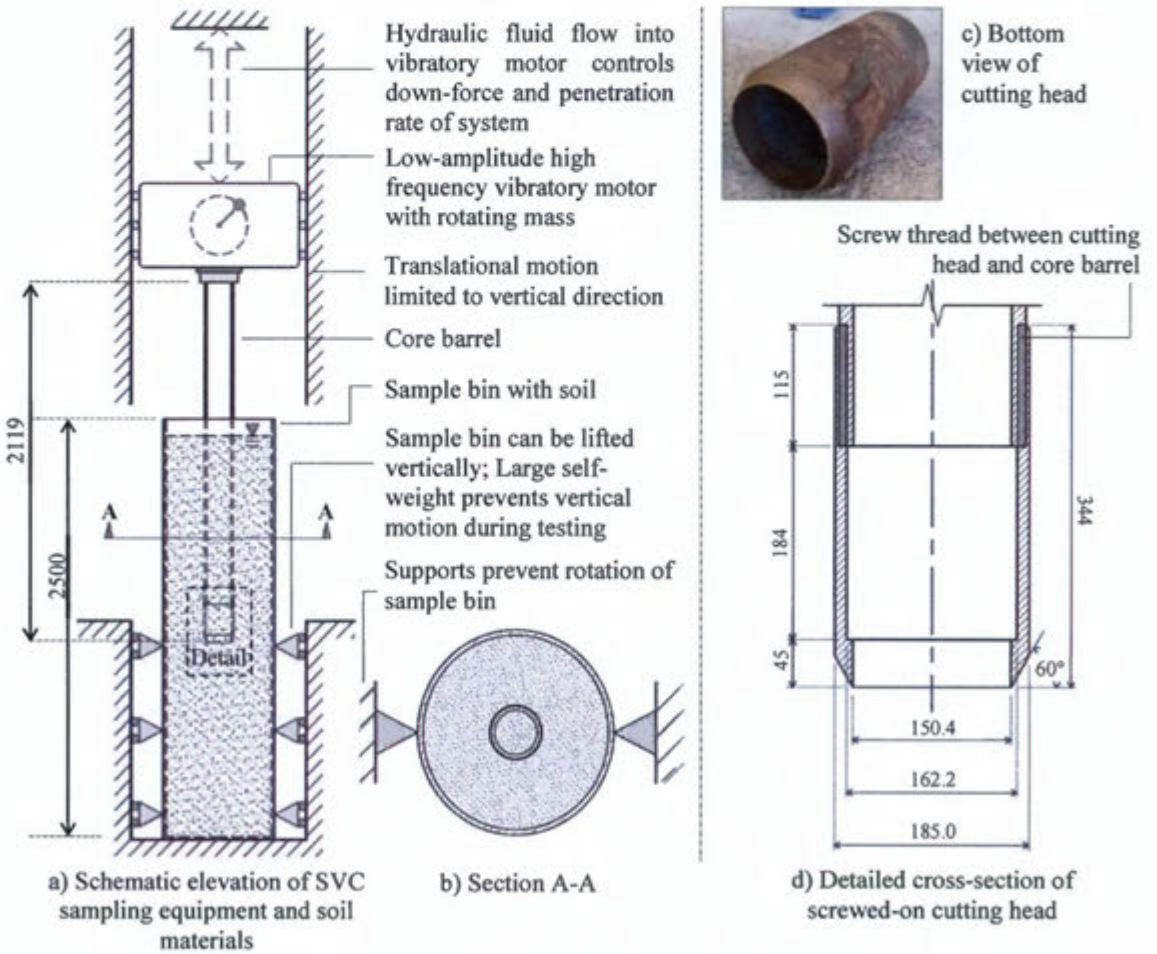

Figure 8-4: Diagrams detailing the SVC sampling equipment setup

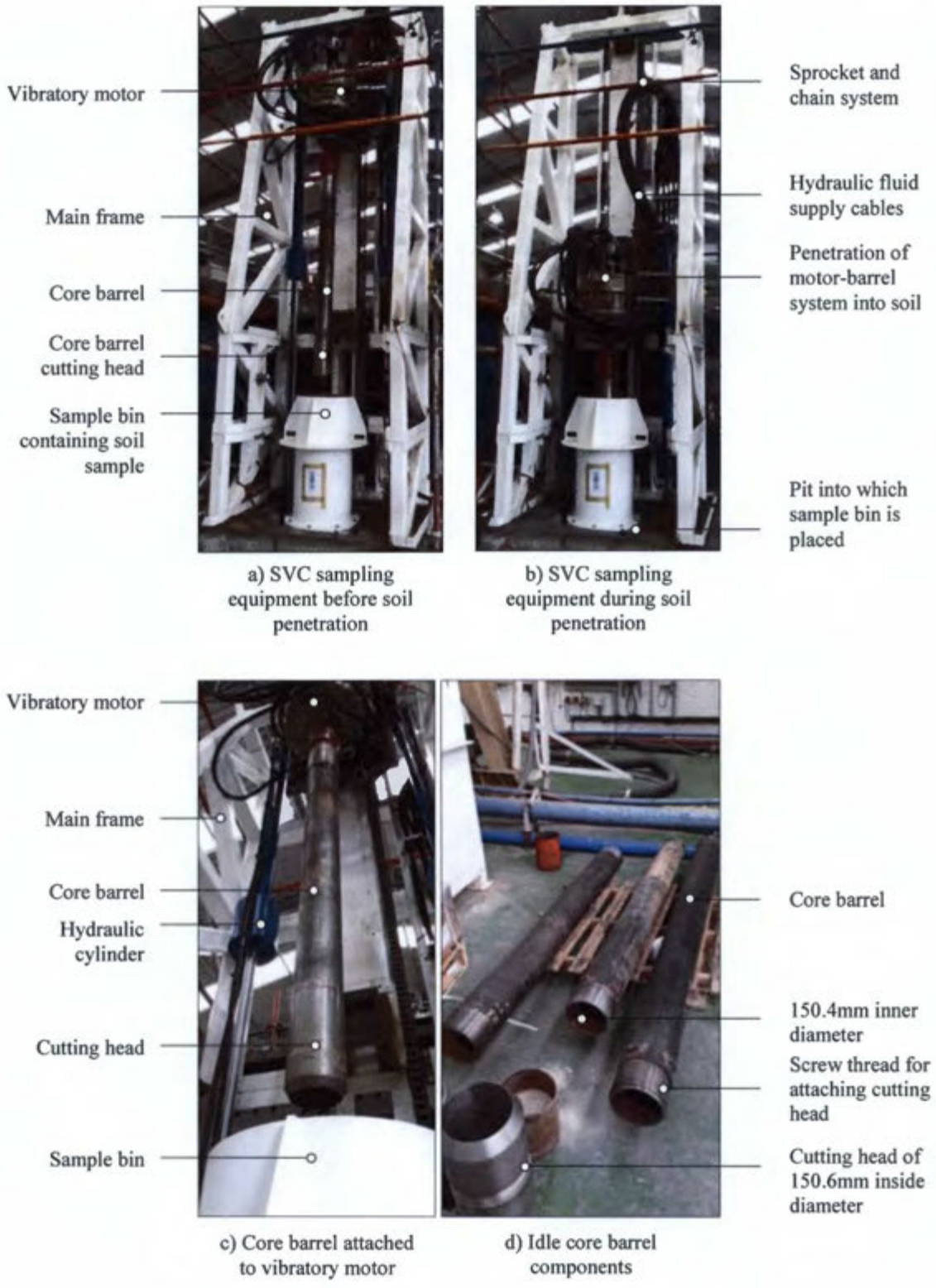

Figure 8-5: Sampling equipment of the SVC system

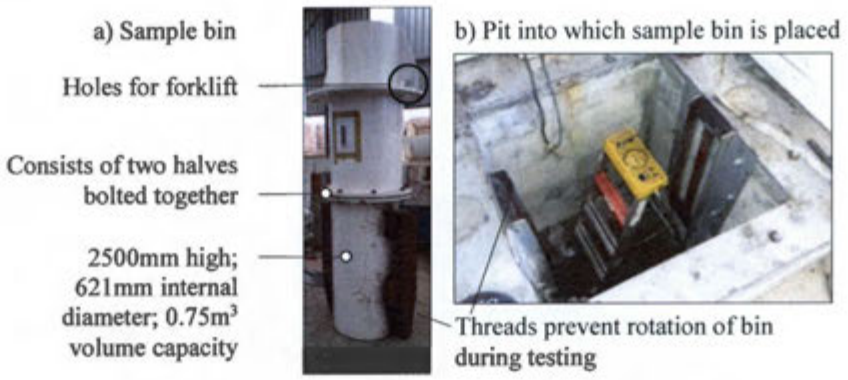

Figure 8-6: Sample bin used for SVC testing

8.2.1. Idealization of SVC system for dynamic analysis

Figure 8.7 illustrates how the SVC vibratory motor and core barrel system – henceforth referred to as the *motor-barrel* system – were idealised as single degree of freedom model for dynamic analysis. The vibratory motor consisted of a rotating mass, m_{ru}. This mass rotated at an angular rotation frequency of ω_r, a distance, r, from the centre of rotation. The motion of the motor, and therefore the core barrel, was limited to translation in the vertical direction by friction-free guides. Oscillatory motion of the motor-barrel system was resisted by stiffness and damping due to both the internal spring mechanism of the motor and the soil into which the core barrel was driven. Stiffness due to the motor and soil was modelled as two springs in parallel of stiffness k_m and k_s, respectively (Fig. 8.7a). From dynamics theory, it is known that the system equivalent stiffness k_{eq} is given by $k_{eq} = k_m + k_s$. The equivalent damping coefficient was termed c_{eq}.

For the dynamic analysis, the core barrel was assumed to be rigid. Axial strains in the core barrel were neglected – i.e. the harmonic displacement of the vibratory motor centre, $x(t)$, was equal to that of the core barrel cutting head.

8.2.2. Harmonic amplitude of core barrel: Estimation from theory

Inman (2001) gives an equation for the harmonic displacement of the motor-barrel system:

$$x(t) = X \cdot \sin(\omega_r t - \theta) \qquad (8.1)$$

X is the harmonic response amplitude (m), ω_r is the angular frequency of rotation (rad/s), t is the time (s), and θ is the angular displacement (rad), given by

$$\theta = \tan^{-1}\left(\frac{2\zeta\beta}{1-\beta^2}\right) \qquad (8.2)$$

ζ is the damping ratio given by $\zeta = c_{eq}/2\sqrt{k_{eq}m}$, and β is the frequency ratio given by $\beta = \omega_r/\omega_n$, where ω_n is the undamped natural angular frequency, given by $\omega_n = \sqrt{k_{eq}/m}$. X was calculated using:

$$X = \left(\frac{m_{ru}r}{m}\right)\left(\frac{\beta^2}{\sqrt{(1-\beta^2)^2 + (2\zeta\beta)^2}}\right) \qquad (8.3)$$

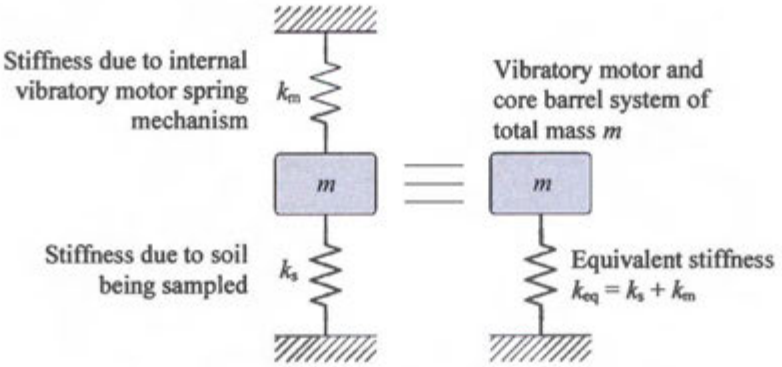

a) Springs in parallel: Determining equivalent stiffness of motor-barrel system due to both k_m and k_s

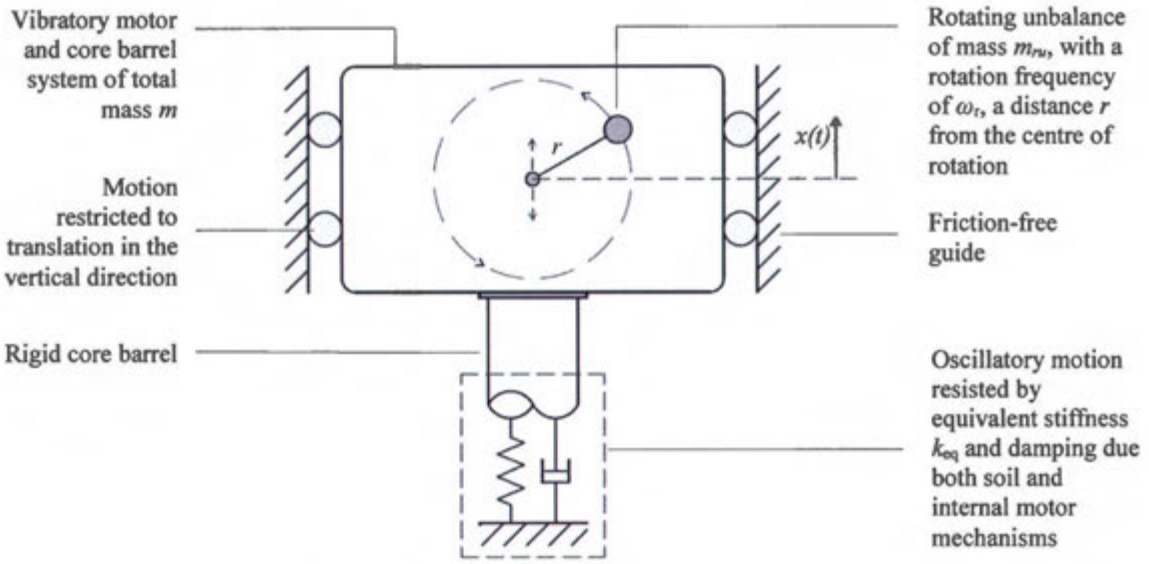

b) Model of motor-barrel system with oscillatory motion due to rotating unbalance

Figure 8-7: Idealization of SVC motor-barrel system for dynamic analysis

For the motor-barrel system used in this study, m_{ru} = 15.7kg, r = 0.01026m, and m = 510kg. The operating frequency of the motor during testing was ω_r = 986rad/s, or f_r = 157Hz. The value of k_m was known to be 20×10^6 N/m. Prior to testing, the values of k_s and ζ were unknown.

Immediately before core barrel penetration, the soil was not yet acting on the motor-barrel system. Therefore, it was reasonable to assume k_s to be zero at this point. It was expected that k_s would increase from this initial value to a maximum value k_{smax} when the barrel was at final penetration depth, d_{max}. It was hypothesised that the amplitude of the SVC vibratory motion would increase from a minimum value X_{min} when penetration depth is zero, to a maximum value X_{max} at final penetration depth. Expressed mathematically:

$$\text{If } d = 0 \Rightarrow k_s = 0 \Rightarrow k_{eq} = k_m \Rightarrow X = X_{\min}$$

$$\text{If } d = d_{\max} \Rightarrow k_s = k_{s\max} \Rightarrow k_{eq} = k_m + k_{s\max} \Rightarrow X = X_{\max}$$

Figure 8.8 and Table 8.4 show calculated values of X for a multiple order of magnitude range of k_{eq} and ζ values. Given that k_m = 20MN/m, the figure indicates that the theoretical value for X_{min} is approximately 0.32mm. Also apparent in the graph is that the effect of damping is negligible for low stiffness values. As stiffness increases, the effect of damping ratio on harmonic amplitude becomes more pronounced. However, even for the multiple order-of-magnitude range of damping ratios and stiffness values considered, X differs by less than 0.6mm. This is due to the fact that, for the majority of stiffness values considered, $\omega_r >> \omega_n$. Since the vibratory motor is operating at a frequency significantly higher than the natural frequency of the system, the effects of resonance are small (Fig. 8.9). More importantly, the variance in amplitude as result of a change in stiffness or damping is relatively small. The evolution of k_{eq}, and thus k_s, with penetration depth can be estimated if the harmonic amplitude of the system is known.

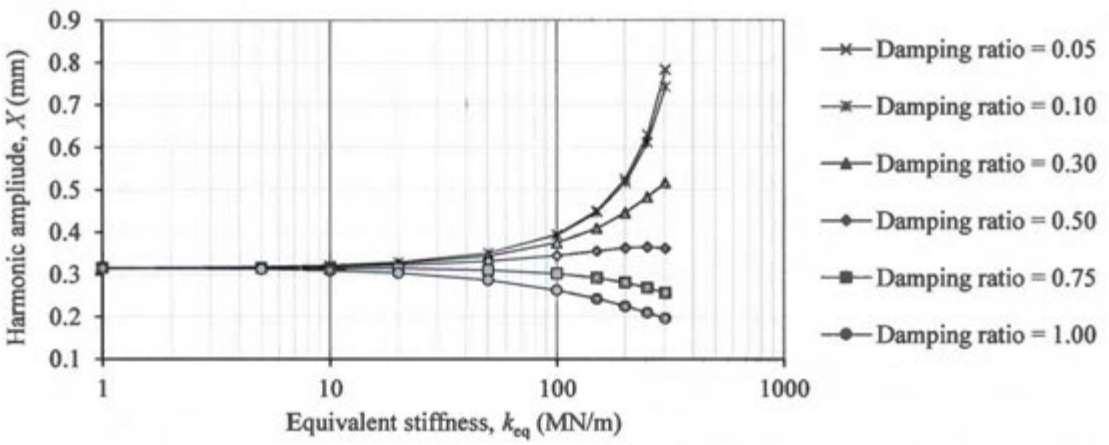

Figure 8-8: Theoretical harmonic amplitude of the SVC oscillatory motion
Plotted values given in Table 8.4

Table 8-4: Theoretical harmonic amplitude of the SVC oscillatory motion

Equivalent stiffness, k_{eq} (MN/m)	Undamped natural angular frequency, ω_n (rad/s)	Undamped natural frequency, f_n (Hz)	Frequency ratio, β, with f_f = 157Hz	Harmonic Amplitude, X (mm)					
				ζ =	ζ =	ζ =	ζ =	ζ =	ζ =
				0.05	0.10	0.30	0.50	0.75	1.00
1	44.3	7.0	22.3	0.316	0.316	0.316	0.316	0.316	0.315
5	99.0	15.8	10.0	0.319	0.319	0.318	0.317	0.315	0.313
10	140.0	22.3	7.0	0.322	0.322	0.321	0.319	0.315	0.310
20	198.0	31.5	5.0	0.329	0.329	0.327	0.322	0.314	0.304
50	313.1	49.8	3.2	0.351	0.350	0.344	0.331	0.310	0.287
100	442.8	70.5	2.2	0.395	0.393	0.375	0.345	0.302	0.263
150	542.3	86.3	1.8	0.451	0.447	0.409	0.356	0.292	0.243
200	626.2	99.7	1.6	0.526	0.517	0.446	0.362	0.281	0.225
250	700.1	111.4	1.4	0.630	0.612	0.483	0.365	0.269	0.210
300	767.0	122.1	1.3	0.784	0.743	0.516	0.362	0.256	0.197

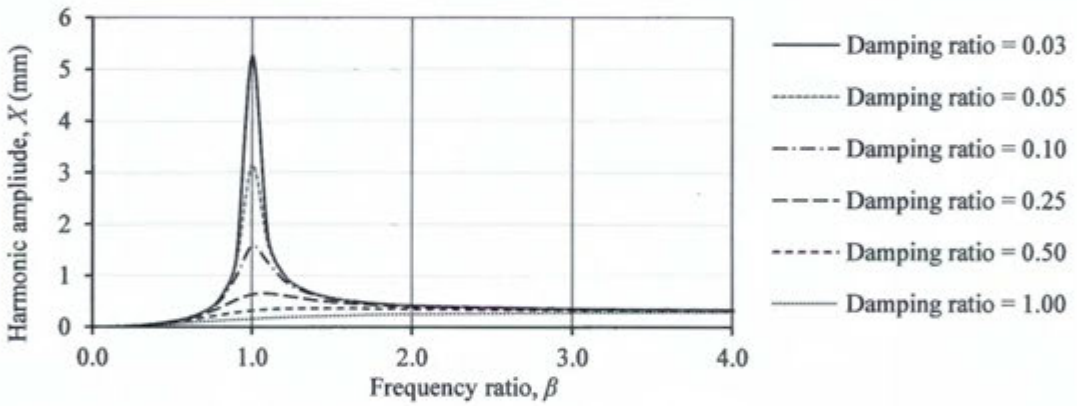

Figure 8-9: Harmonic amplitude as a function of frequency ratio

8.3. Monitoring devices

Four monitoring devices were used during SVC testing to obtain data for analysis - summarised in Table 8.5. These devices were a) The existing SVC monitoring system, b) A recovery measurement weight, c) An accelerometer, and d) Strain gauges.

Prior to physical testing, preliminary DEM models had been computed and an understanding of the required input parameters gained. Thus, in addition to allowing a more in-depth analysis of the physical results, the above-mentioned monitoring devices provided the data required for calibration of a Rocky DEM model to the physical results.

8.3.1. Existing SVC monitoring system

At the time of physical testing, the SVC had built-in devices for monitoring a number of system variables at a sample rate of 1Hz. The three variables applicable to this study were the rotation frequency of the vibratory motor f_r, the penetration depth of the core barrel d, and the hydraulic pressure in the cylinders controlling the vertical movement of the motor-barrel system, P.

8.3.2. Recovery measurement device

To measure the recovery ratio of a given gravel sample, a 'recovery measurement device' was fabricated, consisting of a cable and a weight – shown in Figure 8.10. The cable was attached to the top of the weight and then thread through a hole in the side of the vibratory motor sub-assembly - termed the *measurement point*. This allowed the weight to be lowered and raised from this point by releasing or pulling the cable. For every test, before the core barrel was attached, the weight was lowered to rest on the initial level of gravel within the sample bin. Using spray paint, a mark was made on the cable at the measurement point. The core barrel was then attached and the sampling conducted, with the weight raised as high as possible so not to obstruct attachment of the core barrel. Immediately after the core barrel reached final penetration depth, the weight was once again lowered to rest on top of the gravel – this time within the core barrel. Another mark was made on the cable at the measurement point. The decrease in height of gravel within the core barrel during sampling was indicated by the length of cable between the two marks. Thus, since the penetration depth was known, the recovery ratio could be calculated. Figure 8.11 shows a schematic of the recovery measurement method described above. The weight was heavy enough such that it would sink in water, but light enough such that it would not affect the level of gravel within the sample tube. The RR was chosen to be measured before core barrel extraction for a number of practical reasons:

i) The need for a core-catcher was removed, thus simplifying subsequent DEM modelling, and preventing any potential damage to a core-catcher repeatedly used for testing.

ii) It was deemed to be the stage in the sampling process that would yield the most accurate RR measurement; Errors in RR measurement due to volume changes in gravel within the core barrel during extraction would not occur.

iii) It removed the need to extrude core samples from the barrel after every test for observation and measurement, therefore allowing a greater number of tests to be completed in a shorter period of time.

8.3.3. Accelerometer

An accelerometer was bolted to the SVC motor sub-assembly during testing (Fig. 8.10). The device had a sample rate of 775Hz and provided the time-variable acceleration a of the core barrel oscillatory motion. From this, the harmonic displacement of the barrel, x, could be calculated. Details of the accelerometer are provided in Appendix 2.

8.3.4. Strain gauges

Gauges could not be placed on the core barrel during SVC testing. At final penetration depth, the core barrel would be fully inserted into saturated gravel and any gauges attached to the barrel would likely be damaged. Furthermore, it was expected that vibrations would damage or disturb the strain-reading apparatus. Therefore, gauges were placed on the 'cradle' of the SVC (Fig. 8.12). A series of preliminary coring tests – fully detailed in Appendix 3 - were conducted to determine an empirical equation between the vertical force acting on the core barrel during its penetration into the gravel F_B, and the cradle strain ε_C. Results indicated that the relationship between ε_C and F_B could be approximated by the following linear equation:

$$F_B = E_B A_B [0.1799(\varepsilon_C) - 12.2633] \qquad (8.4)$$

Where F_B is the vertical force acting on the core barrel in kN

E_B is the Young's modulus of the core barrel material in GPa = 200GPa (EN24 High Tensile Steel Condition V)

A_B is the cross-sectional of the core barrel in m^2 = 7.072 $\times 10^{-3}$ m^2 (177.8mm outer diameter; 150.4mm inner diameter)

ε_C is the microstrain measured in the cradle of the SVC system

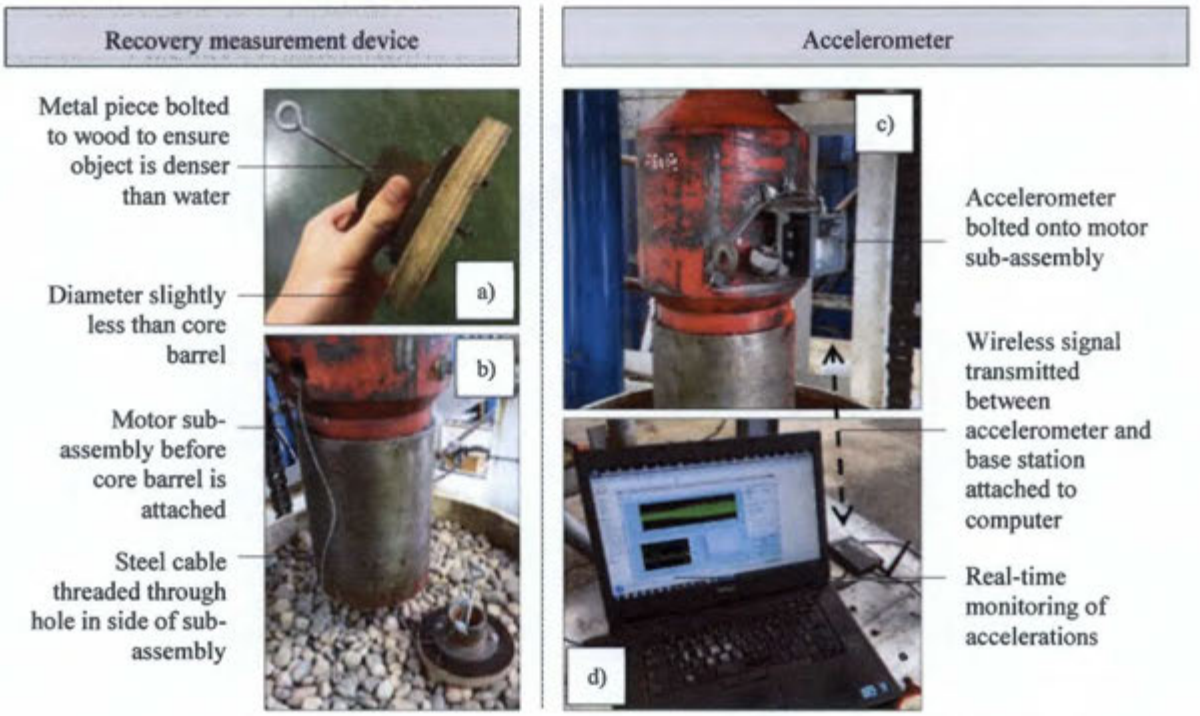

Figure 8-10: The recovery measurement device and accelerometer

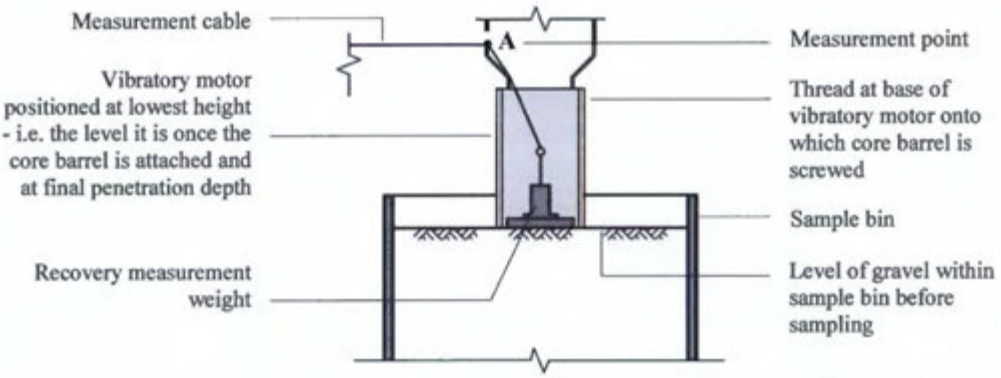

a) Before core penetration: Weight resting on initial level of gravel within sample bin; Core barrel not yet attached to vibratory motor; Point A marked on measurement chord

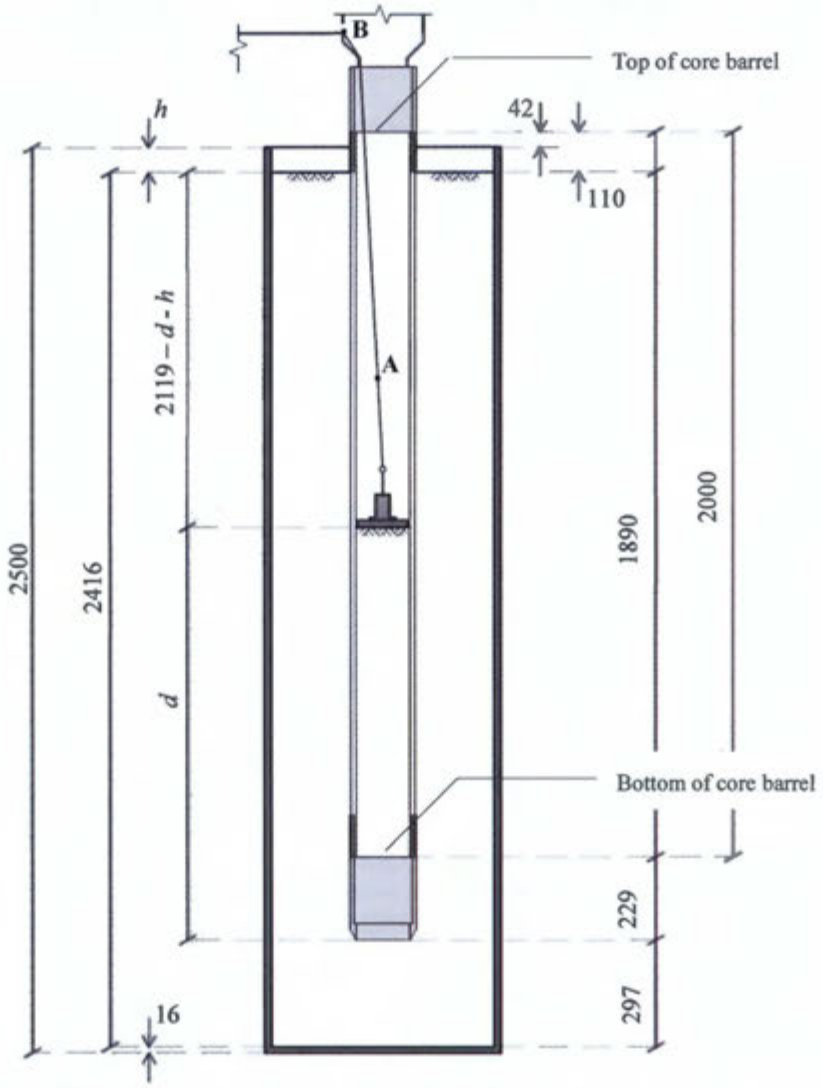

b) After core penetration: Core barrel at final depth; Weight resting on gravel level within core barrel; Point B marked on measurement chord; Length of chord between A and B = $2119 - d - h$

Figure 8-11: Schematic diagram: Use of weight and cable to measure recovery ratio

All dimensions in mm

Table 8-5: Summary of data provided by monitoring devices

Monitoring device	Data provided
Existing SVC monitoring system	Rotation frequency of the vibratory motor f_t, Penetration depth of the core barrel d, Hydraulic pressure in the cylinders controlling the vertical movement of the motor-barrel system, P
Recovery measurement device	Recovery ratio at final penetration depth
Accelerometer	Acceleration of core barrel, a Harmonic displacement of core barrel, x
Strain gauges	Strain of SVC cradle, ε_C Vertical force on core barrel, F_B

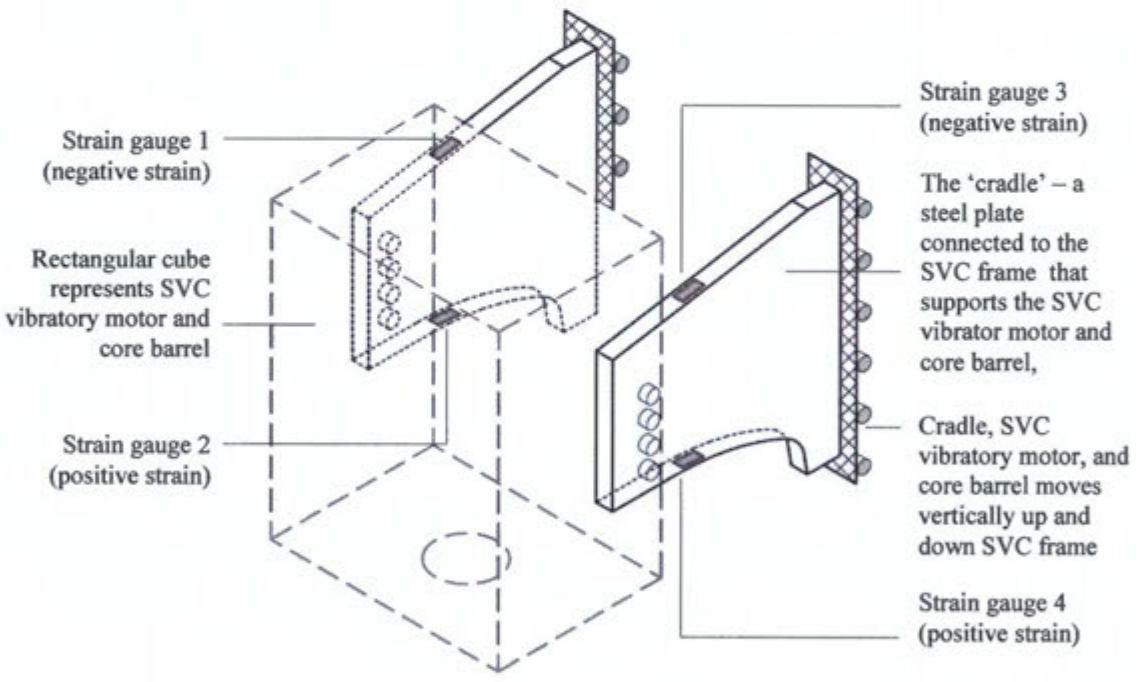

Figure 8-12: Placement of strain gauges on SVC cradle

See Appendix 3 for detailed description of strain gauge calibration

9. Physical test methodology

9.1. Overview of monitoring procedure

A total of seven SVC tests were conducted. Table 9.1 shows what system variables were measured in each test. Due to wireless signal interference, strain and acceleration could not be monitored simultaneously. Before every test, the average void ratio, e, and the average specific gravity, G_s, of the particles in the sample bin were determined. These properties were required for DEM model calibration. The method used for measuring these parameters is described in the next section.

Table 9-1: Summary of variables monitored during SVC testing

Y = Yes ; N = No

Variable measured	Stage of testing measured	Test Number						
		1	2	3	4	5	6	7
Initial average void ratio of gravel in sample bin, e	Before core barrel penetration	Y	Y	Y	Y	Y	Y	Y
Average specific gravity of gravel particles in sample bin, G_s		Y	Y	Y	Y	Y	Y	Y
Core barrel penetration depth, $d(t)$	During core barrel penetration	Y	Y	Y	Y	Y	Y	Y
Hydraulic pressure in cylinders, $P(t)$		Y	Y	Y	Y	Y	Y	Y
Vibratory motor rotation frequency, $f_r(t)$		Y	Y	Y	Y	Y	Y	Y
Cradle strain, $\varepsilon_C(t)$		N	Y	Y	Y	Y	Y	N
Core barrel acceleration, $a(t)$		N	N	N	N	N	N	Y
Recovery ratio, RR	After core barrel penetration	Y	Y	Y	Y	Y	Y	Y

9.2. Gravel sample preparation

All seven gravel samples used for SVC testing were prepared in the same way:

i) The inside of the empty sample bin was cleaned and allowed to dry

ii) Once dry, the empty sample bin was weighed and its mass m_0 recorded (Fig. 9.1)

iii) The D16-64 gravel mix was prepared using 650kg dry D16-32 gravel and 650kg dry D32-64 gravel

iv) The mixed dry D16-64 gravel was placed in a skip

v) Using a forklift, the skip was raised and tilted to empty the dry D16-64 gravel into the sample bin until the top of the gravel was approximately 110mm from the top of the sample bin; No compaction technique was used

vi) Excess D16-64 was sieved again into separate D16-32 and D32-64 bunkers for use in future sample preparation

vii) The sample bin containing the dry gravel was weighed and its mass m_1 recorded

viii) The sample bin was filled with fresh water until the surface of the water was approximately level with the average level of the top gravel particles

ix) The sample bin containing the saturated gravel was weighed and its mass m_2 recorded

Using the recorded masses of the sample bin during sample preparation, and knowing the geometry of the sample bin, the average void ratio and specific gravity of the gravel was calculated using the following equations:

$$e = \frac{V_v}{V_s} = \frac{V_w}{V_{TOT} - V_w} = \frac{\rho_w (m_2 - m_1)}{\pi (D_{sb}/2)^2 H_{sb} - \rho_w (m_2 - m_1)} \qquad (9.1)$$

$$G_s = \frac{\rho_s}{\rho_w} = \frac{m_s/V_s}{\rho_w} = \frac{(m_1 - m_0)/V_s}{\rho_w} \qquad (9.2)$$

where V_v is the volume of voids in the sample bin (m^3), V_s is the volume of solid particles in the sample bin (m^3), V_w is the volume of water in the sample bin (m^3), V_{TOT} is the total volume of gravel within the sample bin (m^3), ρ_w is the density of water = 1000kg/m^3, D_{sb} is the internal diameter of the sample bin (m), H_{sb} is the height of gravel within the sample bin (m), and ρ_s is the average density of the gravel particles (kg/m^3).

In developing equations 9.1 and 9.2, it was assumed that, once the sample bin is filled with water, the gravel is fully saturated – i.e. there are no air voids. Therefore:

$$V_V = V_W = V_{TOT} - V_S \qquad (9.3)$$

There was no need to ensure the gravel was prepared to a specific void ratio, and thus no need to use any compaction technique. The DEM modelling process required only that the void ratio for each sample be known. This was achieved using the above-described sample preparation method and application of Equation 9.1.

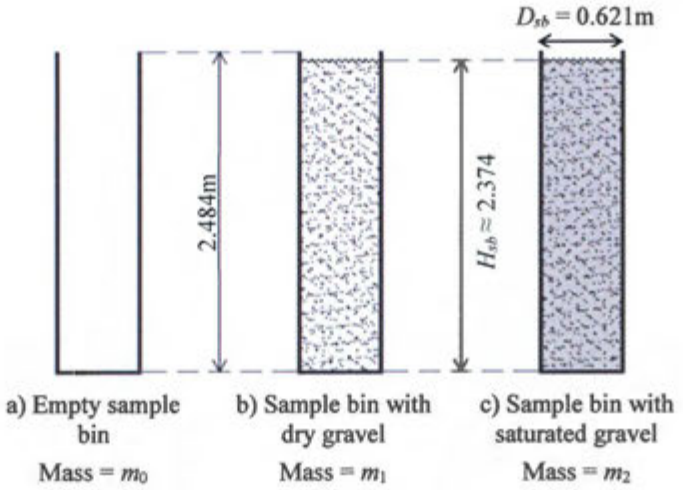

Figure 9-1: Bin masses recorded during sample preparation

9.3. Operation of vibratory motor and core barrel

For all seven tests, the core barrel penetration rate $\Delta d/\Delta t$ and SVC vibratory motor frequency f_r were held constant. These values were selected to be: $\Delta d/\Delta t \approx 24$mm/s ≈ 42s/m, and $f_r \approx 157$Hz. There were various factors influencing the selection of both $\Delta d/\Delta t$ and f_r:

The core barrel penetration rate was manually controlled by adjusting the hydraulics of the system. If $\Delta d/\Delta t$ was too high (approximately 40mm/s), the mechanical system reached its upper operating limits. Therefore, to avoid potential damage to the SVC system, the penetration rate was chosen to be sufficiently lower than 40mm/s. Conversely, if $\Delta d/\Delta t$ was too low, the time required to be simulated in the calibrated DEM model would increase. This could lead to an increase in computation time of as much as a few days.

The vibratory motor rotational frequency was also manually controlled. Similar to the control of penetration rate, it was required that f_r be low enough such that the mechanical system was not damaged from repeated testing at operational limits. It was also required that f_r be high enough such that the system did not operate close to its natural frequency. The effects of resonance would cause large and unpredictable variations in core barrel amplitude.

For every test, the initial lowering of the barrel into the gravel was without vibratory action. Once the base of the core barrel was observed to have penetrated approximately 50mm into the gravel, penetration was manually stopped. At this point, the frequency was gradually increased to 157Hz. Once f_r was stable at 157Hz, core barrel penetration at a constant rate of 24mm/s commenced. This continued until the motor-barrel system reached its lowest point. The point of zero penetration was considered the level from which the barrel began its descent once vibrating at 157Hz. Depending on the height of the soil in the bin, final penetration depth was approximately 1.975m.

10. Physical testing: Results and discussion

10.1. Measured soil properties

Table 10.1 summarises the measured soil properties for each of the seven SVC tests:

Table 10-1: Measured void ratios and specific gravities

Calculated using equations 9.1 and 9.2

Parameter measured/calculated	SVC Test Number						
	1	2	3	4	5	6	7
Mass of sample bin, m_0 (kg)	794.8	792.5	801.5	795.7	793.0	800.3	795.7
Mass of sample bin and dry gravel, m_1 (kg)	1958.5	1996.5	1964.0	1975.0	2010.2	1968.3	1965.8
Mass of sample bin and saturated gravel, m_2 (kg)	2196.0	2230.8	2204.3	2230.0	2240.5	2214.5	2220.8
Mass of gravel, m_1-m_0 (kg)	1163.7	1204.0	1162.5	1179.3	1217.2	1168.0	1170.2
Mass of water, m_2-m_1 (kg)	237.5	234.3	240.3	255.0	230.3	246.2	255.0
Height of soil from top of sample bin, H_{sb} (m)	0.100	0.125	0.070	0.115	0.105	0.120	0.115
Volume of water (voids) , V_v (m^3)	0.2375	0.234	0.240	0.255	0.230	0.246	0.255
Volume of gravel (solids), Vs (m^3)	0.479	0.488	0.474	0.476	0.487	0.474	0.463
Void ratio, $e = V_v / V_s$	**0.496**	**0.480**	**0.507**	**0.536**	**0.473**	**0.519**	**0.551**
Specific gravity of particles, G_s	**2.432**	**2.469**	**2.452**	**2.477**	**2.498**	**2.462**	**2.530**

The above table shows the average void ratio to be 0.509, with a coefficient of variability of 5.2%. The coefficient of variability C is defined as the ratio between the standard deviation and average of a data set.

While variation between the measured void ratios was small, it was worth considering the cause of these deviations: In practice, small differences in bulk density of the prepared gravel samples cannot be avoided. While a consistent method was used to mix and prepare every D16-64 sample, variation in grading can occur due to loss of particles during a) the placing of the mixed gravel into the skip, or b) a emptying the gravel into the sample bin. Furthermore, when emptying the particles into the bin, the extent to which they were compacted was influenced by the rate the gravel entered the bin. If the rate was high, the weight of the particles entering and falling onto the lower particles would provide increased energy for compaction. However, a C of 5.2% suggests that these causes of variation in e were not significant.

The average specific gravity is 2.474 with C = 1.2%. G_s is not influenced by sample preparation. Therefore, the measured G_s values have a lower coefficient of variability.

10.2. Data collected during core barrel penetration

This section presents the various data recorded during core barrel penetration. The hydraulic pressure, P, did not serve as input data for DEM modelling and therefore was not reported in this part of the dissertation. P was monitored during testing only to ensure the system did not reach its operational limits. Appendix 4 provides detailed results of all data collected during SVC testing.

10.2.1. Penetration rate, frequency and force results

Figure 10.1 shows time-variable plots of core barrel penetration depth d and vibratory motor rotation frequency f_r for each of the seven SVC tests. The cradle strain was measured only for tests two to six. Therefore, only for these tests were graphs provided that indicated the vertical force on the core barrel F_B. The following is a discussion the results given in Figure 10.1:

The approximately straight lines of the d-plots indicate a constant penetration rate for each test. Similar gradients between successive lines confirm that the penetration rate was constant between tests. The average penetration rate between all tests was 24.1mm/s. For all tests, the core barrel penetrated to a depth just less than 2m in a time of approximately 85s. The average maximum d was 1.975m.

A slight decrease in gradient of the test two d-plot within the last 5-10s of penetration can be observed. In this test, the penetration rate needed to be manually decreased due to a sudden rise in hydraulic pressure. This rise in P was likely due to increased resistance from the soil. The 'spike' in the F_B-plot for test two immediately before the decrease in d confirms this. The observed decrease in F_B subsequent to this 'spike' corresponds to the decrease in penetration rate. The sudden rise in P and F_B can be attributed to a layer of gravel within the sample bin of significantly higher density than that corresponding to its average void ratio.

The frequency plots show variation in f_r with time. This was unavoidable. Frequency was manually controlled. Since f_r was significantly larger than the theoretical natural frequency of the system, the small deviations in f_r apparent in Figure 10.1 would have little effect on the dynamic response of the system. Thus, the variation in f_r from its average value of 157Hz was considered negligible.

The F_B results show the greatest variability. This is in accordance to the literature. The 'slip-stick' nature of soil entry into a penetrating core barrel described by De Nicola and Randolph (1997) is the cause of the marked local variation in force plots apparent in both Figure 4.3 and Figure 10.1. Due to natural randomness in particle arrangement and orientation within gravel, no two force plots were expected to be the same. Thus, attention was rather given to whether the F_B-plots shared common trends. Indeed, it was observed that the maximum F_B values for all tests tended towards -65kN and these maximums occurred within the last ten seconds (~0.25m) of penetration. The negative force values indicate compression. The sharp decrease in F_B within the last 1-2s of every test was due to the decrease in penetration rate to zero.

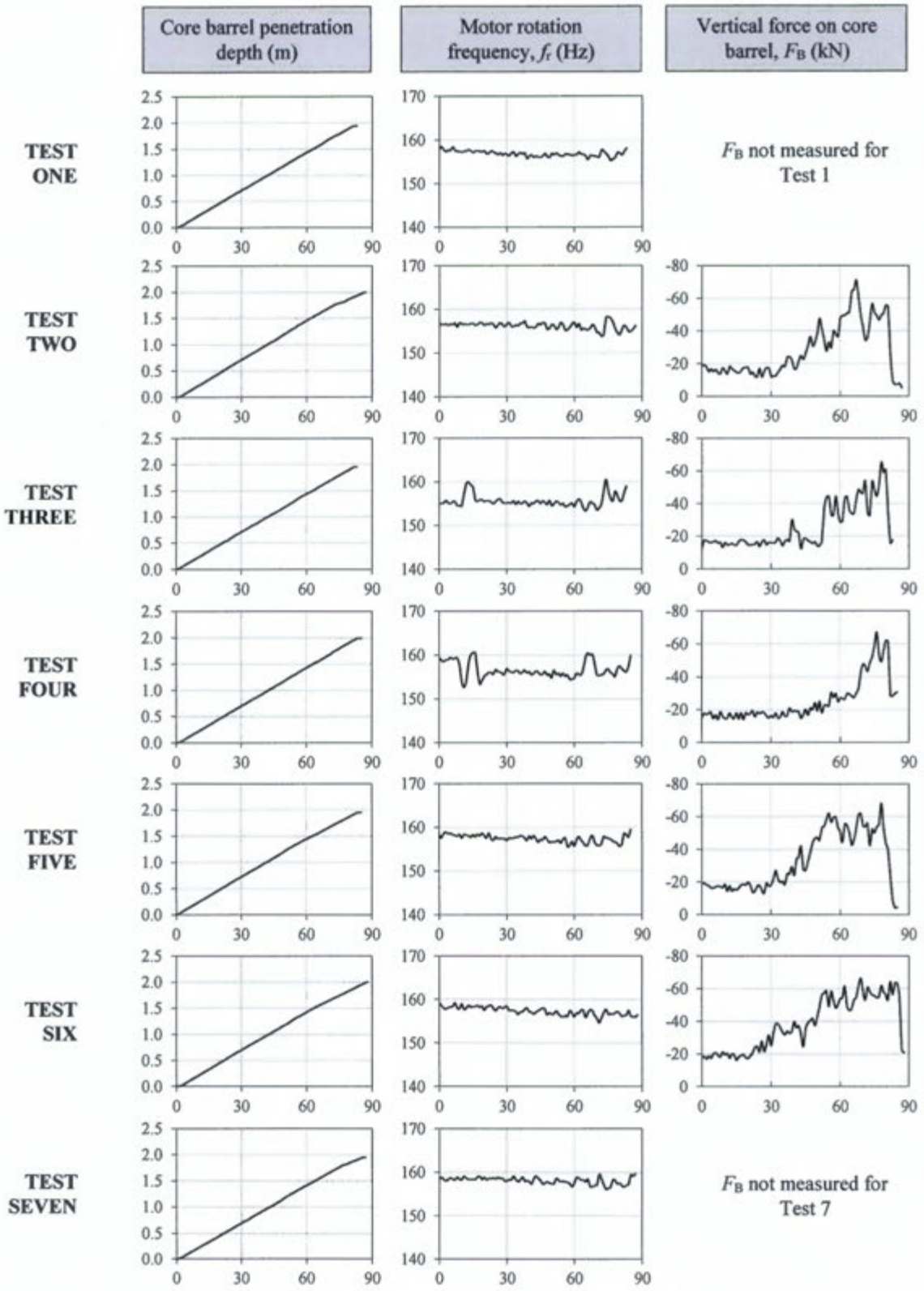

Figure 10-1: Selected results from SVC testing

Time (s) is the unit for all horizontal axes; Vertical axes are as indicated for each column

Intuitively, it was expected that the force acting on the core barrel be zero at zero penetration depth. The plots of measured F_B in Figure 10.1 indicate that this is not the case. A 'plateau' in the F_B plots within the first 20-30s of penetration can be noted, where the compressive force is approximately constant at ~18kN. Part of this non-zero force would be due to the positioning of the barrel into the top ~50mm of gravel before penetration. However, it was unreasonable to assume that such a relatively small penetration depth would result in a force of this magnitude acting on the barrel. By considering the weight and hydraulics of the SVC system, the reason for the large magnitude of the non-zero initial F_B value was realised:

The vertical movement of the motor-barrel system was controlled by hydraulic cylinders. Before soil penetration, the weight of the dynamic parts of the SVC system w_d was supported solely by these mechanisms. In other words, the cylinders prevented the downwards sliding of the motor-barrel system and cradle on the SVC frame. Therefore, before sampling began, the cylinders were providing an upwards force. As sampling commenced, the upwards force acting on the core barrel F_B increased. At a certain penetration depth - termed the critical depth d_{crit} - the weight of the components supported by cylinders would equal F_B. At this point, the cylinders no longer supported the motor-barrel system, but rather provided the downwards driving force required for further penetration. Figure 10.2 shows a generic plot of the process described above. The diagonal dashed line represents the general increasing relationship between penetration depth and F_B. The horizontal line represents the constant weight of the dynamic SVC parts.

The equation for F_B (Eq. 8.4) was developed by calibrating measured core barrel strains to measured cradle strains and hydraulic cylinder pressures. In Appendix 3, it was illustrated that this equation provided a reasonable estimate of F_B for depths greater than d_{crit}. However, the empirical equation does not account for the increase in F_B between $d = 0$ and $d = d_{crit}$. This is because, during initial stages of sampling, the measured cradle strain ε_C is primarily a function of the weight of the motor-barrel system, rather than F_B.

In viewing the force plots yielded by Equation 8.4, d_{crit} was considered the depth at which F_B begins to show an increasing trend. Therefore, the physical results shown in Figure 10.1 suggest that d_{crit} is between 0.5-0.7m.

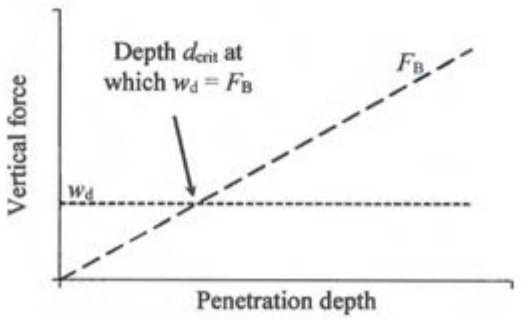

Figure 10-2: Definition of critical depth d_{crit} for SVC system

10.2.2. Accelerometer readings

Figure 10.3a shows the accelerations of the core barrel measured during test seven as a function time. The 'band' of acceleration apparent in Figure 10.3a can be attributed to the 775Hz data sample rate. The individual cycles cannot be observed at the scale shown. To illustrate the shape of the acceleration plot, Figure 10.3b shows the recorded accelerations over 0.1s of core barrel penetration.

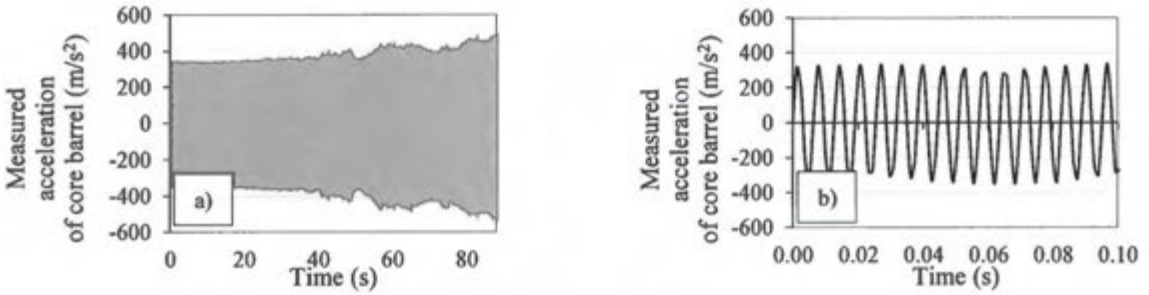

Figure 10-3: Measured core barrel accelerations

A further two observations can be made from Figure 10.3a: a) The accelerations are symmetrical around the horizontal zero axis, and b) The amplitude of the acceleration curve gradually increases as time, or penetration depth, increases. Figure 10.3b clearly shows the acceleration plot to be sinusoidal. Therefore, the acceleration $a(t)$ can be expressed as:

$$a(t) = A\sin(2\pi f_r t) \qquad (10.1)$$

where A is the acceleration amplitude (m/s^2), $2\pi f_r$ represents the conversion of f_r (157Hz) to angular rotation frequency ω_r (rad/s), and t is time (s). To determine the harmonic displacement of the core barrel $x(t)$, Equation 10.1 was integrated twice. By introducing the condition that $x(0) = 0$, the integration constant becomes zero. Therefore, $x(t)$ is given by:

$$x(t) = \left(\frac{-A}{(2\pi f_r)^2}\right)\sin(2\pi f_r t) \qquad (10.2)$$

The absolute value of the amplitude term in Equation 10.2, $\left| -A/(2\pi f_r)^2 \right|$, represents the harmonic response amplitude, X, equal to that given by Equation 8.3. Since only the amplitude magnitude was of concern, the absolute value could be considered; The sign of the amplitude term was arbitrary. Figure 10.4a shows the evolution of X with penetration depth, calculated from the recorded values of $a(t)$ shown in Figure 10.3b. Included in the plot is a moving average trendline which approximates the variable amplitude.

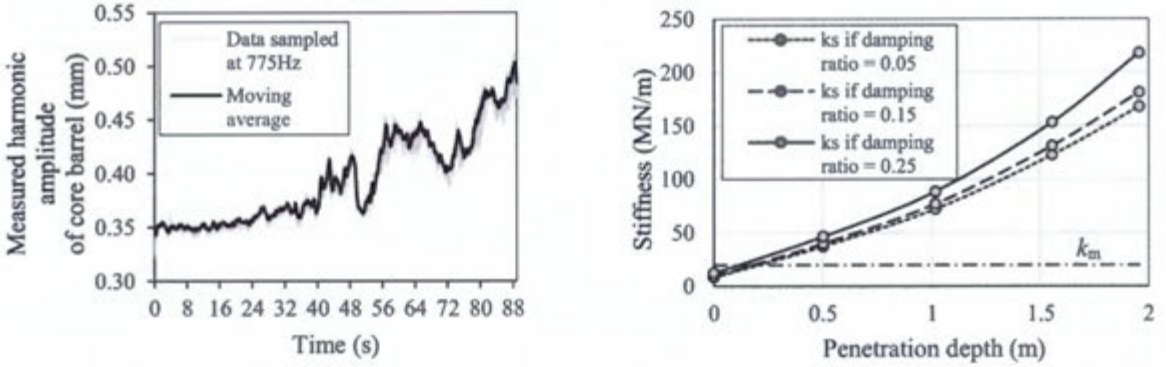

a) Measured core barrel displacement amplitude

b) Increase is soil stiffness with penetration depth

Figure 10-4: Evaluation of core barrel displacement amplitude

Figure 10.4a indicates that the value of $x(t)$ at zero penetration depth, ~0.34mm, is very similar to that estimated from theory, ~0.32mm. The measured amplitude is slightly higher than the theoretical value due to the fact that k_s was in fact not zero immediately before core barrel penetration began. Some stiffness was offered by the top ~50mm of gravel in which the cutting head was positioned immediately prior to sampling. Since k_s is non-zero positive, k_{eq} and $x(t)$ would both increase. Also clear in Figure 10.4a is an increase in amplitude with penetration depth. This too agrees with the theoretical predictions. The final value of $x(t)$ is approximately 0.50mm. With both $x(t)$ and k_m known, the increase in soil stiffness k_s with penetration depth was estimated by rearranging the equation for harmonic amplitude (Eq. 8.3). Figure 10.4b shows calculated values of k_s at penetration depths corresponding to times 0s, 22s, 44s, 66s and 88s during test seven. Also included for reference is the constant value of k_m. Although the damping ratio of the system was not known, comparison between the measured and theoretical displacement amplitude suggested that the system has a low damping ratio. Therefore, three plots of k_s were calculated, for damping ratios of 0.05, 0.15 and 0.25.

Figure 10.4b indicates significant increase in soil stiffness with core barrel penetration. At final depth, the soil offers a stiffness an order of magnitude larger than the internal SVC spring mechanism – as high as 215MN/m. As expected from theory (Inman, 2001), an increase in damping ratio corresponds to an increase in stiffness. The non-zero value of k_s at zero penetration can be attributed to the stiffness offered by the top ~50mm of gravel. This initial k_s was marginally less than k_m for all damping ratios considered.

10.3. Recovery ratios of gravel samples

Table 10.2 summarises the void ratio and recovery ratio results for each SVC test. The recovery ratios of the sampled gravel cores were very poor. Two samples yielded recovery of less than 50%. The average RR was 53%. This suggests a clear difficulty in practically achieving high quality samples in gravel soils.

Table 10-2: Summary of void ratio and recovery ratio results

Test number	1	2	3	4	5	6	7
Void ratio, *e*	0.496	0.480	0.507	0.536	0.473	0.519	0.551
Recovery ratio, RR (%)	52.0	53.2	50.7	46.6	59.0	64.9	46.1

A trend between void ratio and recovery ratio was noted. If the RR for test six is considered and outlier and neglected, the correlation coefficient *r* between *e* and RR is 0.935, suggesting a strong decreasing linear relationship between the two parameters (Fig. 10.5). The correlation coefficient as a tool for statistical analysis is described in Appendix 5. The relatively high RR of 64.9% for test six was unexpected. No irregularities were observed in the corresponding penetration rate, force or frequency results. Similarly, the void ratio and specific gravity of the gravel was not abnormal. Thus, the RR result for test six was deemed an anomaly.

The observed decrease in recovery with increasing void ratio may be explained through consideration of the gravel bulk density. A higher void ratio indicates a gravel of lower bulk density. The particles of a loose gravel – i.e. low number of particles per unit volume - are more prone to rearrangement and displacement around a descending core barrel head. For a higher bulk density, the particles are more densely packed, allowing a greater number of particles to enter the sampler during penetration, ultimately increasing recovery ratio. The trend between *e* and RR may also be attributed to the influence of void ratio on shear strength and bearing capacity. This is in accordance with theory described in the literature (De Nicola & Randolph, 1997; Skinner & McCave, 2003). Assuming negligible influence on shear strength parameters, a lower bulk density corresponds to a lower bearing capacity. A soil with a low bearing capacity is more likely to fail in shear and be displaced around the penetrating core barrel. A soil with a higher bearing capacity is more likely to provide the bearing force required to drive the soil contained in the sampling tube upwards – thus improving soil recovery. However, for the highly coarse gravels tested in this study, it was considered more appropriate to attribute the trend between *e* and RR directly to the variation in bulk density, rather than shear strength or bearing capacity.

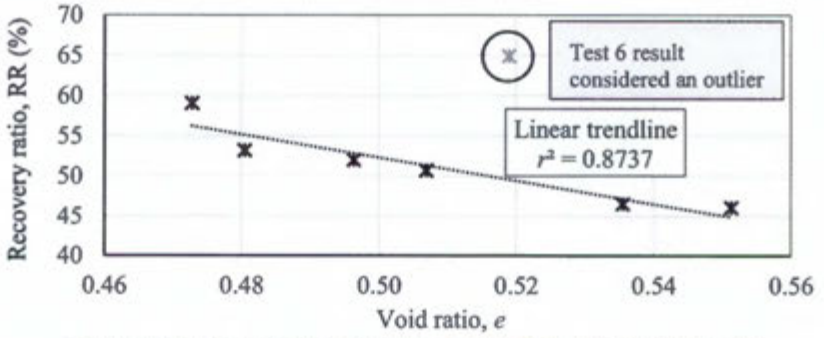

Figure 10-5: Recovery ratio plotted against void ratio

11. Summary and conclusions: Part III

The following is a summary of the physical test procedure:

- Seven SVC Tests were conducted on poorly-graded gravel samples consisting of mostly hard, quartzitic sandstone particles; Particle sizes ranged between 16mm and 64mm in diameter; All gravel samples were prepared using an identical procedure, with the intention of achieving identical particle gradings between samples
- Slight differences in void ratios between gravel samples were observed; These were attributed to unavoidable particle losses during sample preparation in practice
- For the seven gravel samples, the average void ratio was 0.509, and the average specific gravity was 2.474
- For all seven tests, core barrel penetration rate and motor rotation frequency were manually operated to be 24mm/s and 157Hz, respectively
- During core barrel penetration, the following variables were measured and recorded: core barrel penetration rate, motor rotation frequency, vertical force on core barrel, and core barrel vibratory amplitude
- The recovery ratio of each gravel sample was measured before core barrel extraction using a device fabricated from a weight and a cable

Test results - summarised in Table 11.1 - showed that the recovery in gravels was poor, averaging 53%. This highlights the practical difficulty in achieving high quality gravel samples. Plots of the development of force acting on the core barrel with increasing penetration indicated an increasing trend between the two variables. Of the tests conducted, the average maximum compressive force was ~65kN, which occurred within the final ~0.25m of penetration. In accordance with theory, a decrease in recovery with increasing void ratio was observed. During the descent of the core barrel, its harmonic displacement amplitude increased from ~0.34mm to ~0.50mm, indicating a marked increase in the soil stiffness with penetration depth. At maximum barrel penetration, gravel stiffness influencing the dynamic response of the vibratory motor was as high as ~215MN/m.

Table 11-1: Summary of select physical test results

M able	Test 1	Test 2	Test 3	Test 4	Test 5	Test 6	Test 7
Initial void ratio, e	0.496	0.480	0.507	0.536	0.473	0.519	0.551
Specific gravity, G_s	2.432	2.469	2.452	2.477	2.498	2.462	2.530
Recovery Ratio, RR (%)	52.0	53.2	50.7	46.6	59.0	64.9	46.1
Maximum F_B (kN)	*na*	71.2	65.3	67.2	68.2	66.4	*na*

PART IV

Discrete element model calibration and results

Part IV contents

Chapter 12 – Assembly of discrete element model

The input parameters of the Rocky DEM model are specified, including all geometries, materials, and particle properties; Reasons for multiple model computations are provided;

Chapter 13 – Numerical results and calibration

The variance in results between numerical models is assessed, followed by the comparison of these results to findings of the physical testing

Chapter 14 – Summary and conclusions: Part IV

The outcomes of Part IV are summarised and concluded

12. Assembly of discrete element model

12.1. Preamble to application of Rocky

The Rocky DEM software package was developed primarily for the analysis of devices used to transport or process granular material in the mining industry. Such devices include transfer chutes, vibrating screens, grinding mills and crushers (Engineering Simulation and Scientific Software [ESSS], 2015). To date, no studies have been found that use the DEM to investigate vibrocoring. The application of Rocky to a vibrocore-soil system highlights the power of the DEM. Although the software was not designed or developed for such a study, the method is capable of simulating the motion of every solid particle within any given system.

The 3D numerical DEM model of the physical SVC system shall henceforth be referred to as the *model*. The parameters needed to define the model were considerably different to that which would be required in a FEM analysis of the SVC. In describing the various properties of the model, they were split into three sections, illustrated in Fig. 12.1:

i) Definition of geometries: The chosen shape and size of the modelled core barrel, sample bin, and particles are defined and justified.

ii) Selection of material properties: The density, stiffness and friction properties of the materials in the model are specified

iii) Dynamic considerations: The input of the particles into the model, as well the various movements of the core barrel, is detailed.

All DEM parameters other than those specified in this chapter were according to the default settings in Rocky software (see ESSS *et al.*, 2015).

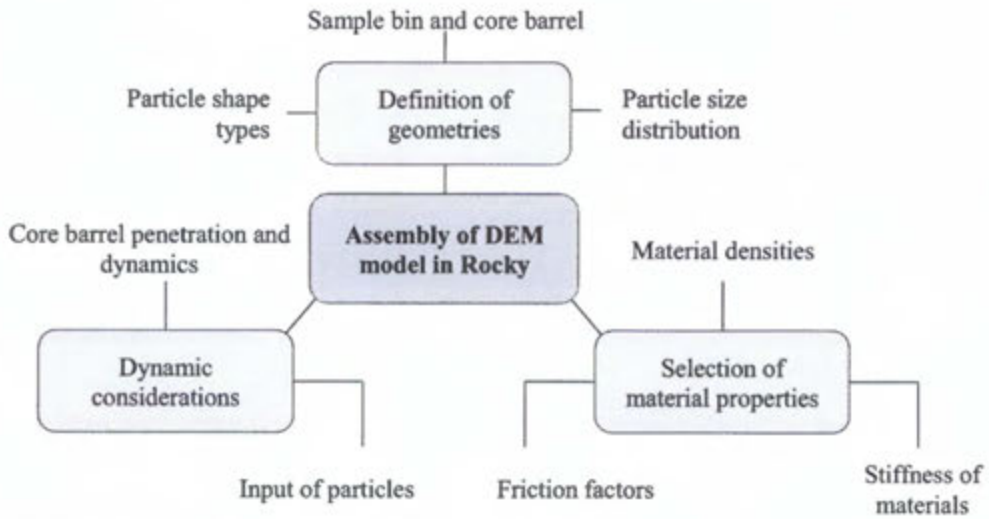

Figure 12-1: Components of the DEM model assembly

12.2. Definition of geometries

12.2.1. Sample bin and core barrel

The sample bin and core barrel were modelled as two separate solid 3D objects. Their dimensions in Rocky were the same as their real-scale geometry specified in Part III. The base of the core barrel included the detailed geometry of the cutting head. Both the bin and barrel were drawn in AutoCAD drafting software and then imported into Rocky. The position and orientation of the imported geometries were able to be adjusted in Rocky. A 3D Cartesian coordinate system is adopted in the software, where Y is the vertical axis, and X and Z are the horizontal axes. The initial position of the barrel was such that a) The base of the cutting head was a height of 3.034m above the base of the bin, and b) If the geometries were viewed in plan, the barrel was in the centre of the bin (Fig. 12.2a). Both objects were positioned with their longitudinal axis vertical. Rocky calculations assumed these geometries to be fixed in their initial position unless movements were specified. No support conditions needed to be specified.

The sample bin was considered to represent the boundary of the model in the horizontal plane. The core barrel was a separate object, the vertical movement of which, relative to the sample bin, could be controlled. The height of the sample bin and core was arbitrary – provided their heights were above that which was required to simulate the penetration depths of the SVC. To accommodate potential use of the model to investigate greater penetration depths in the future, the heights of the imported geometries were 5m - significantly higher than their true value (Fig. 12.2b). To illustrate the detailed core barrel and sample bin geometry simultaneously, the barrel was temporarily lowered to near the bottom of the bin (Fig.12.2c).

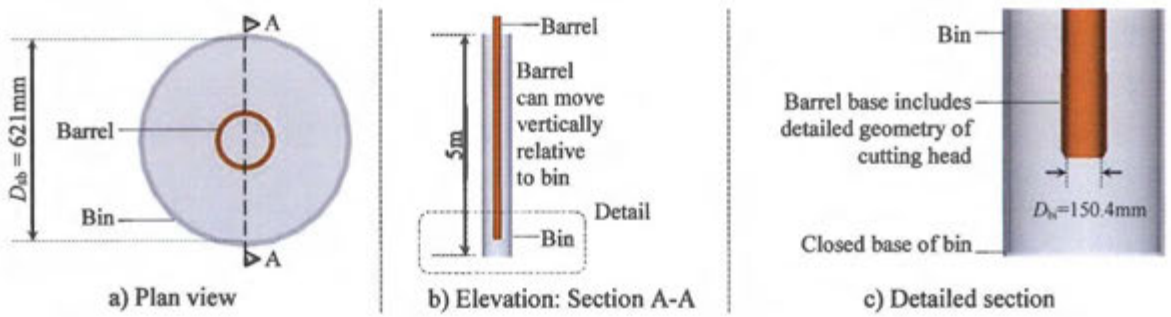

Figure 12-2: Geometry of sample bin and core barrel

12.2.2. Particle shapes

Rocky was able to model a great variety of particle shapes, ranging from relatively simple spheres to more complex rounded polyhedrons. The various parameters that defined the modelled particle shapes are described in Table 12.1.

Table 12-1: Parameters defining particle shapes in Rocky

After ESSS *et al.* (2015)

Parameter	Description	Range of options/values
Particle shape	The general shape category for the particle. Each type has different parameters that can be modified.	Spherical, faceted, rounded cylinder, rounded polygon, rounded polygon
Rolling resistance	Influences how particles roll on a surface. A higher value reduces rolling.	0-1
Vertical aspect ratio (VAR)	Changes the height (Y value) of a particle assuming a Z value of 1	0.70-2.70
Horizontal aspect ratio (HAR)	Changes the width (X value) of a particle assuming a Z value of 1	0.70-2.70
Smoothness	Controls how smooth or sharp the particle edges are. The higher the value, the smoother the edges.	0.10-1.00
Number of corners	Changes how many points the surface of a particle has.	4-104
Superquadric degree (SQD)	Influences how square or elliptical a particle appears. The higher the value, the more square the shape.	2.0-12.0

Preliminary DEM work was conducted to assess the influence of modelled particle shape types on computation time. A series of relatively brief simulations (40-310s run-time) were generated, in which the falling and settling of a relatively small number of particles (170-700) in the sample bin was modelled. Results, detailed in Appendix 6, indicated that the shape types simulated had a drastic effect on computation time. The shape types resulting in the quickest run-times were - in ascending order - spheres, rounded cylinders, rounded polygons, rounded polyhedrons, and faceted. Decreasing the number of corners of a particle reduced run-time. Computational requirements were not significantly influenced by rolling resistance, VAR, HAR, smoothness, or SQD. In choosing the combination of particle shape types to model the D16-64 mix, consideration was given to the computational expense of the selected shapes, as well as the PSMs of both the D16-32 and D32-64 gravel. An accurate representation of the true particle shapes was desired. However, the inclusion of overly-complex shape types would result in impractically long computation times. Since the D16-64 gravel was 50% D16-32 and 50% D32-64, its PSM was estimated by averaging the PSMs of the two constituent gravels (Table 12.2).

Table 12-2: Estimated particle shape matrix of observed D16-64 gravel

	L	M	H	
AR	2.75	5.50	1.75	10.0
SA	3.44	6.88	2.19	12.5
SR	7.56	15.13	4.81	27.5
RD	13.75	27.50	8.75	50.0
	27.5	55.0	17.5	100

Table 12.2 shows that the majority of particles in the D16-64 gravel are rounded of medium sphericity (RDM). Rounded and sub-rounded particles significantly outnumber angular and sub-angular particles. There are more particles of low sphericity than of high sphericity. In reality, a great variety of particle geometries would exist within the gravel mix tested – far more than can be practically simulated. In modelling the gravel, it was assumed that:

- All particles would be sorted into one of the 12 broad shape types defined by the PSM,
- The percentage of each of the 12 shape types within the bulk gravel was given by the corresponding PSM entry, and
- Each of the 12 PSM shape types has a corresponding particle geometry modelled in Rocky, with a fixed set of parameters

The particle shapes shape types included in the model, as well as their corresponding relative quantity within the bulk gravel, are given in Table 12.3. The chosen value for rolling resistance of 0.25 was based on Donohue (2015), a report which recommends DEM parameters for a gravel mix of similar PSD and PSM to those tested in this study. The modelled shape type, VAR, HAR, smoothness, number of corners, and SQD were all selected based on visual judgement. Chosen parameters were intended to yield particle shapes similar to the shapes observed in the D16-64 gravel. The number of corners was chosen to be as few as possible.

Table 12-3: Particle shape types included in the model

PSM shape category	Modelled shape type	Percentage of soil mass	Rolling resistance	VAR	HAR	Smoothness	No. of corners	SQD
ARH	Rounded polyhedron	1.75	0.25	1.00	1.00	0.25	5	2.0
ARL	Rounded polyhedron	2.75	0.25	1.70	0.70	0.25	5	2.0
ARM	Rounded polyhedron	5.50	0.25	1.35	0.85	0.25	5	2.0
SAH	Rounded polyhedron	2.19	0.25	1.00	1.00	0.50	5	2.0
SAL	Rounded polyhedron	3.44	0.25	1.70	0.70	0.50	5	2.0
SAM	Rounded polyhedron	6.88	0.25	1.35	0.85	0.50	5	2.0
SRH	Rounded polygon	4.81	0.25	1.15	0.85	*na*	3	*na*
SRL	Rounded polygon	7.56	0.25	1.55	0.50	*na*	3	*na*
SRM	Rounded polygon	15.13	0.25	1.35	0.60	*na*	3	*na*
RDH	Rounded polygon	8.75	0.25	*na*	*na*	*na*	*na*	*na*
RDL	Rounded polygon	13.75	0.25	1.45	0.45	*na*	10	*na*
RDM	Sphere	27.50	0.25	1.35	0.60	*na*	10	*na*

Figure 12.3 shows images, sourced from the Rocky display, of each of the 12 particle shapes modelled. The geometries are presented in the form of a PSM. Computational requirements tend to decrease from the top left of the PSM (ARL) to its bottom right (RDH)

	Low sphericity (L)	Medium sphericity (M)	High sphericity (H)
Angular (AR)	Rounded polyhedron 	Rounded polyhedron 	Rounded polyhedron 
Sub-angular (SA)	Rounded polyhedron 	Rounded polyhedron 	Rounded polyhedron 
Sub-rounded (SR)	Rounded polygon 	Rounded polygon 	Rounded polygon 
Rounded (RD)	Rounded polygon 	Rounded polygon 	Sphere 

Figure 12-3: Modelled particle shapes

12.2.3. Particle size distribution

Rocky allowed the detailed specification of the PSD of each particle shape. If the accuracy of the modelling process was prioritised, each shape type would be assigned the PSD of the bulk gravel as specified in Part III. However, it was found that such a model would yield unreasonably long calculation times – in excess of three weeks. The application of force-displacement laws between the many thousands of smaller non-spherical particles resulted in radical computational expense of the simulation. Therefore, a number of simplifying assumptions were made for the final model:

- The percentage of particles in the bulk mix passing a 19mm sieve diameter was decreased from 19% to 15%
- The percentage of particles in the bulk mix passing a 26.5mm sieve diameter was decreased from 47% to 45%
- No particles $\leq$ 37.5mm sieve diameter were modelled as an angular shape type,
- No particles $\leq$ 26.5mm sieve diameter were modelled as an sub-angular shape type, or rounded of low or medium sphericity,
- No particles $\leq$ 19.0mm sieve diameter were modelled as an sub-rounded shape type
- All particles $\leq$ 19.0mm were modelled as spheres

Thus, in modelling this simplified gravel mass, a revised PSM was developed. Since particle shape types of the smaller, more-complex particles were changed to simpler geometries, the percentage of simpler geometries increased and more complex geometries decreased. The modelled PSM and corresponding PSDs for each particle shape are given in Tables 12.4 and 12.5, respectively:

Table 12-4: Particle shape matrices of D16-64 gravel

a) Estimated from observation

	L	M	H	
AR	2.75	5.50	1.75	10.00
SA	3.44	6.88	2.19	12.50
SR	7.56	15.13	4.81	27.50
RD	13.75	27.50	8.75	50.00
	27.50	55.00	17.50	100

b) Modelled

	L	M	H	
AR	1.18	2.48	0.85	4.50
SA	1.71	3.51	1.17	6.39
SR	6.27	13.30	4.61	24.18
RD	7.69	16.12	41.12	64.93
	16.84	35.41	47.75	100

Table 12-5: Particle size distributions for each of the 12 shape types

Sieve size (mm)	Percentage passing for various particle shape types											
	ARH	ARL	ARM	SAH	SAL	SAM	SRH	SRL	SRM	RDH	RDL	RDM
64.0	100.0	100.0	100.0	100.0	100.0	100.0	100.0	100.0	100.0	100.0	100.0	100.0
53.0	17.6	25.5	22.2	40.1	48.7	45.2	62.0	65.1	63.8	90.6	37.4	34.3
37.5	0	0	0	20.8	22.4	21.7	52.3	50.8	51.4	89.0	19.9	19.0
26.5	0	0	0	0	0	0	40.7	37.4	38.8	86.6	0	0
19.0	0	0	0	0	0	0	0	0	0	36.5	0	0

In viewing Tables 12.4 and 12.5, note that the revised PSM and PSDs were calculated in such a way as to ensure the PSD of the bulk gravel was preserved. In other words, for a given particle size, if the percentages of particles passing this size for each shape type are multiplied by the corresponding PSM entry, and then summed, the result is the percentage of particles within the bulk mix smaller than the given particle size. For example, 45% of the gravel should be less than 26.5mm in diameter. This is shown using values from the above tables for SRH, SRL, SRM and RH shape types:

PSM entry

Percentage passing

$$\frac{40.7}{100}(4.61) + \frac{37.4}{100}(6.27) + \frac{38.8}{100}(13.30) + \frac{86.6}{100}(41.12) = 45\%$$

SRH SRL SRM RDH

12.3. Selection of material properties

12.3.1. Material densities

The material density for the sample bin and core barrel was selected to be 7800kg/m^3 as the approximate density of steel. When specifying the density of particles in Rocky, the density of the individual particles may be defined, or a bulk density may be specified. The first approach was adopted in this study. In selecting an appropriate particle density ρ_s, consideration had to be given to the fact that the granular medium modelled in Rocky was dry. The software did not allow the simulation of water in the analysis. Given that the average specific gravity of the gravels physically tested was 2.474, the density of the particles was approximately 2474kg/m^3. To account for the effect of buoyancy, the density of water was subtracted from this value. Therefore, the density of all modelled particles ρ_{sm} was selected to be $\rho_{sm} = G_s(1000)-\rho_w = 2.474(1000)–1000 = 1474$kg/m^3.

12.3.2. Stiffness of materials

Rocky requires the specification of the stiffness, or Young's Modulus E, for all modelled materials. The sample bin and core barrel were assumed to both have a stiffness of 200GPa. This is the typical stiffness of commercial steel. Palmstrom and Singh (2001) provide a summary of typical values of E for various rock types. A stiffness of 28GPa is recommended for sandstone. This value was selected for the modelled gravel particles.

12.3.3. Friction factors

The friction between two materials modelled in Rocky is defined by two positive-value factors (ESSS *et al.*, 2015): A static friction factor μ_s, and a dynamic friction factor μ_d. The static and dynamic factors are the maximum ratio of contact tangential force to normal force before and after the onset of sliding, respectively. In most cases, $\mu_s > \mu_d$.

ESSS *et al.* (2015) and Donohue (2015) provide recommendations for friction values between various materials modelled using the DEM. These factors were not used in the final model, but rather served as the basis for parameter selection. Due solely to their shape, particles of higher angularity are, in a bulk granular medium, less prone to inter-particle sliding than spheres. Therefore, to account for the smooth, round surfaces of the simulated spheres within the simplified gravel mass, the selected friction factors for the final model were estimated to be a value marginally greater than the preliminary values (Table 12.6).

It was assumed the gravel was a purely frictional material with zero adhesion or cohesion. During physical testing, it was observed that the inside surface of the sample bin had a significantly rougher surface than that of the core barrel (Fig. 12.4). For this reason the friction factors between the gravel and sample bin were selected to be higher than that of the gravel and core barrel.

Table 12-6: Selected friction factors for the model

Material interaction	Preliminary values		Final values		Reference on which friction value selection was based
	Static Friction	Dynamic friction	Static Friction	Dynamic friction	
Gravel-gravel	0.650	0.650	0.725	0.725	ESSS *et al.* (2015)
Gravel-Core barrel	0.700	0.650	0.725	0.675	Donohue (2015)
Gravel-Sample bin	0.750	0.700	0.750	0.700	Donohue (2015)

Figure 12-4: Relatively rough inside surface of sample bin
Pen for scale

12.4. Dynamic considerations

12.4.1. Overview of geometry movements in Rocky

The total time simulated in the model was 98s. Let any instant during this simulation be denoted by time t_s. The simulation started with the entry of particles into the sample bin (t_s=0s) and ended with the stationary core barrel at final penetration depth (t_s=98s). In defining the dynamic model, movements of the core barrel and sample bin could be specified to start or stop at any point during the simulation time. Such movements included translation and vibration.

12.4.2. Input of particles into sample bin

Particles entering a Rocky simulation do so by 'falling' under the influence of gravity in the negative Y direction through an inlet of specified position and shape. The inlet for the model was selected to be circular and horizontal, with a radius of 0.3m, and at a height of 2.984m above the base of the sample bin. The rate at which the particles flowed into the bin was 270kg/s. This flow rate was calculated based on the desired void ratio of the modelled gravel e, the desired height of the gravel within the sample bin H_{sb} = 2.374m, the selected density of the gravel particles ρ_s, and the specified time in which all particles entered the simulation. Small differences in the void ratio of the modelled soil mass and the tested gravels were unavoidable, due to the following reasons:

i) The shapes and sizes of the modelled soil mass are not the same as the physical samples.

ii) In reality, there was a small fraction of particles smaller than 16mm diameter; These particles were not included in the DEM model to avoid excessive computation times

iii) The modelled gravel consists of a significantly higher number of spherical particles than the real gravel. A sample of spheres is less prone to large decreases in volume as a result of compaction due to the uniformity of the individual particle geometries. For a sample consisting of more angular particles, there is greater scope for densification due to particle rearrangement. Thus, the compaction-induced difference between maximum and minimum void ratio would be greater.

iv) A spherical particle that passes through a given sieve diameter occupies a greater volume than an angular particle passing through the same diameter. A possible exception is if the angular particle considered is approximately cubic. However, the SQD for all modelled angular and sub-angular particles was 2.0, indicating they were more elliptical than square.

v) The density of the real particles was roughly 1.7 times greater than those modelled. As a result, the physical particles falling into the sample bin supplied a greater compactive energy to the underlying particles than that of the modelled particles.

Therefore, the void ratio of the modelled gravel was expected to be higher than that of the physical samples tested. To increase the bulk density of the simulated soil, the following actions were included in the model:

i) The time in which all particles entered the simulation was chosen to be 2.5s. This is much shorter than the time it took to empty the gravel into the sample bin in practice – a matter of minutes. A shorter in-flow time corresponds to a higher the gravel input flow rate, which results in an increase in compactive energy supplied by the entering particles.

ii) The sample bin was vibrated as the particles 'flowed' into the model. In addition to the 2.5s during particle entry, the barrel vibrated for 3.5s in horizontal direction at 100Hz with an amplitude of 7.5mm.

iii) After 6s of simulation time, horizontal vibration of the bin was stopped and the bin vibrated in the vertical direction for 6s at a frequency of 100Hz with an amplitude of 3mm. Vibration permitted the rearrangement and densification of particles.

Once the simulated vibrations had ceased and the gravel had settled, the modelled soil had a void ratio of ~0.585. In total, the soil was subject to 12s of vibration. It was found that the vibration-induced decrease in volume of the soil stopped after approximately 11s of vibration. Thus, the void ratio of the modelled soil was considered close to its minimum value e_{min}. The process of soil entry and subsequent vibrocompaction is illustrated in Figure 12.5a. The model consisted of 47,536 particles.

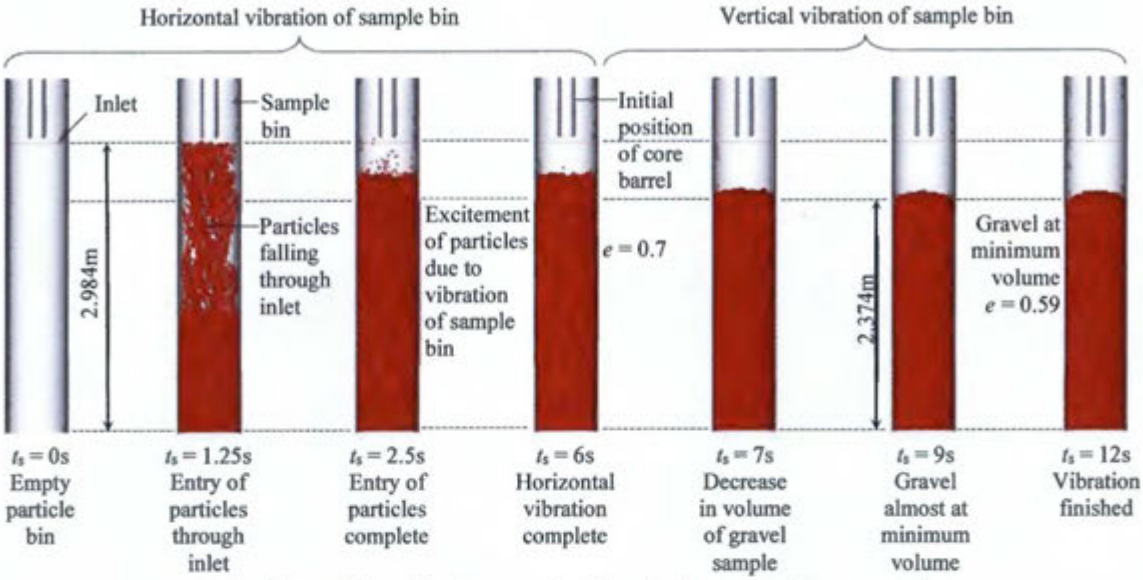

a) Entry of particles into sample bin and subsequent vibrocompaction

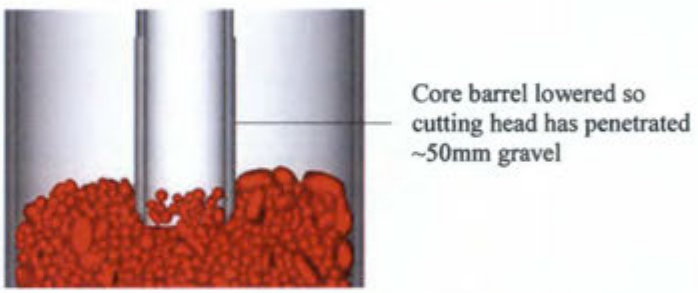

b) t_s = 13s : Detailed cross-section of sample bin, cutting head, and gravel mass

Figure 12-5: Simulated input of gravel particles into sample bin

12.4.3. Core barrel penetration and dynamics

After the simulated compaction of the gravel was complete, the core barrel was lowered so that its base was a height 2.358m above the base of the sample bin. This downward vertical movement was specified to occur between t_s =12s and t_s = 13s. At t_s = 13s, the base of the cutting head was in contact with the top ~50mm of the gravel (Fig 12.5b). At t_s = 14s, the modelled core barrel was set to start vibrating at a frequency of 157Hz at an amplitude of 0.352mm. These oscillatory properties were selected based on the dynamic movement of the barrel during physical testing. Rocky did not allow the simultaneous vibration and translation of a modelled object. Therefore, the core barrel could not be lowered while vibrating. Instead, the global position of the vibrating core barrel remained fixed and the sample bin was set into motion at a constant upward velocity of 24mm/s at t_s = 15s. This represented the 24mm/s penetration rate of the core barrel during SVC testing. The frequency of the modelled core barrel was 157Hz throughout its penetration into the gravel.

Over any given period of time, only a constant barrel amplitude could be specified in the model. To simulate the increase in amplitude with penetration depth observed during physical testing, the constant and continuous descent of the modelled barrel consisted of five successive stages. Each stage had a different barrel amplitude, the value of which was the average of the measured amplitudes over the period of the stage considered. The intervals of t_s which defined the stages, as well as the corresponding amplitudes for each stage, are given in Table 12.7 and illustrated in Figure 12.6.

The upward translation of the sample bin was set to stop at $t_s = 97.3$s. This corresponded to a barrel penetration depth of 1.975m. Oscillatory motion of the core barrel was specified to cease at $t_s = 97.5$s. The simulation ended at $t_s = 98$s.

Table 12-7: Modelled core barrel amplitudes

Time interval, Δt_s (s)	Penetration depth interval, Δd (m)	Harmonic amplitude, X (mm)
15 - 34	0.000 – 0.456	0.352
34 - 59	0.456 – 1.056	0.378
59 - 79	1.056 – 1.536	0.419
79 - 89	1.536 – 1.776	0.424
89 – 97.5	1.776 – 1.975	0.475

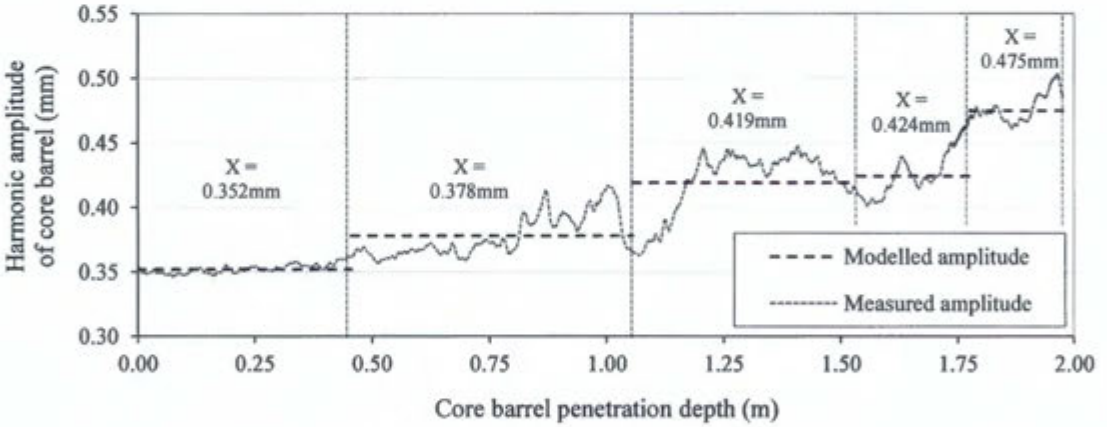

Figure 12-6: Modelled core barrel amplitudes

12.4.4. Summary of simulation process

Figure 12.7 provides a scaled representation of the modelled gravel input and vibrocoring process. The various instances of significance within the simulation are illustrated on a horizontal time plot.

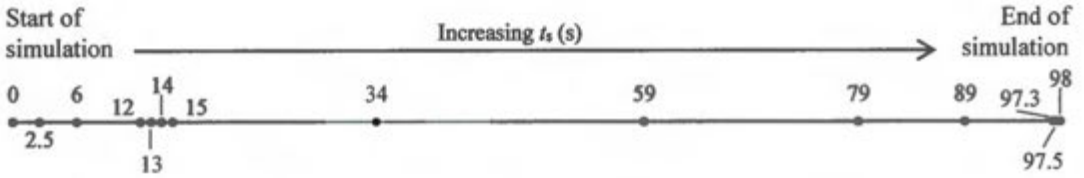

0s	Start of simulation; Particles entering bin at 270kg/s; Horizontal vibration of bin (100Hz frequency;7.5mm amplitude)	34s	Core barrel amplitude increased to 0.378mm
		59s	Core barrel amplitude increased to 0.419mm
2.5s	Particle entry finished	79s	Core barrel amplitude increased to 0.424mm
6s	Horizontal vibration of bin stops; Vertical vibration of bin starts (100Hz; 3mm)	89s	Core barrel amplitude increased to 0.475mm
12s	Bin vibration stops; Core barrel lowered to top of gravel	97.3s	Upwards movement of sample bin stopped
13s	Core barrel base on top of gravel; Particles allowed to settle	97.5s	Vibration of core barrel stops
14s	Barrel starts vibrating (157Hz; 0.352mm)	98s	End of simulation
15s	Upward movement of sample bin at 24mm/s starts		

Figure 12-7: Summary of simulation process

12.5. The need for multiple model computations

The numerical results produced by Rocky Software were probabilistic: Two models with identical input parameters yielded non-identical results. This variance was due to the randomness of particle orientation and arrangement within the modelled soil mass.

Based on preliminary DEM modelling of the vibrocore system, fully detailed in Appendix 7, it was expected that multiple runs of the model would produce insignificantly different results. However, the input parameters defining these preliminary simulations were different to that specified in this chapter. It was not certain whether the variance between successive runs of the model would be negligible. Therefore, it was decided that a) The model described in this chapter be computed three times, and b) Before calibration to physical results, the variance in results between these three models be assessed.

To determine conclusively whether this variance was insignificant, plots of the change in vertical force on the core barrel F_B with penetration depth d were compared. The two sample Kolmogorov-Smirnov (KS) method was the statistical tool used for this comparative analysis. The method is described in the following chapter.

13. Numerical results: Variance and calibration

13.1. Variance in model results

This section begins with a description of the KS method. The F_B-d plots and recovery ratios of the model results are then presented and their variance assessed.

13.1.1. The Kolmogorov-Smirnov method

The two sample KS test is a nonparametric statistical method used to determine whether two samples come from the same distribution – i.e. whether there is a significant difference in the distributions of the two samples (Zaiontz, 2014). The test does not assume the two data sets are sampled from any defined distribution. The two sample test follows a very similar procedure to the one sample KS test, described in detail by Massey (1951).

Consider two observed samples. The first sample has m data points and a cumulative distribution function of $F(x)$. The second sample has n data points with a cumulative distribution function of $G(x)$. The test statistic $D_{m,n}$ is defined as

$$D_{m,n} = \max\left|F(x) - G(x)\right| \qquad (13.1)$$

The null hypothesis is that both samples come from a population with the same distribution. The null hypothesis is rejected, at a significance level α, if $D_{m,n} > D_{m,n,\alpha}$, where $D_{m,n,\alpha}$ is the critical value. For m and n sufficiently large (greater than 50), $D_{m,n,\alpha}$ is defined by

$$D_{m,n,\alpha} = c(\alpha)\sqrt{\frac{m+n}{mn}} \qquad (13.2)$$

Where $c(\alpha)$ is the inverse of the Kolmorogov distribution at α, defined by Zaiontz (2014). For m and n sufficiently large, the values of $c(\alpha)$ for various levels of significance are defined in Table 13.1. Let the Kolmogorov-Smirnov ratio, or KSR, be defined as KSR = $D_{m,n}/D_{m,n,\alpha}$. Therefore, given two F_B-d plots of vibrocore model results, if the KSR for these distributions is less than unity, the difference in results between the two corresponding models may be considered negligible.

Table 13-1: $c(\alpha)$ values for various levels of significance
After Massey (1951) and Zaiontz (2014)

Significance level, α	0.15	0.10	0.05	0.01
$c(\alpha)$	1.14	1.22	1.36	1.63

The KS test was chosen for use as it was deemed an effective means to compare the shape of two bivariate data distributions. Such a comparison cannot be done using the two sample *t*-test.

13.1.2. Force-penetration and core recovery results

The force-penetration plots of each of the three models computed are shown in Figure 13.1. At this stage, assessment of the results is limited to the variance between the F_B-d distributions. Differences between the plots are apparent. This was expected. As shown in previous studies (Parker and Sills, 1990; De Nicola & Randolph, 1997), and as observed in the physical test results, no two F_B-d plots were identical. While all numerical F_B distributions showed a similar increasing trend with penetration, it is clear the peaks and troughs of the various plots very rarely coincide. The rapid local variations of the F_B-d graph correspond to the micro-scale response and rearrangement of the sampled particles as they enter the core barrel. Since the particle arrangement is random in Rocky, it followed that the resultant F_B-d plots were not indistinguishable.

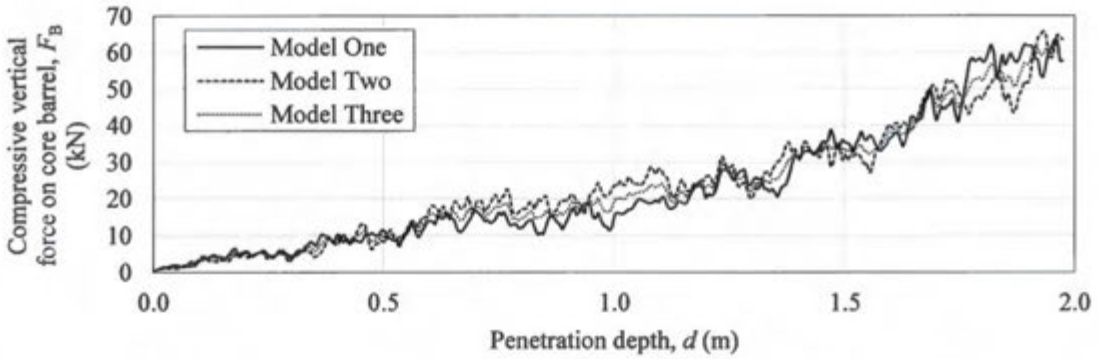

Figure 13-1: Force-penetration plots generated from numerical modelling results

It was of greater importance to determine whether the difference between force plots was significant. The graphs were compared by determining a KSR value for each of the three possible pairs of modelling results: models one and two, models one and three, and models two and three. The cumulative distribution function (CDF) of each F_B-d plot within each pair is given in Figure 13.2a, b, and c, with the cumulative distribution indicated on the left vertical axis. Also shown in these figures are two lines plotted according to the right vertical axis: Firstly, the absolute difference between the CDFs; and secondly, the critical value $D_{m,n,\alpha}$, shown as a constant horizontal line and representing the value of $D_{m,n}$ at which KSR is unity. The KSR for all three model comparisons was less than 1.0. Therefore, results show that no two F_B-d plots are significantly different.

Figure 13.2d shows the averaged F_B value of the three models at each penetration depth. A KS test between the results of each model and the average results showed that model three yielded a F_B-d plot most similar to the mean distribution, with a KSR of 0.12.

a) Comparison of **Models One and Two**

KSR = 0.48

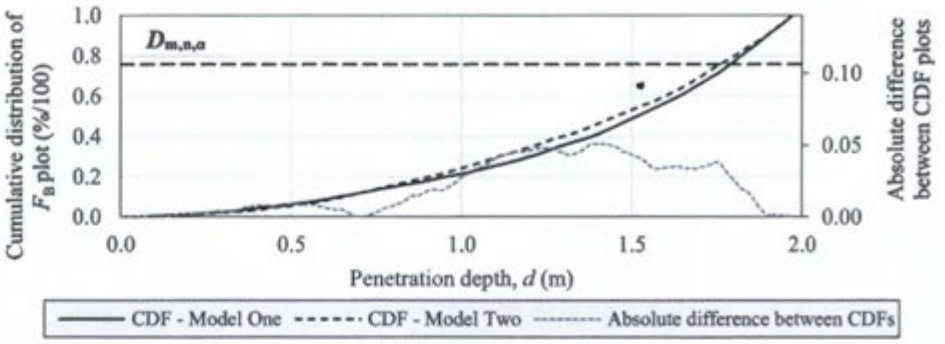

b) Comparison of **Models One and Three**

KSR = 0.40

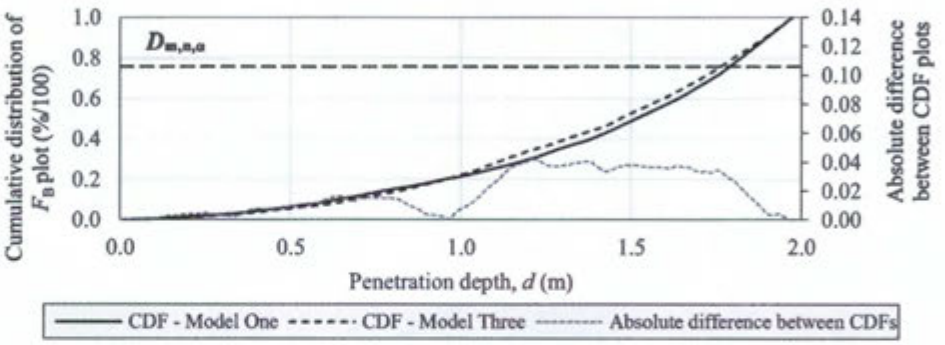

c) Comparison of **Models Two and Three**

KSR = 0.23

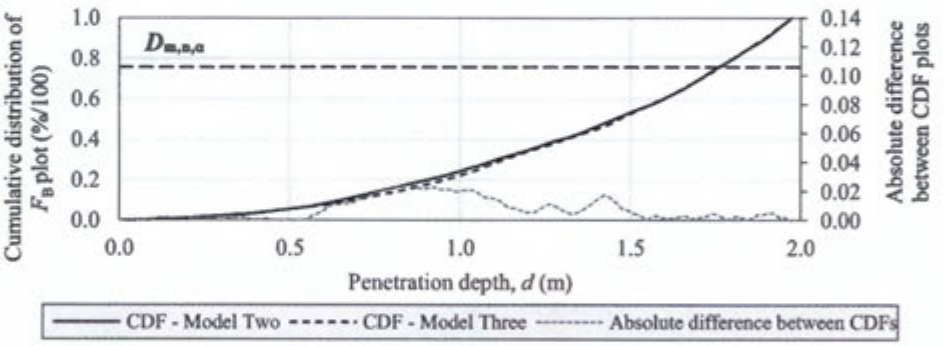

d) Plot showing average F_B-d distribution

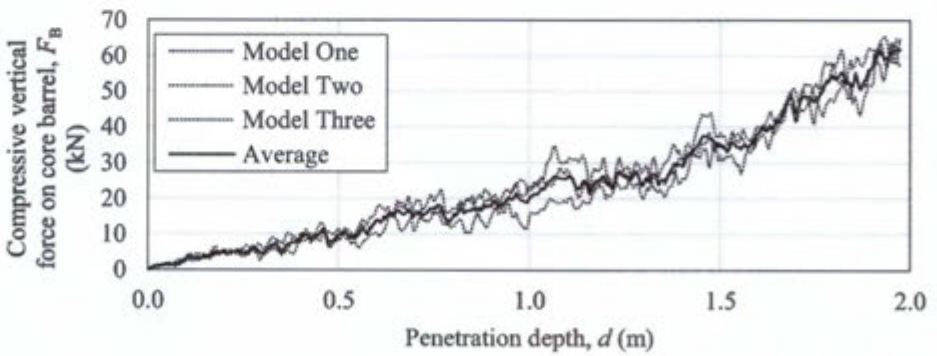

Figure 13-2: a), b) and c) Results of KS test used to compare F_B-d plots of numerical models; d) The average F_B-d plot

The final recovery ratios of the core samples achieved in each model are given in Table 13.2 and illustrated in Figure 13.3. The data set has a coefficient of variability of 1.34%. This low C value indicates negligible variance between the RR results.

Table 13-2: Recovery ratios yielded by model results

Model	Recovery ratio of core sample (%)
One	54.2
Two	53.1
Three	54.9
Average	54.1

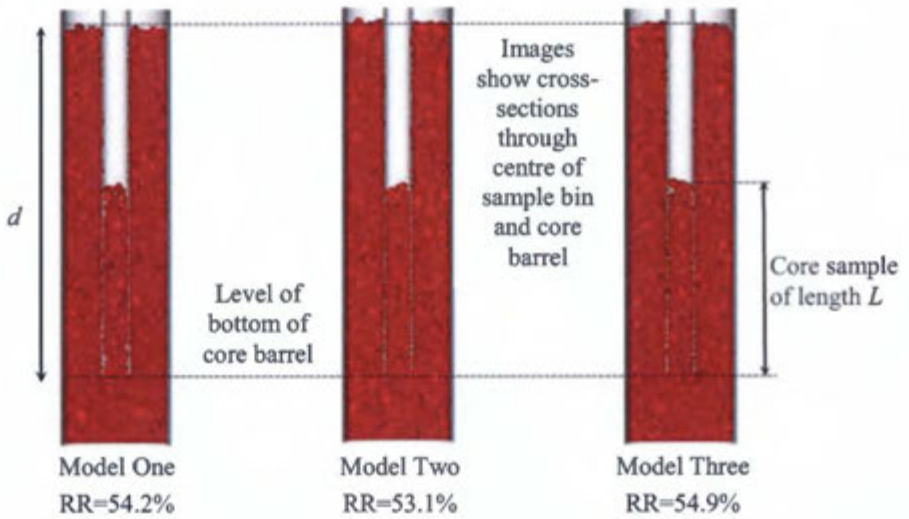

Figure 13-3: Recovery ratios at final penetration depths for each numerical model

13.2. Comparison of physical and numerical results

13.2.1. Assessment of force-penetration plots

Figure 13.4a shows four F_B-d distributions. The dark, bold line represents the average force-penetration yield by the three numerical models – the same as that given in Figure 13.2d. The remaining three are results of physical tests three, four, and five. Neglected in this comparative analysis were the irregular results of a) Test two, due to the need to decrease the core barrel penetration rate during sampling (Section 10.2.1), and b) Test six, due to the achieved anomalous recovery ratio (Section 10.3). The graph shows marked differences between the physical and numerical results for the first ~0.6m (~25s) and last ~0.05m (2s) of penetration. This was expected. As highlighted in the discussion of the physical results, plots of measured F_B for depths

less than d_{crit} (~0.6m) may be considered non-representative of the true F_B distribution. The sharp decrease in physical plots during the last ~0.05m of penetration was due to the decrease in core barrel penetration rate immediately prior to the end of sampling. Figure 13.4b illustrates the same plots as those shown in Figure 13.4a, but with the first ~0.6m and last ~0.05m of penetration depth neglected. Notwithstanding the unavoidable local variability of the F_B plots, similarity between the trends of this resultant set of 'trimmed' distributions can be noted. Therefore, the graphs suggest that the numerical models simulated the penetration of the core barrel into the gravel with reasonable accuracy. In quantifying the difference between physical and numerical F_B-d plots, focus was given to the results of physical test four. This test was selected because the gravel sampled in this test had an initial average void ratio e_0 of 0.536, which, of the tests considered, was the most similar to the e_0 of the simulations: $e_0 = 0.585$. Figure 13.5 shows the F_B-d plots of the numerical average and of physical test four. Clear similarity between the plots is apparent. Indeed, with the first ~0.6m and last ~0.05m of penetration depth neglected, the two plots have a KSR of 0.10. Thus, the F_B-d results of the numerical models were considered accurate representations of the true force acting on the core barrel during penetration into the gravel during SVC testing. DEM results indicate that F_B of the vibrocore system increases approximately linearly with depth from zero to a maximum value of ~62kN.

a) Complete F_B-d plots

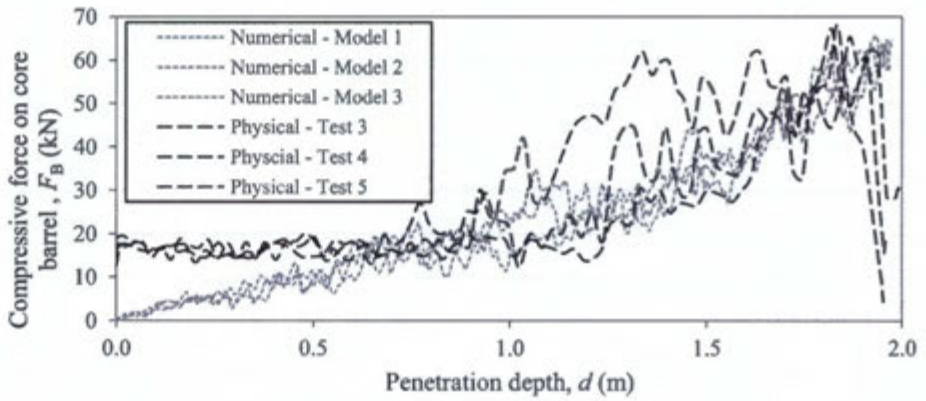

b) F_B-d plots with first ~0.6m and last ~0.05m of penetration depth neglected

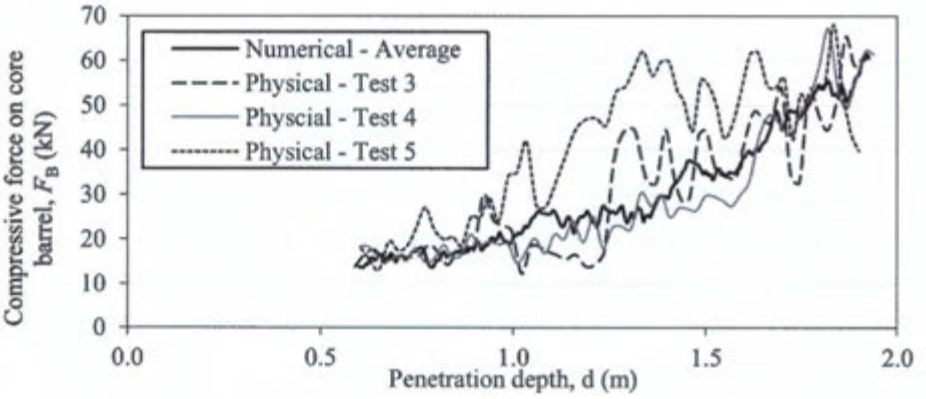

Figure 13-4: F_B-d plots yielded by numerical and physical results

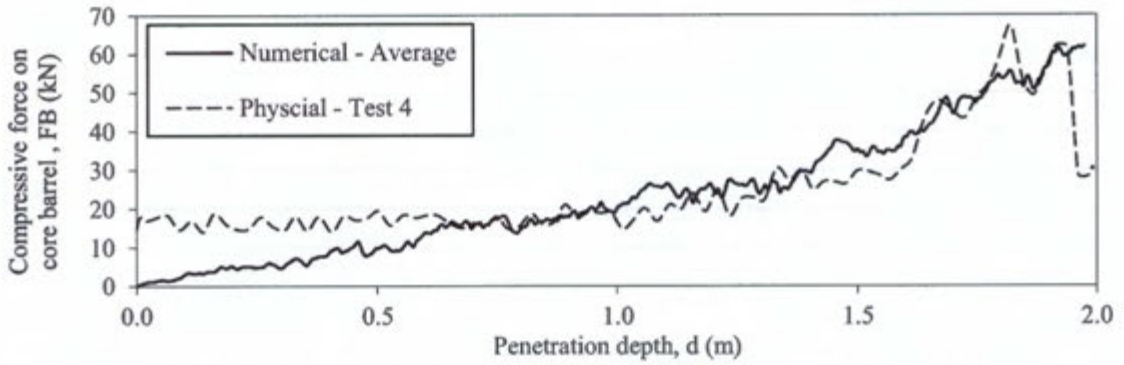

Figure 13-5: F_B-d plots of physical test four and average numerical model results

13.2.2. Comparison of recovery ratios

Table 13.3 provides the recovery ratios of the cores at final penetration depth for physical tests three, four, and five, as well as those of numerical models one, two and three. To determine whether the two univariate data sets are significantly different from each other, a two sample t-test was conducted. Both data sets have sample size $n = 3$. The t-test statistic was calculated to be 0.622. The critical one-tailed and two-tailed t-values, at 95% confidence, are 2.920 and 4.303. Both these critical value are higher than the test statistic. Therefore, there is no statistical difference between the recovery ratios yielded by the physical and numerical results. The procedure of the two sample t-test is described fully in Appendix 5.

Table 13-3: Recovery ratios obtained from physical and numerical results

Physical results		**Numerical results**	
Test number	Recovery ratio (%)	Model number	Recovery ratio (%)
Three	50.7	One	54.2
Four	46.6	Two	53.1
Five	59.0	Three	54.9
Average	52.1	Average	54.1

Thus, through critical assessment of recovery ratios and F_B-d plots, it was shown that there was negligible difference between the results of physical testing and numerical modelling. Since the accuracy of the simulations were validated, the DEM model could be considered calibrated, and a more detailed evaluation of the numerical results was conducted. This evaluation is discussed in Part V.

14. Summary and conclusions: Part IV

The following is a summary of the numerical modelling procedure:

- The assembly of the DEM model required the specification of geometric, friction, density, and stiffness properties for all materials.
- The sample bin and core barrel were modelled to have the same geometry as those used during physical testing. Movements of these geometries, including translation or vibration, could be specified to start or stop at any point during the simulation.
- Several assumptions were made to reduce the computational expense of simulating the gravel micro-scale behaviour. The particle shape matrix (PSM) of the modelled soil had a far greater percentage of spherical particles than the real soil. However, the PSM and particle size distribution (PSD) for each shape type were calculated such that the PSD of the bulk gravel was maintained.
- To allow for assessment of variation between probabilistic numerical results, the DEM model was computed three times. Each simulation had identical input parameters.
- The initial average void ratio of the modelled gravel was ~0.585. This void ratio was achieved by vibrating the sample bin – for 2.5s during, and 9.5s after - the particles entered the simulation.
- The simulated core barrel penetration rate was 0.024mm/s.
- Only a constant barrel amplitude could be specified in the model. To simulate the observed increase in amplitude with penetration depth during physical testing, the constant and continuous descent of the modelled barrel consisted of five successive stages. Each stage had a different barrel amplitude, the value of which was the average of the measured amplitudes during SVC monitoring over the period of the stage considered.

Through use of the Kolmogorov-Smirnov test to quantify the difference between any two given F_B-d plots, the variance between the three numerical model results was evaluated to be insignificant. DEM results indicated that the vertical force on the vibrocore barrel increases approximately linearly with depth from zero to a maximum value of ~62kN. The average recovery ratio of the modelled core samples was 54.1%.

Critical assessment of recovery ratios and F_B-d plots using statistical methods indicated negligible difference between the results of physical testing and numerical modelling. Therefore, the DEM model was considered calibrated and an accurate representation of the physical system. The assumptions made in selecting the parameters that defined the modelled soil were valid.

PART V

Assessment of results and recommendations

Part V contents:

Chapter 15 – Assessment of numerical results

The results of the DEM simulations are reviewed in greater detail. Focus is given to the incremental recovery of the core samples, as well as the change in void ratios and disturbance indices of various soil elements throughout the sampling process.

Chapter 16 – Summary and conclusions: Chapter 15

The findings of Chapter 15 are summarised and conclusions drawn

Chapter 17 – Conclusions for dissertation

The main conclusions of the dissertation are highlighted and linked to the research objectives

Chapter 18 – Recommendations for further research

The body of the dissertation ends with recommendations for future investigation into vibrocore-soil interaction using the calibrated DEM model

15. Assessment of numerical results

All analyses discussed in this chapter are based on the numerical results. Through detailed assessment of the DEM model outputs, the aim was to quantify the micro-scale changes in gravel recovery or density during the sampling process. The chapter consists of three sections:

i) Incremental recovery of vibrocore samples: The increase in height of the sampled soil column within the core barrel during penetration was evaluated; Focus was given to the IFR of the cores during sampling

ii) Disturbance of soil below core barrel: The disturbance index of various elements of soil below the core barrel during sampling were determined and assessed.

iii) Void ratio of soil within core barrel: The void ratios of various elements of sampled soil within the core barrel during its penetration were evaluated

15.1. Incremental recovery of vibrocore samples

Plots of the change in sampled soil column height L with penetration depth d are shown for all three of the numerical models in Figure 15.1a. Also indicated is a dotted line representing ideal recovery, or $L = d$. At $d = 0$m, the L-d plots are all above the dotted line. This is because, as detailed in the physical test procedure, the point at which barrel penetration was treated as zero was ~50mm below the top of the gravel. Thus, before barrel descent commenced, a small height of gravel had entered the sample tube. As observed by Parker and Sills (1990), the values of L deviate further from the ideal recovery line as d and the force required for soil to enter the core barrel increases. In simpler terms, the quality of the sample decreases with penetration depth. A scatter plot of the L-d data is well approximated by a second-order polynomial (Fig. 15.1b), suggesting that this decrease in quality accelerates with penetration depth:

$$L = -0.0985d^2 + 0.7648d \qquad (15.1)$$

Therefore, the recovered core length can be estimated if the penetration depth is known. It must be noted that this equation should only be applied to gravel and sampling procedures similar to that described in this study.

The development of recovery ratio with penetration depth is illustrated in Figures 15.1c and d. Figure 15.1c shows the RR calculated assuming the point of zero penetration is as previously defined. A more realistic representation of the core recovery is illustrated in Figure 15.1d, which accounts for the slight increase in d due to the top ~50mm of soil. While marked differences between the shapes of these two plot sets are apparent during initial stages of sampling, this is only due to the sensitivity of the RR value to small changes in d for small values of L. As penetration increases, these slight deviations have a less pronounced effect and the two data sets exhibit similar distributions.

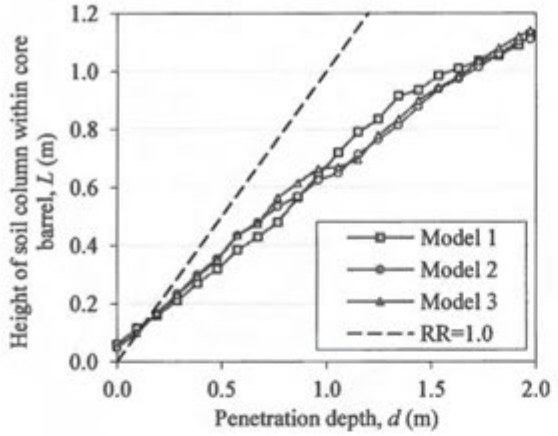

a) *L-d* plots for numerical model results

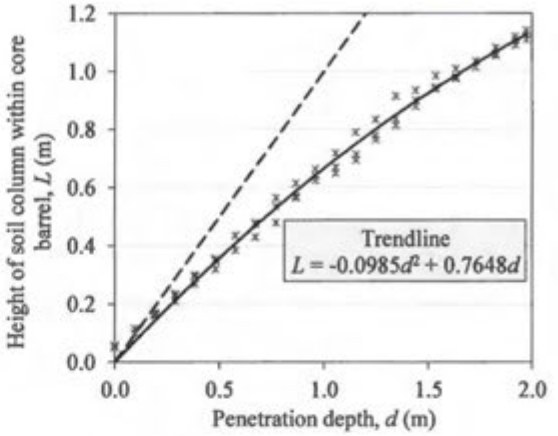

b) Scatter plot with trendline approximation

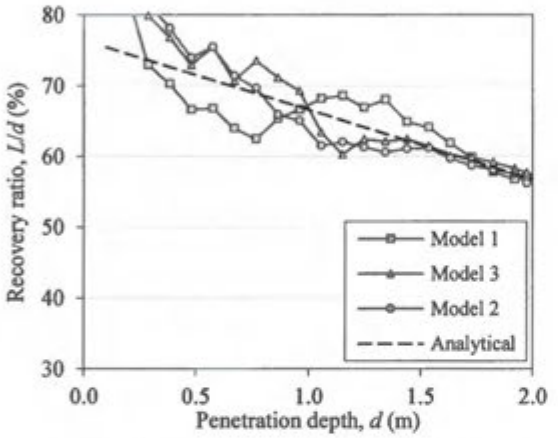

c) Development of RR with *d*, neglecting top ~50mm of gravel

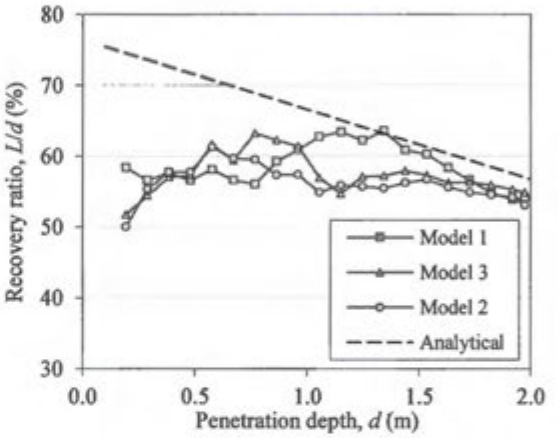

d) Development of RR with *d*, accounting for top ~50mm of gravel

Figure 15-1: Core recoveries yielded by numerical results

The dotted line shown in Figures 15.1c and d represents the analytical RR calculated using L/d, where L was determined using Equation 15.1. Due to the consideration of the top ~50mm of gravel, the true recovery plots shown in Figure 15.1d differ significantly to the analytical line. For $d <$ ~1.4m, the RR graphs vary erratically. This indicates that, over small depths, the specific arrangement and orientation of the sampled particles have a distinct influence on the entry of gravel into the sampling tube. The effect of random gravel particle arrangement within the soil mass appears to become negligible at a penetration depth of d = ~1.5m, at which point RR plots converge. For the full range of penetration considered, recoveries at initial penetration depths (<0.4m) are approximately equal to recoveries at final depth. As depth increases, the recovery plots approach the analytical result. This suggests that if a test were to be conducted where penetration exceeds 2m, the true RR plots will begin to show a marked decrease with d – in accordance with theory.

Figure 15.2 displays the change in IFR with penetration depth for each of the DEM models. The IFRs were calculated using the true RR values shown in 15.1d. The results confirm that the sampler penetrated primarily in a partially plugged mode ($0 < IFR < 1$). A very low IFR (< 5%) for 0.960m < d < 1.056m in model three indicates plugging over this depth. This low IFR is immediately followed by a sharp rise in value to ~90%, highlighting the highly variable 'slip-stick' nature of soil entry into the barrel. Evidence of plugging is also apparent over the last 0.475m of penetration in model two. While variation between the IFR graphs is clear, the averaged IFRs for each set are similar: 54.2%, 53.1%, and 54.9%. The mathematical definition of IFR is such that the average of the IFRs shown in Figure 15.2 equal the cumulative recovery ratios at final depth for each model.

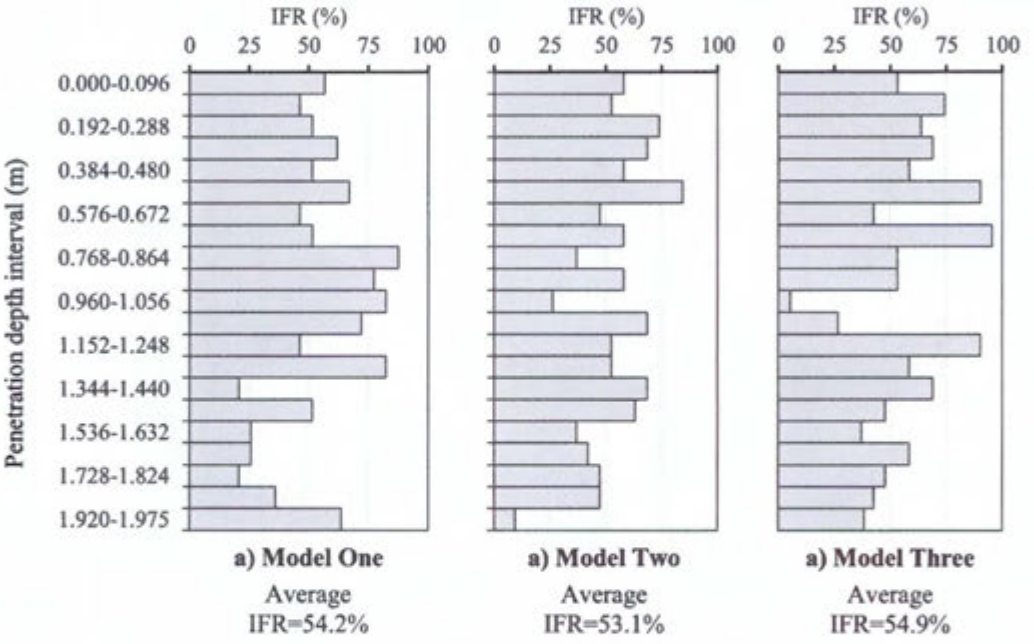

Figure 15-2: Incremental recoveries of core samples given by numerical results

15.2. Disturbance of soil below core barrel

In processing the data obtained through the DEM simulations in Rocky, the mass of particles M_s within any cylindrical soil element of defined height and diameter could be determined. Since all modelled particles had the same density ρ_s = 1474kg/m3, and the volume of a given cylinder V_{TOT} was known, the average void ratio of the soil within the element could be calculated using:

$$e = \frac{V_v}{V_s} = \frac{V_{TOT} - V_s}{V_s} = \frac{V_{TOT} - (M_s/\rho_s)}{(M_s/\rho_s)} \qquad (15.2)$$

Six cylindrical soil elements were considered for analysis of disturbance below the barrel during sampling. The elements were named Below Barrel (BB) elements and were numbered 0-5. All six cylinders had a diameter equal to the inside diameter of the sample bin $D = 0.621$m. No two cylinders overlapped; Successive elements were positioned directly adjacent to each other. The heights of each element and their positions within the sample bin are detailed in Figure 15.3. Note that the top surface of BB5 is the level of the base of the cutting head at final penetration depth – i.e. 383mm above the base of the sample bin.

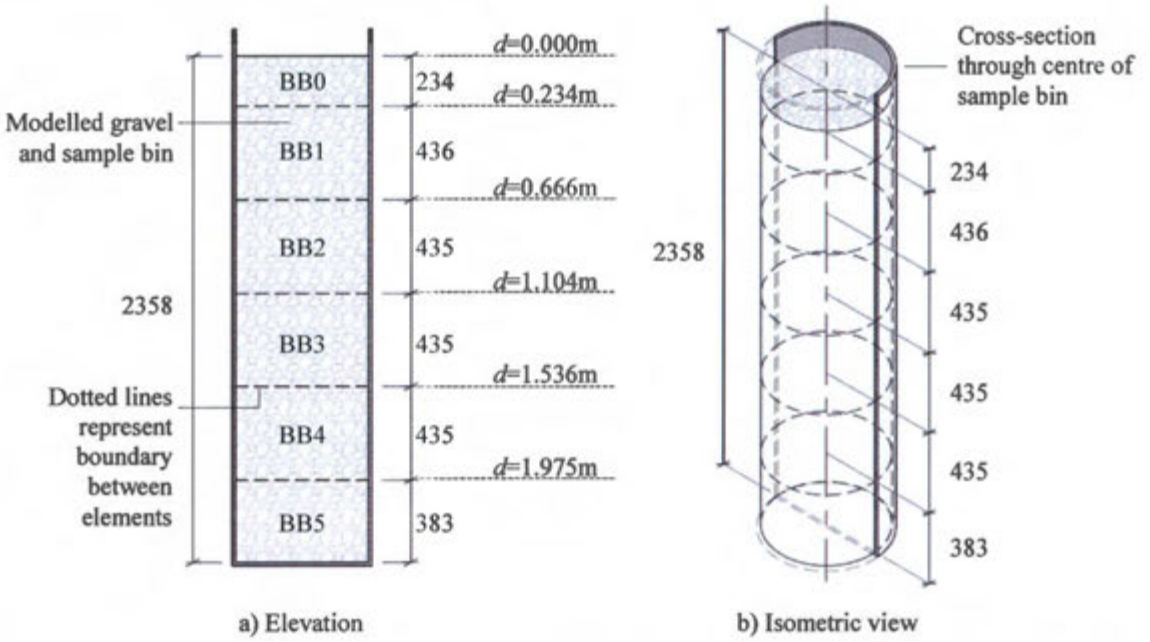

Figure 15-3: Cylindrical elements of soil considered for analysis of disturbance below the core barrel during sampling

All dimensions in mm

Since, of the three DEM models, the results of model three were shown to be the most similar to the average numerical results, the evaluation of disturbance was based only on the output of model three. To assess changes in soil density due to the descending barrel head, the disturbance index I_d for each element was calculated for various barrel penetration depths. The initial void ratio e_0 used in the calculation of each I_d value was the void ratio for each element at $d = 0$m. These e_0 values are specified in Table 15.1. The average of the e_0 values represents of the initial e of the bulk sample.

Table 15-1: Initial void ratio of each BB soil element

Element	BB0	BB1	BB2	BB3	BB4	BB5	Average
e_0	0.671	0.588	0.582	0.585	0.545	0.553	0.587

In addition to $d = 0$m, the penetration depths (m) considered were: 0.234, 0.450, 0.666, 0.888, 1.104, 1.320, 1.536, 1.758, and 1.975. These depths corresponded to the core barrel base at the middle of, or directly above, each soil element. Element BB5 was the exception: the barrel did not descend into the bottom 383mm of the sample bin. Figure 15.4 gives the development of I_d for each of the cylinders for the relevant penetration depths. Once the core barrel penetrated a given element, the volume of the barrel in the element influenced the mass of soil in this element, and therefore its I_d was neglected. Thus, the lower the position of a given element within the sample bin, the more data points within its curve. BB5, the lowest-lying element in the sample bin, had 10 data points. The BB1 curve only had two. A negative disturbance index indicates compaction of the soil, as the new void ratio is less than the initial value. A positive disturbance index indicates expansion.

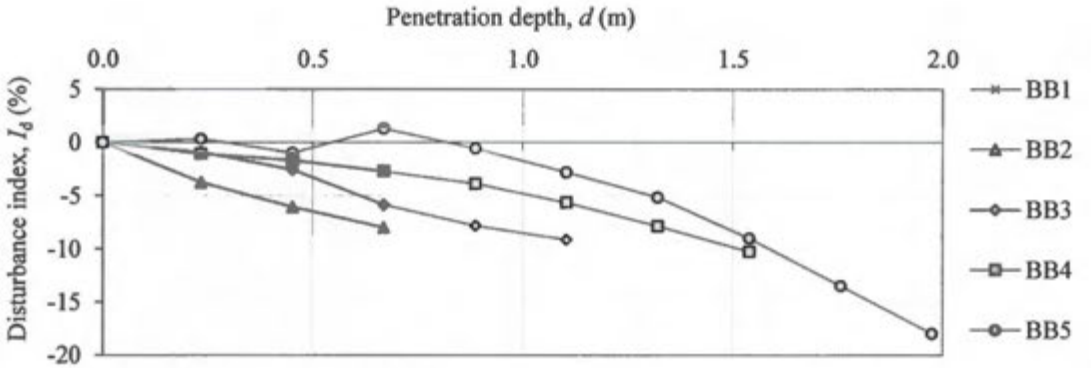

Figure 15-4: Disturbance indices for each soil element as core barrel penetrates soil

In viewing the above figure, it is clear that the soil within the various elements was compacted significantly as the core barrel descended. For all cylinders, the I_d value immediately before barrel penetration was negative. Furthermore, it was noted that the total extent of compaction increased for lower lying elements. It was worth considering why the I_d value of BB5 was significantly greater in magnitude than that of BB2, BB3, and BB4. The middle three elements had final disturbance indices of -7.97, -9.13, and -10.26, respectively. However, the percentage decrease in void ratio of BB5 was much higher, at approximately 18%. This was attributed to the influence of the sample bin wall on the movement of particles below the advancing sample tube. The base provided a rigid boundary, preventing the downward flow of particles ahead of the core barrel. Therefore, as the barrel descended, particles in BB5 were not able to flow downwards as the particles of BB2, BB3, and BB4 were. Instead, they were forced to rearrange into a bulk state of even greater density.

Such a phenomenon would also influence recovery, as the bin floor effectively served as a boundary of infinite bearing capacity. Therefore, it was reasonable to assume that the sample RR would have been lower if not for the influence of the sample bin base.

In continuing assessment of Figure 15.4, the disturbance of bottom soil element is negligible up to a d of ~0.9m. For depths greater than d = ~0.9m, the I_d of BB5 decreases for increasing d. Thus, since final penetration depth is 1.975m, this suggests that compaction of the soil at the bottom element of the bin began when the core barrel base was ~1m above the top boundary of the element. However, this is not necessarily an accurate estimate of the depth of the 'bulb' of disturbed soil extending below the cutting head. This is because the calculation of BB5 I_d is based on the average void ratio within a cylinder of height 383mm. To approximate the depth of this 'bulb', the I_d plots of the various elements were compared: It was noted that the lines formed by the last three data points of BB2, BB3, and BB4 are – relative to the line formed by that of BB5 - approximately parallel. The depth at which the gradient of the BB5 line shows a marked deviation from that of the higher-lying elements is d = ~ 1.35m. This was considered the penetration depth at which the sample bin base began to significantly influence soil particle displacement. In other words, results suggest that the 'bulb' of soil influence extending below the base of the descending core barrel head was approximately ~0.65m, or ~4.3D_{bi}.

15.3. Void ratio of soil within core barrel

In assessing the density of the soil within the core barrel, a similar approach was adopted to that used for investigating the soil below the barrel. Five cylindrical soil elements were defined, the geometries of which are detailed in Table 15.2 and Figure 15.5. These elements were named Inside Barrel (IB) elements, since their position remained fixed inside the barrel, and were relative to the base of the cutting head. Cylinders were numbered 1-5. The height of each of the five cylinders was made equal to the height of soil inside the barrel L when the barrel base is directly above the corresponding BB element. In other words, the height of IB1 is equal to the soil column height when d = 0.234m. The height of IB5 is equal to that of the total core sample at final penetration depth: d = 1.975m.

The analysis of IB soil differed to BB soil in that the void ratio of each IB soil element was evaluated, not the disturbance index. Since the IB element positions were fixed relative to the cutting head base, the initial void ratio of each IB element changed as d increased, and I_d could not be determined with confidence.

Table 15-2: Definition of IB element geometries

Inside barrel (IB) soil element	Element height h (m)	Total volume V_{TOT} ($10^{-3}m^3$)	Core barrel penetration depth d (m) at which gravel first completely fills IB element (L=h)
IB1	0.200	3.553	0.234
IB2	0.474	8.421	0.666
IB3	0.667	1.185	1.104
IB4	0.944	1.677	1.536
IB5	1.140	2.025	1.975

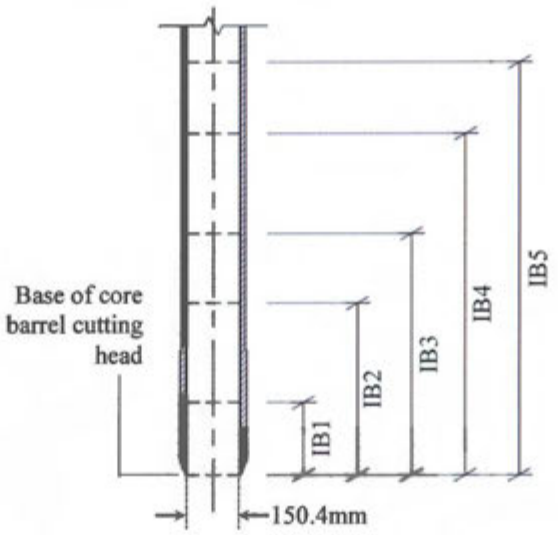

Figure 15-5: Cylindrical elements of soil considered for analysis of void ratio of soil within barrel during sampling

Figure 15.6 provides plots of the change in e with d for elements IB1, IB2, IB3, and IB4. The largest cylinder IB5 was not included because only at final penetration depth $d = 1.975$m was the element completely filled with soil. The vertical dotted lines in each graph represent the minimum d at which gravel first completely fills the cylinder. The horizontal dotted line in each graph represents e of the sampled soil at final penetration depth – in other words, the average void ratio of IB5 $e = 0.645$.

Plots show clear micro-variation in e. These local deviations represent the rapid change of particle mass in the element due to a) rearrangement of particles at the border of the element, and/or b) flow of particles into or out of the element as the barrel descends. However, the general trend of the plots suggests that the soil in each element became denser as d increased. The soil in IB1 is initially in a relatively loose state, with a void ratio markedly higher than that of IB5 at maximum d. Over the last ~0.44m of penetration, where all cylinders are filled with soil, the e values of IB1 have decreased to be mostly less than $e = 0.645$. This signifies compaction of the soil in this element. Similar decreases in e with d, although not as pronounced as that in IBI, can be noted in the other element plots.

Furthermore, during the last ~0.44m of penetration, results show that, in general, the larger the element size, the less the average density the soil. Indeed, at final penetration depth, average void ratio increases from a minimum in IB1 to a maximum in IB5. This is illustrated in Figure 15.7. Therefore, numerical results agreed with the findings of the reviewed literature (De Nicola and Randolph, 1997).

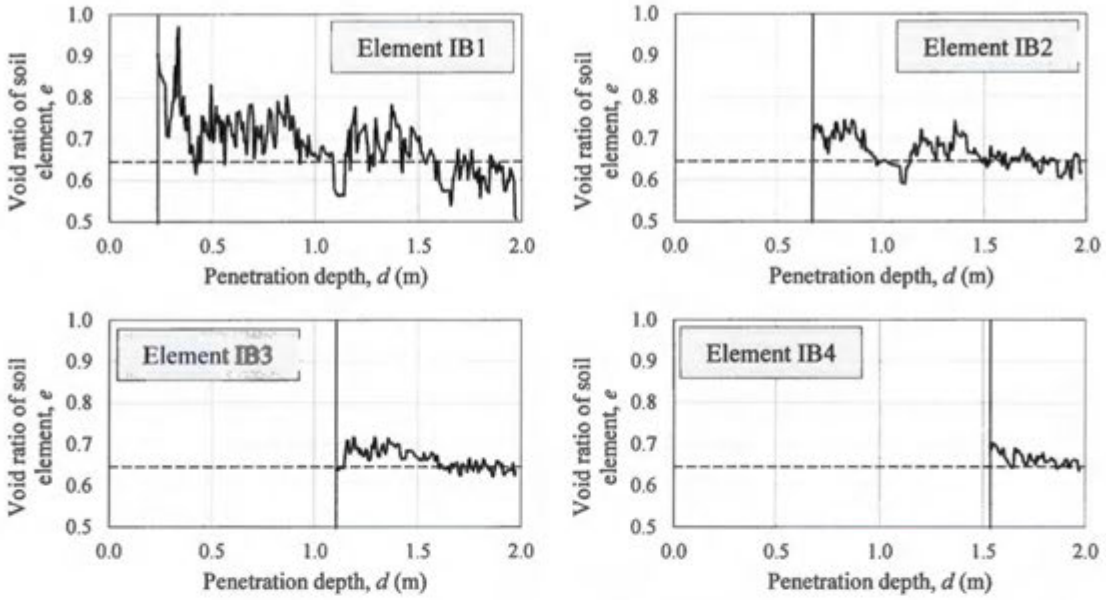

a) Change in void ratio with penetration depth in IB elements

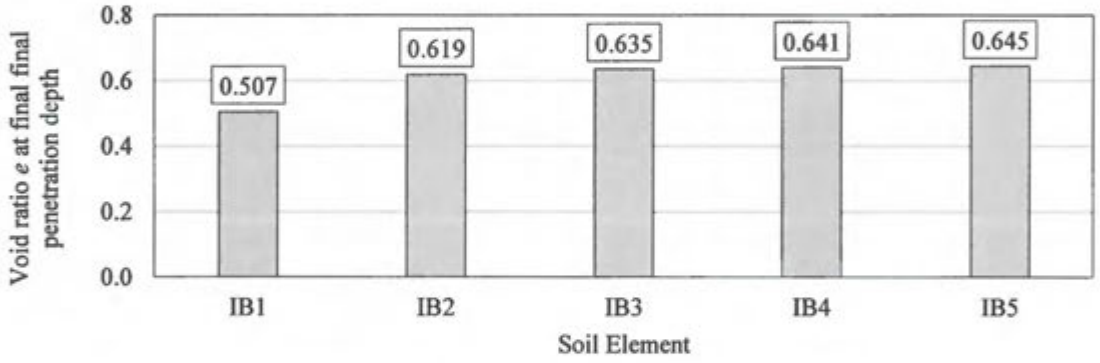

b) Void ratios within final IB elements at final penetration depth

Figure 15-6: Void ratio of elements of soil within core barrel

16. Summary and conclusions: Chapter 15

Having validated the accuracy of the numerical results, the calibrated DEM results were assessed in greater detail. More specifically, focus was given to the incremental core recoveries, the disturbance of soil below the core barrel, and the void ratio of the sampled soil.

Using the output data from all three models, a scatter plot of sampled core length L against penetration depth d was generated. It was shown that the relationship between the two variables was well approximated by a second-order polynomial of the form $L = -0.0985d^2 + 0.7648d$. For $d < \sim 1.4$m, the core recovery ratios varied erratically both with depth and between models. This suggests that, during initial stages of penetration, the specific arrangement of the sampled particles has a distinct effect on the entry of gravel into the barrel. For $d > \sim 1.4$m, the influence of random particle arrangement appeared to become negligible, indicated by a convergence of RR results between the three models. From the analysis of IFR plots, it was clear that the core barrel penetrated primarily in partially plugged mode, with all IFR values between zero and unity. Local variability in the IFR distributions were observed. This corresponds to the 'slip-stick' nature of soil entry into the barrel as described in the literature.

In assessing soil disturbance I_d below the descending core barrel, the change in void ratio of various distinct, cylindrical soil elements, of diameter $D = 0.621$m, within the sample bin were evaluated for various penetration depths. Since, of the three DEM models, the results of model three were shown to be the most similar to the average numerical results, the evaluation of disturbance was based only on the output of model three. Assessment indicated that the soil within the various elements was compacted significantly as the barrel descended. The percentage change in void ratio was as high as 18% for the lowest-lying soil element. In addition, it was apparent from reviewing plots of the change in I_d with d that the sample bin wall had a significant influence on particle displacements. It was estimated that the bulb of soil influence extending below the base of the descending cutting head was approximately 0.65m in height.

In assessing the density of the soil within the core barrel, a similar approach was adopted to that used for investigating the soil below the barrel. Various cylindrical soil elements were defined, the positions and geometry of which remained fixed inside the barrel, and were relative to the base of the cutting head. For these elements, void ratios, not disturbance indices, were evaluated. The analysis showed that a) micro-variations in the density of the sampled soil occurred as a result of particle flow in or out of the element considered, and b) soil density decreased from a maximum at the cutting head base to a minimum at the top of sampled core.

17. Conclusions for dissertation

The objectives of this dissertation were achieved. More specifically:

i) The soil mechanics phenomena controlling the recovery of granular seabed soils in vibrocores was identified and investigated through a review of relevant literature. Core shortening, or a decrease in recovery, often occurs in practice due to the plugging of soil inside the sample tube. The plugging mechanism is highly non-linear and a function a number of geometric and material factors – including core barrel cutting head design, rate and method of core barrel penetration, penetration depth, soil properties, and friction between barrel and soil. Noted was a marked dearth in literature examining the influence of cyclic action on sediment recovery in vibrocores. Therefore, an understanding of soil recovery in vibrocores was developed primarily through review of studies which gave focus to a) Core samplers penetrating the seabed under the influence of gravity, and b) The installation and monitoring of driven or jacked open-ended, tubular offshore piles.

ii) Physical testing of a vibrocore-soil system was conducted. The achieved gravel core recoveries were low, averaging 53%. This suggests a practical difficulty in achieving high quality gravel samples. The downwards force required for maximum core barrel penetration, ~2.0m, was approximately 65kN.

iii) Statistical methods were used to compare physical test results to the final recovery ratios and force-penetration plots yielded by DEM simulations. The analysis showed there to be negligible difference between the physical and numerical output. Thus, the accuracy of the various assumptions made in defining the vibrocore-gravel system for DEM simulation were validated and a calibrated 3D DEM model was achieved.

iv) Numerical results offered insight into the micro-scale response of the vibrocore-soil system. The sample tube penetrated primarily in a partially plugged mode, with $0 < IFR < 1$. The compaction of the soil below the descending core barrel was significant: Disturbance indices as high as 18% were observed. The 'bulb' of soil influence extending below the base of the sample tube was estimated to be ~0.65m, or ~$4.3D_{bi}$. Model output confirmed that the density of the sampled core decreases from a maximum at the cutting head base to a minimum at the top of the sampled soil column.

18. Recommendations for further research

The calibrated numerical model provides scope for additional research into vibrocore-soil interaction and the achievement of higher quality soil samples. Using the validated DEM particle properties for the physical D16-64 gravel, there is potential for further study into the following elements of the SVC system:

i) **Influence of the sample bin boundary**: Obtained numerical results suggest that, for the particle sizes considered, the sample bin influenced soil particle movements. Numerical investigations may be conducted where the sample bin geometry is adjusted to quantify the effect of sample bin diameter on soil displacements. What is the minimum sample bin geometry required for negligible influence on soil recovery and disturbance? Or phrased differently, what is the extent of the zone of influence surrounding the penetrating core barrel head in which the soil is disturbed?

ii) **Greater penetration depths**: Tests of greater penetration can be simulated. In doing so, the following may be assessed: a) The required driving forces required for penetration depths exceeding 2m, b) Whether the increase in F_B with d would continue to be approximately linear for depths greater than 2m, and c) The development of incremental and cumulative recovery ratio with increased d. If increased penetrations wish to be modelled, the core barrel harmonic amplitude input would need to be estimated for depths exceeding 2m. This can be done using the calculated trends for increase in soil stiffness with d. If soil stiffness is known and damping assumed, the amplitude may be approximated.

iii) **Effect of core barrel dynamics**: It is of practical value to investigate which penetration rate would yield the optimum core recovery. Consideration may also be given to the influence of vibrational frequency. In other words, which combination of core barrel vibratory properties would result in the highest quality gravel sample?

iv) **Influence of cutting head geometry**: How may recovery be improved by adjusting the core barrel geometry? By altering the diameter, area ratio, and cutting edge angle of the cutting head, the influence of its design on recovery may be quantified. It is likely such analyses would need to be coupled with finite element calculations, as the geometry of the cutting head is limited by its material strength.

PART VI

End matter

References and appendices

19. References

American Petroleum Institute. 2003. Recommended Practice for Planning, Designing and Constructing Fixed Offshore Platforms – Working Stress Design. (API RP 2A-WSD). Washington D.C., United States of America: API Publishing Services.

Baligh, M.M. 1985. Strain path method. Journal of Geotechnical Engineering, ACSE. 111(9): 1108-1136.

Baligh, M.M., Azzouz, A.S. Chin, C.T. 1987. Disturbance due to ideal tube sampling disturbance. Journal of Geotechnical Engineering, ACSE. 113(7):739-757.

Barbour, S.L. & Krahn, J. 2004. Numerical modelling – prediction or process? Geotechnical News. December, 44:52. Available: http://www.geo-slope.com/res/Numerical%20Modelling%20-%20Prediction%20or%20Process.pdf [2015, August 22].

Bouma, A.H. & Boerma, J.A.K. 1968. Vertical disturbances in piston cores. Marine geology. 6(3):231-241.

British Standards Institution. 1999. Code of practice for site investigations. (BS 5930:1999). United Kingdom: British Standards Institution.

Buckley, D.E., Mankinnon, W.G., Cranston, R.E., & Christian, H.A. 1994. Problems with piston core sampling: Mechanical and geochemical diagnosis. Marine Geology. 177(1-4):95-106.

Burger, U. 2015. Personal communication [2015, July 22].

Burland, J.B. 1987. Nash Lecture: The teachings of soil mechanics – A personal view [Lecture]. Imperial College, London. Available: http://www.researchgate.net/publication/273978671_The_teaching_of_soil_mechanics_a_personal_view [2015, August 22].

Clarke, S.D. & Hird, C.C. 2012. Modelling of viscous effects in natural clays. Canadian Geotechnical Journal. 49(2):129-140.

Clayton, C.R.I., Siddique, A., & Hopper, R.J. 1998. Effects of sampler design on tube sampling disturbance – numerical and analytical investigations. Geotechnique. 48(6):847-867.

Clayton, C.R.I., Simons, N.E. & Matthews, M.C. 1995. Site Investigation. 2nd ed. Wiley-Blackwell.

Craig, R.F. 2004. Craig's Soil Mechanics. 7th ed. London, United Kingdom: Spon Press.

Cundall, P.A. & Strack, O.D.L. 1979. A discrete numerical model for granular assemblies. Geotechnique. 29(1):47-65.

Cundall, P.A. 2001. A discontinuous future for numerical modelling in geomechanics? Proceedings of the ICE – Geotechnical Engineering. 49(1):41-47.

Danson, E. 2005. Geotechnical and Geophysical Investigations for Offshore and Nearshore Developments. Netherlands: Technical Committee 1, International Society for Soil Mechanics and Geotechnical Engineering.

Das, B.M. 2010. Principles of Geotechnical Engineering. 7th ed. Connecticut, United States of America: Cengage Learning.

Das, B.M. 2011. Principles of Foundation Engineering. 7th ed. Connecticut, United States of America: Cengage Learning.

De Nicola, A. & Randolph, M.F. 1997. The plugging behaviour of driven and jacked piles in sand. Geotechnique. 47(4):841-856.

De Vries, G. 2015. Personal communication [2015, July 25].

Dean, E.T.R. 2010. Offshore Geotechnical Engineering – Principles and practice. Westminster, London: ICE Publishing.

Devore, J.L. 2008. Probability and Statistics for Engineering and the Sciences. 7th Ed. Toronto, Canada: Thomson Brooks/Cole.

Donohue, T. 2015. Discrete Element Modelling (DEM) Calibration and Classification of Bulk Material (Report#8470). New South

Wales, Australia: Tunra Bulk Solids Handling Research Associates.

Engineering Simulation and Scientific Software (ESSS). 2015. Rocky Discrete Element Method Package. Available: www.rocky-dem.com/images/pdf/Rocky_DEMP.pdf [2015, September 8].

ESSS, GDI & RDI. 2015. Rocky 3 User Manual (V 3.7.0). Engineering Simulation and Scientific Software (ESSS), Granular Dynamics International (GDI), and Rocky DEM, Inc. (RDI).

Fugro. 2001. Geophysical and geotechnical techniques for the investigation of near seabed soils and rocks – A handbook for non-specialists. Available: http://www.fugro.com/ [2015, February 6].

Henke, S. & Grabe, J. 2008. Numerical investigation of soil plugging inside open-ended piles with respect to the installation method. Acta Geotechnica. 3(3):215-223.

Henke, S. & Grabe, J. 2013. Field measurements regarding the influence of the installation method on soil plugging in tubular piles. 8(3):335-352.

Hvorslev, M.J. 1949. Subsurface exploration and sampling of soils for civil engineering purposes. (Report on the research project of the Committee on Sampling and Testing Soil Mechanics and Foundation Division, American Society of Civil Engineers). Vicksberg, Mississippi: The Waterways Experiment Station: Corps of Engineers, U.S Army. Available: http://babel.hathitrust.org/cgi/pt?id=mdp.39015002125634;view=1up;seq=12 [2015, August 26].

Inman, D.J. 2001. Engineering Vibration. 2nd ed. New Jersey, United States of America: Prentice Hall International, Inc.

Jeng, D.S. & Brandes, H.G. 2011. Developments in Offshore Geotechnics – Preface. Ocean Engineering. 38:815-817.

Jiang, M. & Yu, H.S. 2006. Application of Discrete Element Method to Geomechanics. In Modern Trends in Geomechanics. Wu, W. & Yu, H.S., Eds. The Netherlands: Springer.

Kennett, J.P. 1982. Marine Geology. New Jersey, United States of America: Prentice-Hall, Inc.

Lambe, T.W. & Whitman, R.V. 1969. Soil Mechanics. New York, United States of America: John Wiley & Sons, Inc.

Lees, A. 2012. Obtaining Parameters for Geotechnical Analysis. International Association for the Engineering Modelling, Analysis and Simulation Community (NAFEMS).

Long, M. 2003. Sampling disturbance effects in soft laminated clays. Proceedings of the Institution of Civil Engineers – Geotechnical Engineering. 156(4):213-224.

Lunne, T. & Long, M. 2006. Review of long seabed samplers and criteria for new sampler design. Marine Geology. 226(1-2):145-165.

Lunne, T., Berre, T., Strandvik, S. 1997. Sample disturbance effects in soft low plastic Norwegian clay. Proceedings of Symposium on Recent Developments in Soil and Pavement Mechanics. 25-27 June 1997. Rio de Janeiro: Brazil. 81-102.

Massey, F.J. 1951. The Kolmogorov-Smirnov Test for Goodness of Fit. Journal of American Statistical Association. 46(253):68-78.

National Instruments Corporation. 2014. Measuring Strain with Strain Gages. Available: http://www.ni.com/white-paper/3642/en/ [2015, July 19].

National Oceanic and Atmospheric Administration - National Geophysical Data Center. 2003. Total Sediment Thickness of the World's Oceans & Marginal Seas. Available: http://www.ngdc.noaa.gov/mgg/sedthick/sedthick.html [2015, February 4].

Naylor, D.J. 1978. Stress-Strain Laws for Soils. In Developments in Soil Mechanics – 1. C.R. Scott, Ed. London, United Kingdom: Applied Science Publishers Ltd.

Ng, T. & Meyers, R. 2015. Side resistance of drilled shafts in granular soils investigated by DEM. Computers and Geotechnics. 68(7):161-168.

Osinov, V.A. 2013. Application of a high-cycle accumulation model to the analysis of soil liquefaction around a vibrating pile toe. Acta Geotechnica. 8(6):675-684.

Osinov, V.A., Chrisopulos, S. & Triantafyllidis, T. 2013. Numerical study of the deformation of saturated soil in the vicinity of a vibrating pile. Acta Geotechnica. 8(4):439-446.

O'Sullivan, C., Bray, J.D. & Cui, L. 2006. Experimental validation of particle-based discrete element methods. Proceedings of the Geocongress 2006: Geotechnical Engineering in the Information Technology Age. February 26-March 1, 2006. Atlanta, Georgia: United States of America. 1-18.

Paikowsky, S.G., Whitman, R.V., Baligh, M.M. 1989. A new look at the phenomenon of offshore pile plugging. Marine Geotechnology. 8(3):213-230.

Palmström, A & Singh, R. 2001.The deformation modulus of rock masses – comparisons between in situ tests and indirect estimates. Tunnelling and Underground Space Technology. 16(3):115-131.

Parker, W.R. & Sills, G.C. 1990. Observation of Corer Penetration and Sample Entry During Gravity Coring. In Marine Geological Surveying and Sampling. E.A. Hailwood et al., Eds. Dordrecht, Netherlands: Kluwer Academic Publishers. 101-107.

Potts, D.M. & Zdravković. 1999. Finite Element Analysis in Geotechnical Engineering – Theory. London, United Kingdom: Thomas Telford Publishing.

Power, P. & Colliat, J.L. 2000. Guidance Notes on Geotechnical Investigations for Subsea Structures. Subsea Working Group, Offshore Soil Investigation Forum. Available: http://d3c6l3uum4x5po.cloudfront.net/wp-content/uploads/2014/03/subseaguidancenotes.pdf [2015, January 28].

Randolph, M. & Gourvenec, S. 2011. Offshore Geotechnical Engineering. Abingdon, United Kingdom: Spon Press.

Randolph, M.F., Leong, E.C. & Houlsby, G.T. 1991. One-dimensional analysis of soil plugs in pipe piles. Geotechnique. 41(4):587-598.

Raubenheimer, G. 2015. Personal communication [2015, July 16].

Shukla, S.K. & Sivakugan, N. 2011. Site Investigation and In-situ Tests. In Geotechnical Engineering Handbook. B.M. Das, Ed. Florida: J. Ross Publishing, Inc. Chapter 10.

Skinner, L.C. & McCave, I.N. 2003. Analysis and modelling of gravity- and piston coring based on soil mechanics. Marine Geology. 199(1):181-204.

Smith, D.G. 1998. Vibracoring: a new method for coring deep lakes. Palaeogeography, Palaeoclimatology, Palaeoecology. 140(1):433-440.

United States Army Corps of Engineers. 2006. Coastal Engineering Manual. Available: http://app.knovel.com/hotlink/toc/id:kpCEM0000P/coastal-engineering-manual [2014, May 1].

Weaver, P.P.E. & Schultheiss, P.J. 1990. Current methods for Obtaining, Logging and Splitting Marine Sediment Cores. In Marine Geological Surveying and Sampling. E.A. Hailwood et al., Eds. Dordrecht, Netherlands: Kluwer Academic Publishers. 85-100.

Woodward, C.A. & Sloss, C.R. 2013. Coring and Augering. In: Reference Module in Earth Systems and Environmental Sciences – Treatsie on Geomorphology: Volume 14, Methods in Geomorphology. 199-137. John F. Scroder (ed.). San Diego: Academic Press.

Yang, X.S. 2008. Mathematical Modelling for Earth Sciences. Edinburgh, Scotland: Dunedin Academic Press Ltd.

Zaiontz, C. 2014. Real Statistics using Excel – Two Sample Kolmogorov-Smirnov Test. Available: http://www.real-statistics.com/non-parametric-tests/two-sample-kolmogorov-smirnov-test/ [2015, February 18].

Appendix 1

Particle size distribution of gravels tested

This appendix details the results of the sieve analyses conducted to determine the PSD of the gravel samples (D16-32, D32-64, and D16-64). All tests were performed between the 22nd-27th June 2015 at the Civil Engineering Laboratories in the New Engineering Building, Upper Campus, University of Cape Town.

The gravel samples were collected from the DBM Test Facility in Paarden Eiland on the 19th June 2015. Two samples were collected: one 16-32mm gravel sample, and one 32-64mm gravel sample – each sample approximately 35kg. It was assumed that the collected samples were representative samples. The D16-64 sample was mixed in the laboratory immediately prior to sieve testing, the mix consisting of 50% D16-32 and 50% D32-64 by mass. For each of the three mixed gravel samples, a number of sieve tests were conducted in effort to more accurately determine the PSD of the representative sample. For a given sample, the soil retained within each test was summed, with these values, as well as the total mass of sample sieved, used to calculate the total percentage passing for each sieve opening.

The mass of each sample sieved is summarised in Table A1.1. The test results are detailed in Tables, A1.2, A1.3, and A1.4. Figure A1.1 shows the sieves used to conduct the tests.

Table A1-1: Mass sieved for each mixed gravel sample

Gravel sample	No. of independent sieve tests	Approximate mass of sample for each independent sieve test (kg)	Approximate total mass of sample sieved
D16-32	7	2.5	17.5
D32-64	7	5.0	35.0
D16-64	4	9.0 (4.5 M16-32; 4.5 M32-64)	36.0

Table A1-2: Sieve test results for D16-32 sample

Tests conducted on 22/06/2015

Sieve opening diameter (mm)		32.0	26.5	19.0	13.2	9.5	Pan	
Mass of empty sieve (g)		*na*	1631	1506	1352	1415	1183	
Mass of sieve + Soil retained (g)	Test 1	*na*	1717	3132	2137	1419	1185	
	Test 2	*na*	1854	2596	2546	1422	1254	
	Test 3	*na*	1798	2836	2353	1418	1183	
	Test 4	*na*	1989	2647	2347	1416	1184	
	Test 5	*na*	1863	2734	2387	1421	1184	
	Test 6	*na*	1714	3036	2226	1425	1184	
	Test 7	*na*	1793	2999	2195	1416	1184	
Mass of soil retained (g)	Test 1	0	86	1626	785	4	2	2503
	Test 2	0	223	1090	1104	7	71	2495
	Test 3	0	167	1330	1001	3	0	2501
	Test 4	0	358	1141	995	1	1	2496
	Test 5	0	232	1228	1035	6	1	2502
	Test 6	0	83	1530	874	10	1	2498
	Test 7	0	162	1493	843	1	1	2500
Sum of soil retained (g)		0	1311	9438	6637	32	77	17495
Percentage retained of sum (%)		0.00	7.49	53.95	37.94	0.18	0.44	100
Cumulative percentage retained (%)		0.0	7.5	61.4	99.4	99.6	100.0	
Percentage passing (%)		**100.0**	**92.5**	**38.6**	**0.6**	**0.4**	**0.0**	

Table A1-3: Sieve test results for D32-64 sample

Tests conducted on 23/06/2015

Sieve opening diameter (mm)		64.0	53.0	37.5	26.5	19.0	Pan	
Mass of empty sieve (g)		*na*	1901	1614	1631	1506	1183	
Mass of sieve + Soil retained (g)	Test 1	*na*	5405	2867	1939	1506	1183	
	Test 2	*na*	5010	2575	2566	1506	1183	
	Test 3	*na*	5203	2824	2128	1506	1183	
	Test 4	*na*	4822	2972	2354	1506	1183	
	Test 5	*na*	5260	2934	1999	1506	1183	
	Test 6	*na*	4172	3562	2493	1506	1183	
	Test 7	*na*	2676	3110	2546	1506	1183	
Mass of soil retained (g)	Test 1	0	3504	1253	308	0	0	5065
	Test 2	0	3109	961	935	0	0	5005
	Test 3	0	3302	1210	497	0	0	5009
	Test 4	0	2921	1358	723	0	0	5002
	Test 5	0	3359	1320	368	0	0	5047
	Test 6	0	2271	1948	862	0	0	5081
	Test 7	0	775	1496	915	0	0	3186
Sum of soil retained (g)		0	19241	9546	4608	0	0	33395
Percentage retained of sum (%)		0.00	57.62	28.59	13.80	0.00	0.00	100.0
Cumulative percentage retained (%)		0.0	57.6	86.2	100.0	100.0	100.0	
Percentage passing (%)		**100.0**	**42.4**	**13.8**	**0.0**	**0.0**	**0.0**	

Table A1-4: Sieve test results for D16-64 sample

Tests conducted on 27/06/2015

Sieve opening diameter (mm)		64.0	53.0	37.5	26.5	19.0	13.2	9.5	Pan	
Mass of empty sieve (g)		*na*	1900	1614	1631	1506	1352	1415	1181	
Mass of sieve + Soil retained (g)	Test 1	*na*	4725	2525	2805	4175	2773	1415	1182	
	Test 2	*na*	5369	2290	2280	4262	2801	1415	1182	
	Test 3	*na*	5882	2011	1865	4164	3057	1424	1187	
	Test 4	*na*	4316	3216	2367	3543	3520	1429	1218	
Mass of soil retained (g)	Test 1	0	2825	911	1174	2669	1421	0	1	9001
	Test 2	0	3469	676	649	2756	1449	0	1	900
	Test 3	0	3982	397	234	2658	1705	9	6	8991
	Test 4	0	2416	1602	736	2037	2168	14	37	9010
Sum of soil retained (g)		0	12692	3586	2793	10120	6743	23	45	36002
Percentage retained of sum (%)		0.00	35.25	9.96	7.76	28.11	18.73	0.06	0.12	100.0
Cumulative percentage retained (%)		0.0	35.3	45.2	53.0	81.1	99.8	99.9	100.0	
Percentage passing (%)		**100.0**	**64.7**	**54.8**	**47.0**	**18.9**	**0.2**	**0.1**	**0.0**	

53mm sieve opening

37.5mm sieve opening

26.5mm sieve opening

19mm sieve opening

13.2mm sieve opening

9.5mm sieve opening

Combined 6-sieve array

Figure A1-1: 300mm diameter sieves used for determination of PSD

Photos taken by Sam Wegener (22-27th June 2015) - Pen for scale

Appendix 1
Particle size distribution of gravels tested

UNIVERSITY OF CAPE TOWN
IYUNIVESITHI YASEKAPA · UNIVERSITEIT VAN KAAPSTAD

Test	Sieve analysis	Signed	Tested at	UCT Civil Laboratories	Page 1 of 2
Tested by	Sam Wegener		Test date	22nd-27th June 2015	

Sample	Sieve opening diameter (mm)	Mass of empty sieve (g)	Mass of sieve + Soil retained (g)							Mass of soil retained (g)							Sum of soil retained (g)	% Retained	Cumulative percentage retained (%)	Percentage passing (%)
			Test 1	Test 2	Test 3	Test 4	Test 5	Test 6	Test 7	Test 1	Test 2	Test 3	Test 4	Test 5	Test 6	Test 7				
D16-32	32.0	*na*	*na*	*na*	*na*	*na*	*na*	*na*	*na*	0	0	0	0	0	0	0	0	0.00	0.0	100.0
	26.5	1631	1717	1854	1798	1989	1863	1714	1793	86	223	167	358	232	83	162	1311	7.49	7.5	92.5
	19.0	1506	3132	2596	2836	2647	2734	3036	2999	1626	1090	1330	1141	1228	1530	1493	9438	53.95	61.4	38.6
	13.2	1352	2137	2456	2353	2347	2387	2226	2195	785	1104	1001	995	1035	874	843	6637	37.94	99.4	0.6
	9.5	1415	1419	1422	1418	1416	1421	1425	1416	4	7	3	1	6	10	1	32	0.18	99.6	0.4
	Pan	1183	1185	1254	1183	1184	1184	1184	1184	2	71	0	1	1	1	1	77	0.44	100.0	0.0
										2503	2495	2501	2496	2502	2498	2500	17495	100.0		
D32-64	64.0	*na*	*na*	*na*	*na*	*na*	*na*	*na*	*na*	0	0	0	0	0	0	0	0	0.00	0.0	100.0
	53.0	1901	5405	5010	5203	4822	5260	4172	2676	3504	3109	3302	2921	3359	2271	775	19241	57.62	57.6	42.4
	37.5	1614	2867	2575	2824	2972	2934	3562	3110	1253	961	1210	1358	1320	1948	1496	9546	28.59	86.2	13.8
	26.5	1631	1939	2566	2128	2354	1999	2493	2546	308	935	497	723	368	862	915	4608	13.80	100.0	0.0
	19.0	1506	1506	1506	1506	1506	1506	1506	1506	0	0	0	0	0	0	0	0	0.00	100.0	0.0
	Pan	1183	1183	1183	1183	1183	1183	1183	1183	0	0	0	0	0	0	0	0	0.00	100.0	0.0
										5065	5005	5009	5002	5047	5081	3186	33395	100.0		
D16-64	64	*na*	*na*	*na*	*na*	*na*				0	0	0	0				0	0.00	0.00	100.0
	53.0	1900	4725	5369	5882	4316				2825	3469	3982	2416				12692	35.25	35.25	64.7
	37.5	1614	2525	2290	2011	3216				911	676	397	1602				3586	9.96	45.21	54.8
	26.5	1631	2805	2280	1865	2367				1174	649	234	736				2793	7.76	52.97	47.0
	19.0	1506	4175	4262	4164	3543				2669	2756	2658	2037				10120	28.11	81.08	18.9
	13.2	1352	2773	2801	3057	3520				1421	1449	1705	2168				6743	18.73	99.81	0.2
	9.5	1415	1415	1415	1424	1429				0	0	9	14				23	0.06	99.88	0.1
	Pan	1181	1182	1182	1187	1218				1	1	6	37				45	0.12	100.00	0.0
										9001	9000	8991	9010				36002	100.0		

Appendix 2

Details of accelerometer

LORD DATASHEET

G-Link2™-LXRS®

Wireless Accelerometer Node

G-Link2™-LXRS® - *ruggedized node with high-speed sampling and optional integrated three-axis accelerometer or an external single-axis accelerometer*

LORD MicroStrain® LXRS® Wireless Sensor Networks enable simultaneous, high-speed sensing and data aggregation from scalable sensor networks. Our wireless sensing systems are ideal for sensor monitoring, data acquisition, performance analysis, and sensing response applications.

The **gateways** are the heart of the LORD MicroStrain wireless sensing system. They coordinate and maintain wireless transmissions across a network of distributed wireless sensor **nodes**. The LORD MicroStrain LXRS wireless communication protocol between LXRS nodes and gateways enable high-speed sampling, ±32 microseconds node- to- node synchronization, transmission range up to 2 kilometers, and lossless data throughput under most operating conditions.

Users can easily program nodes for data logging, continuous, and periodic burst sampling with the **Node Commander®** software. The web-based **SensorCloud™** interface optimizes data aggregation, analysis, presentation, and alerts for gigabytes of sensor data from remote networks.

Wireless Simplicity, Hardwired Reliability™

Product Highlights

- On-board triaxial, or external single axis MEMS accelerometer with up to +/-200 *g* measurement range
- Wireless framework is ideal for measuring vibration and acceleration in remote applications.
- High resolution data with 16-bit A/D converter
- User-programmable sample rates up to 10 KHz
- Transmit real-time data or log to internal memory.
- Small, lightweight IP67 enclosure rated for outdoor use

Features and Benefits

High Performance

- Node-to-node synchronization up to ±32 microseconds
- Scalable, long range wireless sensor networks up to 2 km
- User-programmable filters for optimized anti-aliasing

Ease of Use

- Internal or external accelerometer option for installation versatility
- Remotely configure nodes, acquire and view sensor data with Node Commander®.
- Optional web-based SensorCloud™ interface optimizes data storage, viewing, and analysis.
- Easy integration via comprehensive SDK

Cost Effective

- Out-of-the box wireless sensing solution reduces development and deployment time.
- Volume discounts

Applications

- Condition-based monitoring
- Health monitoring of rotating components, aircraft, structures, and vehicles
- Vibration monitoring
- Vehicle dynamics testing
- Product testing

LORD MicroStrain®
SENSING SYSTEMS

Appendix 3

Calibration of strain gauge data to determine core barrel axial force

Introduction

F_B denotes the axial, or vertical, force acting on the core barrel during penetration into soil. Calibration between physical and numerical results required that plots of F_B as a function of penetration depth be generated. Such plots could be easily obtained from the numerical results yielded by Rocky software. However, it was less simple to achieve such plots using data collected through physical testing. At the time of testing, the existing SVC monitoring system did not provide the appropriate data. Therefore, strain gauges were used in a series of preliminary coring tests – henceforth termed the *calibration tests*. These tests were conducted to generate an empirical equation for estimating F_B. This appendix details the observation of this empirical relationship, found to be:

$$F_B = E_B A_B [0.1799(\varepsilon_C) - 12.2633] \qquad (A3.1)$$

Where F_B is the vertical force acting on the core barrel in kN

E_B is the Young's modulus of the core barrel material in GPa = 200GPa (EN24 High Tensile Steel Condition V)

A_B is the cross-sectional of the core barrel in m^2 = $7.072 \times 10^{-3} m^2$ (177.8mm outer diameter; 150.4mm inner diameter)

ε_C is the microstrain measured in the 'cradle' of the SVC system (Fig. A3.2i, A3.3c)

Overview of objectives and methodology

The objective of the strain gauge (SG) calibration was to generate an equation which gives the axial strain on the core barrel as a function a SVC system variable that a) can be easily and repeatedly measured during SVC testing without damage to the strain-measuring apparatus, and b) is independent of the soil type and penetration rate. This variable was chosen to be the strain of the SVC cradle, ε_C. Gauges could not be placed on the core barrel during SVC testing. At final penetration depth, the core barrel would be fully inserted into saturated gravel. Any gauges attached to the core barrel would likely be damaged. Furthermore, it was expected that vibrations would damage or disturb the strain-reading apparatus. Therefore, the calibration tests were conducted using a dry coarse sand, which filled approximately only 75% of the sample bin (Fig. A3.2d), and the core barrel was pushed into the soil at constant penetration (±8.7mm/s) without

vibratory action. Penetration was stopped manually when the peak allowable hydraulic pressure of the system was reached (±11.5MPa).

The calibration tests consisted of two sub-sets of tests, distinguished by the placement of the strain gauges. First, strain gauges were placed on the outside surface of the upper part core barrel not inserted into the soil (Fig. A3.2b, A3.3b) – termed the *barrel tests*. Secondly, strain gauges were placed on the cradle of the SVC system (Fig. A3.2i, A3.3c) – termed the *cradle tests*. Figure A3.1 below summarises the chronological process of the physical testing and data processing:

1	Full-bridge strain gauge (SG) circuit and sensor node connected to core barrel (Fig. A3.2f; Fig. A3.3a)	Physical testing; Barrel tests
2	Core barrel pushed into sand at constant penetration rate of 8.7mm/s until peak allowable pressure (±115bar) reached; P and ε_{Bm} measured; Repeated four times	
3	Data collected; ε_{Bm} plotted as a function of P; Eq. A3.2 generated, giving empirical relationship between hydraulic pressure and core barrel strain, ε_{Bc1}	Data processing
4	Statistical analysis conducted to confirm negligible difference between plots of ε_{Bm} and ε_{Bc1} (Fig. A3.6)	
5	Full-bridge strain gauge circuit and sensor node connected to cradle (Fig. A3.2i; Fig. A3.3c)	Physical testing; Cradle tests
6	Core barrel pushed into sand at constant penetration rate of 8.7mm/s until peak allowable pressure (±11.5MPa) reached; P and ε_C measured; Repeated five times	
7	Data collected; Plot of ε_{Bc1} generated using Eq. A3.2 and P readings from cradle test (Fig. A3.7)	Data processing
8	ε_{Bc1} plotted as a function of ε_C; Eq. A3.3 generated, giving empirical relationship between cradle strain and core barrel strain, ε_{Bc2} (Fig. A3.8)	
9	Plots of ε_{B2} generated using Eq. A3.3 and ε_C readings from step 6 (Fig. A3.9)	
10	Statistical analysis conducted to confirm negligible difference between plots of ε_{Bc1} and ε_{Bc2} (Fig. A3.9)	
11	Equation generated to express vertical force on core barrel, F_B, as a function of core barrel axial strain, ε_B, cross-sectional area of core barrel, A_B, and stiffness of core barrel material, E_B (Eq. A3.1)	

Notation	
P	Hydraulic pressure of cylinder pushing core barrel downwards (MPa)
ε_{Bm}	Measured core barrel axial strain
ε_C	Measured cradle strain
ε_{Bc1}	Core barrel axial strain calculated using Eq. A3.2
ε_{Bc2}	Core barrel axial strain calculated using Eq. A3.3
ε_B	The core barrel axial strain used to calculate F_B (taken to be equal to ε_{Bc2})

Figure A3-1: Methods used in strain gauge calibration and derivation of Eq. A3.1

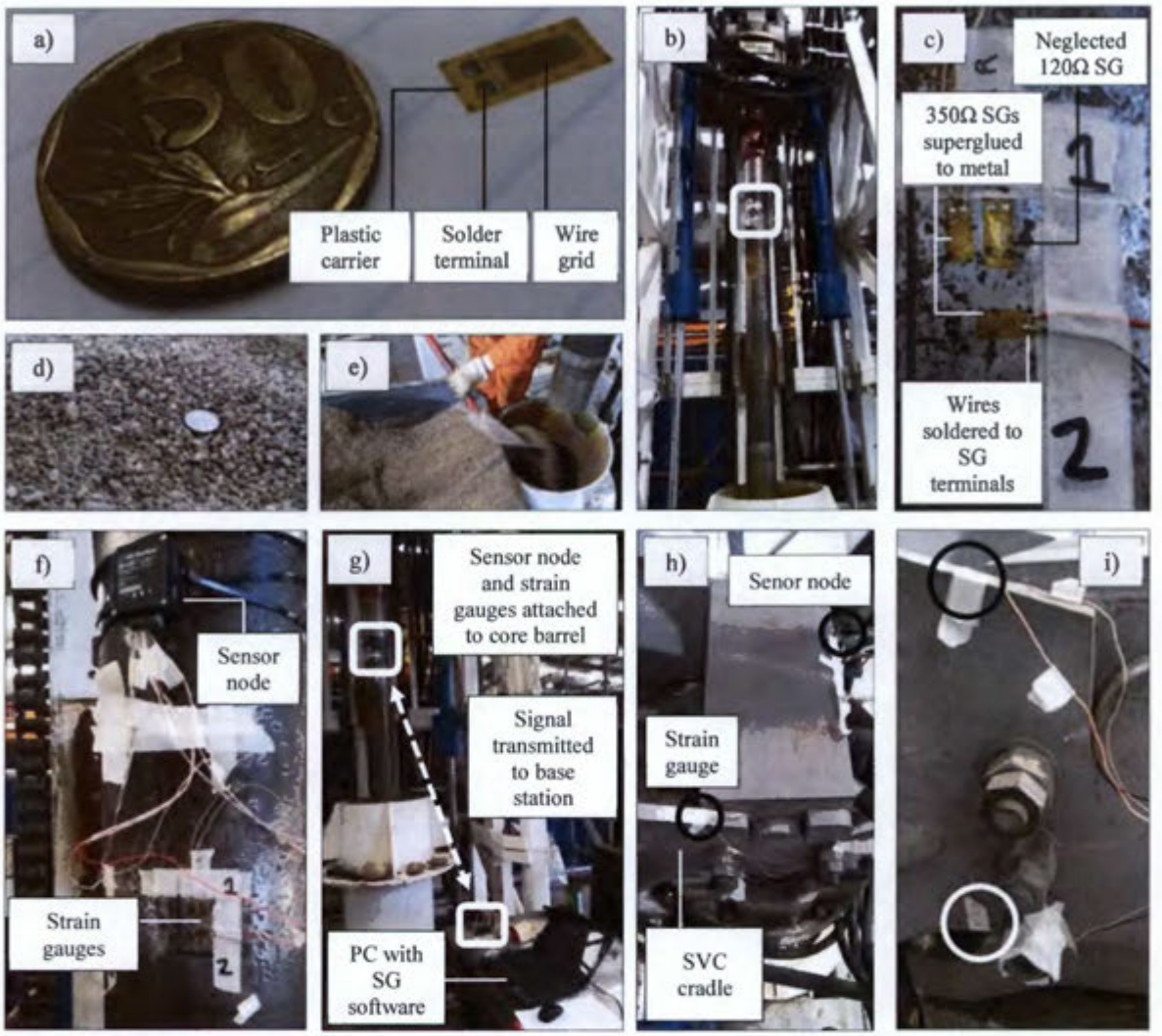

a) A single 350Ω strain gauge (coin for scale)
b) SG circuit positioned approximately 70mm from top of core barrel for barrel tests
c) Strain gauges attached to core barrel with superglue
d) Coarse sand used for strain gauge calibration (coin for scale)
e) Placement of sand into sample bin
f) Sensor node attached to core barrel with wires connected to strain gauges (barrel tests)
g) Physical setup of schematic shown in Fig. A3.3a
h) View of the SVC motor from above showing gauges attached to cradle for cradle tests
i) Side view of the cradle with strain gauges attached

Figure A3-2: Various images depicting the strain gauge calibration

Strain gauge details

A full-bridge circuit consisting of 350Ω strain gauges (gauge factor = 2.04) was used in the calibration tests (Fig. A3.3a). The circuit was connected to a sensor node which transmitted a wireless signal to a base station. The base station was connected to a PC with strain-reading software installed, where the strain data was collected. Appendix 8 provides a summary of strain gauge theory. Appendix 9 details the specifications for the sensor node used.

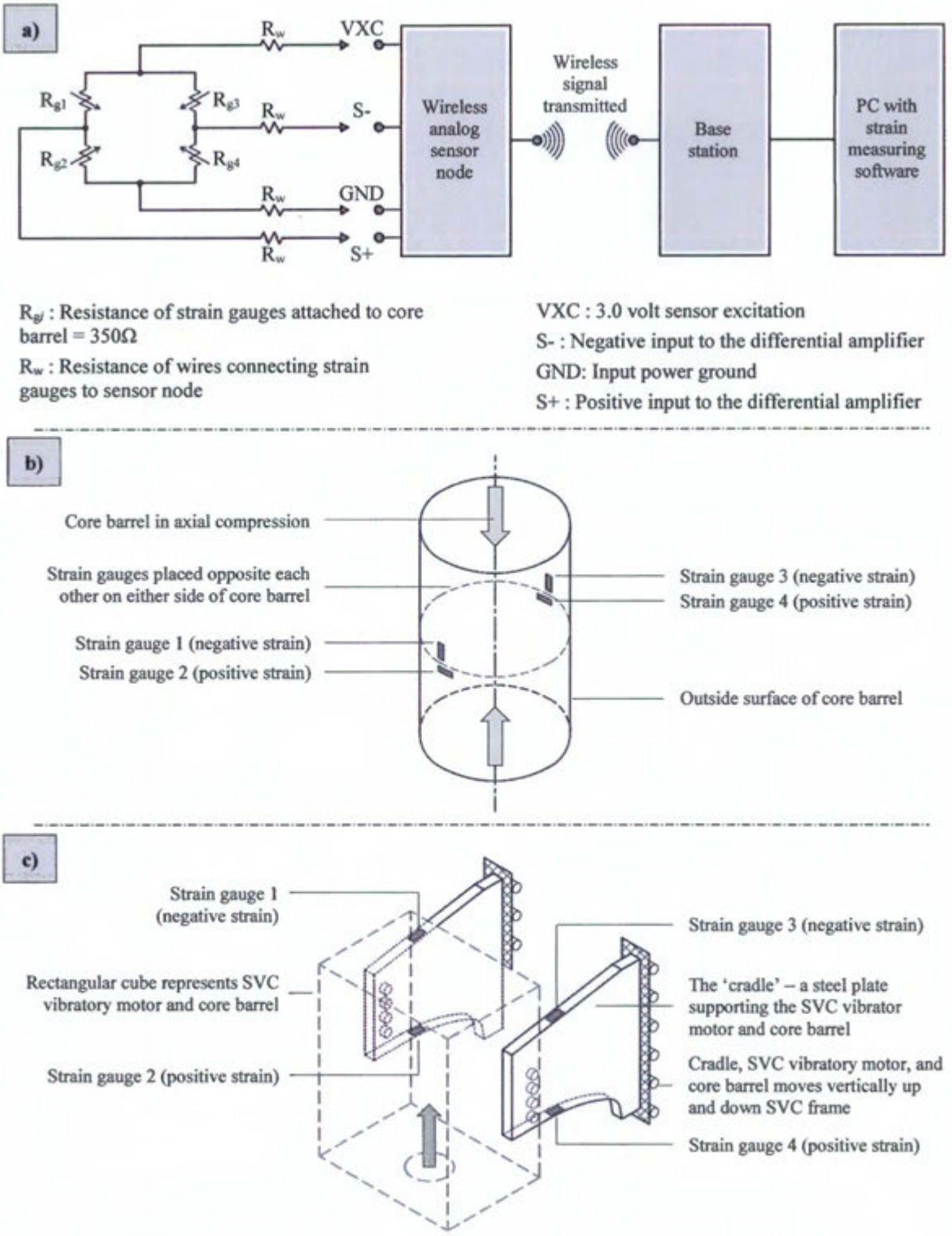

Figure A3-3: Schematic diagrams of a) Full-bridge strain gauge circuit and strain-reading equipment; Placement of gauges on **b)** core barrel, and **c)** SVC cradle

Barrel test results

Fig. A3.4 shows the results of the barrel tests. Clear consistency in results between the four tests was noted. The difference between core barrel penetration rate (8.7mm/s) and final penetration depth (0.50m) for each of the four tests was negligible (Fig. A3.4a). Hydraulic pressure, P, increased from its initial value of 6MPa to its peak value of ±11.5MPa, at which point penetration was stopped manually (Fig. A3.4b). Since the barrel was pushed into dry soil, there was no reduction in soil-barrel friction resulting from vibration-induced liquefaction, and peak pressure was reached after only 0.50m. The trend of the measured core barrel axial microstrain, ε_{Bm}, showed increasing compressive strain until the test was stopped (Fig. A3.4c).

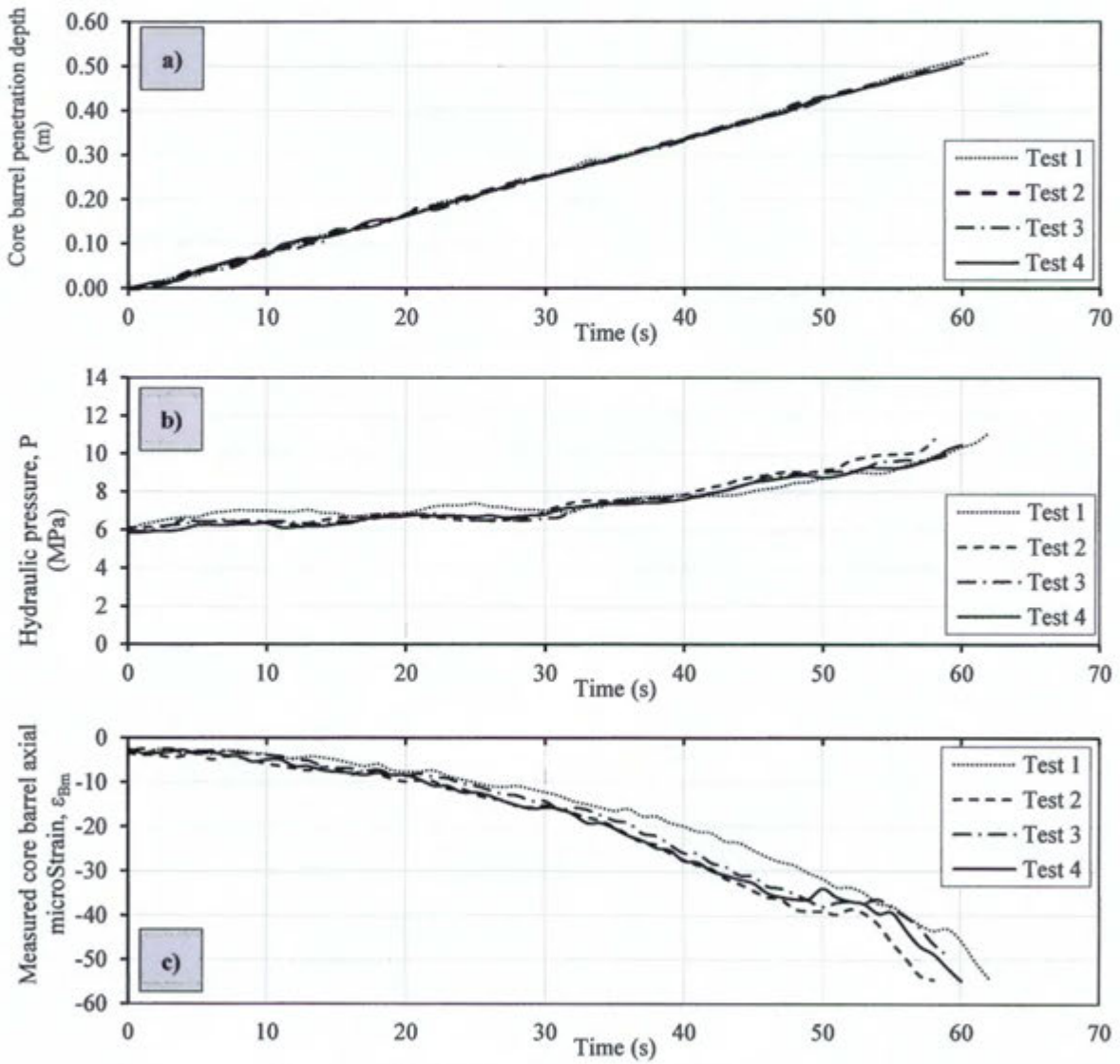

Figure A3-4: Measured results for barrel tests

Plots of the variation with time of a) Penetration depth, b) Pressure, and c) Microstrain

The ε_{Bm} values and P values shown in Fig. A3.4b and A3.4c were then plotted against each other (Fig. A3.5) to determine their empirical relationship. The plot shows there to be a strong decreasing linear relationship (squared correlation coefficient $r^2 = 0.93$) between ε_{Bm} and P, approximated by the equation:

$$\varepsilon_{Bcl} = -11.2685(P) + 65.8500 \qquad (A3.2)$$

where units for P must be in MPa, and ε_{Bcl} is given in microstrain.

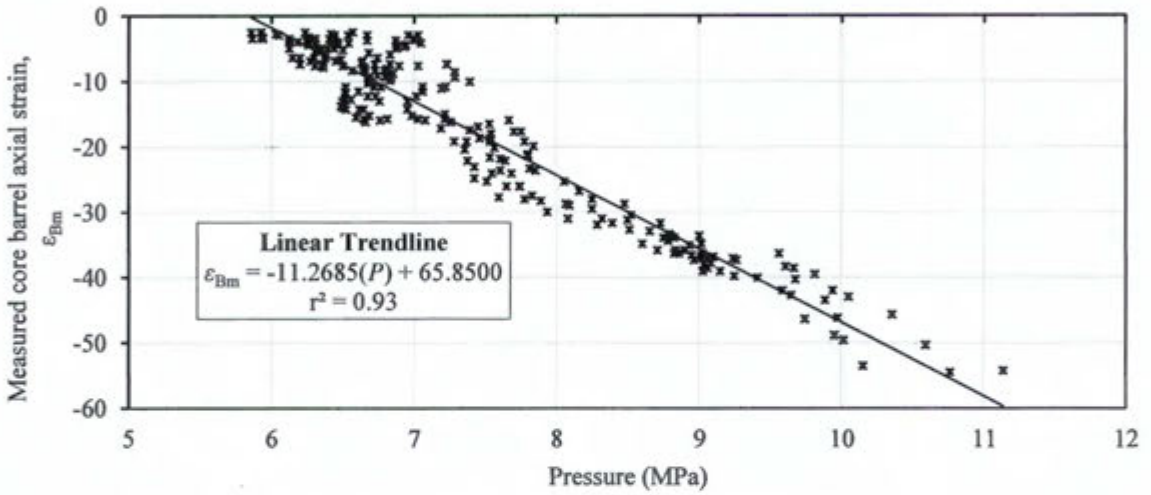

Figure A3-5: Determining the empirical relationship between ε_{Bm} and P

Statistical analysis of barrel test results

Using the pressure readings for each of the four barrel tests shown in Fig. A3.4b, values of strain were calculated using Eq. A3.2 (ε_{Bcl}) and compared with the measured strain values (ε_{Bm}) shown in Fig. A3.4c. This was to assess whether Eq. A3.2 provided a reasonable estimate of measured core barrel axial strain.

The two sample Kolmogorov-Smirnov (KS) method was used to determine whether, for each test, the time-variable plots of ε_{Bm} and ε_{Bcl} differed significantly. Both the SVC system and strain-reading apparatus has a sampling rate of 1Hz. Thus, data was recorded at one second intervals and the statistical sample size for the tests ranged between $n = 58$ and $n = 62$. For each test, a $D_{m,n,\alpha}$ value was calculated at 95% confidence. The KS calculations showed that $D_{m,n} < D_{m,n,\alpha}$ for all four of the KS tests. Therefore, Eq. A3.2 approximated ε_{Bm} with reasonable accuracy. Plots of the variation in ε_{Bm} and ε_{Bcl} with time for each of the four barrel tests are shown in Fig. A3.6.

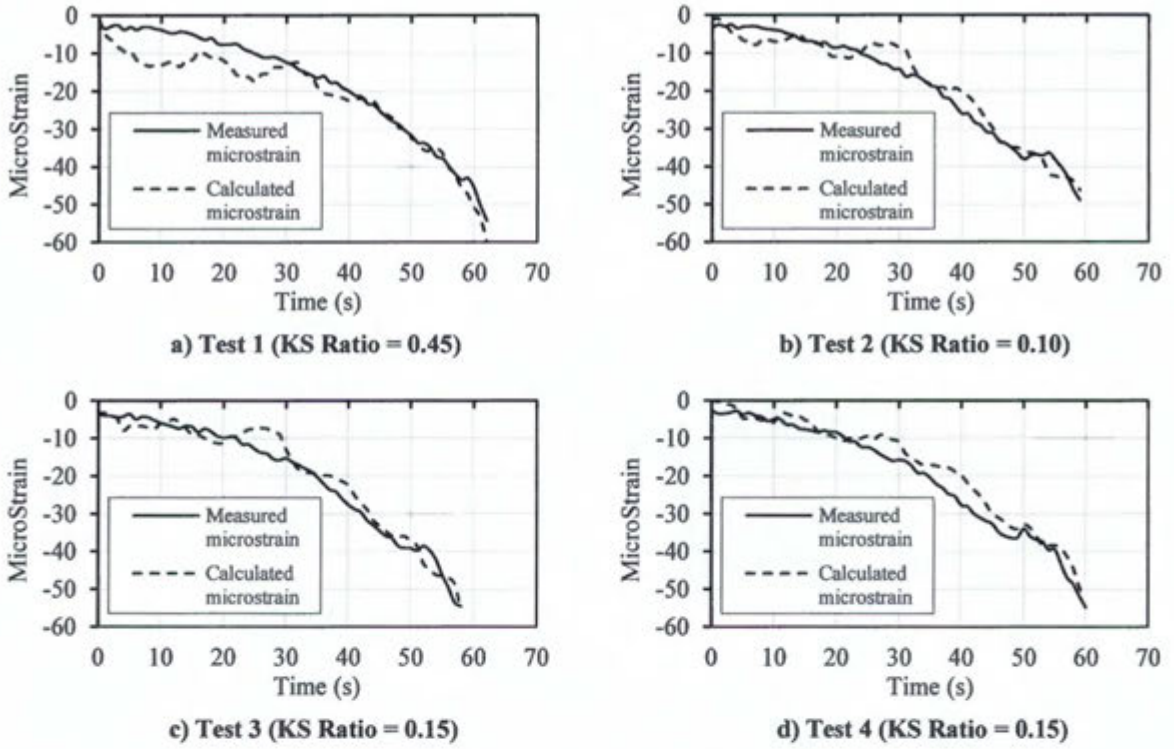

Figure A3-6: Comparing plots of measured strain ε_{Bm} and calculated strain ε_{Bc1}

KS Ratio = $D_{m,n} / D_{m,n,\alpha}$; If KS ratio < 1.0, plot of ε_{Bm} is not significantly different to plot of ε_{Bc1}

Cradle test results

Fig. A3.7a, b and c shows the penetration depths, pressures, and cradle strains recorded during the cradle tests. The core barrel axial strain was not measured during the cradle tests. Therefore, using Eq. A3.2, plots of ε_{Bc1} were generated using the pressure readings from the cradle tests (Fig A3.7d).The ε_C values and ε_{Bc1} values shown in Fig. A3.7c and A3.7d were then plotted against each other (Fig. A3.8) to determine their empirical relationship. The plot shows there to be a strong increasing linear relationship (squared correlation coefficient $r^2 = 0.93$) between ε_C and ε_{Bc1}, approximated by the equation (both strain parameters in microstrain):

$$\varepsilon_{Bc2} = 0.1799(\varepsilon_C) - 12.2633 \qquad (A3.3)$$

The plots of ε_{Bc1} and ε_{Bc2} for each of the five cradle tests were then compared using the KS method to check that Eq. A3.3 approximates ε_{Bc1}, and ultimately ε_{Bm}, with reasonable accuracy. Calculations showed that $D_{m,n} < D_{m,n,\alpha}$ for all four of the KS tests (Fig. A3.9). Taking ε_{Bc2} to represent the core barrel axial strain ε_B, and noting that $F = EA\varepsilon$ from elastic theory, Eq.A3.1 can be derived from Eq. A3.3.

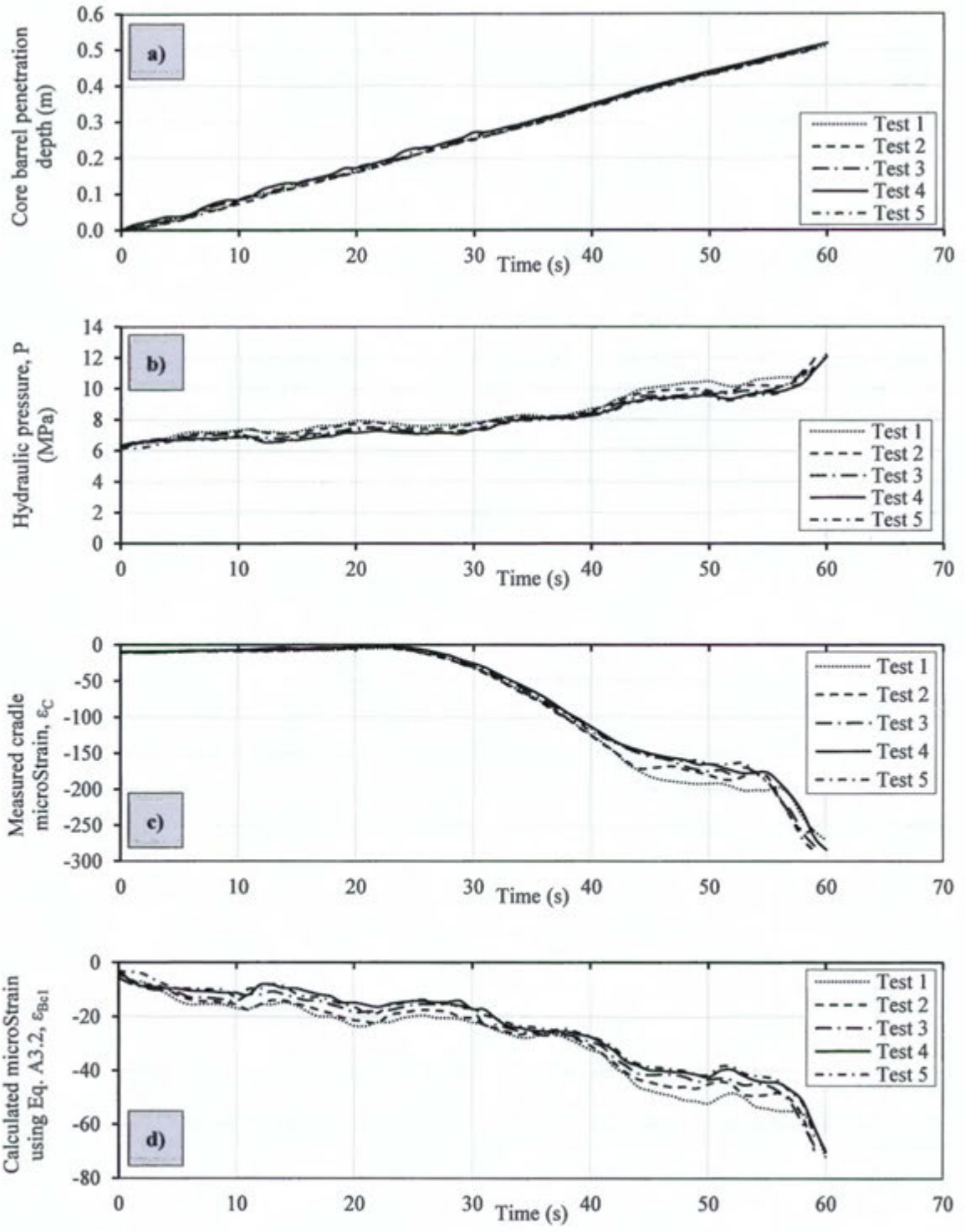

Figure A3-7: Results of cradle tests

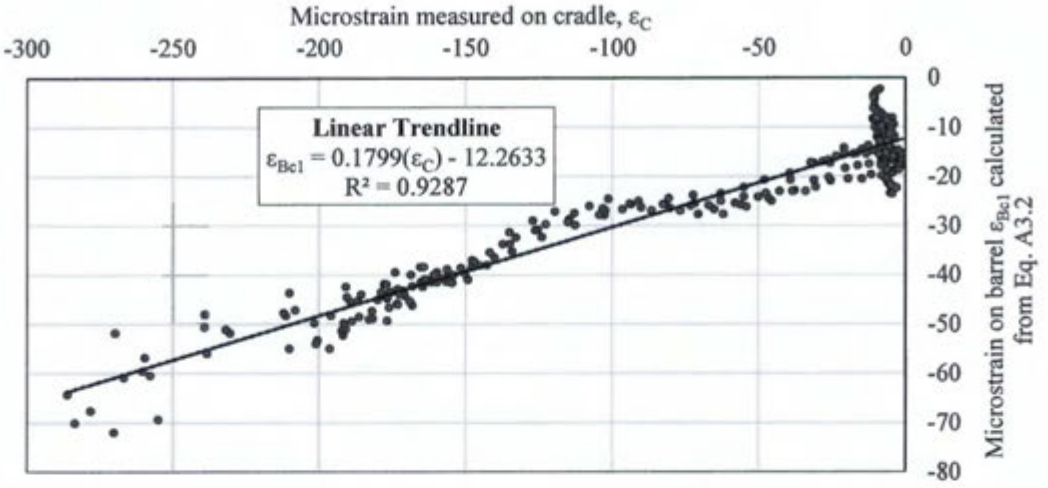

Figure A3-8: Determining the empirical relationship between ε_C and ε_{Bc1}

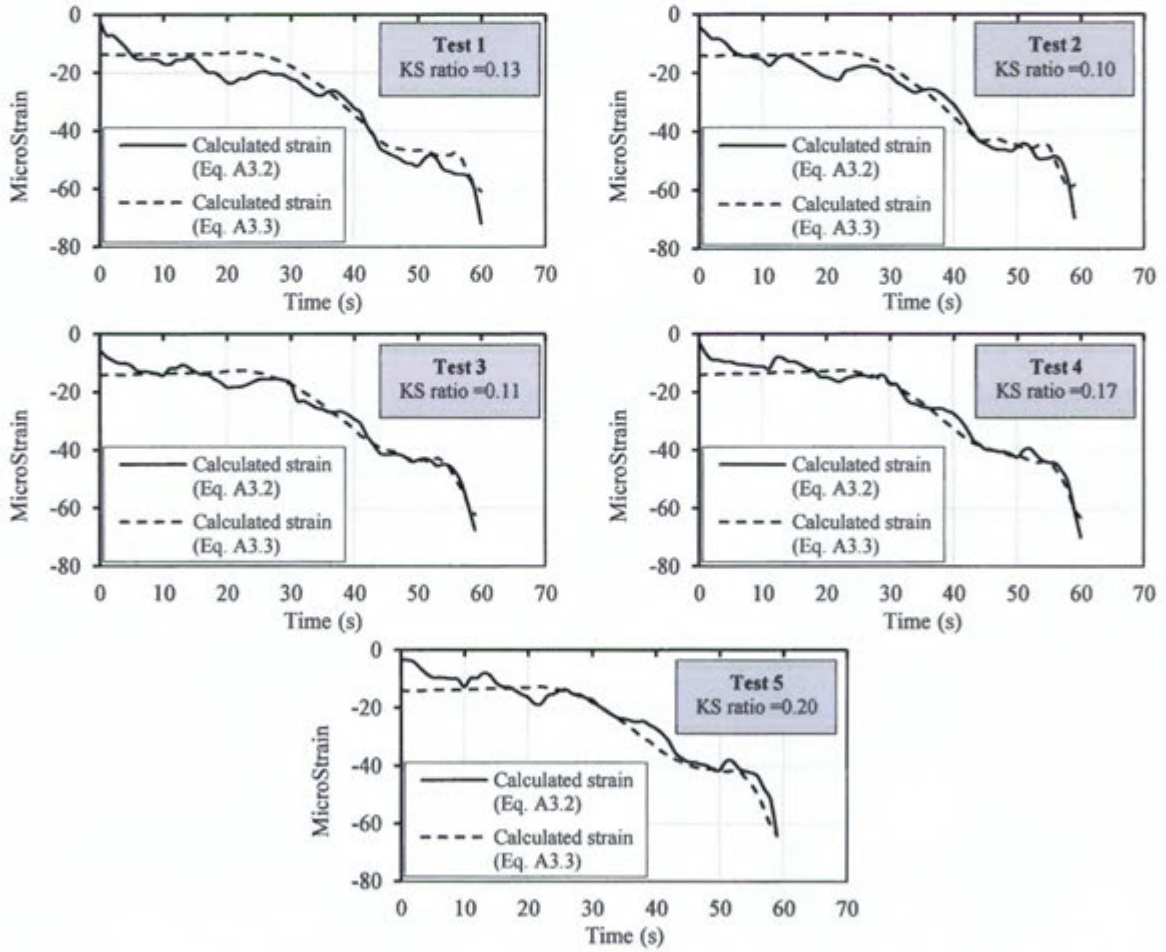

Figure A3-9: Comparing plots of calculated strain ε_{Bc1} and calculated strain ε_{Bc2}

KS Ratio = $D_{m,n} / D_{m,n,a}$; If KS ratio < 1.0, plot of ε_{Bc1} is not significantly different to plot of ε_{Bc2}

Appendix 4

Results of physical SVC testing

Appendix 4

Results of physical SVC testing

SVC Testing Results			Test No.	1	Page 1 of 7
Prepared by	Sam Wegener		Bin no.	3	

Test date	19/08/2015	Conducted by	Oscar Peterson, Gert Raubenheimer, Sam Wegener
Test time	09h10	Location	De Beers Marine R&D Testing Facility, Paarden Eiland

Mass of sample bin (kg)	794.8	Height of soil from top of bin (m)	0.12
Mass of sample bin + gravel (kg)	1958.5	Cable length difference (m)	0.935
Mass of sample bin+gravel+water (kg)	2196.0	Final penetration depth (m)	1.948
Mass of gravel (kg)	1163.7	Recovery at final depth (%)	52.0
Mass of water (kg)	237.5		
Volume of water (voids) , V_v (m^3)	0.238	Average penetration rate (mm/s)	24.3
Volume of gravel (solids), Vs (m^3)	0.479	Average penetration rate (s/m)	41.2
Initial void ratio, V_v/V_s	0.496		
Average specific gravity of particles	2.432		

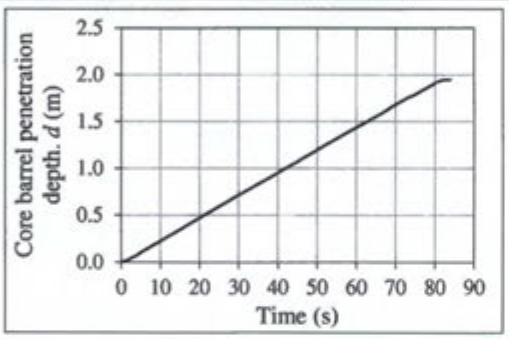

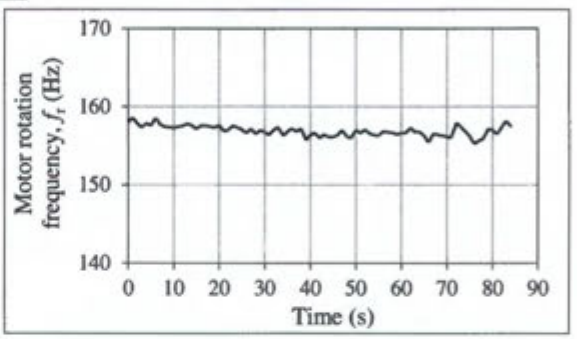

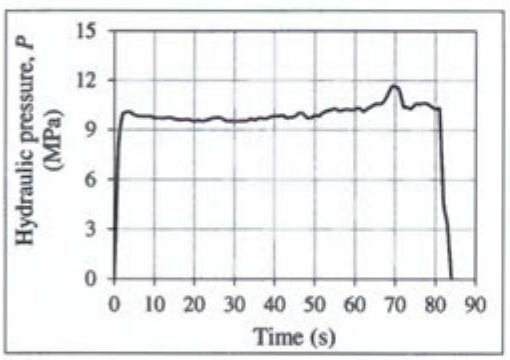

SVC Testing Results			Test No.	3	Page 3 of 7
Prepared by	Sam Wegener		Bin no.	2	

Test date	14/08/2015	Conducted by	Oscar Peterson, Gert Raubenheimer, Sam Wegener
Test time	11h40	Location	De Beers Marine R&D Testing Facility, Paarden Eiland

Mass of sample bin (kg)	801.5	Height of soil from top of bin (m)	0.125
Mass of sample bin + gravel (kg)	1964.0	Cable length difference (m)	0.965
Mass of sample bin+gravel+water (kg)	2204.3	Final penetration depth (m)	1.958
Mass of gravel (kg)	1162.5	Recovery at final depth (%)	50.7
Mass of water (kg)	240.3		
Volume of water (voids) , V_v (m^3)	0.240	Average penetration rate (mm/s)	24.1
Volume of gravel (solids), Vs (m^3)	0.474	Average penetration rate (s/m)	41.5
Initial void ratio, V_v/V_s	0.507		
Average specific gravity of particles	2.452		

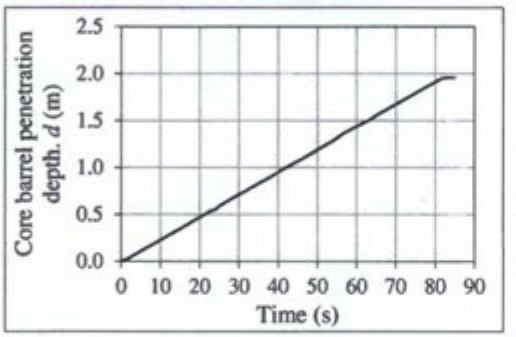

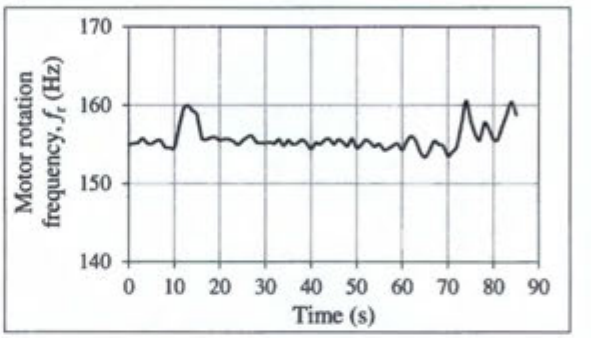

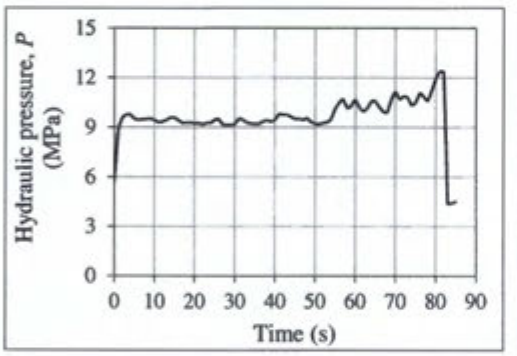

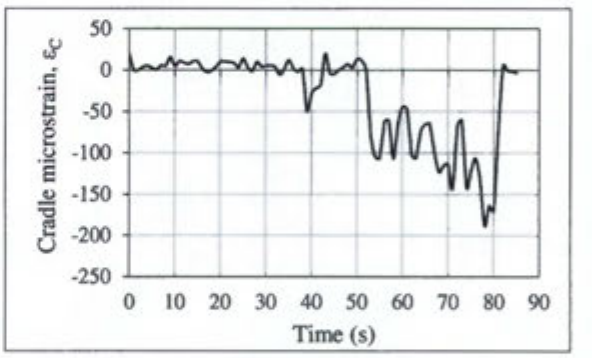

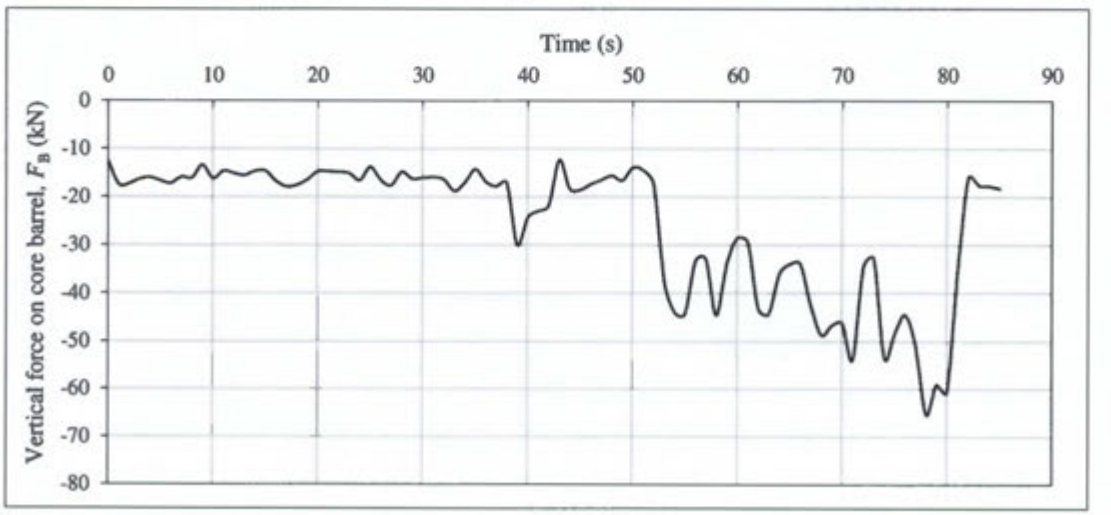

SVC Testing Results			Test No.	5	Page 5 of 7
Prepared by	Sam Wegener		Bin no.	1	

Test date	18/08/2015	Conducted by	Oscar Peterson, Gert Raubenheimer, Sam Wegener
Test time	09h20	Location	De Beers Marine R&D Testing Facility, Paarden Eiland

Mass of sample bin (kg)	793.0	Height of soil from top of bin (m)	0.115
Mass of sample bin + gravel (kg)	2010.2	Cable length difference (m)	0.800
Mass of sample bin+gravel+water (kg)	2240.5	Final penetration depth (m)	1.953
Mass of gravel (kg)	1217.2	Recovery at final depth (%)	59.0
Mass of water (kg)	230.3		
Volume of water (voids) , V_v (m^3)	0.230	Average penetration rate (mm/s)	23.8
Volume of gravel (solids), Vs (m^3)	0.487	Average penetration rate (s/m)	42.1
Initial void ratio, V_v/V_s	0.473		
Average specific gravity of particles	2.498		

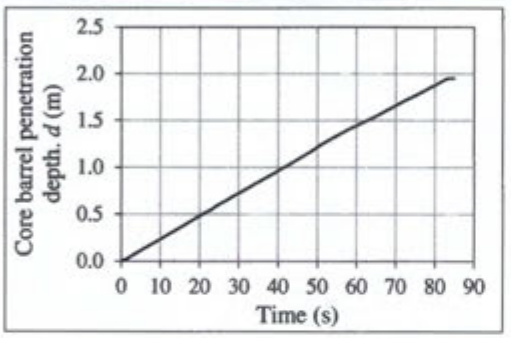

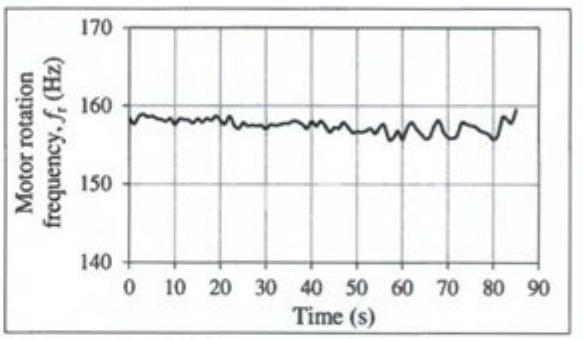

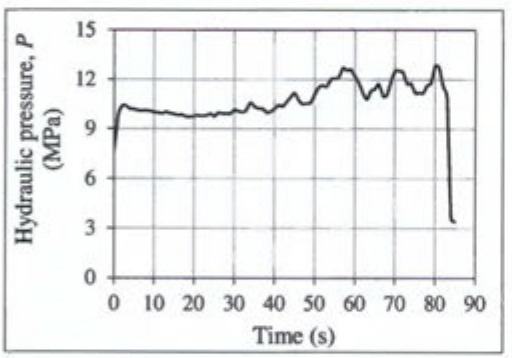

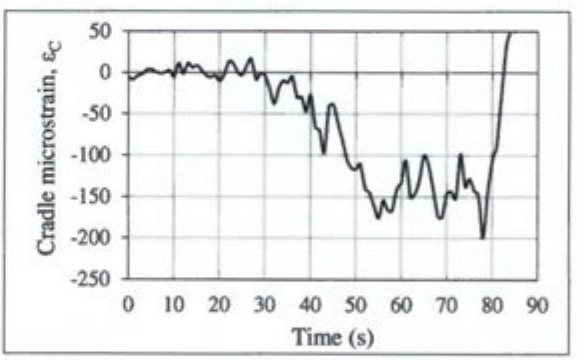

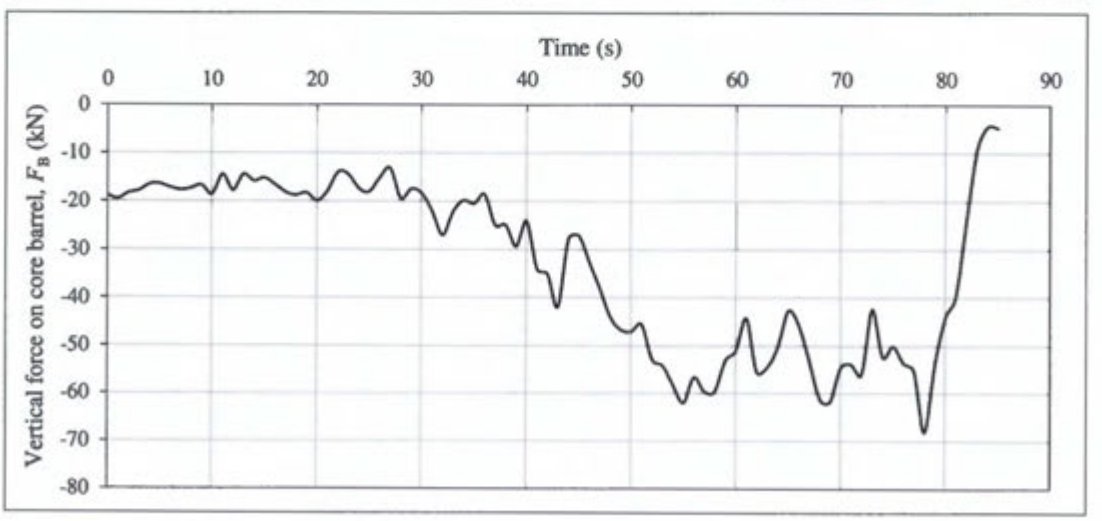

Appendix 4

Results of physical SVC testing

SVC Testing Results			Test No.	7	Page 7 of 7
Prepared by	Sam Wegener		Bin no.	3	

Test date	18/08/2015	Conducted by	Oscar Peterson, Gert Raubenheimer, Sam Wegener
Test time	11h40	Location	De Beers Marine R&D Testing Facility, Paarden Eiland

Mass of sample bin (kg)	795.7	Height of soil from top of bin (m)	0.115
Mass of sample bin + gravel (kg)	1965.8	Cable length difference (m)	1.055
Mass of sample bin+gravel+water (kg)	2220.8	Final penetration depth (m)	1.957
Mass of gravel (kg)	1170.2	Recovery at final depth (%)	46.1
Mass of water (kg)	255.0		
Volume of water (voids) , V_v (m^3)	0.255	Average penetration rate (mm/s)	23.9
Volume of gravel (solids), Vs (m^3)	0.463	Average penetration rate (s/m)	41.9
Initial void ratio, V_v/V_s	0.551		
Average specific gravity of particles	2.530		

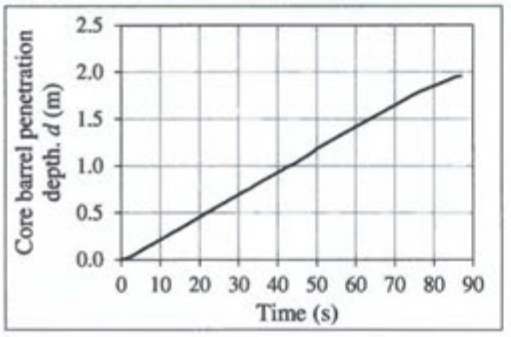

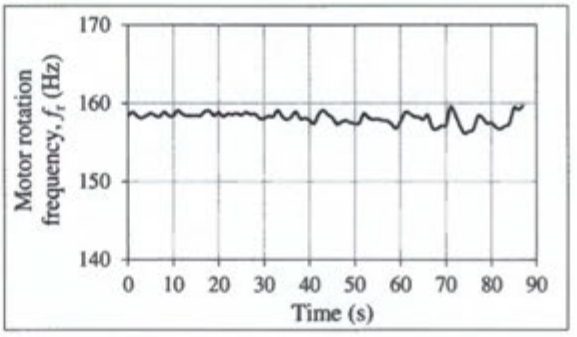

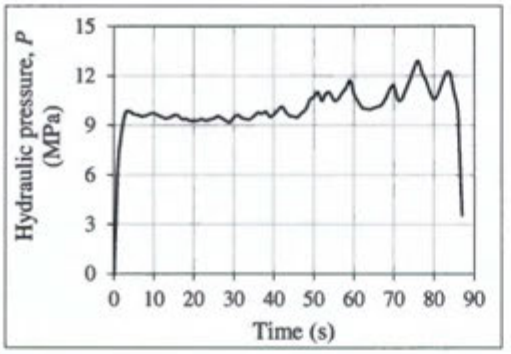

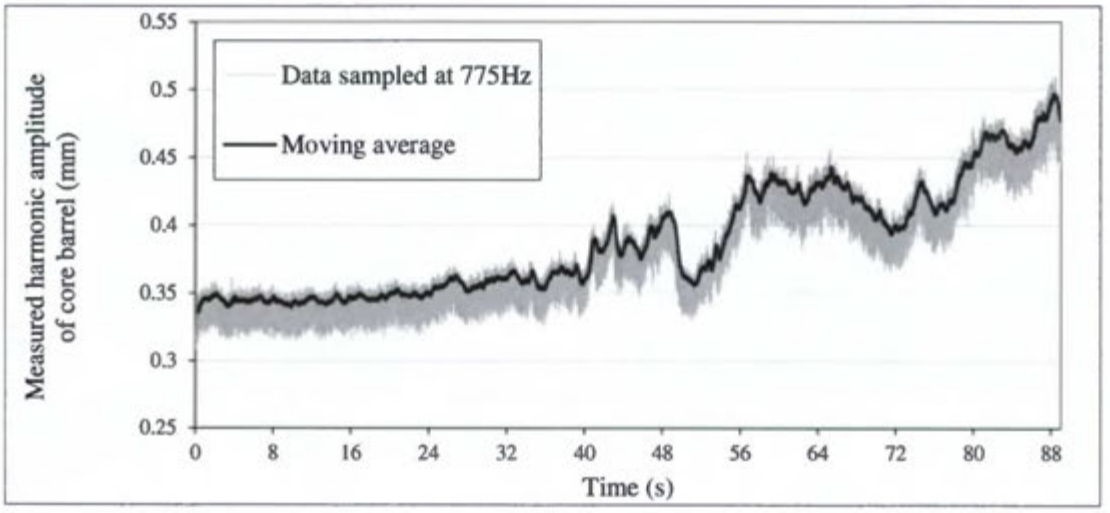

Appendix 5

Description of statistical methods used

This appendix details the statistical methods used to analyse and interpret the various forms of numerical and physical data. The methods defined in this appendix are described fully by Devore (2008) and Yang (2008).

Coefficient of variability

The coefficient of variability C of a sample is defined as the ratio between its standard deviation σ and mean μ. The mean μ and standard deviation σ of a sample are well-known statistical parameters, defined in most statistical texts.

Correlation coefficient

The correlation coefficient r is described by Yang (2008) as a very useful parameter for finding the potential relationship between two sets of data x_i and y_i for two random variables x and y, respectively. If $r = 0$, the two variables are independent – i.e. there is no correlation between them. If $r^2_{x,y} = 1$, then there is a linear relationship between the two variables. If $r_{x,y} = 1$, this indicates an increasing linear relationship, where the increase of one variable will lead to an increase of the other. $r_{x,y} = -1$ indicates a decreasing relationship, where one variable increases while the other variable decreases.

For a set of n data points (x_i, y_i), the correlation coefficient can be calculated by:

$$r = \frac{n\sum_{i=1}^{n} x_i y_i - \sum_{i=1}^{n} x_i \sum_{i=1}^{n} y_i}{\sqrt{\left[n\sum_{i=1}^{n} x_i^2 - \left(\sum_{i=1}^{n} x_i\right)^2\right]\left[n\sum_{i=1}^{n} y_i^2 - \left(\sum_{i=1}^{n} y_i\right)^2\right]}} \qquad (A5.1)$$

Two sample *t*-test

The two sample t-test is a method for testing the null hypothesis to see if the means of two normally distributed samples are equal. In other words, assuming that two pairs of n sample data sets X_i and Y_i are independent and drawn from the same normal distribution, the paired t-test is used to determine whether they are significantly different from each other. The basic steps of a t-test are as follows:

i) Develop the null hypothesis. For a two sample test, the null hypothesis would be H_0: $\mu_X = \mu_Y$.

ii) Calculate the t-test statistic and find the critical value θ for a given confidence interval

iii) If $|t| > \theta$, reject the hypothesis. Otherwise, accept the hypothesis.

For, two samples of equal size n, the t-variable is defined by

$$t = \frac{(\bar{X} - \bar{Y})}{S_d / \sqrt{n}} \qquad (A5.2)$$

where S_d is the combined sample variance given by

$$S_d = \sqrt{\frac{1}{n-1} \sum_{i=1}^{n} (\tilde{X}_i - \tilde{Y}_i)^2} \qquad (A5.3)$$

and $\tilde{X}_i = X_i - \bar{X}$ and $\bar{Y}_i = Y_i - \bar{Y}$

Appendix 6

Preliminary DEM study: Effect of particle shape on computation time

Preliminary DEM study: The Effect of Particle Shape on Computation Time

Results of a series of preliminary DEM models developed to quantify the influence of particle shape type on computation time - Conducted using Rocky DEM Software - Page 1 of 4

ROUNDED POLYHEDRONS

Influence of No. of Corners on Computation Run-time

Particle shape type	Rounded polyhedron	VAR/HAR	1.14/0.70
Size (mm)/In-flow rate (kg/s)	100/100	Smoothness	1.00
Rolling resistance	0.3	Superquadric degree	6.200

Test	No. corners	No. particles	Run-time (s)	Run-time/Particles
1	5	456	105.007	0.230
2	8	347	101.583	0.293
3	11	307	104.657	0.341
4	14	290	116.656	0.402
5	17	280	119.632	0.427
6	20	272	136.256	0.501
7	30	260	190.991	0.735
8	40	254	209.407	0.824

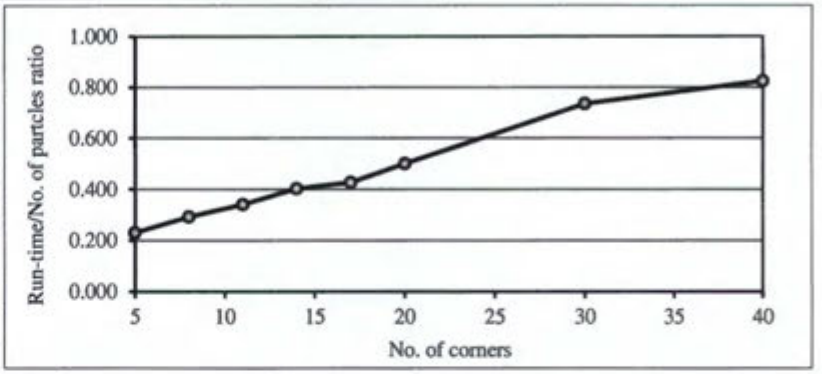

Influence of Superquadric Degree on Computation Run-time

Particle shape type	Rounded polyhedron	VAR/HAR	1.14/0.70
Size (mm)/In-flow rate (kg/s)	100/100	Smoothness	1.00
Rolling resistance	0.3	No. of corners	15

Test	SQD	No. particles	Run-time (s)	Run-time/Particles
1	2.00	362	145.84	0.403
2	3.40	317	122.73	0.387
3	4.80	297	113.449	0.382
4	6.20	285	102.458	0.360
5	7.60	278	104.912	0.377
6	9.00	273	98.234	0.360
7	10.40	269	96.032	0.357
8	12.00	266	88.584	0.333

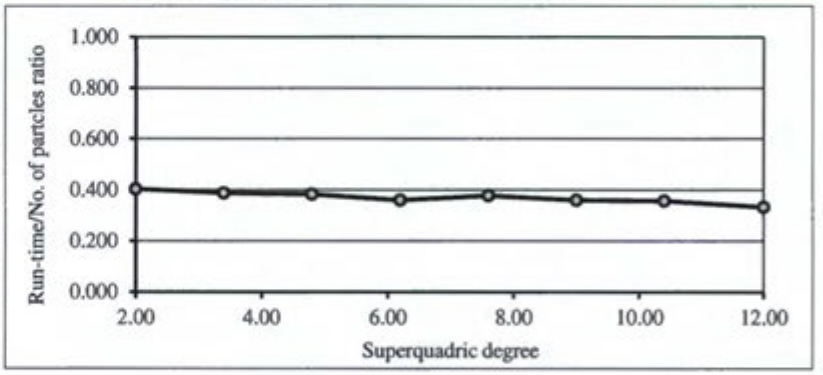

Influence of Smoothness on Computation Run-time

Particle shape type	Rounded polyhedron	VAR/HAR	1.14/0.70
Size (mm)/In-flow rate (kg/s)	100/100	Superquadric degree	7.00
Rolling resistance	0.3	No. of corners	20

Test	Smooth-ness	No. particles	Run-time (s)	Run-time/Particles
1	0.100	277	123.789	0.447
2	0.230	282	113.641	0.403
3	0.350	283	116.451	0.411
4	0.480	282	113.700	0.403
5	0.600	279	124.825	0.447
6	0.730	275	114.991	0.418
7	0.850	271	111.649	0.412
8	1.000	268	107.986	0.403

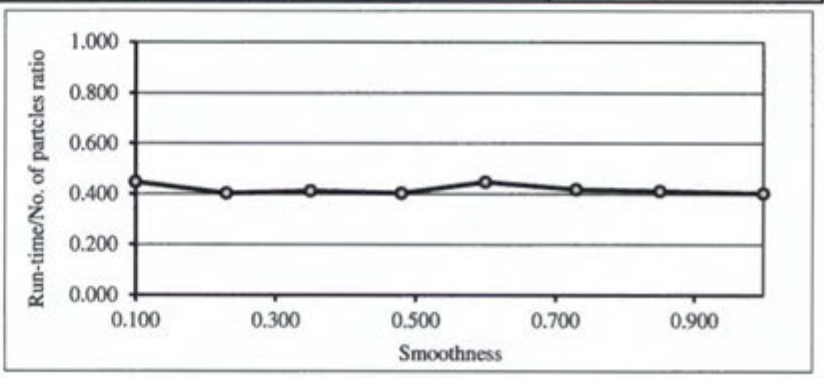

Preliminary DEM study: The Effect of Particle Shape on Computation Time

Results of a series of preliminary DEM models developed to quantify the influence of particle shape type on computation time - Conducted using Rocky DEM Software - Page 3 of 4

ROUNDED CYLINDERS

Influence of Vertical aspect ratio on Computation Run-time

Particle shape type	Rounded cylinder
Size (mm)/In-flow rate (kg/s)	100/100
Rolling resistance	0.3

Test	VAR	No. particles	Run-time (s)	Run-time/Particles
1	1.05	259	22.945	0.089
2	1.10	242	21.527	0.089
3	1.15	227	16.975	0.075
4	1.20	214	17.785	0.083
5	1.25	203	18.344	0.090
6	1.30	192	15.821	0.082
7	1.35	183	15.007	0.082
8	1.40	174	14.904	0.086

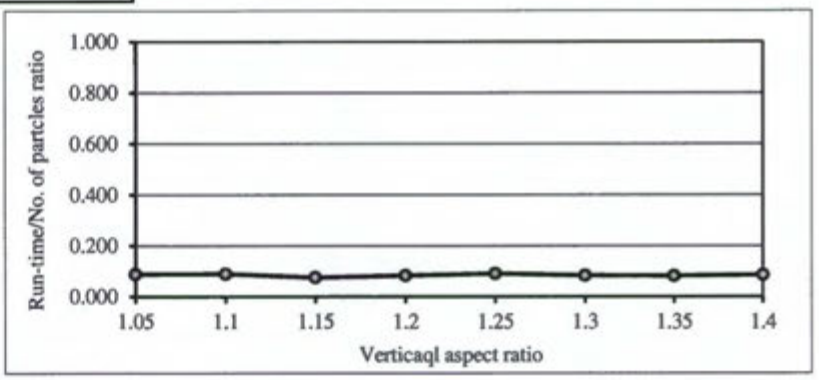

FACETED

Influence of No. of corners on Computation Run-time

Particle shape type	Faceted	VAR/HAR	1.14/0.70
Size (mm)/In-flow rate (kg/s)	100/100	Smoothness	na
Rolling resistance	0.3	Superquadric degree	5.000

Test	No. corners	No. particles	Run-time (s)	Run-time/Particles
1	10	460	165.451	0.360
2	14	603	300.83	0.499
3	18	574	303.802	0.529
4	22	557	356.584	0.640
5	26	548	392.389	0.716
6	30	534	421.013	0.788
7	34	468	360.099	0.769
8	38	486	461.62	0.950

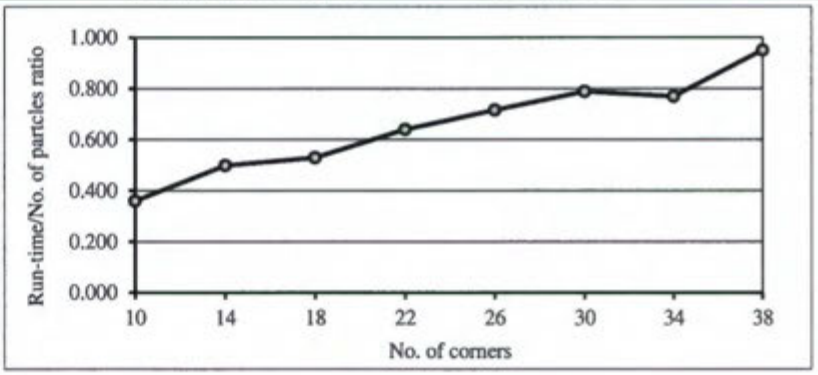

Influence of Superquadric Degree on Computation Run-time

Particle shape type	Faceted	VAR/HAR	1.14/0.70
Size (mm)/In-flow rate (kg/s)	100/100	Smoothness	na
Rolling resistance	0.3	No. of corners	15

Test	SQD	No. particles	Run-time (s)	Run-time/Particles
1	2.00	504	253.898	0.504
2	3.40	504	251.036	0.498
3	4.80	566	286.202	0.506
4	12.00	700	390.19	0.557

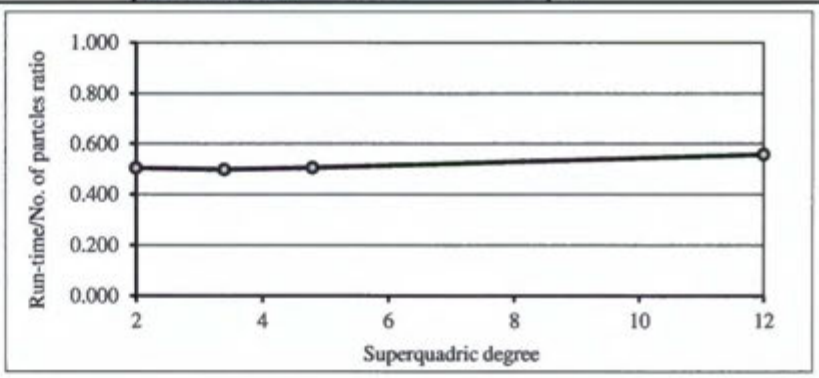

Appendix 7

Preliminary DEM study: Effect of particle size on variance in results

Considering the extensive computation time of a DEM model, it was of practical value to estimate the particle size at which multiple simulations of the same model would produce insignificantly different results. Therefore, a series of DEM models were computed to approximate the particle size at which the statistical difference between core barrel force-penetration plots of two identically assembled models became negligible.

Three particle diameter sizes were considered: 100mm, 82mm, and 64mm. For each particle size, three models – all of identical soil parameters and boundary conditions – were computed. Input parameters for all nine of these models are specified below in Table A7.1, A7.2 and A7.3. The modelled particle shapes are shown in Figure A7.1. It must be emphasized that the micro-investigation detailed in this appendix was concerned more with the effect of particle size on the variance in numerical results, rather than the actual quantitative results of the modelling process.

Table A7-1: Properties of SVC and boundary conditions

Parameter	Value/Description
Geometry of sample bin, core barrel, and cutter head	Same as that described in Section 15.2
Penetration rate of core barrel	15mm/s
Frequency of SVC vibratory motion	170Hz
Amplitude of SVC vibratory motion	0.18mm (Estimated value)
Final penetration depth	2.0m

Table A7-2: Particle properties

Parameter	Value
Particle rolling resistance	0.25
Particle specific gravity	1.375
Particle stiffness	30×10^6 N/m^2
Static/Dynamic friction between particles	0.55/0.50
Static/Dynamic friction between particles and core barrel	0.70/0.50
Static/Dynamic friction between particles and sample bin	0.75/0.55

Table A7-3: Definition of particle shape types in Rocky

Roundness	% of particle shape type in modelled soil mass		Particle shape type in Rocky	VAR	HAR	Smoothness	No. of corners	SQD
AH	2.00		Rounded polyhedron	1.00	1.00	0.25	7	2
AM	6.50	10	Rounded polyhedron	1.35	0.85	0.25	7	2
AL	1.50		Rounded polyhedron	1.70	0.70	0.25	7	2
SAH	4.00		Rounded polyhedron	1.00	1.00	0.50	9	2
SAM	13.00	20	Rounded polyhedron	1.35	0.85	0.50	9	2
SAL	3.00		Rounded polyhedron	1.70	0.70	0.50	9	2
SRH	4.00		Rounded polyhedron	1.00	1.00	1.00	4	2
SRM	13.00	20	Rounded polyhedron	1.35	0.85	1.00	4	2
SRL	3.00		Rounded polyhedron	1.70	0.70	1.00	4	2
RH	10.00		Sphere	*na*	*na*	*na*	*na*	*na*
RM	32.50	50	Rounded polygon	1.35	0.70	*na*	10	*na*
RL	7.50		Rounded polygon	1.50	0.50	*na*	10	*na*

Figure A7-1: Sample of modelled soil mass

Figure A7.2 presents modelling results for the effect of particle size on cumulative recovery ratio (RR). There is no clear trend between particle diameter and RR. However, the variance in RR values for each particle size does clearly decrease.

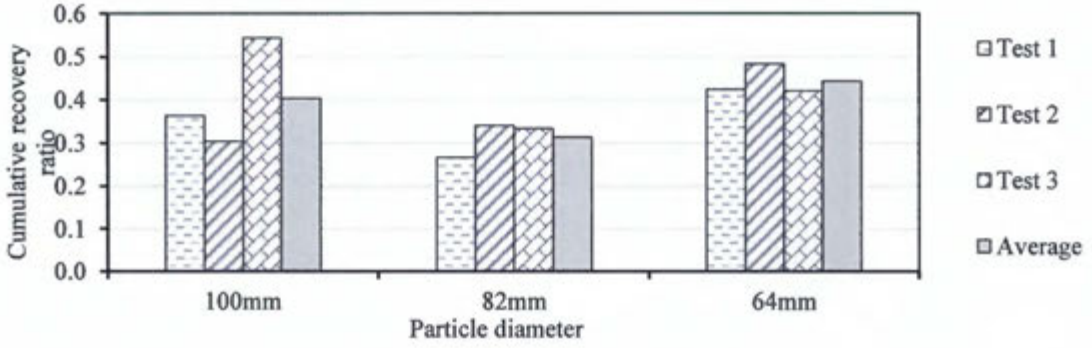

Figure A7-2: The effect of particle size on cumulative recovery ratio

Using the results shown in Figure A7.2, this decrease in variance was quantified by calculating the coefficient of variability C for each of the three sets of recovery ratios (Figure A7.3). The correlation coefficient between particle diameter and C was calculated to be 0.95, indicating a strong increasing linear relationship.

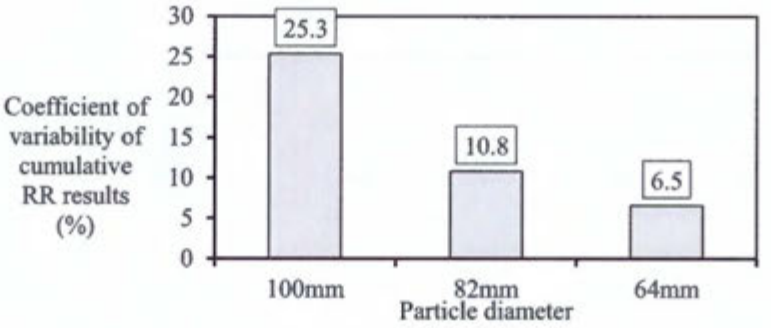

Figure A7-3: The influence of particle size on C of recovery ratio results

Figure A7.4 shows, for each particle size, the change in vertical force acting on the core barrel due to an increase in penetration depth. Results clearly show a) a decrease in force with decreasing particle size, and b) a decrease in variance in results with decreasing particle size.

To determine conclusively whether the variance in results of a given particle size was negligible, the two sample Kolmogorov-Smirnov (KS) method was used. Three KS tests were conducted for the set of results for each particle size, in which the core barrel force-displacement plots for Test 1 and 2, Test 1 and 3, and Test 2 and 3 were successively compared. The statistical sample size for every test was large, with $n = 2668$. This was due to Rocky software providing results data every 0.05s of simulation time. Therefore, $D_{m,n,\alpha} = 0.037$ for all KS tests (95% confidence). If $D_{m,n} > D_{m,n,\alpha}$ for any KS test (Eqns. 13.1 and 13.2, Section 13.1.1), the results of the respective particle size were deemed to have significant variance. Figure A7.5 shows that only for the 64mm particle size are all $D_{m,n} < D_{m,n,\alpha}$. Therefore, for the particle properties and boundary conditions specified in Tables A7.1-3, the variance in results for Rocky models consisting of particles sizes $\leq$ 64mm may be considered negligible.

Conclusions drawn from this micro-investigation should be considered limited to the specified boundary conditions and particle properties. It is worth noting that the computation time for the models of 64mm diameter particles was close to 13 hours. These models contained approximately 4000 discrete particles.

100mm particle size

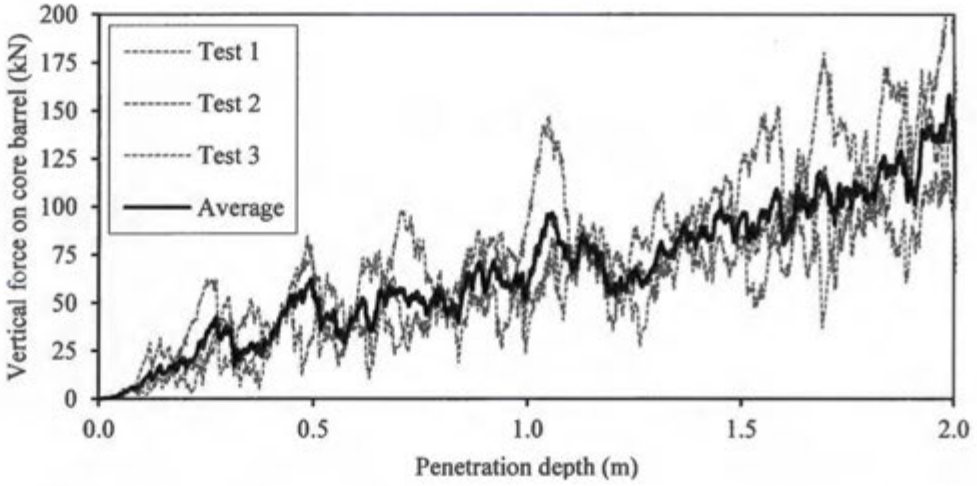

82mm particle size

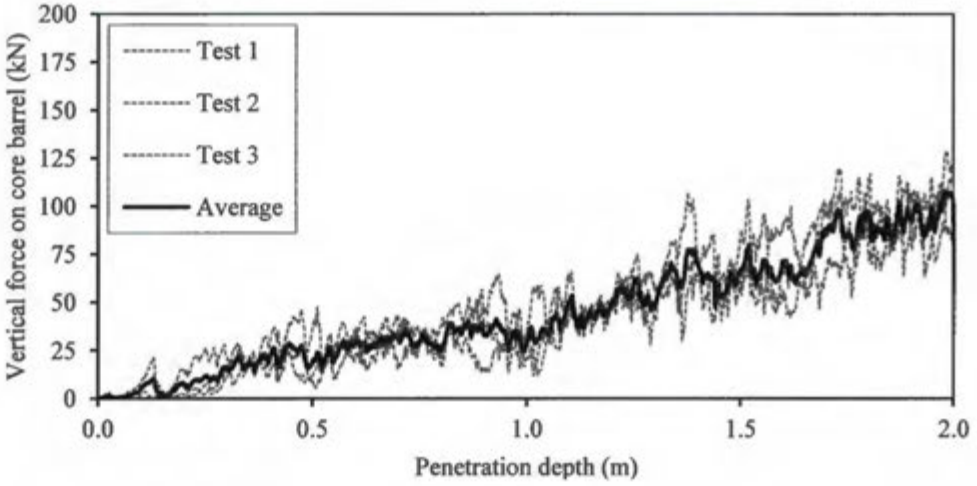

64mm particle size

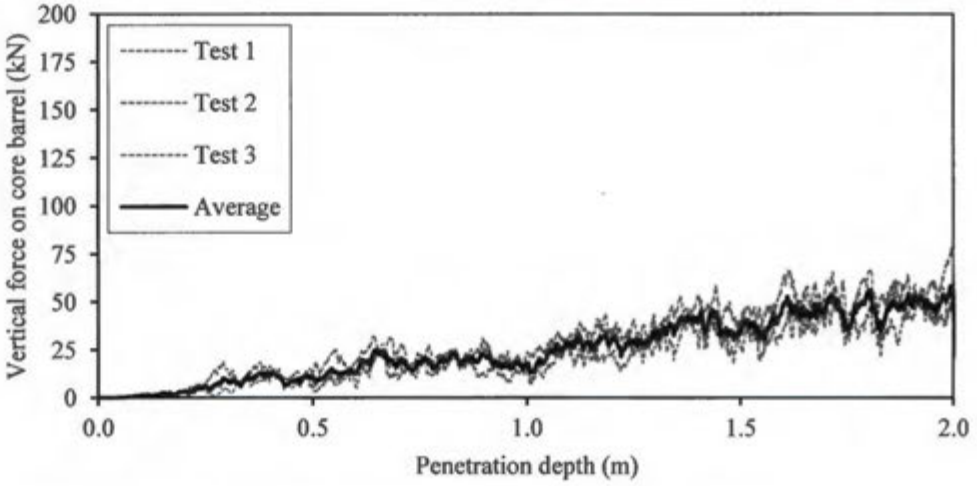

Figure A7-4: Numerical results for force-penetration plots

100mm, 82mm, and 64mm particles

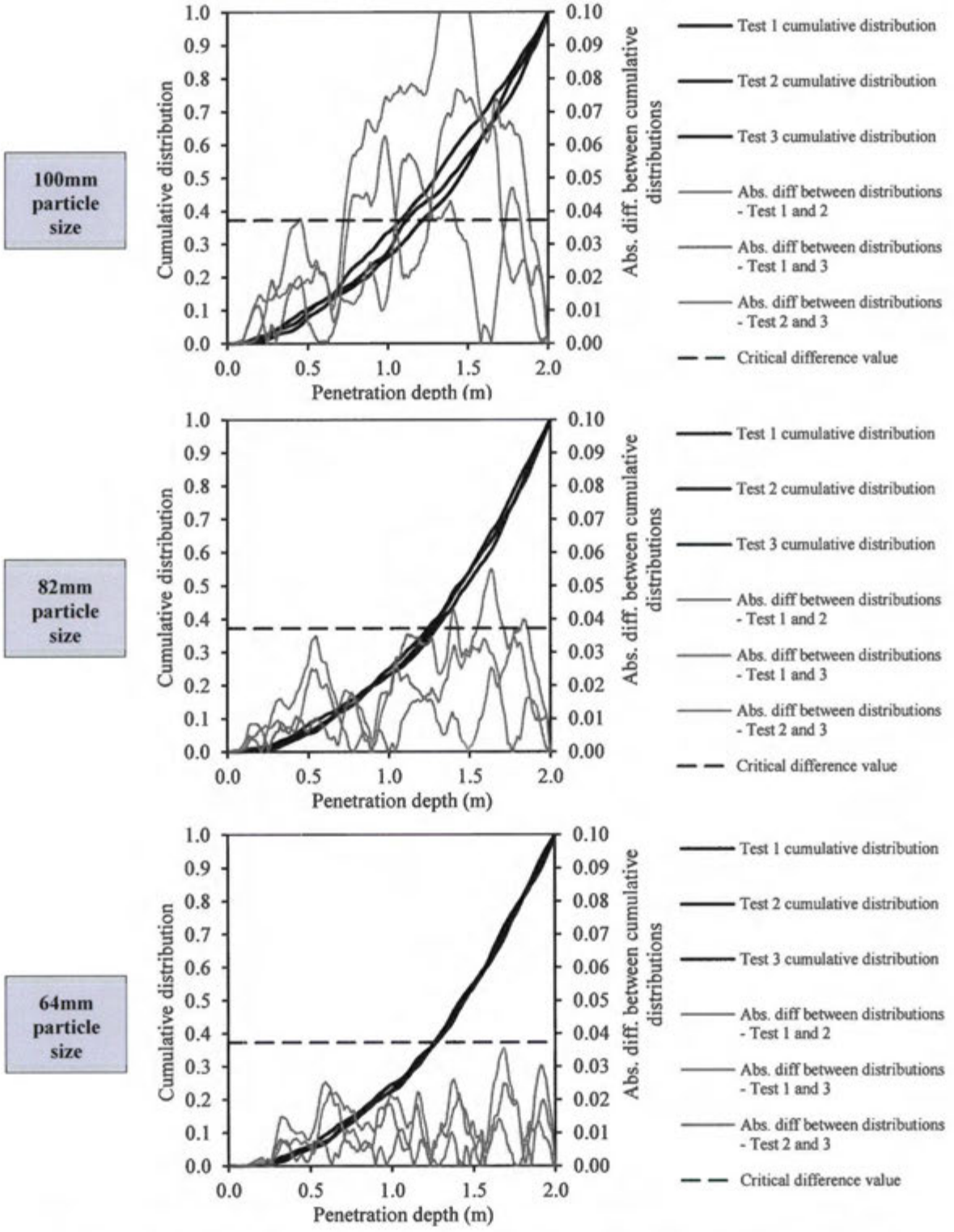

Figure A7-5: Results of KS tests comparing numerical force-penetration results

100mm, 82mm, and 64mm particle sizes

Appendix 8

Overview of strain gauge theory

National Instruments Corporation (2014)

NATIONAL INSTRUMENTS™

Application Note 078

Strain Gauge Measurement – A Tutorial

What is Strain?

Strain is the amount of deformation of a body due to an applied force. More specifically, strain (ε) is defined as the fractional change in length, as shown in Figure 1 below.

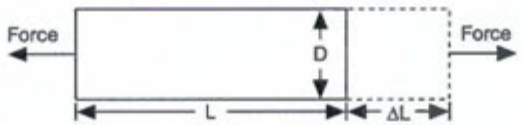

$$\varepsilon = \frac{\Delta L}{L}$$

Figure 1. Definition of Strain

Strain can be positive (tensile) or negative (compressive). Although dimensionless, strain is sometimes expressed in units such as in./in. or mm/mm. In practice, the magnitude of measured strain is very small. Therefore, strain is often expressed as microstrain (με), which is $\varepsilon \times 10^{-6}$.

When a bar is strained with a uniaxial force, as in Figure 1, a phenomenon known as Poisson Strain causes the girth of the bar, D, to contract in the transverse, or perpendicular, direction. The magnitude of this transverse contraction is a material property indicated by its Poisson's Ratio. The Poisson's Ratio ν of a material is defined as the negative ratio of the strain in the transverse direction (perpendicular to the force) to the strain in the axial direction (parallel to the force), or $\nu = -\varepsilon_T/\varepsilon$. Poisson's Ratio for steel, for example, ranges from 0.25 to 0.3.

The Strain Gauge

While there are several methods of measuring strain, the most common is with a strain gauge, a device whose electrical resistance varies in proportion to the amount of strain in the device. For example, the piezoresistive strain gauge is a semiconductor device whose resistance varies nonlinearly with strain. The most widely used gauge, however, is the bonded metallic strain gauge.

The metallic strain gauge consists of a very fine wire or, more commonly, metallic foil arranged in a grid pattern. The grid pattern maximizes the amount of metallic wire or foil subject to strain in the parallel direction (Figure 2). The cross sectional area of the grid is minimized to reduce the effect of shear strain and Poisson Strain. The grid is bonded to a thin backing, called the carrier, which is attached directly to the test specimen. Therefore, the strain experienced by the test specimen is transferred directly to the strain gauge, which responds with a linear change in electrical resistance. Strain gauges are available commercially with nominal resistance values from 30 to 3000 Ω, with 120, 350, and 1000 Ω being the most common values.

341023C-01 *August 1998*

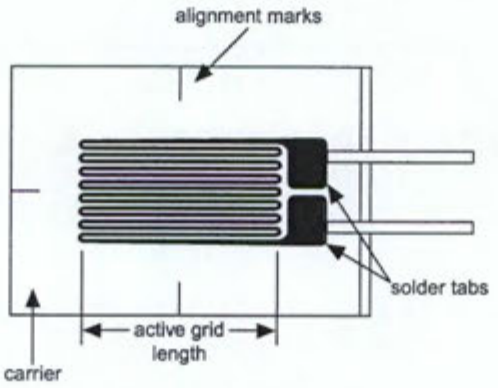

Figure 2. Bonded Metallic Strain Gauge

It is very important that the strain gauge be properly mounted onto the test specimen so that the strain is accurately transferred from the test specimen, though the adhesive and strain gauge backing, to the foil itself. Manufacturers of strain gauges are the best source of information on proper mounting of strain gauges.

A fundamental parameter of the strain gauge is its sensitivity to strain, expressed quantitatively as the gauge factor (GF). Gauge factor is defined as the ratio of fractional change in electrical resistance to the fractional change in length (strain):

$$GF = \frac{\Delta R/R}{\Delta L/L} = \frac{\Delta R/R}{\varepsilon}$$

The Gauge Factor for metallic strain gauges is typically around 2.

Ideally, we would like the resistance of the strain gauge to change only in response to applied strain. However, strain gauge material, as well as the specimen material to which the gauge is applied, will also respond to changes in temperature. Strain gauge manufacturers attempt to minimize sensitivity to temperature by processing the gauge material to compensate for the thermal expansion of the specimen material for which the gauge is intended. While compensated gauges reduce the thermal sensitivity, they do not totally remove it. For example, consider a gauge compensated for aluminum that has a temperature coefficient of 23 ppm/°C. With a nominal resistance of 1000 Ω, GF = 2, the equivalent strain error is still 11.5 με/°C. Therefore, additional temperature compensation is important.

Strain Gauge Measurement

In practice, the strain measurements rarely involve quantities larger than a few millistrain ($\varepsilon \times 10^{-3}$). Therefore, to measure the strain requires accurate measurement of very small changes in resistance. For example, suppose a test specimen undergoes a substantial strain of 500 με. A strain gauge with a gauge factor GF = 2 will exhibit a change in electrical resistance of only $2 \bullet (500 \times 10^{-6}) = 0.1\%$. For a 120 Ω gauge, this is a change of only 0.12 Ω.

To measure such small changes in resistance, and compensate for the temperature sensitivity discussed in the previous section, strain gauges are almost always used in a bridge configuration with a voltage or current excitation source. The general Wheatstone bridge, illustrated below, consists of four resistive arms with an excitation voltage, V_{EX}, that is applied across the bridge.

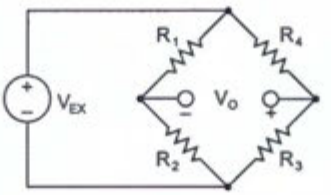

Figure 3. Wheatstone Bridge

The output voltage of the bridge, V_O, will be equal to:

$$V_O = \left[\frac{R_3}{R_3 + R_4} - \frac{R_2}{R_1 + R_2}\right] \bullet V_{EX}$$

From this equation, it is apparent that when $R_1/R_2 = R_{G1}/R_{G2}$, the voltage output V_O will be zero. Under these conditions, the bridge is said to be *balanced*. Any change in resistance in any arm of the bridge will result in a nonzero output voltage.

Therefore, if we replace R_4 in Figure 3 with an active strain gauge, any changes in the strain gauge resistance will unbalance the bridge and produce a nonzero output voltage. If the nominal resistance of the strain gauge is designated as R_G, then the strain-induced change in resistance, ΔR, can be expressed as $\Delta R = R_G \bullet GF \bullet \varepsilon$. Assuming that $R_1 = R_2$ and $R_3 = R_G$, the bridge equation above can be rewritten to express V_O/V_{EX} as a function of strain (see Figure 4). Note the presence of the $1/(1+GF \bullet \varepsilon/2)$ term that indicates the nonlinearity of the quarter-bridge output with respect to strain.

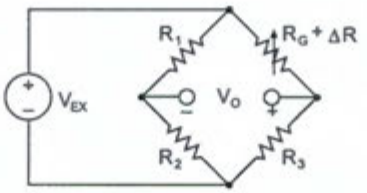

$$\frac{V_O}{V_{EX}} = -\frac{GF \bullet \varepsilon}{4}\left(\frac{1}{1 + GF \bullet \frac{\varepsilon}{2}}\right)$$

Figure 4. Quarter-Bridge Circuit

By using *two* strain gauges in the bridge, the effect of temperature can be avoided. For example, Figure 5 illustrates a strain gauge configuration where one gauge is active ($R_G + \Delta R$), and a second gauge is placed transverse to the applied strain. Therefore, the strain has little effect on the second gauge, called the dummy gauge. However, any changes in temperature will affect both gauges in the same way. Because the temperature changes are identical in the two gauges, the ratio of their resistance does not change, the voltage V_O does not change, and the effects of the temperature change are minimized.

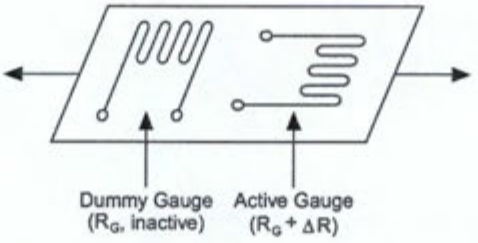

Figure 5. Use of Dummy Gauge to Eliminate Temperature Effects

Alternatively, you can double the sensitivity of the bridge to strain by making both gauges active, although in different directions. For example, Figure 6 illustrates a bending beam application with one bridge mounted in tension ($R_G + \Delta R$) and the other mounted in compression ($R_G - \Delta R$). This half-bridge configuration, whose circuit diagram is also illustrated in Figure 6, yields an output voltage that is linear and approximately doubles the output of the quarter-bridge circuit.

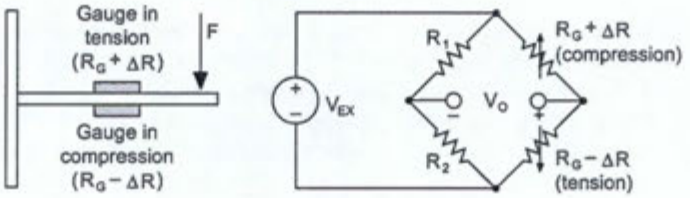

$$\frac{V_O}{V_{EX}} = -\frac{GF \bullet \varepsilon}{2}$$

Figure 6. Half-Bridge Circuit

Finally, you can further increase the sensitivity of the circuit by making all four of the arms of the bridge active strain gauges, and mounting two gauges in tension and two gauges in compression. The full-bridge circuit is shown in Figure 7 below.

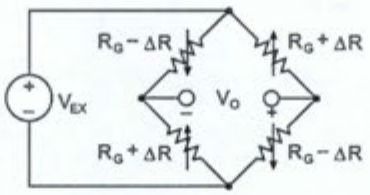

$$\frac{V_O}{V_{EX}} = -GF \bullet \varepsilon$$

Figure 7. Full-Bridge Circuit

The equations given here for the Wheatstone bridge circuits assume an initially balanced bridge that generates zero output when no strain is applied. In practice however, resistance tolerances and strain induced by gauge application will generate some initial offset voltage. This initial offset voltage is typically handled in two ways. First, you can use a special offset-nulling, or balancing, circuit to adjust the resistance in the bridge to rebalance the bridge to zero output. Alternatively, you can measure the initial unstrained output of the circuit and compensate in software. At the end of this application note, you will find equations for quarter, half, and full bridge circuits that express strain that take initial output voltages into account. These equations also include the effect of resistance in the lead wires connected to the gauges.

Lead Wire Resistance

The figures and equations in the previous section ignore the resistance in the lead wires of the strain gauge. While ignoring the lead resistances may be beneficial to understanding the basics of strain gauge measurements, doing so in practice can be very dangerous. For example, consider the two-wire connection of a strain gauge shown in Figure 8a. Suppose each lead wire connected to the strain gauge is 15 m long with lead resistance R_L equal to 1 Ω. Therefore, the lead resistance adds 2 Ω of resistance to that arm of the bridge. Besides adding an offset error, the lead resistance also desensitizes the output of the bridge. From the strain equations at the end of this application note, you can see that the amount of desensitization is quantified by the term $(1 + R_L/R_G)$. You can compensate for this error by measuring the lead resistance R_L and using the measured value in the strain equations. However, a more difficult problem arises from changes in the lead resistance due to temperature changes. Given typical temperature coefficients for copper wire, a slight change in temperature can generate a measurement error of several με.

Therefore, the preferred connection scheme for quarter-bridge strain gauges is the three-wire connection, shown in Figure 8b. In this configuration, R_{L1} and R_{L3} appear in adjacent arms of the bridge. Therefore, any changes in resistance due to temperature cancel each other. The lead resistance in the third lead, R_{L2}, is connected to the measurement input. Therefore, this lead carries very little current and the effect of its lead resistance is negligible.

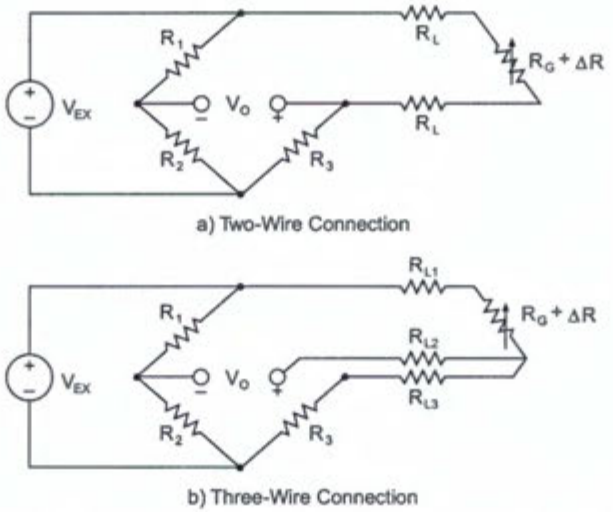

Figure 8. Two-Wire and Three-Wire Connections of Quarter-Bridge Circuit

Signal Conditioning for Strain Gauges

Strain gauge measurement involves sensing extremely small changes in resistance. Therefore, proper selection and use of the bridge, signal conditioning, wiring, and data acquisition components are required for reliable measurements.

Bridge Completion – Unless you are using a full-bridge strain gauge sensor with four active gauges, you will need to complete the bridge with reference resistors. Therefore, strain gauge signal conditioners typically provide half-bridge completion networks consisting of two high-precision reference resistors. Figure 9 diagrams the wiring of a half-bridge strain gauge circuit to a conditioner with completion resistors R_1 and R_2. The nominal resistance of the completion resistors is less important than how well the two resistors are matched. Ideally, the resistors are well matched and provide a stable reference voltage of $V_{EX}/2$ to the negative input lead of the measurement channel. For example, the half-bridge completion resistors provided on the SCXI-1122 signal conditioning module are 2.5 kΩ resistors a ratio tolerance of 0.02%. The high resistance of the completion resistors helps minimize the current draw from the excitation voltage.

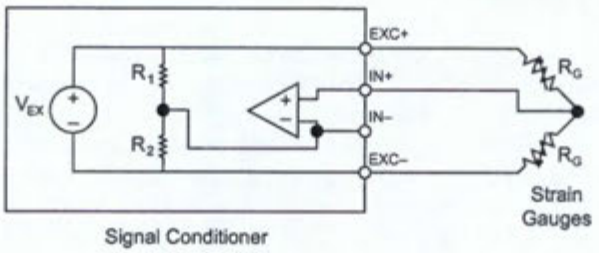

Figure 9. Connection of Half-Bridge Strain Gauge Circuit

Bridge Excitation – Strain gauge signal conditioners typically provide a constant voltage source to power the bridge. While there is no standard voltage level that is recognized industry wide, excitation voltage levels of around 3 V and 10 V are common. While a higher excitation voltage generates a proportionately higher output voltage, the higher voltage can also cause larger errors due to self-heating. Again, it is very important that the excitation voltage be very accurate and stable. Alternatively, one can use a less accurate or stable voltage, and accurately measure, or sense, the excitation voltage so the correct strain can be calculated.

Excitation Sensing – If the strain gauge circuit is located a distance away from the signal conditioner and excitation source, a possible source of error is voltage drops caused by resistance in the wires connecting the excitation voltage to the bridge. Therefore, some signal conditioners include a feature called *remote sensing* to compensate for this error. There are two common methods of remote sensing. With feedback remote sensing, you connect extra sense wires to the point where the excitation voltage wires connect to the bridge circuit. The extra sense wires serve to regulate the excitation supply to compensate for lead losses and deliver the needed voltage *at* the bridge. This scheme is used with the SCXI-1122.

An alternative remote sensing scheme uses a separate measurement channel to measure directly the excitation voltage delivered across the bridge. Because the measurement channel leads carry very little current, the lead resistance has negligible effect on the measurement. The measured excitation voltage is then used in the voltage-to-strain conversion to compensate for lead losses.

Signal Amplification – The output of strain gauges and bridges is relatively small. In practice, most strain gauge bridges and strain-based transducers will output less than 10 mV/V (10 mV of output per volt of excitation voltage). With a 10 V excitation voltage, the output signal will be 100 mV. Therefore, strain gauge signal conditioners usually include amplifiers to boost the signal level to increase measurement resolution and improve signal-to-noise ratios. SCXI signal conditioning modules, for example, include configurable gain amplifiers with gains up to 2000.

Bridge Balancing, Offset Nulling – When a bridge is installed, it is very unlikely that the bridge will output exactly zero volts when no strain is applied. Rather, slight variations in resistance among the bridge arms and lead resistance will generate some nonzero initial offset voltage. There are a few different ways that a system can handle this initial offset voltage.

1. Software Compensation – The first method compensates for the initial voltage in software. With this method, you take an initial measurement before strain input is applied. This initial voltage is then used in the strain equations listed at the end of this application note. This method is simple, fast, and requires no manual adjustments. The disadvantage of the software compensation method is that the offset of the bridge is not removed. If the offset is large enough, it limits the amplifier gain you can apply to the output voltage, thus limiting the dynamic range of the measurement.
2. Offset-Nulling Circuit – The second balancing method uses an adjustable resistance, or potentiometer, to physically adjust the output of the bridge to zero. For example, Figure 10 illustrates the offset nulling circuit of the SCXI-1321 terminal block. By varying the position of the potentiometer (R_{POT}), you can control the level of the bridge output and set the initial output to zero volts. The value of R_{NULL} sets the range that the circuit can balance. On the SCXI-1321, this resistor is socketed for easy adjustment of the balancing range.

3. Buffered Offset Nulling – The third method, like the software method, does not affect the bridge directly. With buffered nulling, a nulling circuit adds an adjustable DC voltage to the output of the instrumentation amplifier. For example, the SC-2043-SG strain gauge accessory uses this method. The SC-2043-SG includes a user-adjustable potentiometer that can add ±50 mV to the output of an instrumentation amplifier that has a fixed gain of 10. Therefore, the nulling range, referred to input, is ±5 mV.

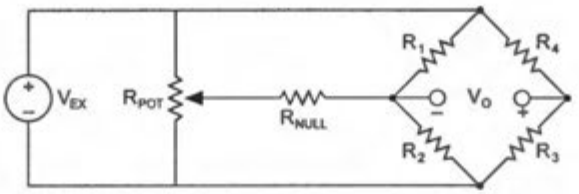

Figure 10. Offset-Nulling Circuit of SCXI-1321 Terminal Block

Shunt Calibration – The normal procedure to verify the output of a strain gauge measurement system relative to some predetermined mechanical input or strain is called shunt calibration. Shunt calibration involves simulating the input of strain by changing the resistance of an arm in the bridge by some known amount. This is accomplished by shunting, or connecting, a large resistor of known value across one arm of the bridge, creating a known ΔR. The output of the bridge can then be measured and compared to the expected voltage value. The results can then be used to correct span errors in the entire measurement path, or to simply verify general operation to gain confidence in the setup.

SCXI and Strain Gauge Measurement

Signal Conditioning eXtensions for Instrumentation (SCXI) is a signal conditioning and data acquisition system for PC-based instrumentation applications. An SCXI system consists of a shielded chassis that houses a combination of signal conditioning input and output modules, which perform a variety of signal conditioning functions. You can connect many different types of transducers, including strain gauges, directly to SCXI modules. The SCXI system can operate as a front-end signal conditioning system for PC plug-in or PCMCIA data acquisition boards. Alternatively, you can use an SCXI data acquisition module that digitizes the analog signals and connects directly to the parallel port of the PC.

Two SCXI modules, the SCXI-1121 and SCXI-1122, are designed for use with strain gauge transducers. Table 1 summarizes some the of the module features that relate to strain gauge measurements.

SCXI-1121 – The SCXI-1121 is a 4-channel isolation amplifier module with transducer excitation. The SCXI-1121 includes an independent gain amplifier and lowpass noise filter on each channel with complete channel-to-channel electrical isolation. Each channel also includes a completely isolated excitation source and a half-bridge completion circuit. The SCXI-1321 terminal block, used with the SCXI-1121 module, adds manual offset-nulling and programmable shunt calibration for each channel.

SCXI-1122 – The SCXI-1122 is a 16-channel signal conditioning module. The SCXI-1122 combines a 16-channel input multiplexer with a single programmable gain isolation amplifier for economical, isolated measurements. The SCXI-1122 also includes a half-bridge completion circuit, shunt calibration, and a single voltage excitation source of 3.333 V.

Table 1. SCXI-1121 and SCXI-1122 Features for Strain Gauges

	SCXI-1121	SCXI-1122
Number of channels	4	16
Electrical isolation	channel-to-channel	input-to-output
Multiplexer scan rate[1]	to 333 kS/s	100 S/s
Amplifier gain	1 to 2000	0.01 to 2000
Excitation voltage source	3.333 V or 10.0 V (one per channel)	3.333 V (one per module)
Excitation current drive	28 mA at 3.333 V 14 mA at 10.0 V (per channel)	225 mA (per module)
Half-bridge completion	Yes	Yes
Offset nulling	Yes[2]	No
Shunt calibration	Yes[2]	Yes
Remote excitation sensing	No	Yes

[1] Multiplexer (mux) scan rate depends on DAQ board or module. Specified rate of 333 kS/s is attaiable with AT-MIO-16E-2 or AT-MIO-16E-1.

[2] With SCXI-1321 terminal block.

Note that Table 1 lists the current drive of the excitation voltage sources. The current drawn by the strain gauge bridge circuit will depend on the gauge resistance, bridge configuration (quarter, half, or full), and the voltage level. Table 2 summarizes the current requirements of common strain gauge bridge configurations. For example, a half-bridge circuit with 120 Ω strain gauges will draw 14 mA from a 3.333 V source, or 43 mA from a 10.0 V source. Therefore, you must configure the SCXI-1121 for 3.333 V excitation, because each channel can provide 28 mA at 3.333 V, but only 14 mA at 10.0 V. The SCXI-1122 can provide 225 mA at 3.333 V, which is enough to drive sixteen 120 Ω half-bridge circuits.

Table 2. Current Requirements for Typical Strain Gauge Circuits

Bridge Configuration	Excitation Voltage	
	3.333 V	10 V
120 Ω full-bridge	28 mA	*83 mA*[1]
120 Ω quarter or half-bridge[2]	14 mA	*43 mA*[1]
350 Ω full-bridge	10 mA	*29 mA*[1]
350 Ω quarter or half-bridge[2]	5 mA	15 mA
1000 Ω full-bridge	3.3 mA	10 mA
1000 Ω quarter or half-bridge[2]	2 mA	6 mA

[1] These configurations exceed the current drive capabilities of the SCXI-1121

[2] Assuming half-bridge completion resistors of R = 4.5 kΩ

SCXI Strain Gauge Application

We will use a real-world application to illustrate the use of SCXI to acquire strain gauge measurements. An experimental aircraft model is instrumented with 16 half-bridge, 350 Ω strain gauge transducers (GF = 2). The model will be placed in a wind tunnel where its performance under simulated wind forces will be measured. From past tests, we can expect strain values to reach no higher than 600 με. A PC will monitor and record the 16 strain parameters.

From the half-bridge equation in Figure 6, the magnitude of the half-bridge output at full strain input will be $(GF \bullet \varepsilon)/2 = 0.3$ mV/V. Therefore, the full-scale bridge output will be 1 mV if the excitation voltage is 3.333 V or 3 mV if the excitation voltage is 10 V.

If per-channel filtering and/or high-speed acquisition are required, then four SCXI-1121 modules should be used. Each channel of the SCXI-1121 would be configured for half-bridge completion, a voltage excitation of 10 V, and a gain of 1000. At this gain, the input range of each channel will be ±5 mV, which can accommodate the ±3 mV output of the bridge. The 16 strain gauge bridges are wired to screw terminals of four SCXI-1321 terminal blocks. This configuration in illustrated in Figure 11.

Alternatively, you could use one SCXI-1122 module to acquire all 16 strain gauge inputs. The maximum scan rate of the SCXI-1122 module is 100 S/s, which for this application will yield a per channel sampling rate of about 6 S/s. If this rate is sufficient, and the per channel filtering and isolation are not required, then the SCXI-1122 may be used. The voltage excitation of the SCXI-1122 is 3.333 V, meaning the strain gauge bridges will output 1 mV. At a gain of 2000, the SCXI-1122 input range is ±5 mV.

Whether the SCXI-1121 or SCXI-1122 is used, the conditioned input signals are multiplexed back to a single plug-in DAQ board or PCMCIA DAQCard. Alternatively, an SCXI digitizer module, such as the SCXI-1200, can digitize the signals locally, communicating to the PC digitally via the PC parallel port or serial communications.

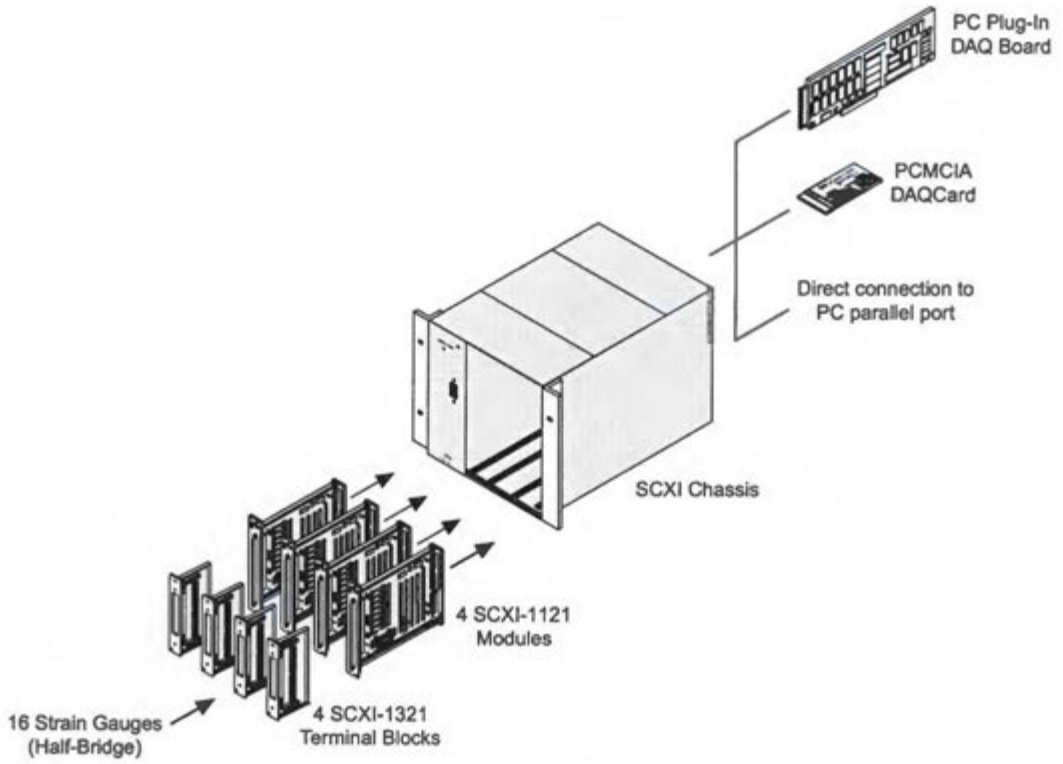

Figure 11. Example SCXI System Configuration for Strain Gauges

SC-2043-SG – Low-Cost Signal Conditioner

For applications that don't require the flexibility, expandability, or rugged packaging of an SCXI system, the SC-2043-SG provides eight channels of low-cost strain gauge signal conditioning. The SC-2043-SG is a circuit board with screw terminals for direct sensor wire connections. A cable connects the output signals from the SC-2043-SG directly to a plug-in DAQ board, PCMCIA DAQCard, or DAQPad-1200 parallel port device, as illustrated in Figure 12. Features of the SC-2043-SG are listed in Table 3.

Table 3. SC-2043-SG Features for Strain Gauges

	SC-2043-SG
Number of channels	8
Amplifier gain	10 (in addition to DAQ board gain)
Excitation voltage source	2.5 V, or user can supply voltage
Excitation current drive	167 mA
Excitation sensing	Yes, local sensing
Half-bridge completion	Yes (with sockets for quarter-bridge completion resistors)
Offset nulling	Yes
Shunt calibration	No

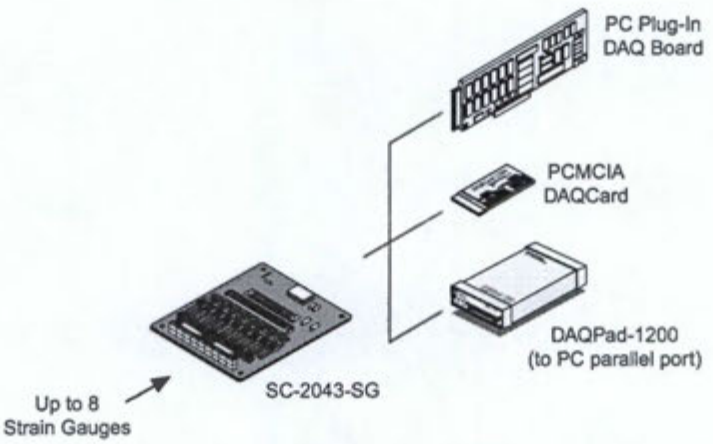

Figure 12. Strain Gauge Measurement with SC-2043-SG Signal Conditioner

Strain Gauge Equations

This section includes the complete strain gauge equations for several types of bridge configurations. These equations are included as callable functions (with source code) with the NI-DAQ driver software. The function names are `Strain_Convert` and `Strain_Buf_Convert`. With LabVIEW, these equations are included in the *Convert Strain Gauge Reading.vi* in the DAQ Utilities menu.

To simplify the equations and account for unbalanced bridges in the nonstrained state, let us introduce the ratio V_r:

$$V_r = \frac{V_{O(strained)} - V_{O(unstrained)}}{V_{EX}}$$

where $V_{O(strained)}$ is the measured output when strained, and $V_{O(unstrained)}$ is the initial, unstrained output voltage. V_{EX} is the excitation voltage.

Also, the designation (+ε) and (–ε) indicates active strain gauges mounted in tension and compression, respectively. The designation (–νε) indicates that the strain gauge is mounted in the transversal direction, so that its resistance change is primarily due to the Poisson's Strain, whose magnitude is given as –νε.

Other nomenclature used in the equations include:

R_G = nominal resistance value of strain gauge

GF = gauge factor of strain gauge

R_L = lead resistance

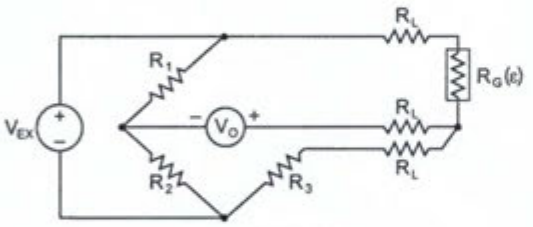

Quarter-Bridge I

$$\text{strain}(\varepsilon) = \frac{-4V_r}{GF(1+2V_r)} \bullet \left(1 + \frac{R_L}{R_G}\right)$$

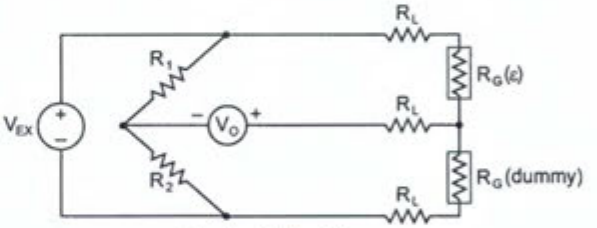

Quarter-Bridge II

$$\text{strain}(\varepsilon) = \frac{-4V_r}{GF(1+2V_r)} \bullet \left(1 + \frac{R_L}{R_G}\right)$$

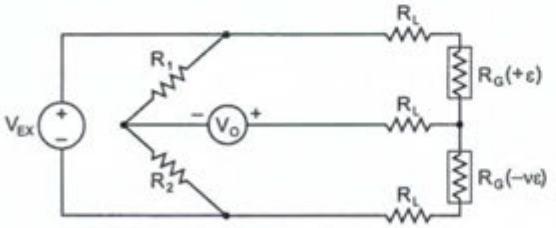

Half-Bridge I

$$\text{strain}(\varepsilon) = \frac{-4V_r}{GF[(1+\nu) - 2V_r(\nu - 1)]} \bullet \left(1 + \frac{R_L}{R_G}\right)$$

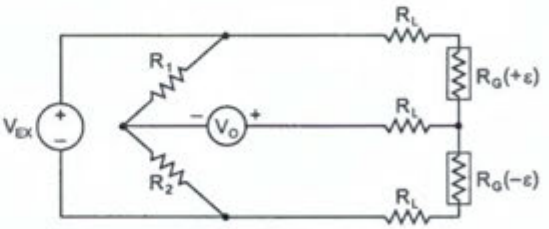

Half-Bridge II

$$\text{strain}(\varepsilon) = \frac{-2V_r}{GF} \bullet \left(1 + \frac{R_L}{R_G}\right)$$

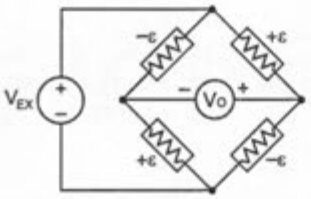

Full-Bridge I

$$\text{strain}(\varepsilon) = \frac{-V_r}{GF}$$

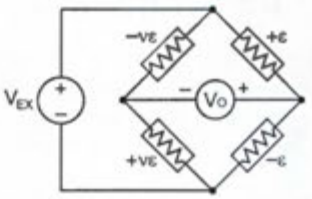

Full-Bridge II

$$\text{strain}(\varepsilon) = \frac{-2V_r}{GF(\nu + 1)}$$

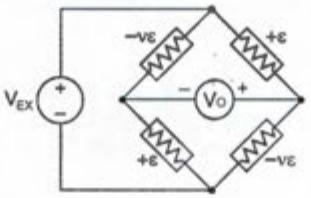

Full-Bridge III

$$\text{strain}(\varepsilon) = \frac{-2V_r}{GF[(\nu + 1) - V_r(\nu - 1)]}$$

341023C-01 Aug98

Appendix 9

Datasheet of used strain gauge apparatus

LORD DATASHEET

SG-Link®-LXRS®

Wireless 2 Channel Analog Input Sensor Node

SG-Link®-LXRS® - *small, low-power two-channel analog sensor node with many sampling options*

LORD MicroStrain® LXRS® Wireless Sensor Networks enable simultaneous, high-speed sensing and data aggregation from scalable sensor networks. Our wireless sensing systems are ideal for sensor monitoring, data acquisition, performance analysis, and sensing response applications.

The **gateways** are the heart of the LORD MicroStrain wireless sensing system. They coordinate and maintain wireless transmissions across a network of distributed wireless sensor **nodes**. The LORD MicroStrain LXRS wireless communication protocol between LXRS nodes and gateways enable high-speed sampling, ±32 microseconds node- to- node synchronization, transmission range up to 2 kilometers, and lossless data throughput under most operating conditions.

Users can easily program nodes for data logging, continuous, and periodic burst sampling with the **Node Commander®** software. The web-based **SensorCloud™** interface optimizes data aggregation, analysis, presentation, and alerts for gigabytes of sensor data from remote networks.

Wireless Simplicity, Hardwired Reliability™

Product Highlights

- One differential and one single-ended analog input channel and an internal temperature sensor
- Ideal for remote and long term measurement of many Wheatstone bridge and analog-type sensors including: strain, force, torque, pressure, acceleration, vibration, magnetic field, displacement and geophones
- Supports continuous, burst, and event-triggered sampling and datalogging to internal memory
- User-programmable sample rates up to 4096 Hz
- IP65/66 environmental enclosures available

Features and Benefits

High Performance

- Scalable, long range wireless sensor networks up to 2 km
- Lossless data throughput under most operating conditions

Ease of Use

- Rapid deployment with wireless framework
- Low power consumption allows extended use.
- Remotely configure nodes, acquire and view sensor data with Node Commander®.
- Optional web-based SensorCloud™ interface optimizes data storage, viewing, and analysis.
- Easy integration via comprehensive SDK

Cost Effective

- Out-of-the box wireless sensing solution reduces development and deployment time.
- Volume discounts

Applications

- Condition-based monitoring
- Health monitoring of rotating components, aircraft, structures, and vehicles
- Experimental test and measurement
- Robotics and machine control

LORD MicroStrain®
SENSING SYSTEMS

SG-Link®-LXRS® Wireless 2 Channel Analog Input Sensor Node

Specifications

General	
Sensor input channels	**Differential analog,** 1 channel **Single-ended analog,** 1 channel
Integrated sensors	**Internal temperature,** 1 channel
Data storage capacity	2 M bytes (up to 1,000,000 data points, data type dependent)
Analog Input Channels	
Measurement range	Differential: full-bridge, ≥ 350 Ω (factory configurable) Single-ended: 0 to 3 V dc
Accuracy	±0.1% full scale typical
Resolution	12 bit
Anti-aliasing filter bandwidth	Single-pole Butterworth -3 dB cutoff @ 250 Hz (factory configurable)
Bridge excitation voltage	+3 V dc, 50 mA total for all channels (pulsed @ sample rates ≤ 16 Hz to conserve power)
Measurement gain and offset	User-selectable in software on differential channels, gain values from 104 to 1800
Integrated Temperature Channel	
Measurement range	-40 °C to 85 °C
Accuracy	±2 °C (at 25 °C) typical
Resolution	12 bit
Sampling	
Sampling modes	Synchronized, low duty cycle, datalogging
Sampling rates	**Continuous sampling:** 1 sample/hour to 512 Hz **Periodic burst sampling:** 32 Hz to 4096 Hz **Datalogging:** 32 Hz to 4096 Hz
Sample rate stability	±3 ppm
Network capacity	Up to 2000 nodes per RF channel (and per gateway) depending on the number of active channels and sampling settings. Refer to the system bandwidth calculator: http://www.microstrain.com/configure-your-system
Synchronization between nodes	± 32 µsec
Operating Parameters	
Radio frequency (RF) transceiver carrier	2.405 to 2.470 GHz direct sequence spread spectrum over 14 channels, license free worldwide, radiated power programmable from 0 dBm (1 mW) to 16 dBm (39 mW); low power option available for use outside the U.S.- limited to 10dBm (10mW)
RF range	**70 m to 2 km line of sight** with RF power setting
RF communication protocol	IEEE 802.15.4
Power source	Internal: 3.7 V dc, 250 mAh Lithium ion rechargeable battery External: +3.2 to +9.0 V dc
Power consumption	See power profile : http://files.microstrain.com/SG-Link-LXRS-Power-Profile.pdf
Operating temperature	-20 °C to +60 °C (extended temperature range available with custom battery/enclosure, -40 °C to +85 °C electronics only)
Acceleration limit	500 *g* standard (high *g* option available)
Physical Specifications	
Dimensions	58 mm x 50 mm x 21 mm
Weight	42 grams
Environmental rating	Indoor use (IP65/66 enclosures available)
Enclosure material	ABS plastic
Integration	
Compatible gateways	All WSDA® base stations and gateways
Compatible sensors	Bridge type analog sensors, 0 to 3 V dc analog sensors
Connectors	Screw terminal block
Shunt calibration	Internal shunt calibration resistor 499 KΩ, differential channel
Software	SensorCloud™, Node Commander®, Windows XP/Vista/7
Software development kit (SDK)	Data communications protocol available with EEPROM maps and sample code (OS and computing platform independent) http://www.microstrain.com/wireless/sdk
Regulatory compliance	FCC (U.S.), IC (Canada), CE, ROHS

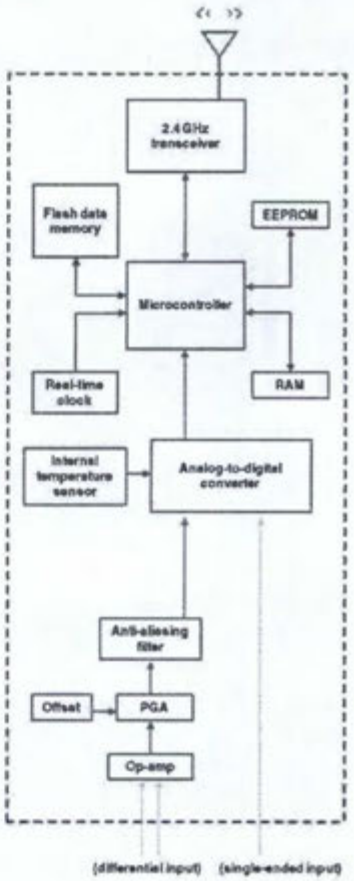

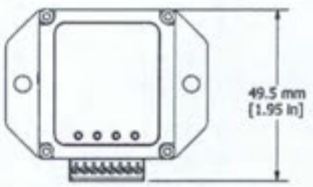

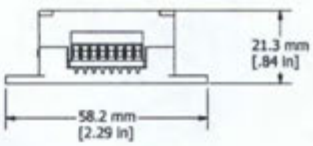

LORD Corporation
MicroStrain® Sensing Systems
459 Hurricane Lane , Suite 102
Williston, VT 05495 USA
www.microstrain.com

ph: 802-862-6629
fax: 802-863-4093
sensing_sales@LORD.com
sensing_support@LORD.com